

AD626185

STUDY OF HEAT TRANSFER AND FOULING OF  
HEAT TRANSFER SURFACES IN THE DEEP OCEAN

FINAL REPORT

U S NAVAL CIVIL ENGINEERING LABORATORY

PORT HUENEME, CALIFORNIA

CONTRACT NBy 32274

Project 2650-P

November 26, 1965

**Best  
Available  
Copy**

US NAVAL CIVIL ENGINEERING LABORATORY  
PORT HUENEME, CALIFORNIA  
STUDY OF HEAT TRANSFER AND FOULING OF  
HEAT TRANSFER SURFACES IN THE DEEP OCEAN  
FINAL REPORT

CONTRACT NBy 32274

PROJECT 2650-P

C F BRAUN & CO  
ALHAMBRA, CALIFORNIA  
NOVEMBER 26, 1965

## ABSTRACT

The aim of this study is to furnish enough information to adequately design natural convection heat rejection surfaces in medium to deep ocean environments (300 to 20,000 feet). We developed information on heat transfer, biological fouling, and corrosion under the given conditions.

Several corrosion and marine fouling tests on heated metal surfaces were performed in the ocean. These experiments consisted of a 120-day shallow ocean test and two 5-day deeper ocean tests at depths of 300 and 4,500 feet in Southern California waters. Four cylindrical elements, each containing three different metals electrically isolated from one another, comprised the test unit.

Test results revealed that marine fouling did not occur on heated metal surfaces above 100 F. Corrosion scale formation was not greatly affected by temperature over the range 100 to 140 F. However, corrosion scale lowered overall heat transfer coefficients of some of the metal elements.

A literature survey of natural convection heat transfer from both single and multiple vertical surfaces to water indicated that additional experimentation was necessary in the turbulent region. No published data were found for natural convection heat transfer from vertical finned surfaces at the high Rayleigh numbers expected in seawater. Only a small portion of an undersea heat rejection surface is likely to operate in the laminar region.

A semiempirical mathematical model was proposed for turbulent natural convection heat transfer and flow. It demonstrated that boundary layer growth can limit fin spacing or height of surface. We also presented a new technique to optimize the geometry of a finned heat transfer surface with respect to the gross heat transfer coefficient. This technique includes fin spacing in addition to generally accepted variables and allows for nonuniformity of heat transfer coefficient over a finned surface.

Turbulent natural convection heat transfer experiments were performed with electrically heated flat-plate and cylindrical modules in a 5.5-foot diameter, 25-foot high column simulator filled with water. Vertical flat plate experimental results verified Saunders' equation over a Rayleigh number range of  $2.0 \times 10^9$  to  $3.6 \times 10^{12}$ . In the case of vertical cylinders, experimental Nusselt numbers fell higher than Saunders' equation at high-heat fluxes and fell lower at low-heat fluxes. Measured boundary layer temperature profiles indicated that over 10 percent of the total temperature driving force is present at the predicted boundary layer thickness.



## ABSTRACT Continued

Agreement between predicted and observed gross heat transfer coefficients was quite good for finned vertical flat plates. For vertical finned cylinders, the predicted coefficients greatly exceeded the measured ones. Spacing between finned flat plates or finned cylinders within the experimental range did not measurably affect gross heat transfer coefficients.

Chimney and inlet flow restriction experiments revealed a strong side flow effect which must be recognized when extrapolating these data to larger units. Small crosscurrents significantly increased gross heat transfer coefficients of the finned units.

A conceptual design study was conducted for an undersea convector section of a 500 kw (e) fuel cell. We constructed a prototype unit and tested it for 54 hours in Port Hueneme harbor. Experimental data confirmed the laboratory test data and the design approach.

To establish the factors affecting the penetration and propagation of the upwelling from an underwater heat source, normally referred to as the plume, we surveyed the literature on the dynamics of free jet flow. Generally, the theoretical fundamentals for jet flow agree with experimental data obtained with gases, particularly air. Experimental work on liquid plumes is negligible. In our study, we considered various factors affecting thermal upwelling. For the turbulent flow of the ocean plume, adiabatic cooling will have negligible effect. Directionally, it will tend to reduce the penetration. The extent to which Coriolis force will reduce penetration depends on the magnitude of currents and the latitude. Temperature stratification and ocean currents will limit drastically propagation of the plume.

We developed a mathematical model of the turbulent plume. It predicts the penetration, the entrainment into, and the dissipation of the thermal jet from an underwater heat source. The method provides for the uniform and the stably stratified ocean. The model was applied to three typical applications and four experimental conditions encountered during this study. Experimental plume data from the shallow ocean tests indicate the penetration predicted from the model is generally conservative. The plumes predicted for heat sources located at depths of 300 and 1,000 feet do not reach the surface of the ocean.

The design criteria developed from this investigation are presented in a single chapter. We included step-by-step procedures for designing an undersea finned heat rejection surface and for estimating the flow and penetration of a turbulent plume above an underwater heat source.

## CONTENTS

	PAGE
I Introduction	
Purpose and Scope	I-1
Background of Undersea Power Sources	I-2
Remarks on Report Organization	I-3
II Marine Fouling and Corrosion Tests	
Abstract	II-1
Literature Survey	II-1
General Test Program Criteria	II-3
Shallow Water Test	II-5
300-Foot Test	II-29
4,500-Foot Test	II-41
Discussion	II-51
Conclusions and Recommendations	II-54
Terms and Symbols, Chapter II	II-57
III Natural Convection Heat Transfer	
Abstract	III-1
Literature Survey	III-1
Vertical Flat Plate and Cylinder Mathematical Models	III-17
Optimum Fin Geometry in Free Convection	III-22
Terms and Symbols, Chapter III	III-42
IV Natural Convection Heat Transfer Tests	
Abstract	IV-1
Experimental Equipment and Methods	IV-2
Results and Discussion	IV-16
Conclusions and Recommendations	IV-44
Terms and Symbols, Chapter IV	IV-47
V Flow of a Turbulent Plume	
Abstract	V-1
Literature Survey	V-1
Model of Turbulent Plume	V-15
Applications	V-30
Experimental Results and Discussion	V-40
Conclusions and Recommendations	V-63
Terms and Symbols, Chapter V	V-65

## CONTENTS Continued

	PAGE
VI Designing Underwater Heat Rejection Surfaces	
Abstract	VI-1
General Considerations	VI-1
Marine Fouling, Corrosion, and Material Selection	VI-3
Heat Transfer by Free Convection	VI-4
Design Method	VI-8
Plume Profile Method	VI-11
Terms and Symbols, Chapter VI	VI-15
Appendixes	
A Engineering Agreement	A-1
B Physical Properties of Seawater and Water	B-1
C A Deep Ocean Mooring System	C-1
D Laminar and Turbulent Natural Convection	
Boundary Layer Equations	D-1
E Conceptual Design of An Undersea Heat Rejection	
Surface	E-1
F Case 3 - Plume Calculations	F-1
G Port Hueneme Harbor Test Data	G-1

## LIST OF FIGURES

	PAGE
1 Natural Convection Heat Transfer Unit - Shallow Ocean Tests	II-6
2 Shallow Water Test Unit Photograph	II-7
3 Shallow Water Test Instrumentation	II-10
4A Shallow Water Test - 100 F Element Fouling	II-12
4B Shallow Water Test - 100 F Element Fouling	II-13
5A Shallow Water Test - 120 F Element Fouling	II-14
5B Shallow Water Test - 120 F Element Fouling	II-15
6 Shallow Water Test - 140 F Element Fouling	II-16
7A Shallow Water Test - Fouling of Ambient Specimens	II-17
7B Shallow Water Test - Fouling of Ambient Specimens	II-18
7C Shallow Water Test - Fouling of Ambient Specimens	II-19
8 Shallow Water Test Unit After Recovery	II-20
9 Monel Specimen Appearance After the Shallow Water Test	II-23
10 Appearance of 70 Cu-30 Ni and Aluminum Bronze After the Shallow Water Test	II-24
11 Shallow Water Test Heat Transfer Coefficient Versus Time	II-28
12 Natural Convection Heat Transfer Unit - Deep Ocean Tests	II-31
13 Deep Ocean Test Unit Photograph	II-32
14 Deep Ocean Test Instrumentation	II-34
15 300-Foot Test Mooring Design	II-36
16 Appearance of Aluminum Bronze, Monel, and 70 Cu-30 Ni After the 300-Foot Test	II-39

## LIST OF FIGURES Continued

	PAGE
17 300-Foot Test Heat Transfer Coefficient Versus Time	II-40
18 The Tug Laguna and the Sea Quest	II-42
19 Slack Line Mooring Test System	II-44
20 Taut Line Mooring Test System	II-45
21 Mooring Configurations for Design Conditions	II-46
22 Weak Link Arrangement	II-47
23 Appearance of Monel and 70 Cu-30 Ni After the 4,500-Foot Test	II-50
24 4,500-Foot Test Heat Transfer Coefficient Versus Time	II-52
25 Experimental Data on Laminar Natural Convection Heat Transfer from Vertical Surfaces to Water	III-5
26 Turbulent Natural Convection Heat Transfer Data for Water - Vertical Plates or Cylinders of Diameters Greater than 2 inches	III-7
27 Boundary Layer Thickness in Turbulent Natural Convection	III-23
28 Optimum Fin Thickness Versus Fin Spacing -	III-33
$\left( \frac{2 h_o}{k_m} \right)^{1/2} 0.30 \text{ (inches)}^{-1/2}$	
29 Optimum Fin Thickness Versus Fin Spacing -	III-34
$\left( \frac{2 h_o}{k_m} \right)^{1/2} 0.50 \text{ (inches)}^{-1/2}$	
30 Optimum Fin Thickness Versus Fin Spacing -	III-35
$\left( \frac{2 h_o}{k_m} \right)^{1/2} 0.70 \text{ (inches)}^{-1/2}$	

## LIST OF FIGURES Continued

	PAGE
31 Optimum Fin Thickness Versus Fin Spacing -	III-36
$\left( \frac{2 h_o}{k_m} \right)^{1/2} = 0.90 \text{ (inches) }^{-1/2}$	
32 Optimum Fin Thickness Versus $\left( \frac{2 h_o}{k_m} \right)^{1/2}$ , Fin Spacing = 1.2 inches	III-37
33 Ratio of Gross Heat Transfer Coefficient to Metal Thermal Conductivity Versus Fin Spacing -	III-38
$\left( \frac{2 h_o}{k_m} \right)^{1/2} = 0.3 \text{ (inches) }^{-1/2}$	
34 Ratio of Gross Heat Transfer Coefficient to Metal Thermal Conductivity Versus Fin Spacing -	III-39
$\left( \frac{2 h_o}{k_m} \right)^{1/2} = 0.5 \text{ (inches) }^{-1/2}$	
35 Ratio of Gross Heat Transfer Coefficient to Metal Thermal Conductivity Versus Fin Spacing -	III-40
$\left( \frac{2 h_o}{k_m} \right)^{1/2} = 0.7 \text{ (inches) }^{-1/2}$	
36 Ratio of Gross Heat Transfer Coefficient to Metal Thermal Conductivity Versus Fin Spacing -	III-41
$\left( \frac{2 h_o}{k_m} \right)^{1/2} = 0.9 \text{ (inches) }^{-1/2}$	
37 Column Simulator - P&I Flow Diagram	IV-3
38 Column Simulator	IV-4

## LIST OF FIGURES Continued

	PAGE
39 Plate Natural Convection Heat Transfer Unit	IV-5
40 Vertical Finned Flat Plate Test Unit	IV-7
41 Analog Map of Temperature Distribution in Vertical Finned Flat Plate	IV-8
42 Cylinder Natural Convection Heat Transfer Unit	IV-10
43 Two-Inch Diameter Cylindrical Test Unit	IV-11
44 One-Inch Diameter Cylindrical Test Unit	IV-12
45 Boundary Layer Temperature Probe	IV-14
46 Natural Convection Heat Transfer Test Results Vertical Flat Plate in Water	IV-17
47 Vertical Flat Plate Boundary Layer Temperature Profile	IV-19
48 Vertical Finned Flat Plate Test Results	IV-20
49 Comparison of Observed and Predicted Gross Heat Transfer Coefficients - Finned Vertical Plates	IV-21
50 Channel Temperature Profile for Vertical Finned Flat Plate	IV-24
51 Effect of Spacing Between Two Vertical Finned Flat Plates on $h_G$	IV-26
52 Chimney Test Results - Vertical Finned Flat Plate Test Unit	IV-27
53 Inlet Clearance Test Results - Vertical Finned Flat Plate Test Unit	IV-28
54 Vertical 2-Inch Diameter Cylinder Test Results	IV-30
55 Vertical 1-Inch Diameter Cylinder Test Results	IV-31
56 Effect of Heat Flux on Nusselt Number - Vertical Cylinders	IV-32

## LIST OF FIGURES Continued

	PAGE
57 Vertical Finned 2-Inch Diameter Cylinder Test Results	IV-35
58 Effect of Spacing Between Finned Vertical Cylinders on $h_G$	IV-37
59 Chimney Test Results - Vertical 2-Inch Diameter Finned Cylinder Test Unit	IV-39
60 Inlet Clearance Test Results - Vertical 2-Inch Diameter Finned Cylinder Test Unit	IV-40
61 Current Test Results - Vertical Finned Flat Plate Unit	IV-41
62 Current Test Results - Vertical 2-Inch Diameter Finned Cylinder Test Unit	IV-43
63 Prototype Natural Convection Heat Transfer Unit	IV-44
64 Idealized Plume Development	V-3
65 Plume Entrainment Correlation	V-14
66 Variation of Mean Bulk Temperature Difference with Height above the Heat Exchanger	V-35
67 Case 1 Variation of Temperature Difference and Radius of Plume with Height	V-36
68 Case 1 Variation of Mass Flow Ratio, Vertical Velocity and Radius of Plume with Height	V-37
69 Case 3 Variation of Temperature Difference and Radius of Plume with Height	V-38
70 Case 3 Variation of Mass Flow Ratio, Vertical Velocity and Radius of Plume with Height	V-39
71 Set 1 Mean Plume Temperature at $z_1 = 0$ feet	V-43
72 Set 1 Mean Plume Temperature at $z_2 = 0.5$ feet	V-44
73 Set 1 Plume Temperature Profile	V-45
74 Set 1 Plume Buoyancy Decay	V-46



## LIST OF FIGURES Continued

	PAGES
75 Set 1 Plume Profile	V-48
76 Set 2 Plume Buoyancy at Source	V-49
77 Set 2 Plume Flow Rate and Velocity at Source	V-51
78 Set 2 Intensity of Plume Source	V-52
79 Set 2 Plume Buoyancy Decay	V-53
80 Set 2 Plume Profile	V-54
81 Vertical Finned Cylinder Unit in Shallow Ocean	V-56
82 Plume Temperature Probe for Shallow Ocean Tests	V-57
83 Set 3 Plume Buoyancy Decay without Shroud	V-58
84 Set 4 Plume Buoyancy Decay with Shroud	V-59
85 Sets 3 and 4 Plume Profiles	V-61
86 Correlation of Plume Source Intensity with Development Distance Ratio	V-62
B-1 Vertical Temperature Gradient for Model Ocean	B-4
B-2 Thermal Expansion of Water per Degree F	B-5
B-3 Water Heat Transfer Physical Property Group versus Temperature	B-7
B-4 Water Prandtl Number versus Temperature	B-8
E-1 $N_2H_4 - H_2O_2$ Fuel Cell Simplified Schematic	E-9
G-1 Ocean Tide and Depth	G-2
G-2 Ocean Temperature Profile	G-3
G-3 Ocean Temperature Profile	G-4
G-4 Ocean Ambient Temperature - Plume Temperature Probe Data	G-5

## LIST OF TABLES

	PAGE
I Chemical Composition of Metal Corrosion and Fouling Specimens	II-8
II Shallow Water Test Corrosion Results	II-22
III Shallow Water Test Heat Transfer Data	II-26
IV Sea Quest Specifications	II-30
V 300-Foot Test Corrosion Results	II-37
VI 4,500-Foot Test Corrosion Results	II-49
VII Turbulent Natural Convection Equations	III-13
VIII Vertical Finned Flat Plate Results	IV-22
IX Vertical Finned 2-Inch Diameter Cylinder Results	IV-34
X Case 1 Summary of Calculated Results	V-31
XI Case 2 Summary of Calculated Results	V-32
XII Case 3 Summary of Calculated Results	V-33
XIII Plume Heat Source Dimensions	V-41
B-1 Specific Volume of Seawater	B-1
B-2 Coefficient of Thermal Expansion of Seawater	B-2
B-3 Viscosity of Seawater	B-2
B-4 Specific Heat of Seawater	B-3
E-1 Heat Rejection Surface Design Computations	E-7
G-1 Gross Heat Transfer Coefficient Data	G-1

## CHAPTER I, INTRODUCTION

## PURPOSE AND SCOPE

The intent of this investigation is to furnish enough information to adequately design natural convection heat rejection surfaces for power generators in medium to deep ocean environments (300 to 20,000 feet). Results are to be general enough to cover thermoelectric, steam or other vapor cycle, and fuel cell energy convectors. Information has been developed on heat transfer, biological fouling, and corrosion under the given conditions to meet this goal.

The study was divided into four phases. In Phase I, we summarized pertinent literature and mathematically attacked natural convection flow on vertical surfaces and flow of a plume rising above an underwater heat source.

Phase II consisted of conducting marine fouling and corrosion experiments in the ocean. Cylindrical and flat-plate elements at temperatures of 100, 120, and 140 F were tested at depths of 15 feet (dockside), 300, and 4,500 feet (open ocean). The dockside experiment lasted 120 days, while the two open ocean tests each lasted five days.

At the conclusion of the Phase I mathematical analysis, we started Phase III. It included laboratory experiments on natural convection heat transfer and behavior of the plume. The tests, designed to check mathematical models and to explore circumstances not amenable to mathematical analysis, were performed in a 5.5-foot diameter, 25-foot high column simulator filled with water. Electrically heated modules were suspended in the water for the experiments. At the conclusion of this phase, sufficient information was to be available to design an undersea heat rejection surface. Mathematical solutions were checked and experimental findings were correlated in a scheme useful for design.

In Phase IV, a conceptual design study of heat rejection surfaces was performed. We then fabricated a prototype for testing in a shallow ocean basin. By comparing the prototype test results with design criteria developed in the earlier three phases, we developed finalized design criteria for undersea heat rejection surfaces.

## BACKGROUND OF UNDERSEA POWER SOURCES

Large quantities of electric power will be consumed in man's future exploration and utilization of the ocean depths. Power will be required for undersea construction, lighting, communication, etc. Transmission from a shore station would be impractical in most instances.

The Naval Civil Engineering Laboratory, Port Hueneme, California, performed a brief study of undersea nuclear power in mid-1963 (1). They concluded that a self-regulating, isolated reactor was feasible, provided a number of technical roadblocks were removed. Three problem areas appeared to justify special effort. First, placement of a large reactor appeared to be beyond the state of the art. A reactor-placement study contract was let and the work was completed recently (2). Second, corrosion and marine growth characteristics of heat transfer surfaces in the deep ocean were unknown. Third, more information on natural convection heat transfer and thermal upwelling was necessary to adequately design undersea heat rejection surfaces. The last two problem areas comprise the present study.

Deep ocean power requirements will range from a few milliwatts to megawatts (3,6). Batteries and small isotopic generators should be able to supply the low power requirements. According to Fowler and Sievering (6), radioisotope electric power systems are available today in the range of a few milliwatts to 60 watts. The Atomic Energy Commission plans to extend this range to 200 watts in the SNAP-23 program (6). Several isotope electric power generators are operating now in the ocean at depths to 16,000 feet.

Fuel cells appear to be feasible for deep ocean electric power generation. However, none are known to be operational to date. Theoretically, a fuel cell is a very efficient energy conversion device. Practical operating thermal efficiencies (7) range from 25 percent (hydrocarbon-oxygen) to 70 percent (hydrogen-oxygen). The primary disadvantage of the fuel cell for undersea power generation is its continual need for fuel and oxidant and the resultant storage problem. Fuel cells do not have the capacity for long-term isolated operation that is inherent in a nuclear power plant. They may, however, be used in the future to provide intermediate range power levels.

## BACKGROUND OF UNDERSEA POWER SOURCES Continued

A nuclear power plant will probably be required to supply high energy requirements. One study (4) has proposed a 3-megawatt generator based on a nuclear reactor heat source and lead-telluride thermoelectric convertors. Waste heat from the device would be rejected to the surrounding ocean water from finned-plate surfaces 10 feet long by 2.5 feet high which are mounted above the reactor at a 45-degree angle from horizontal. The control rod positioning device would be the only moving part.

Another conceptual study proposed a completely static energy and power conversion system to produce 100 kw (5). The plant was a self-pressurized, natural circulation, PWR system with a lead telluride and bismuth antimony telluride thermoelectric convertor. Heat was rejected to the ocean water by natural convection from finned-vertical plates over 4 feet high.

The Naval Civil Engineering Laboratory study (1) indicated that the preferred waste heat rejection means from a submerged electric power source would be natural convection heat transfer to the surrounding ocean water. A relatively large temperature difference would be present, since deep ocean waters are typically a few degrees above freezing. By properly using extended surfaces, heat transfer units could be relatively compact.

## REMARKS ON REPORT ORGANIZATION

This report primarily presents results, discussion, and conclusions of heat transfer, corrosion, and marine fouling experiments. However, since the aim of the study is to present information useful for design, we have added Chapter VI, Designing Underwater Heat Rejection Surfaces. This chapter describes the many design criteria that evolved from our investigation without the backup research data presented in the other chapters. We hope that this approach will best fill the needs of both designers and researchers.

## CHAPTER II, MARINE FOULING AND CORROSION TESTS

## ABSTRACT

Results of a series of corrosion and fouling tests on heated surfaces in the ocean are given in this chapter. The experimental program consisted of a 120-day shallow water test and two 5-day ocean tests conducted at depths of 300 and 4,500 feet in Southern California waters. Four 2-inch OD cylindrical elements, each containing three different metals electrically insulated from one another, made up the test unit. The metals included Monel, 90-10 cupronickel, 70-30 cupronickel, aluminum bronze, beryllium copper, HH brass, naval brass, silicon bronze, HC copper, and titanium.

Test results showed that marine fouling did not occur on heated surfaces above 100 F. Corrosion scale formation was not greatly affected by temperature over the range 100 - 140 F. Overall heat transfer coefficients of some of the elements were influenced by scale.

## LITERATURE SURVEY

**MARINE FOULING** A search of the literature yielded no published information on either corrosion or biological fouling of metal surfaces held within a temperature range of 100 - 140 F in an ocean environment. Robert L Eberhardt's\* following summary of published fouling articles points out some of the more important fouling variables and discusses their effects.

Fouling begins with the attachment of embryonic forms upon all surfaces placed in seawater, concluded Stewart (24) and ZcBell (34). These small forms are subsequently replaced by larger and adult organisms, which eventually form a mat or secondary layer. The makeup of this organic assemblage varies in profusion and variety with environmental conditions, Woods Hole Oceanographic Institution (32). However, even though gross environmental parameters are discussed, observations are limited on variations of fouling density related to depth, distance from shore, or aspects of benthal environments. The most specific information can be obtained from references by DePalma (12,13), Gray (14,15), Muracka (19,20), and Reinhart (21). Connolly (10), Hazard (16), and Snoke (22) have reported on fouling on submarine cables.

\*Robert L Eberhardt, Oceanography Department  
Lockheed-California Company

## LITERATURE SURVEY Continued

Perhaps the two most important factors that influence structures upon which fouling has occurred are reduction of the effectiveness of anticorrosion coverings and increased resistance generated to passing currents of water, US Naval Civil Engineering Laboratory (27). A third is that corrosive anaerobic action can take place underneath a protective layer of foulers, per Caldwell (8).

Fouling will ultimately occur upon smooth surfaces, including those as smooth as glass, according to ZoBell (34) and Clapp in Uhlig (26). Bacteria are the first organisms to foul and accompany adsorbed organic material and dissolved substances. This primary film grows, and in doing so, enmeshes additional detritus, bacteria, and next, diatoms. Larvae of sedentary organisms then appear in rapid succession.

Dark colors are preferred by fouling organisms, for it has been noted less fouling occurs on whites, greys, and yellows. Beyond 600 feet, this factor must be of negligible effect, since light virtually disappears between 500 to 1,000 feet.

Moritz (18) notes that beyond 40 feet infestations are light, except near the bottom. In the standard text, "Marine Fouling and Its Prevention", it is stated that fouling can be continuous as far as 462 feet. The reference here is to a hydrozoan. Turner (25) describes anemones, burrowing sponges and small snails at 100 feet in the La Jolla area.

Davis and Barham (11) list fouling species at 200 feet at a location west of San Diego. They report the most common species to be the calcareous false jingle *Pododesmus*, the anemone *Metridium*, the sea lettuce *Ulva*, and red algae with bryozoans. DePalma (12,13) has summarized that fouling organisms in the Tongue of the Ocean, Bahamas, are incidental beyond 500 feet and virtually absent from that level to 5,280 feet, where they are slight or sparse. At 5,730 feet he noted a single *Xylophaga*, a boring mollusc, as has Muraoka (20) at 5,640 feet off Southern California.

Velocity of water will act as an inhibiting factor. Water moving at less than 2 to 4 knots is necessary for sedentary organisms to attach themselves, per Hutchins in Uhlig (26) and Wood (31).

## LITERATURE SURVEY Continued

Two reports note the occurrence of bacteria at 78,000 and 68,000 to 76,500 per square inch on plates exposed for five days at 30 feet in California and Australia, respectively, states ZoBell in Wood (30). Turner, in an unpublished report, noted that the microscopic fouling film in the San Diego area was made up of bacteria, diatoms, and filamentous algae. This same film was replaced in thirty days by encrusting bryozoans and serpulid casts. In previous reports, according to Turner (25), similar assemblages occurred. Vaughan (28) refers to similar successions at 100 feet depth on oil rigs off the California coast.

Milligan (17) has concluded that protection against fouling organisms is not necessary beyond 1,000 feet. Hot water is perhaps the most economical means to use in destroying established colonies of foulers. Wood (31) reports a total kill can be achieved by exposure to ten minutes of 107 F water, and Chadwick (9) used 115 F for hourly periods each five weeks. Barnacles and mussels are killed at 127 F within fifteen minutes. White (29) and Stewart (24) also reported on control by heated water. Steinberg (23) and Connolly (10) cite the relative imperviousness of organic thermoplastics to biological corrosion.

**CORROSION** While we found no published information on corrosion of heated metal surfaces in the deep ocean, some testing has been undertaken with unheated materials. Gray (36) reported on an extensive, long-term corrosion test involving several materials in 1964. Muraoka (37), in 1962, gave the effects of attached marine organisms upon substrate corrosion. Woods Hole Oceanographic Institution (38) also presented some corrosion data in the publication *Marine Fouling and Its Prevention*. Corrosion rates of several metals in Port Hueneme harbor have been documented by Brouillette (35) in 1958.

## GENERAL TEST PROGRAM CRITERIA

The Southern California coast offers a convenient locale to study deep-water fouling, because depths up to 6,000 feet are within a one-day steaming range. Data obtained from this area are, of course, specific to this location only. However, some valuable generalizations can be made.

A depth range of 300 to 20,000 feet is being considered for reactor placement. We chose for convenience to perform ocean tests at 300 feet (the upper limit of reactor placement depth) and 4,500 feet. The latter is deep enough to be beyond the photic zone where the commoner fouling organisms occur, so the results should be representative of deep ocean fouling.



## GENERAL TEST PROGRAM CRITERIA Continued

**MATERIAL SELECTION** We conducted a study of materials before fabricating the test specimens. Alloys for undersea heat rejection surface construction were chosen on the basis of several factors including cost, strength, ease of fabrication, corrosion resistance, resistance to fouling, and thermal conductivity.

A variety of metals were selected for the tests. Antifouling metals commonly used in seawater included copper, brasses, and bronzes. Metals susceptible to marine fouling, but useful in seawater, included cupronickel, Monel, and titanium. Table I shows the chemical composition of the specific alloys tested.

**GEOMETRY CONSIDERATIONS** The shape of the fouling surface may have a slight bearing on the rate and type of biological fouling. There was little literature on the significance of degree of curvature or sharpness of corner angles. We decided to investigate heated and unheated cylinders of a 1-inch radius of curvature and unheated flat plates. These are the expected geometrical shapes for undersea heat transfer surfaces. Corner effects could be ascertained by examination of the specimens after the test period.

Only limited data are available on the relationship between substrate roughness and type and degree of biological fouling. In nature, the substrate rarely, if ever, has a polished surface, whereas in the experiments, we used smooth specimen surfaces. This should have made little difference to the fouling precursors, for they settle very nicely on glass and porcelain.

To test the effect of geometry upon corrosion rate, flat-plate samples were made of some of the same materials used in the cylindrical specimens.

**LENGTH OF TEST PERIOD** The program of field observation to collect data on fouling and corrosion was conducted at both harbor and open-sea stations. The dockside tests were performed in a maximum fouling situation. A 120-day test period was selected. Fouling is usually well established within three months (32). These tests were designed to establish an upper limit on deep ocean fouling and corrosion.

In a randomly chosen deep ocean environment, one would expect much less fouling and corrosion at 300 feet than on the surface, and less yet at 20,000 feet. To test this hypothesis required open sea experimentation. Because power consumption of the test specimens was high, a ship with a power generator had to be present. Experimentation from a remote buoy had to be ruled out. Thus, economics favored a short test period.

## GENERAL TEST PROGRAM CRITERIA Continued

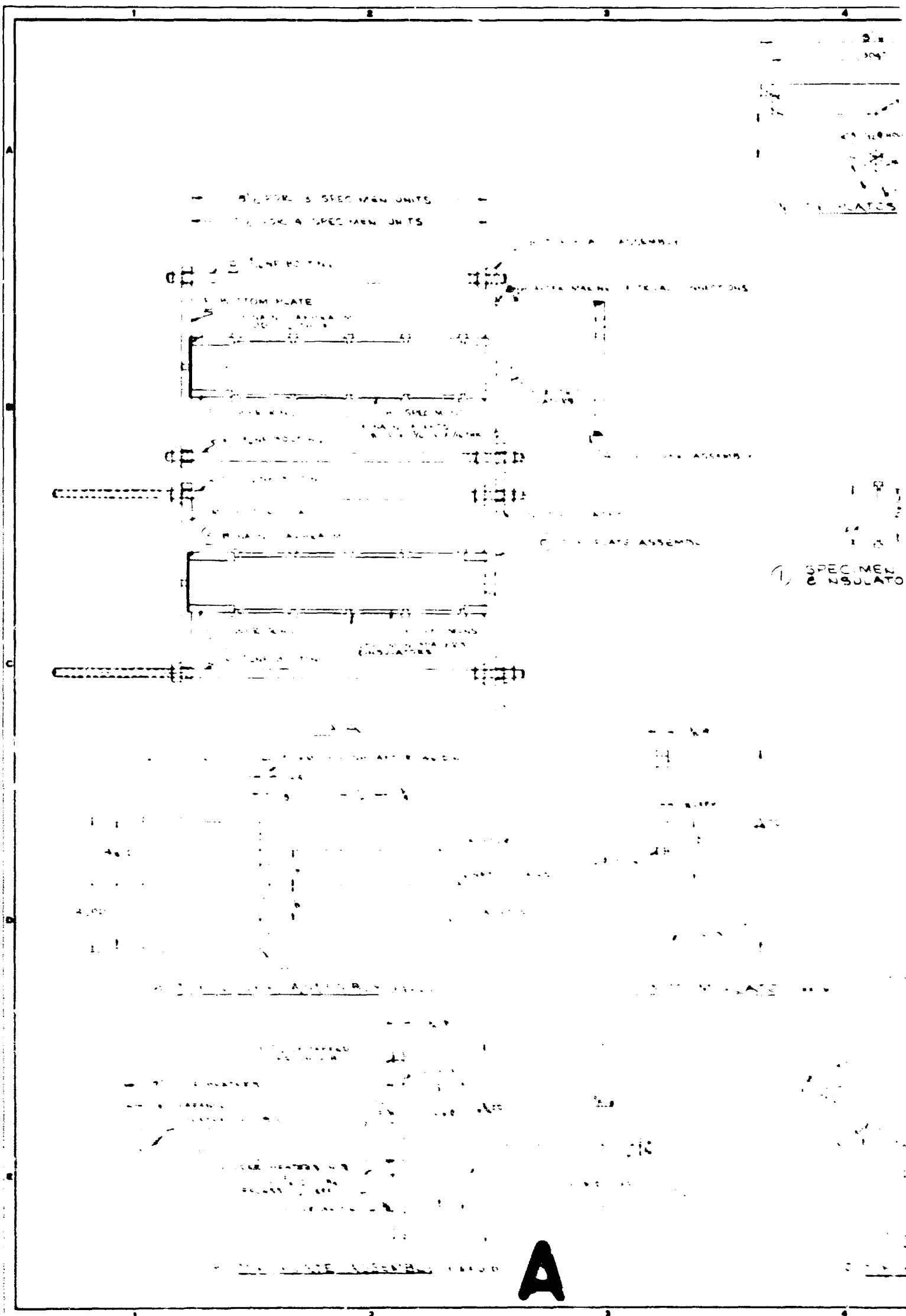
Fouling precursors such as bacteria attach almost immediately to a surface. The fouling cycle usually progresses from bacteria to diatoms, algae, mussels, and barnacles. If a fouling precursor which always occurs within a definite period of time could be chosen as a reference, knowing whether it appeared on a heated surface within the customary period of time would be valuable information. Cyprids were chosen as this reference species. Since they normally set within three to four days, five days were selected as the period for each ocean test.

## SHALLOW WATER TEST

The 120-day shallow water corrosion and fouling test was intended to determine the effect of temperature under conditions of maximum corrosion and biological growth. We chose Shelter Island in San Diego as a test location. The tests were conducted from a pier owned by Mauricio and Sons, Shipbuilders at 2420 Shelter Island Drive in San Diego. This location offered the advantages of available electric power, protection from curious visitors, a clean harbor offering approximately the same dissolved oxygen content as the ocean surface waters, and was convenient for technicians to take the necessary readings.

**EXPERIMENTAL APPARATUS** Figures 1 and 2 picture the test unit. It consists of four cylindrical elements, each containing four different metal specimens electrically isolated from one another with saran plastic spacers. Each metal specimen has a 2-inch OD, a 0.063-inch wall, and is 2 inches long. In addition to the cylindrical specimens, seven flat-plate specimens 3 by 3 inches with a nominal thickness of 0.063 inch are included in the unit. Materials are listed in Table I.

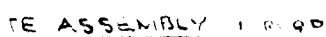
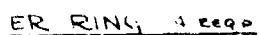
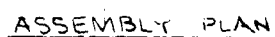
The test unit was suspended from a pier by three 1/2-inch all-thread mild steel rods connected to a mild steel plate bolted to the pier. The rods were 13 feet long, which ensured that the test unit was well below the water surface, even at low tide.





20

TERS



(M) BOTTOM PLATE 12400

3	7-15-68	DELETED RUMK N LABS 77 ADDED SPECIMENS SACATED FOR AS ADULT	GAIL
2	9-19-68	REDEAWN 8 ISSUED PRELIMINARY	GAIL
REV	DATE	DESCRIPTION	APPROVED
NOTICE			
THIS DRAWING HAS BEEN REEVALUATED. IT IS THE SOLE PROPERTY OF C F BRAUN & CO. IT IS LOANED TO THE SUBMITTER FOR HIS INFORMATION ONLY AND NOT TO BE REPRODUCED OR TRANSMITTED IN ANY FORM OR BY ANY MEANS, ELECTRONIC OR MECHANICAL, INCLUDING PHOTOCOPYING, RECORDING, OR BY ANY INFORMATION STORAGE AND RETRIEVAL SYSTEM, WITHOUT PERMISSION IN WRITING FROM C F BRAUN & CO. ANY UNAUTHORIZED REPRODUCTION OR TRANSMISSION OF THIS DRAWING IS PROHIBITED.			
DESIGNED FOR CONSTRUCTION		CUSTOMER APPROVAL	
BY	DATE		
DESIGNED	DRAWN	REVIEWED	APPROVED
GAIL	GAIL		CRUVER
FOR AT			
<p>NATURAL CONVECTION HEAT TRANSFER UNIT</p> <p>TEST MODULE ASSEMBLY &amp; DETAILS SHALLOW OCEAN TESTS</p>			
ALHAMBRA C F BRAUN & CO CALIFORNIA			
SCALE	DRAWING NUMBER		REVISION
1/4" = 1"	2650-100-RD-1		3
DATE			
9-19-68			

FIGURE 2  
SHALLOW WATER TEST UNIT PHOTOGRAPH



TABLE I

CHEMICAL COMPOSITION OF METAL CORROSION AND FOULING SPECIMENS

<u>ALLOYS</u>	<u>CARBON</u>	<u>NICKEL</u>	<u>COPPER</u>	<u>ZINC</u>	<u>SILICON</u>	<u>BERYLLIUM</u>	<u>IRON</u>	<u>ALUMINUM</u>	<u>MANGANESE</u>	<u>TIN</u>
MONEL	0.10	65.15	32.61		0.12		1.06		0.93	
70 CU-30 NI		30.00	68.90				0.48		0.60	
90 CU-10 NI		9.90	88.45				1.25		0.40	
AL BRONZE			90.75		2.00			7.25		
BE COPPER			97.71			1.94				
HH BRASS*			70.00	30.00						
NAVAL BRASS			60.00	39.25						0.75
SI BRONZE			95.80		3.10				1.10	
HC COPPER			99.95							
TITANIUM**										

- \* NOMINAL COMPOSITION, SPECIMEN WAS NOT ANALYZED
- \*\* COMMERCIALLY PURE TITANIUM

## SHALLOW WATER TEST Continued

The test elements were held at temperatures of ambient, 100, 120, and 140 F, respectively. However, flat-plate specimens were exposed to ambient temperature only. Two resistance heaters, each 1 kw capacity at 120 volts, were located in the interior of each cylindrical element. The space between the heaters and the element inner wall was filled with distilled water. A rubber diaphragm was placed inside one end of the element to allow for expansion of the distilled water when heated. The resistance heaters were made of nichrome wire with a 3/8-inch stainless steel sheath. Each heater was bent in a U-shape and was nestled at right angles to the heater beside it. This evened the heat flux as closely as possible. A heater surface was never nearer than 1/4 inch to the inner wall of the element and never farther than 1/2 inch.

Two sheathed 26-gauge iron-constantan thermocouples were silver soldered to the inner wall of the Monel specimen (uppermost) of each element. Parallel connected, they indicated the average temperature of that specimen, and this was taken as the average for the entire element. Each thermocouple signal was fed to an on-off temperature controller, Honeywell Model 105C204PS-22. The controller either allowed current to flow to a heater or interrupted the flow, depending upon whether an element temperature was below or above a predetermined setpoint. Deviations from the setpoint were plus or minus 4 F using this control scheme.

Cumulative power consumption of each heated element was indicated by a Sangamo 120-volt, 15 amp, single-phase, bottom-connected, watt-hour meter. All instrumentation was mounted inside a locked 4- by 3- by 1.2-foot metal cabinet mounted on the pier. Nitrogen purged the cabinet continuously to eliminate any corrosion of the instruments. Figure 3 shows the shallow water test instrumentation.

**EXPERIMENTAL PROCEDURE** After fabrication, we checked out the units and instrumentation at our Alhambra Research Center. They were then transported to San Diego and mounted at the test location on October 26, 1964. Upon installation, and weekly thereafter, the following readings were taken.

- 1 Time of day
- 2 Three watt-hour meter readings
- 3 Ambient water temperature
- 4 Current velocity

Element temperatures were continuously indicated by the temperature controller.

FIGURE 3  
SHALLOW WATER TEST INSTRUMENTATION

II-10





## SHALLOW WATER TEST Continued

At the beginning and end of the test period, the specimens were photographed, and the salinity and dissolved oxygen content of the harbor water were measured. We employed a Beckman oxygen meter to ascertain the amount of dissolved oxygen. Salinity was determined by an electrical salinometer.

Because of salt water leaks, two of the test elements (120 and 140 F) ceased working during the week of December 7, 1964. They were reworked and reinstalled on December 14, 1964. Except for minor power interruptions (less than one hour), all three elements ran continuously from December 14, 1964 to April 12, 1965 when the test was terminated. We photographed the specimens on March 1 and April 12, 1965.

After the inspection for biological fouling, we brought the specimens back to our Alhambra corrosion laboratory. The individual specimens were photographed, corrosion products removed, and they were then reweighed. Corrosion rates were calculated from the data on weight loss and time of exposure.

**FOULING RESULTS** Shallow water corrosion and fouling experimental results are shown in Figures 4 through 10 and Table II. At the termination of the test, the heated metal specimens were clear of any macroscopic fouling, although a gauzy film of slime occurred on many of the specimens. Growths composed of hydrozoan colonies and simple tunicates attached to the plastic spacers and the underside of the upper support flanges. A thin layer of bacterial, algal, and diatomaceous slime covered the ambient cylindrical specimens. The metal squares beneath the array were relatively clean. However, a dense aggregation of tunicates and short lengths of filamentous algae covered the underside of the titanium square.

Such fouling as occurred was composed largely of the erect bryozoans *Bugula neritina* and *Bugula californica*, the encrusting bryozoan *Holoporella brunnea*, and the tunicate *Chione intestinalis*. We noted unidentifiable species of diatoms, bacteria, and filamentous algae in the slimes. Benthic communities of gammarid amphipods lived in the bryozoa.

Heaviest fouling took place on the 100 F set. See Figure 4. An algal slime, which was easily brushed away, covered the metal specimens. While under the upper support plate an association of 60 percent tunicates and 40 percent bryozoans existed, none occurred on the lower support plate. Fringes of the bryozoans lived on the plastic spacers, which were at a lower temperature than the metals.



Profuse fouling took place on the retainer rings (bryozoans) and the upper flange (tunicates and bryozoans) at the 100F set. Photo taken 4-12-65.

FIGURE 4B  
SHALLOW WATER TEST - 100F ELEMENT FOULING

II-13



The lower flange of the 100F element. Bryozoan colonies are attached to the plastic spacers. Photo taken 3-1-65.



Upper flange of the 120F element. The most abundant bryozoan growth was at the top of the set. Filamentous algae attached to the frame members. Slime covered the can. Photo taken 5-1-65.

FIGURE 5B  
SHALLOW WATER TEST - 120F ELEMENT FOULING

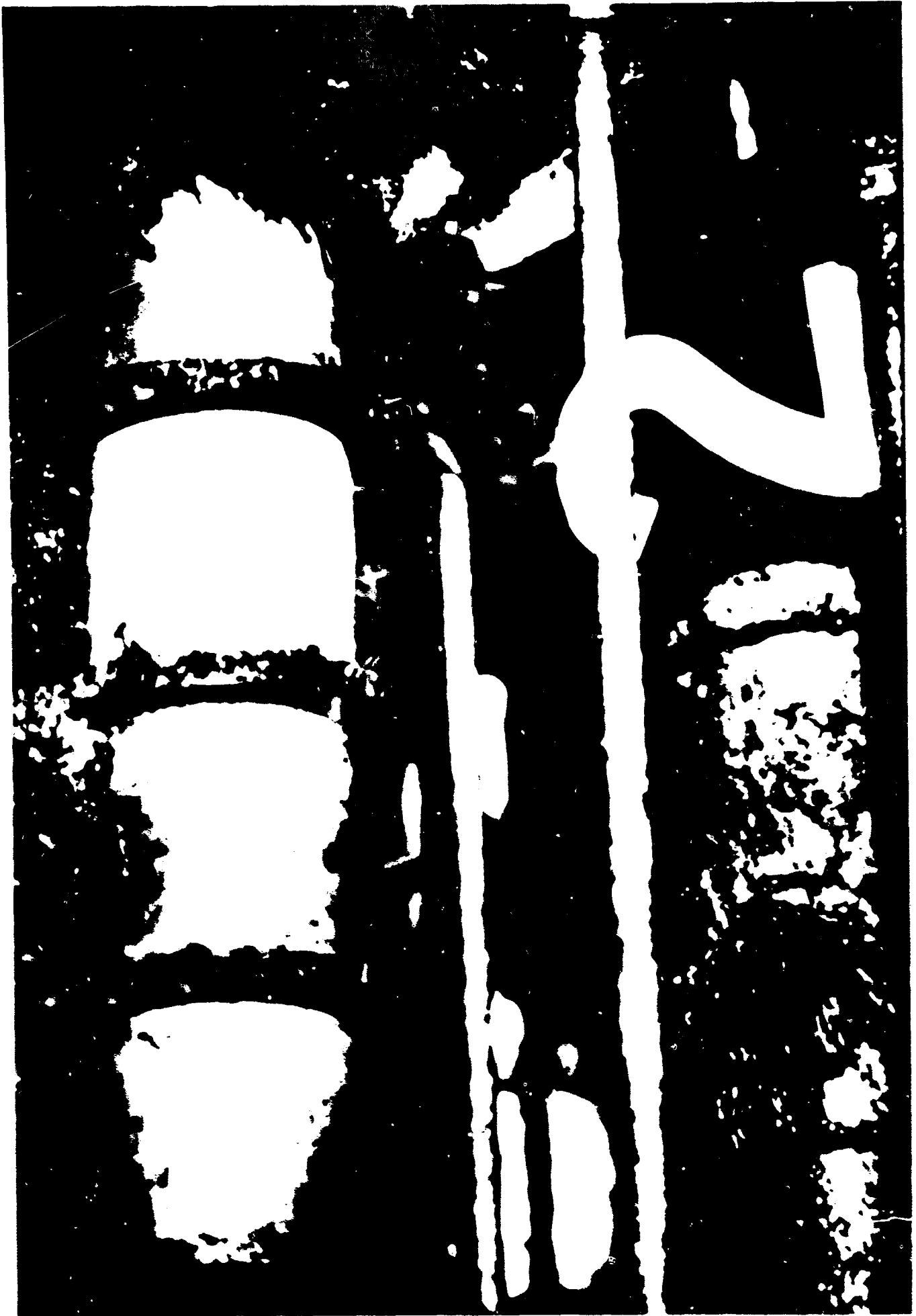
11-10



Underside of the upper flange of the 120F element. A simple tunicate and encrusting bryozoans grew underneath the flange. Stratification of bryozoans is visible. Photo taken 3-1-65.

FIGURE 6  
SHALLOW WATER TEST - 140F ELEMENT FOULING

II-16



No growth occurred on the 140F element on the left. The ambient element is on the right. Photo taken 4-12-65.

FIGURE 7A  
SHALLOW WATER TLST - FOULING OF AMBIENT SPECIMENS

II-17



Ambient element with the 100F element in the left background. A heavy growth of diatomaceous and bacterial slime adheres to the Monel and 70-30 Cupro-nickel specimens. Bryozoans attached to the plastic spacers. Photo taken 4-12-65.



A dense aggregation of tunicates attached to the underside of the titanium plate. Small bryozoans formed on the phenolic spacer separating the aluminum bronze and beryllium copper. Photo taken 4-12-65.

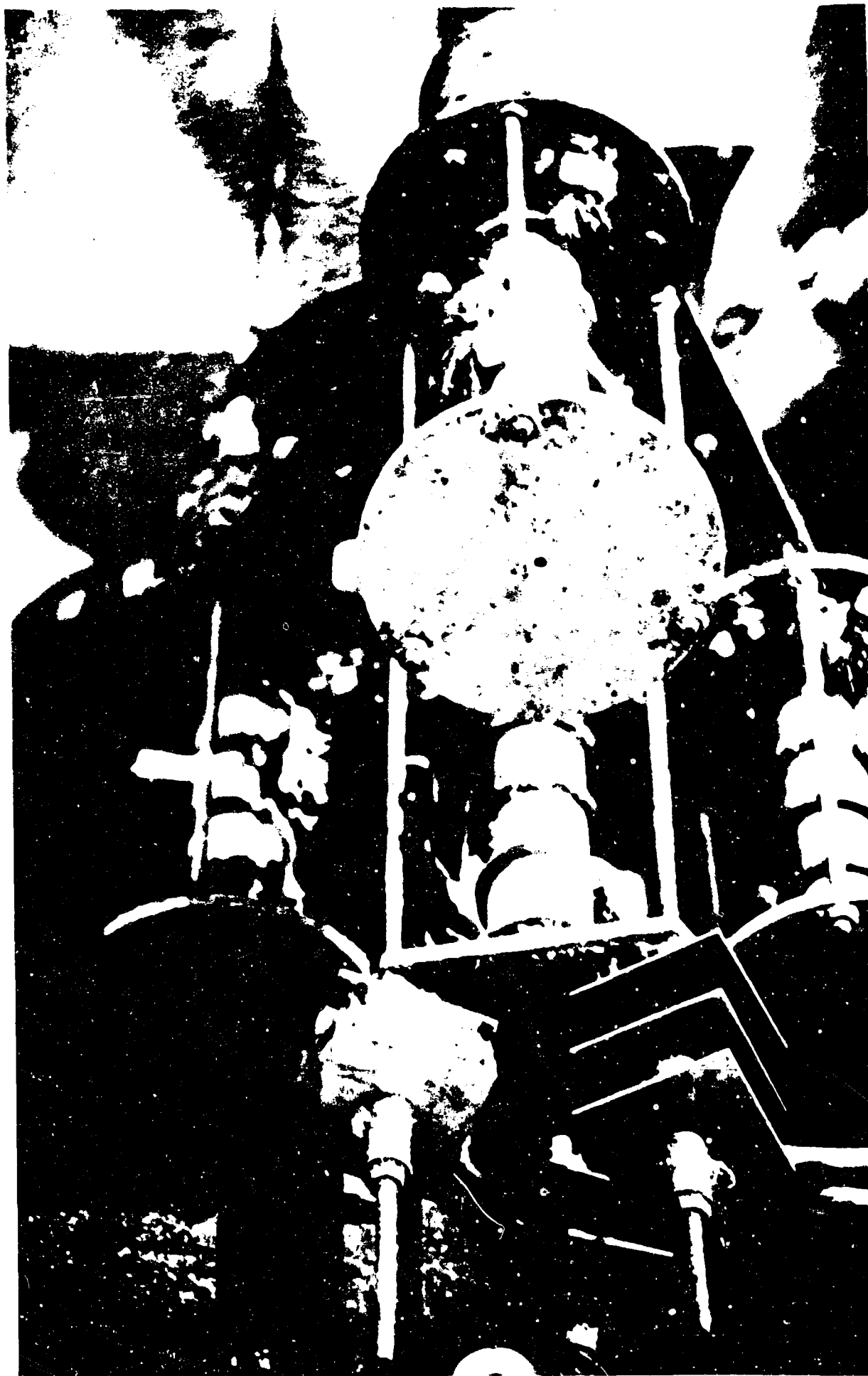




Scattered clusters of bryozoans have attached to the element at ambient temperature, on the left. Tunicates and luxuriant bryozoans show on the 100F set to the right. Photo taken 4-12-65.

FIGURE 8  
SHALLOW WATER TEST UNIT AFTER RECOVERY

II-20



An overall view of the test unit photographed 4-12-65.

## SHALLOW WATER TEST Continued

Metal specimens on the 120 F set were lightly covered with slimy fouling organisms, as shown in Figure 5. This set was not as heavily fouled as the 100 F element, but it did carry a small assemblage of tunicates and bryozoans underneath the upper flange. Bugula growth became less abundant on the plastic spacers going from the upper to the lower flange.

Metals and appurtenances on the 140 F set were scarcely fouled. Less than 15 percent of the upper flange had an encrusting mat, and the lower flange had none at all. Bugula growth on the plastic spacers was incidental near the top and absent at the bottom. See Figure 6.

A relatively dense but thin amorphous algal slime layer and filamentous grass had grown on some of the unheated specimens. The plastic spacers supported scattered Bugula colonies but few tunicates. There was no stratification of bryozoan growth such as occurred near the heated metals. Some metals appeared to allow more biological growth than others. A clump of tunicates had grown on the flat titanium specimen. See Figure 7. A photograph of the shallow water test unit after recovery is shown in Figure 8.

**CORROSION RESULTS** The 120 F and 140 F specimens were exposed a total of 2,854 hours. The 100 F set and the ambient specimens were exposed for 4,026 hours. The dissolved oxygen content of the water was measured at 6.2 ppm at the beginning of the test and at 5.1 ppm at the end of the test. Salinity ranged from 33.91 to 33.93 ppt. The water temperature varied between 55.5 F and 67.6 F. Table II lists the corrosion rates determined for each specimen and a description of the appearance of the specimens after the exposure.

**MONEL** The Monel specimens were used to monitor the metal temperature for heat transfer studies. The attachment of the necessary thermocouples prevented corrosion rate measurements. All four of the Monel specimens had a gray deposit, as described in Table II, and the unheated specimen had marine growth scattered over the surface. See Figure 9. The ambient Monel specimen exhibited severe crevice corrosion beneath the saran spacer. Heated Monel specimens in the same exposure did not show any evidence of crevice corrosion.

**90 CU - 10 NI** Only very slight fouling by marine growth was found on the 90 Cu - 10 Ni at ambient temperature. No evidence of accelerated corrosion was found under the growth. At 100 F, 120 F, and 140 F the samples were free of adherent marine organisms. As shown in Table II, the specimens at 120 F and 140 F had significant increases in corrosion rate. No crevice corrosion was observed on the 90 Cu - 10 Ni specimens.

TABLE II

## SHALLOW WATER TEST CORROSION RESULTS

CYLINDERS			
SPECIMEN	TEMPERATURE	CORROSION RATE MILS/YEAR	APPEARANCE
MONEL	AMBIENT	1.1	FLAKY GRAY DEPOSIT, SEVERE CREVICIAL CORROSION
MONEL	100 F	- )	
MONEL	120 F	- )	FLAKY GRAY DEPOSIT ON ALL THREE SURFACES
MONEL	140 F	- )	
90 CU-10 NI	AMBIENT	0.2	BRONZE YELLOW SCALE, FAIRLY TENACIOUS
90 CU-10 NI	100 F	0.3)	
90 CU-10 NI	120 F	2.0)	SAME BRONZE YELLOW SCALE, NO MARINE GROWTH
90 CU-10 NI	140 F	1.8)	
70 CU-30 NI	AMBIENT	0.2	DULL GREEN SURFACE DISCOLORATION, NO MARINE GROWTH
70 CU-30 NI	100 F	0.2)	
70 CU-30 NI	120 F	2.9)	SAME SURFACE COLOR, FEW PATCHES OF MARINE GROWTH
70 CU-30 NI	140 F	1.8)	
AL BRONZE	AMBIENT	0.9)	
AL BRONZE	100 F	0.8)	HEAVY GREEN DEPOSIT, EASILY FLAKED OFF
AL BRONZE	120 F	3.2)	
AL BRONZE	140 F	2.1	DEPOSIT SOMEWHAT THINNER THAN ON COLD CHAMFER
NAVAL BRASS	AMBIENT	0.7	HEAVY BLUE-GREEN DEPOSIT, FAIRLY TENACIOUS
SI BRONZE	AMBIENT	0.8	HEAVY GREEN-BLUE DEPOSIT, FAIRLY TENACIOUS
PLATES			
BE COPPER	AMBIENT	0.4	UNIFORM GREEN SCALE, NO MARINE GROWTH
AL BRONZE	AMBIENT	0.6	HEAVY GREEN SCALE WITH MARINE GROWTH
TITANIUM	AMBIENT	NIL	EXTREMELY HEAVY MARINE GROWTH ON UNDERSIDE
70 CU-30 NI	AMBIENT	0.2	TOPSIDE HAS UNIFORM AND LIGHT SCALE
HC COPPER	AMBIENT	0.8)	
HH BRASS	AMBIENT	0.6)	THESE LOOK SIMILAR, A BLUE-GREEN DEPOSIT
SI BRONZE	AMBIENT	0.8)	
CONDITIONS OF EXPOSURE		OXYGEN CONTENT	5 - 6 PPM
		TEMPERATURE RANGE	57.1 - 67.6
		TIME	4026 HOURS FOR AMBIENT AND 100 F SPECIMENS 2854 HOURS FOR 120 F AND 140 F SPECIMENS

A

## TABLE 11

## FAST CORROSION RESULTS

A APPEARANCE AFTER EXPOSURE

C1 SEVERE CREVICE CORROSION UNDER SPACER, SCATTERED MARINE GROWTH

S1 ON ALL THREE SPECIMENS, NO CREVICE CORROSION, BRIGHT METAL BENEATH DEPOSIT

C1, FAIRLY TENACIOUS, ONE AREA OF MARINE GROWTH, NO CREVICE CORROSION

IN SCALE, NO MARINE GROWTH AND NO CREVICE CORROSION

, DISCOLORATION, FEW PATCHES OF MARINE GROWTH, NO CREVICE CORROSION

OF FEW PATCHES OF HEAVIER DEPOSIT, NO MARINE GROWTH, NO CREVICE CORROSION

ED, EASILY FLAKED OFF, NO MARINE GROWTH, NO CREVICE CORROSION

INNER THAN ON COOLER SPECIMENS

POSIT, FAIRLY TENACIOUS, NO MARINE GROWTH, NO CREVICE CORROSION

POSIT, FAIRLY TENACIOUS, NO MARINE GROWTH, NO CREVICE CORROSION

RC, NO MARINE GROWTH

WITH MARINE GROWTH

LINE GROWTH ON UNDERSIDE OF SPECIMEN

AL AND LIGHT SCALE, UNDERSIDE HAS HEAVIER DEPOSIT WITH SOME MARINE GROWTH

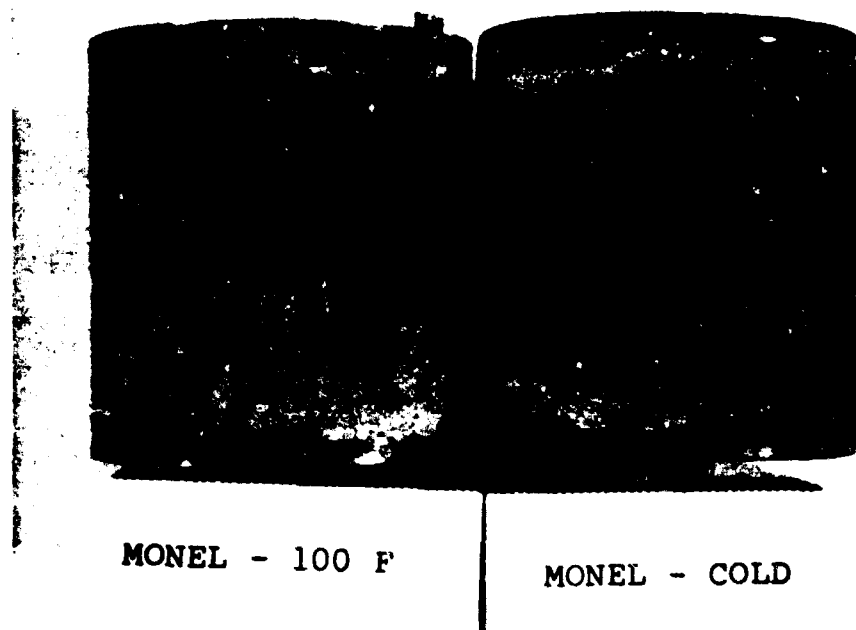
[ A BLUE-GREEN DEPOSIT, SOMEWHAT POWDERY, NO MARINE GROWTH

ENT AND 100 F SPECIMENS

PER AND 140 F SPECIMENS

**B**

FIGURE 9  
MONEL SPECIMEN APPEARANCE AFTER THE  
SHALLOW WATER TEST

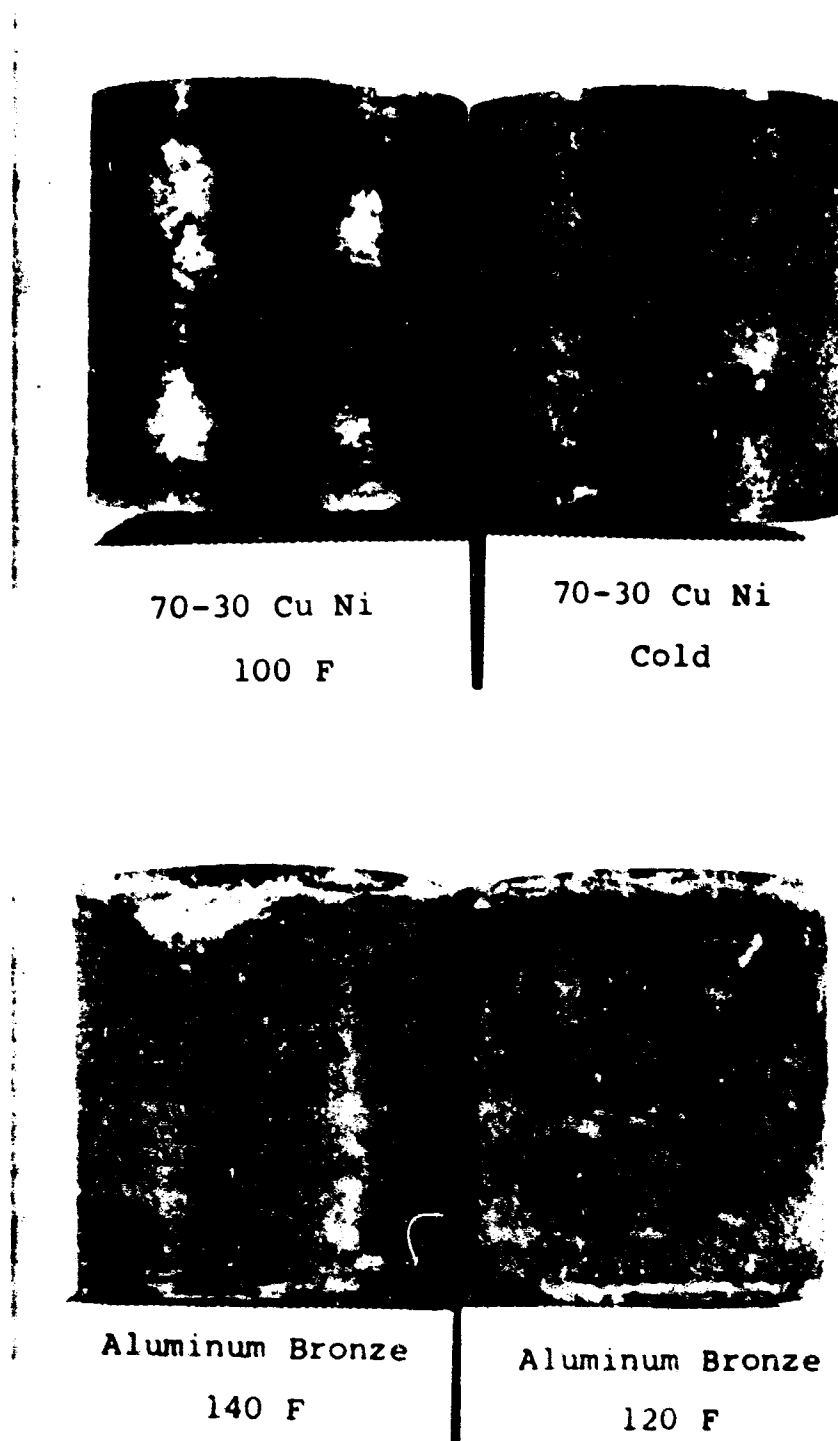


MONEL - COLD  
CLEANED

Crevice corrosion occurred beneath the  
plastic spacer.

FIGURE 10  
APPEARANCE OF 70Cu-30Ni AND ALUMINUM BRONZE  
AFTER THE SHALLOW WATER TEST

Appearance of 70Cu-30Ni and aluminum bronze  
after the shallow water test.



A deposit occurred on the aluminum bronze.

## SHALLOW WATER TEST Continued

70 CU - 30 NI Figure 10 shows the appearance of the ambient and 100 F specimens after the shallow water test. The corrosion rates increased at temperatures of 120 F and 140 F. The ambient specimen showed the attachment of marine organisms. Heated specimens were free of growth. No crevice corrosion was noted on any of the specimens.

ALUMINUM BRONZE The aluminum bronze specimens were coated with a moderately heavy deposit. See Figure 10. No marine growth was observed on these specimens, and there was no evidence of crevice corrosion. The 120 F and 140 F specimens exhibited a somewhat higher corrosion rate than the 100 F specimens.

TITANIUM A flat plate of titanium was exposed in a horizontal position. A heavy marine growth formed on the underside of the specimen as shown in Figure 5. No accelerated corrosion was detected under the deposit.

MISCELLANEOUS A miscellaneous group of flat-plate specimens including copper, brasses, and bronzes were exposed in the shallow water test. The condition of these specimens and the corrosion rates are tabulated in Table II. These materials were free of marine growth, except for slight growths on the aluminum bronze and 70 - 30 cupronickel specimens.

HEAT TRANSFER RESULTS We determined average rate of heat dissipation and average heat transfer coefficient weekly from the power consumption, time, and ambient temperature readings. Overall heat transfer coefficient was calculated from the equation

$$U = \frac{Q}{A\Delta T} \quad (1)$$

To determine heat transfer area, it was assumed that all heat was transferred through the cylindrical elements. Table III lists experimental heat transfer coefficients.

The primary resistance to heat transfer was the natural convection film coefficient. The film coefficient was difficult to calculate because of the flow disturbance of the saran plastic spacers needed to electrically isolate the metal specimens from each other. We assumed, however, that the rings would act as turbulence promoters. This was borne out by visual observation of the flow pattern. Thus, turbulent natural convection heat transfer prevailed outside the metal specimens and probably occurred inside as well. Current velocity in the ambient water was low enough throughout the test to not significantly affect the heat transfer rate.



TABLE 1

## SHALLOW WATER TEST HEAT

OVL  
BAL

WEEK ENDING	AVERAGE AMBIENT WATER TEMPERATURE, F	AVERAGE CURRENT, KNOT	UA (BTU/HR F)		
			100 F	120 F	140 F
11- 2-64	67.6	0.15	23.5	-	-
11- 9-64	66.7	0.15	23.6	-	-
11-16-64	63.7	0.20	23.6	-	-
11-23-64	59.5	0.20	23.4	-	-
11-30-64	58.3	0.05	23.6	-	-
12- 7-64	57.6	0.00	23.9	-	-
12-14-64	57.5	0.00	20.4	-	-
12-21-64	57.7	0.20	22.2	22.6	25.2
12-28-64	57.9	0.25	22.4	20.6	25.3
1- 4-65	57.1	0.20	22.2	20.0	24.2
1-11-65	55.5	0.20	21.0	19.1	23.2
1-18-65	56.6	0.30	20.2	18.4	22.0
1-25-65	58.0	0.25	20.7	17.6	20.0
2- 1-65	58.2	0.00	21.4	18.6	21.5
2- 8-65	58.6	0.05	20.1	17.6	20.2
2-15-65	59.1	0.05	20.7	18.4	21.4
2-22-65	59.5	0.10	24.4	20.6	25.1
3- 1-65	60.6	0.10	21.3	15.8	18.5
3- 8-65	61.7	0.10	23.2	19.1	22.3
3-15-65	61.9	0.10	25.3	19.0	22.0
3-22-65	62.6	0.02	22.8	18.0	20.6
3-29-65	63.4	0.02	22.2	17.7	20.6
4-5-65	63.5	0.01	22.9	19.2	24.3
4-12-65	62.0	0.00	23.0	19.2	23.7

A

TABLE III

## OVER TEST HEAT TRANSFER DATA

OVERALL HEAT TRANSFER COEFFICIENT  
BASED ON ASSUMED AREA OF 0.458 FT<sup>2</sup>U (BTU/HR-FT<sup>2</sup>-F)

OVERALL COEFFICIENTS REFERRED TO 57.7 F

U (BTU/HR-FT<sup>2</sup>-F)

F	100 F	120 F	140 F	100 F	120 F	140 F
	51.2	-	-	46.9	-	-
	51.4	-	-	47.5	-	-
	50.1	-	-	47.6	-	-
	51.0	-	-	50.3	-	-
	51.4	-	-	51.1	-	-
	52.1	-	-	52.1	-	-
	44.4	-	-	44.4	-	-
2	48.4	49.3	54.9	48.4	49.3	54.9
3	48.8	44.9	55.2	48.7	44.8	55.2
2	48.4	43.6	52.8	48.4	43.7	52.9
3.2	45.8	41.6	50.6	46.7	42.1	51.0
2.0	44.0	40.1	48.0	44.5	40.4	48.2
1.0	45.1	38.4	43.6	45.0	38.4	43.6
1.5	46.7	40.5	46.9	46.6	40.4	46.9
0.2	43.8	38.4	44.0	43.7	38.3	43.9
4	45.1	40.1	46.7	44.5	39.7	46.4
1	53.2	44.9	54.7	52.5	44.5	54.3
1.5	46.4	34.4	40.3	45.3	33.8	39.9
2.3	50.6	41.6	48.6	49.0	40.6	47.7
2.0	55.2	41.4	48.0	53.3	40.3	47.2
0.6	49.7	39.2	44.9	47.6	38.2	44.0
0.8	48.4	38.7	45.3	46.1	37.4	44.3
1.3	49.6	41.9	53.0	47.6	40.5	51.7
3.7	50.1	41.9	51.7	48.3	41.0	50.7

B

## SHALLOW WATER TEST Continued

Overall heat transfer coefficients were referred to the ambient temperature of 57.7 F encountered at the beginning of the 120 F and 140 F element test period by multiplying each coefficient by

$$\left[ \frac{T_{\text{Surface}} - T_{\text{Ambient}}}{T_{\text{Surface}} - 57.7} \right]^{\frac{1}{3}}$$

In turbulent natural convection, the heat transfer coefficient is proportional to  $(\Delta T)^{\frac{1}{3}}$ . Since the turbulent mechanism predominated, scatter due to changing ambient water temperature was mostly eliminated. This procedure does cause a small error, however, because fouling and metal conductivity also contribute to the heat transfer resistance. Changes in ambient current also affect the overall heat transfer coefficient. Corrected coefficients are listed in Table III and depicted graphically in Figure 11.

Notice that the 100 F element heat transfer coefficient did not decrease with time. The deviations appear to be random, about a mean value of 47.8 Btu/hr-ft<sup>2</sup>-F, and fall mostly within a band of plus or minus 10 percent. Fouling and corrosion, evidently, did not significantly affect the heat transfer coefficient here.

Overall heat transfer coefficients for the 120 F and 140 F elements did appear to decrease with time. The rate of decrease flattened out after four weeks of exposure. Thereafter, there seemed to be no time dependence. Deviations appeared to be random, about mean values of 39.5 (120 F) and 46.8 (140 F) Btu/hr-ft<sup>2</sup>-F. Again, most of the data fell within a plus or minus 10 percent band.

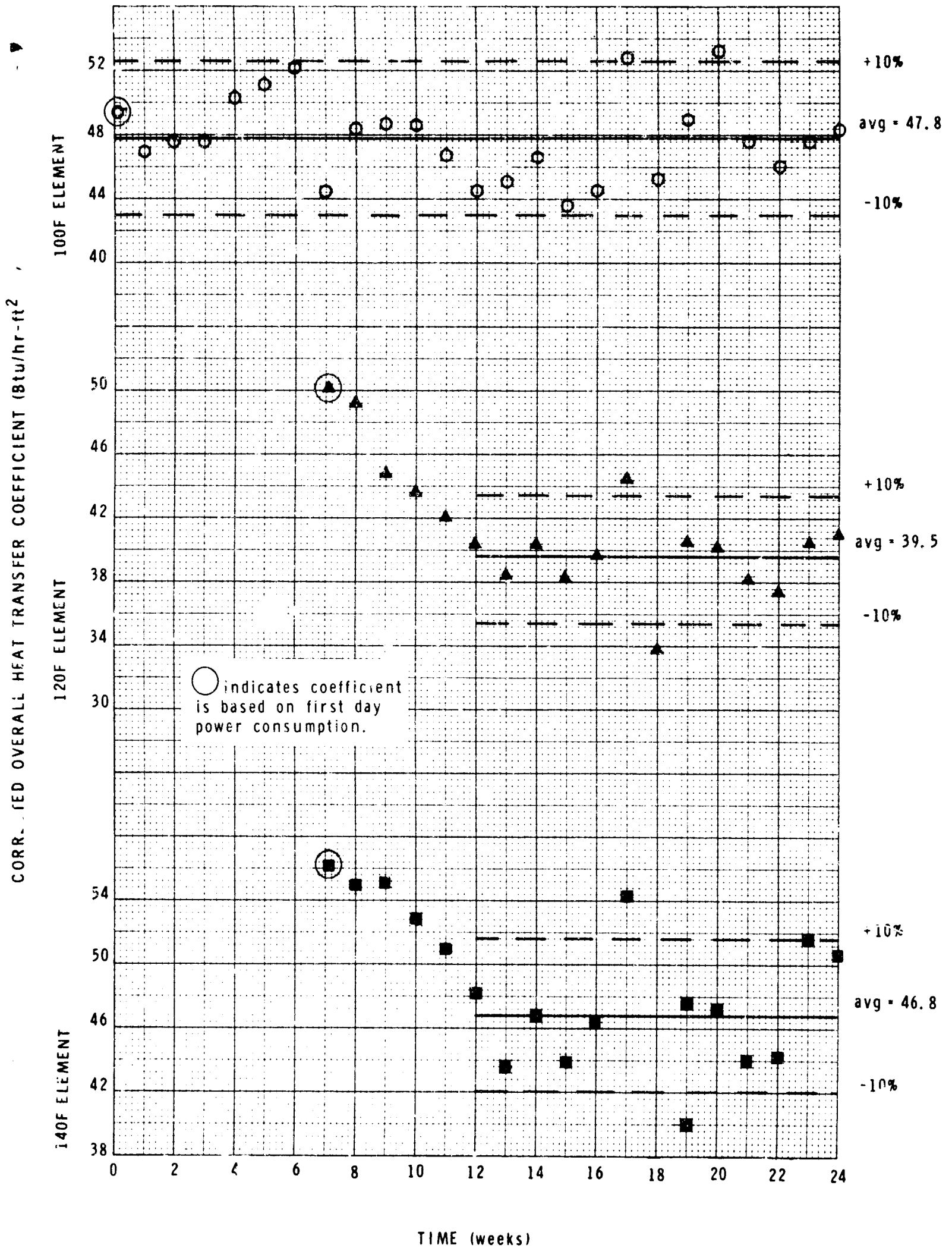
We interpreted the decrease of heat transfer coefficient with time as evidence of a growing scale resistance. Fouling coefficients were calculated for the 120 F and 140 F elements from the equation

$$h_D = \frac{1}{\frac{1}{U_D} - \frac{1}{U_C}} \quad (2)$$

# SHALLOW WATER TEST HEAT TRANSFER COEFFICIENT VERSUS TIME

JEC

FIGURE 11



## SHALLOW WATER TEST Continued

An  $h_D$  of 200 Btu/hr-ft<sup>2</sup>-F was calculated for the 120 F element, while the 140 F had an  $h_D$  of 310 Btu/hr-ft<sup>2</sup>-F. These values are lower than the commonly accepted ones for seawater. McAdams (89) and Kern (79) recommend an  $h_D$  for seawater boiler scale of 2,000 Btu/hr-ft<sup>2</sup>-F if the water temperature and velocity are less than 125 F and 3 feet per second, respectively. Of course, this value is for filtered seawater traveling at a higher velocity than that encountered with this natural convection experiment. The harbor water was sometimes very murky, and particulate matter still clung to parts of the test array upon retrieval. We could find no fouling factors in the literature for natural convection heat transfer in seawater. Additional experimental work is necessary to clarify the roles of velocity and particulate matter in the ambient water.

To compare results with the deep ocean tests, we gathered data on ambient temperature, current velocity, and power consumption of the elements at the end of the first day. Heat transfer coefficients are shown on Figure 11. Note that for each temperature level, the heat transfer coefficient of the first day is higher than the weekly average. If we take these as the initial values, the fouling coefficients become 190 and 280 Btu/hr-ft<sup>2</sup>-F for 120 F and 140 F elements, respectively.

## 300-FOOT TEST

The intent of the 300-foot depth corrosion and fouling test was to determine the effect of metal surface temperature at this upper limit of undersea power source placement. A site five miles due west of Point Loma at 32-40.0 N, 117-20.5 W was selected to perform the five-day experiment. The test started at 2400 hours March 1 and ended at 2400 hours March 6. This experiment was undertaken from the Sea Quest owned by Lockheed-California Company. Its specifications are listed in Table IV.

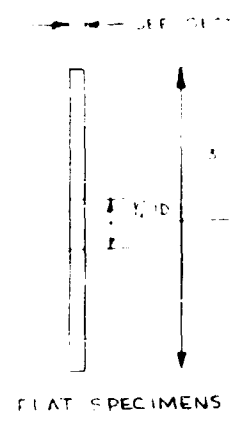
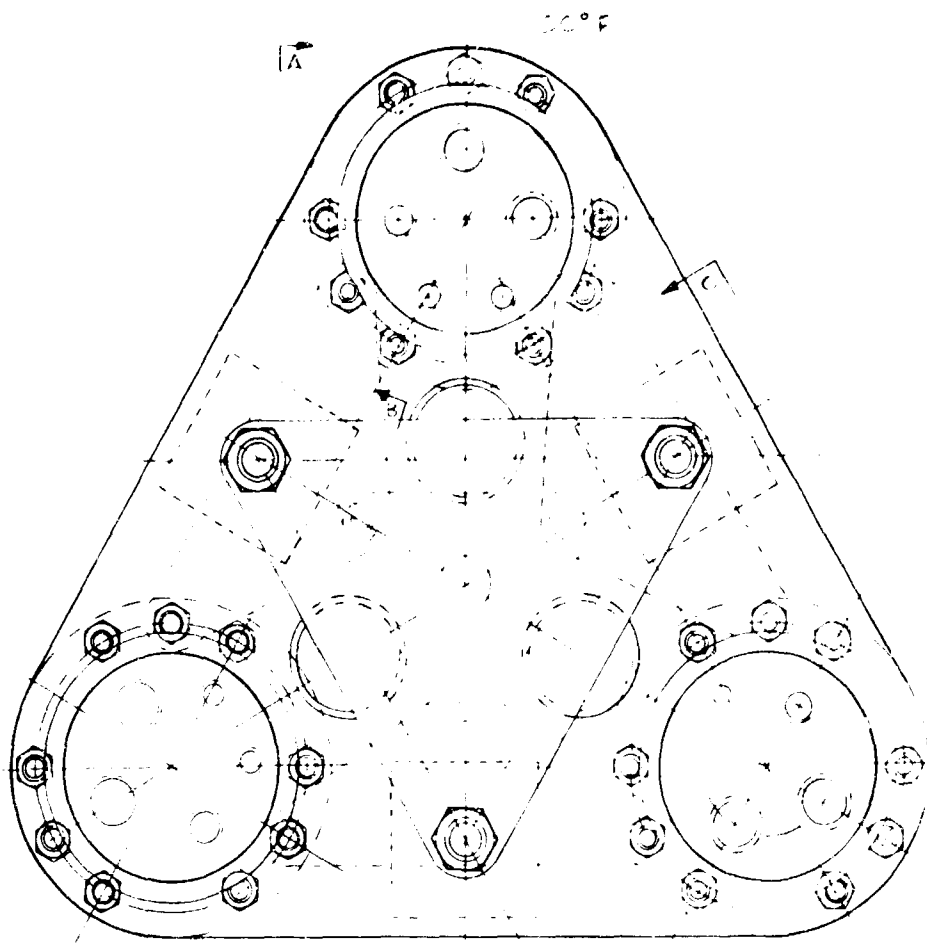
**EXPERIMENTAL APPARATUS** The deep ocean test unit, shown in Figures 12 and 13, is similar to the shallow water unit. One important difference is that each cylindrical element contains three rather than four different materials. Also, electrical connections are made inside a mineral oil-filled bellows section at the top of each element rather than in the rigid can construction employed in the shallow water test.

This allowed pressure equalization, which prevented leaks. Tubular heater configuration was the same as the shallow water unit, except that each heater was 2 inches shorter because of one fewer metal specimen.

TABLE IV

## SEA QUEST SPECIFICATIONS

Overall Length	48.8 feet
Reg Length	44.1 feet
Reg Beam	12.4 feet
Reg Dept	5.3 feet
Displacement	48.0 tons
Net Tonnage	6.0 tons
Draft (Full Load)	6 feet 8 inches
Hull Material	Steel (3/8-inch garboards to 3/16-inch sheerstrakes)
Water Storage	400 gallons
Berths	6
Galley	Electric range and refrigeration
Reefer	45 cubic feet (deep freeze)
Fuel (Diesel)	2,000 gallons (in double bottoms)
Speed	8 knots cruise, 10 knots Flank
Range	4,000 miles (approximate)
Main Engine	140 hp Buda
Battery	150 amp hours/32 volts DC
Aux Power	37.5 kva 110/220 volt 60 cycle single-phase (driven by GM-371 on Korfund mounts) 1 kw of special "silent ship" 110 Volt 60 cycle
Anticorrosion	Lockheed "Cathanode" system
Engine Controls	Westinghouse air (two stations)
Communications	Transmitter Raytheon 85X (MF/HF) (150 watts) Receiver HRO (LF/MF/HF) Transceiver ARC-5 (VHF)
Navigation	Radar (AN/SPS-46)
Echo Sounder	Sonar DE-121 (intermediate depths)
Echo Sounder	Sonar (shallow depths) Loran DF Celestial Autopilot Standard and flying bridge compasses
Echo Sounder	NMC-1 W/recorder (deep)
Meteorological	Anemometer and psychrometer
Winches	Bristol (3/32-inch and 1/8-inch wire) Air cargo (2,500 lb drawbar) Hytech 16,500 feet of 3/16-inch 4-conductor
Booms (2)	2,000 lb capacity each
Diving Air	150 psi continuous
Working Space	Deck (all around) House (entire house except for head and trunk)
License	Documented, Number 260015



ELECTRICAL JUNCTION BOX TRANSFORMER  
FILLED PRESSURE COMPENSATED

POWER CONNECTION  
INSTRUMENT CONNECTION  
2 COLD JUNCTION THERMOCOUPLES

HEAT CHIMNEY

TO 30 COPPER AL  
MONEL NICKEL BRONZE

2 COLD JUNCTION THERMO-  
COUPLES INSIDE FOR  
TEMPERATURE CONTROL

100°F TUBULAR SPECIMEN  
DISTILLED WATER INSIDE

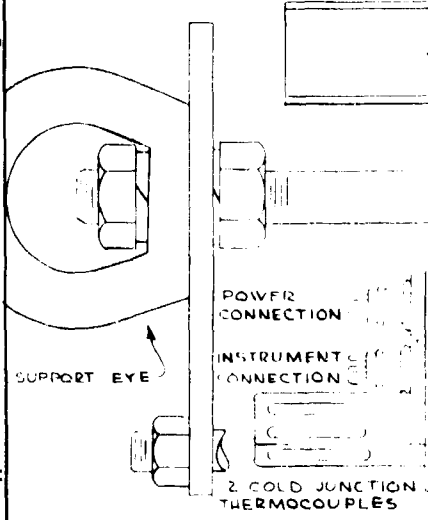
TO 30 COPPER NICKEL MONEL AL BRONZE SILICON BRONZE TO 30 COPPER NICKEL NAVAL BRASS

UNHEATED TUBULAR SPECIMEN  
PLAIN WATER INSIDE

TITANIUM TO 30 COPPER NICKEL

24 1524

FLAT SPECIMEN

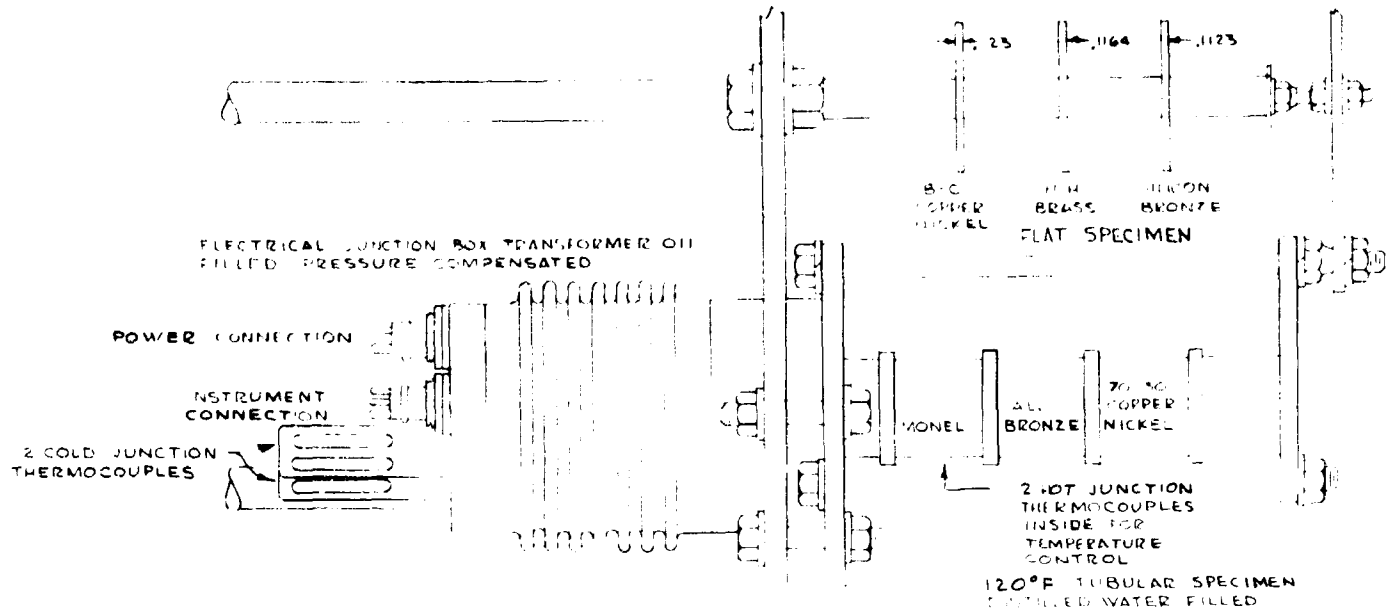


POWER CONNECTION  
INSTRUMENT CONNECTION  
2 COLD JUNCTION THERMOCOUPLES

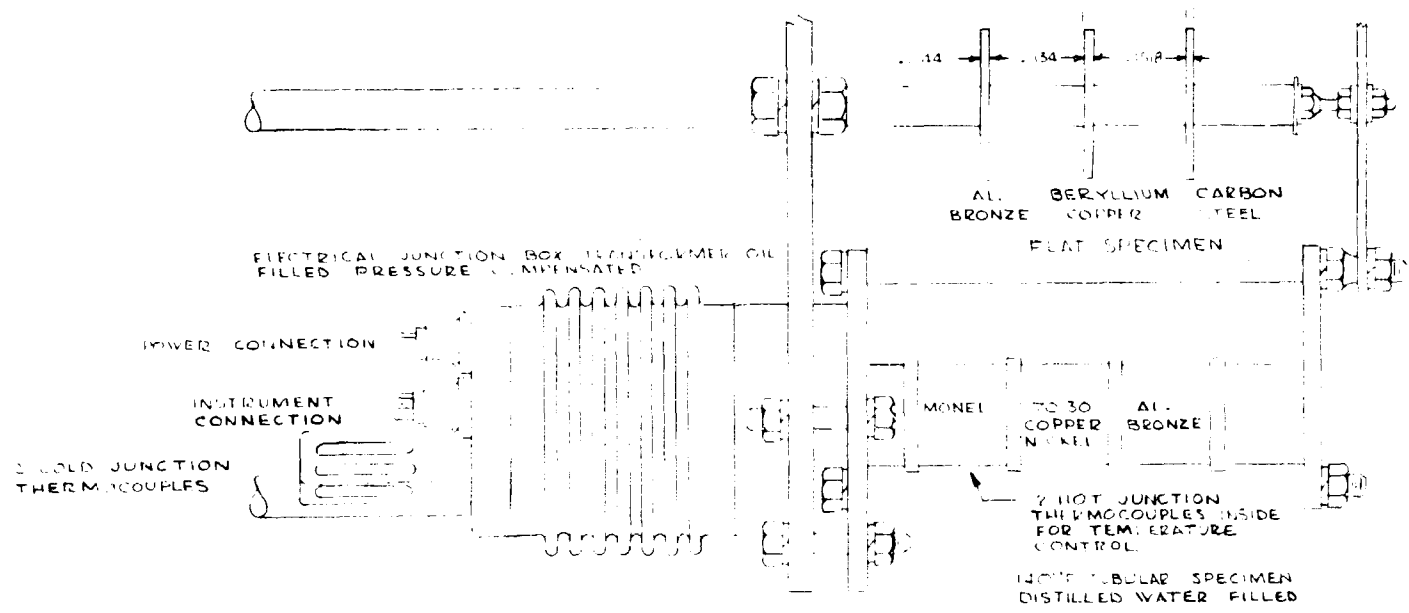
SECTION A-A

**A**

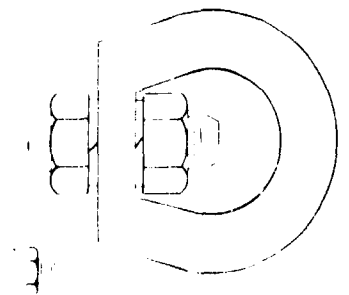
E



SECTION B-B



SECTION C-C



TUBULAR SPECIMEN

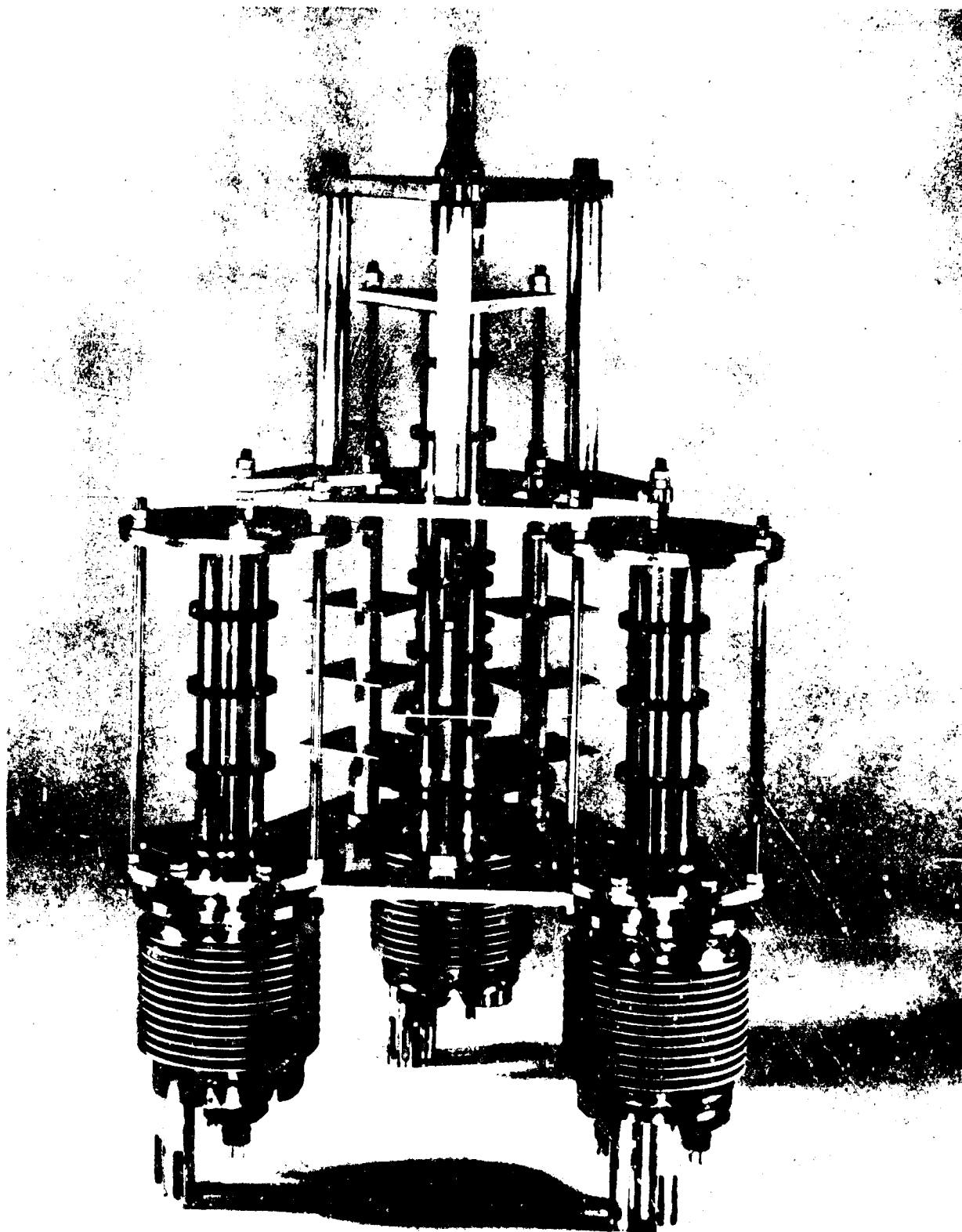
NOTE:  
ALL SPECIMENS ARE ELECTRICALLY  
INSULATED FROM ANY OTHER  
METAL.

B

REV	DATE	DESCRIPTION	APPROVED
NOTICE			
THIS DRAWING HAS NOT BEEN PUBLISHED. IT IS THE SOLE PROPERTY OF C F BRAUN & CO. IT IS LOANED TO THE RESEARCH DEPARTMENT FOR USE ONLY. IT IS TO BE RETURNED TO THE RESEARCH DEPARTMENT OF THE ALHAMBRA, CALIFORNIA, AT THE END OF THE LOAN. THE RESEARCH DEPARTMENT IS RESPONSIBLE FOR THE LOSS OF THIS DRAWING. THE RESEARCH DEPARTMENT IS RESPONSIBLE FOR THE LOSS OF THIS DRAWING. THE RESEARCH DEPARTMENT IS RESPONSIBLE FOR THE LOSS OF THIS DRAWING.			
ISSUED FOR CONSTRUCTION		CUSTOMER APPROVAL	
BY	DATE		
DESIGNED	DRAWN	REVIEWED	APPROVED
R. GAIL	C. DAVIS		
FOR C F BRAUN, RESEARCH DEPARTMENT AT ALHAMBRA, CALIFORNIA			
NATURAL CONVECTION HEAT TRANSFER UNIT SPECIMEN LOCATIONS DEEP OCEAN TESTS			
ALHAMBRA C F BRAUN & CO CALIFORNIA			
SCALE	DRAWING NUMBER		REVISION
1/8" = 1"	2650 100 RD-10		0
DATE	1-26-65		



FIGURE 13  
DEEP OCEAN TEST UNIT PHOTOGRAPH



## 300-FOOT TEST Continued

Two 26-gauge copper-constantan thermocouples were silver soldered to the Monel specimen (uppermost) of each element. They were parallel connected to indicate an average temperature and for reliability. Instead of extending the thermocouple wires to the measuring instrument on the surface, we employed cold junctions at the test depth and 16 AWG copper extension wires. Two parallel connected cold junctions were installed for each element at a location not warmed by the rising water. The ambient temperature was measured independently with a reversing thermometer. Input voltage to the measuring instrument was the difference between the hot and cold junction output voltages. We used Honeywell Electronic 17 recorder-controllers.

Cumulative power consumption of each heated element was indicated by a Sangamo 120/240-volt, single-phase, 15-amp, Type J-3A wattmeter. These readings had to be corrected for power loss in the 350-foot 12 AWG copper lead wires. To accomplish this, we measured the resistance of the heaters at their operating temperatures prior to running the test and installed an ammeter in each circuit.

The ship's generator voltage was adjusted to yield 120 volts across the heaters. Power loss was then the difference between the generator output voltage and the heater voltage drop multiplied by the line current. All instrumentation was mounted on a 60- by 30-inch aluminum panel which was installed in the ship's cabin. See Figure 14.

**EXPERIMENTAL PROCEDURE** After fabrication, we successfully tested the deep ocean elements at pressures up to 4,000 psia at our Alhambra laboratory. The test unit and instrumentation were then shipped to the dock in San Diego and loaded aboard the Sea Quest.

The test unit was operated successfully in the harbor before leaving for the test location. Then it was thoroughly cleaned with acetone and placed under protective cover for the sea voyage.

Upon arriving at the test site, we anchored the boat from the bow allowing a six-to-one scope. A surface buoy was fastened to the anchor line about 150 feet from the boat. This helped to prevent tangling. Before lowering the test unit, we used the ship's hydrowire and winch to obtain the necessary oceanographic data. Samples for dissolved oxygen and salinity determinations were collected in Nanson bottles. The dissolved oxygen test was performed immediately with a Beckman oxygen meter. A reversing thermometer and a bathethermograph indicated the ambient temperature. Salinity determination was made after the test period.

FIGURE 14  
DEEP OCEAN TEST INSTRUMENTATION

II-34



### 300-FOOT TEST Continued

The test unit was suspended off the starboard side of the vessel from a boom. A 3/16-inch hydrowire supported the test unit. The 7/8-inch OD, 6-conductor 12 AWG power cable, and the 5/8-inch OD, 6-conductor 16 AWG instrument cable were attached to the hydrowire every 20 feet with electrical tape. Chafing gear was applied to the electrical cables where they passed over the ship's railing. Figure 15 indicates the mooring design.

After setting the instrument control points for the ambient temperature, the circuits were energized. Metal surface temperature was indicated continuously by the recorder charts. Power consumption readings were taken at four hour intervals initially, but it was found that twice daily was sufficient for heat transfer data because the consumption was rather small.

After retrieval, the unit was photographed and examined for biological fouling. We then brought it back to our Alhambra corrosion laboratory where the individual specimens were photographed, corrosion products removed, and the samples reweighed. Corrosion rates were calculated from the weight loss and exposure time data.

**FOULING RESULTS** No evidence of biological fouling was found on any part of the array. At the test depth, the dissolved oxygen content ranged from 5.2 to 5.8 ppm, the salinity was 33.85 parts per thousand, and the ambient temperature remained constant at 59 F.

**CORROSION RESULTS** The 300-foot and the 4,500-foot tests are relatively short term from a corrosion standpoint. Because of this, the results of these deeper tests are not strictly comparable to the longer-term shallow water tests. It is possible, however, to compare directly the results obtained from the two deep water tests in terms of corrosion tendencies. The overall results of the 300-foot test are tabulated in Table V.

**MONEL** The oxygen content at the 300-foot level was essentially the same as in the shallow water test. In spite of this, no crevice corrosion was found on the Monel specimen at ambient temperature. This may have been due to insufficient time. The heated Monel specimen retained a bright metallic luster with no evidence of pitting or appreciable general corrosion. Figure 16 shows the Monel specimen at 140 F as it looked after the test.

FIGURE 15  
300-FOOT TEST MOORING DESIGN

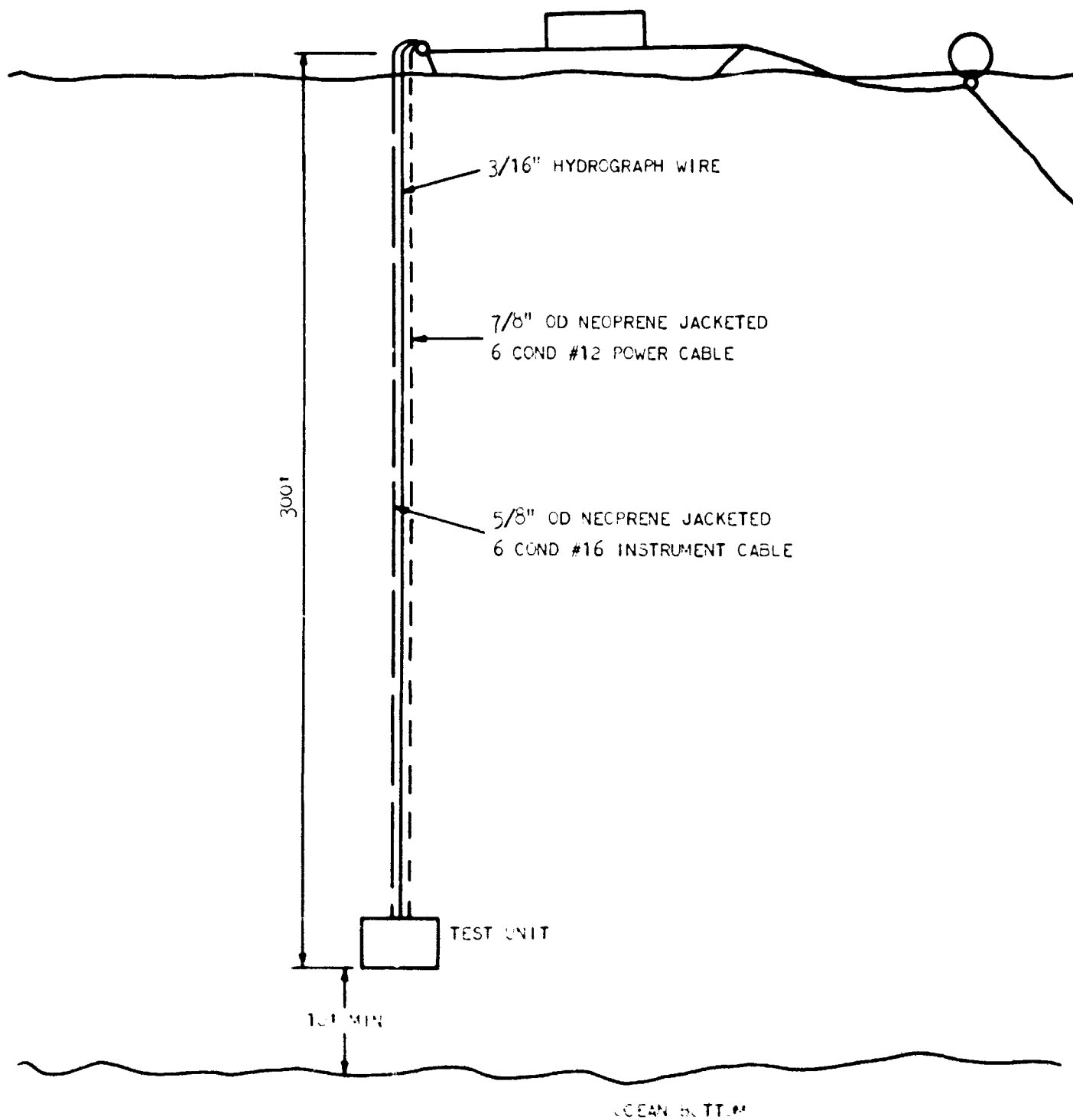


TABLE V

300 FOOT TEST CORROSION

CYLINDERS			
<u>SPECIMEN</u>	<u>TEMPERATURE</u>	<u>CORROSION RATE</u> <u>MILS/YEAR</u>	
MONEL	AMBIENT	0.7	SUPERFICIAL TARNISH, NO EVIDENCE OF
MONEL	100 F	- )	
MONEL	120 F	- )	BRIGHT METALLIC SURFACES, NO EVIDENCE
MONEL	140 F	- )	
90 CU-10 NI	AMBIENT	4.1	SUPERFICIAL TARNISH, MOTTLED YELLOW
70 CU-30 NI	AMBIENT	10.0	VERY CLEAN SURFACE, ONLY A LIGHT TAR
70 CU-30 NI	100 F	8.0)	
70 CU-30 NI	120 F	3.5)	HEAVIER TARNISH THAN AMBIENT SPECIME
70 CU-30 NI	140 F	9.3)	
AL BRONZE	AMBIENT	3.0	MODERATELY THICK AND DARK TARNISH, N
AL BRONZE	100 F	1.4)	
AL BRONZE	120 F	4.3)	TARNISH SOMEWHAT LIGHTER THAN AMBIEN
AL BRONZE	140 F	1.4)	
SI BRONZE	AMBIENT	3.3	MOTTLED SURFACE TARNISH, NO PATCHES
NAVAL BRASS	AMBIENT	4.8	MOTTLED SURFACE TARNISH WITH PATCHES
PLATES			
BE COPPER	AMBIENT	1.4	HEAVY SURFACE TARNISH, SOME REDDISH
AL BRONZE	AMBIENT	0.0	HEAVY SURFACE TARNISH, PATCHES OF BL
TITANIUM	AMBIENT	NIL	BRIGHT METALLIC SURFACE
70 CU-30 NI	AMBIENT	2.3	VERY SUPERFICIAL TARNISH, CLEANER TH
HC COPPER	AMBIENT	1.7	FAIRLY HEAVY TARNISH, PATCHES OF BL
NH BRASS	AMBIENT	1.5	HEAVY MOTTLED TARNISH, PATCHES OF RE
SI BRONZE	AMBIENT	1.1	HEAVY MOTTLED TARNISH, PATCHES OF BL
CARBON STEEL	AMBIENT	30.0	HEAVY RUST SCALE
CONDITIONS OF EXPOSURE		OXYGEN CONTENT	5.2 - 5.8 PPM
		TEMPERATURE	59 F
		TIME	120 HOURS

A

TABLE V

## ON OT TEST CORROSION RESULTS

APPEARANCE AFTER EXPOSURE

F 16, NO EVIDENCE OF PITTING OR CREVICE CORROSION, NO MARINE GROWTH

NO 16, NO EVIDENCE OF PITTING OR CREVICE CORROSION

W 16, MOTTLED YELLOW AND GREEN, NO PITTING OR CREVICE CORROSION

AR 16, A LIGHT TARNISH, NO PITTING OR CREVICE CORROSION

ME 16, AMBIENT SPECIMEN, MOTTLED APPEARANCE, NO PITTING OR CREVICE CORROSION

N 16, DARK TARNISH, NO PITS OR CREVICE CORROSION

EN 16, LIGHTER THAN AMBIENT SPECIMEN AND MORE MOTTLED, NO PITS OR CREVICE CORROSION

F 16, NO PITS OR CREVICE CORROSION

IS 16, NO PITS OR CREVICE CORROSION, RED DEPOSITS AND BLUE-GREEN DEPOSITS

AL 16, SOME REDISH DEPOSIT AROUND SPACER

BL 16, PATCHES OF BLUE-GREEN DEPOSITS

FACE

TR 16, CLEANER THAN C LINDRICAL SPECIMENS

LU 16, PATCHES OF BLUE DEPOSIT, SOME INDICATION OF PITTING

RE 16, PATCHES OF RED AND BLUE DEPOSITS

BL 16, PATCHES OF BLUE DEPOSITS

**B**

## 300-FOOT TEST Continued

70 CU - 30 NI The surface of the ambient specimen was very clean. The heated specimens had a slight tarnish as shown in Figure 16. No pitting or crevice corrosion was detected. The only unusual aspect of the 70 Cu - 30 Ni specimens is the relatively high corrosion rates. See Table V. The rates obtained on the cylinder and the flat plate, both at ambient temperature, do not agree as they did in the shallow water test.

ALUMINUM BRONZE The aluminum bronze cylinders developed a dark mottled tarnish. See Figure 16. The cylinder at 120 F again showed an increase in corrosion rate as compared to the 100 F and the 140 F specimens.

TITANIUM The titanium plate sample retained a bright metallic luster with no evidence of marine fouling. The corrosion rate was too low to calculate.

MISCELLANEOUS In general, the type of deposit or tarnish on the remaining specimens is similar to those found in the shallow water test. The corrosion rates are of the same order of magnitude.

HEAT TRANSFER RESULTS Overall heat transfer coefficients calculated from the power consumption and ambient and metal surface temperatures, are indicated on Figure 17. Notice that there was very little change in this quantity throughout the test. No fouling factor or  $h_p$  was calculated. Dotted lines were drawn through the 120 F and 140 F data points with the same slope as the comparable experimental data points had in the shallow water test. Notice that the points appear to conform to these lines. However, the change in overall coefficient indicated by the dotted lines is within the limits of experimental error. No dotted lines were drawn through the 100 F data because the shallow water experimental heat transfer coefficients did not indicate this decreasing trend with time. The 100 F element heat transfer coefficients for the 300-foot test do, however, appear to decrease with time.



C F BRAUN & CO

FIGURE 16  
APPEARANCE OF ALUMINUM BRONZE, MONEL, AND  
70 Cu-30Ni AFTER THE 300-FOOT TEST

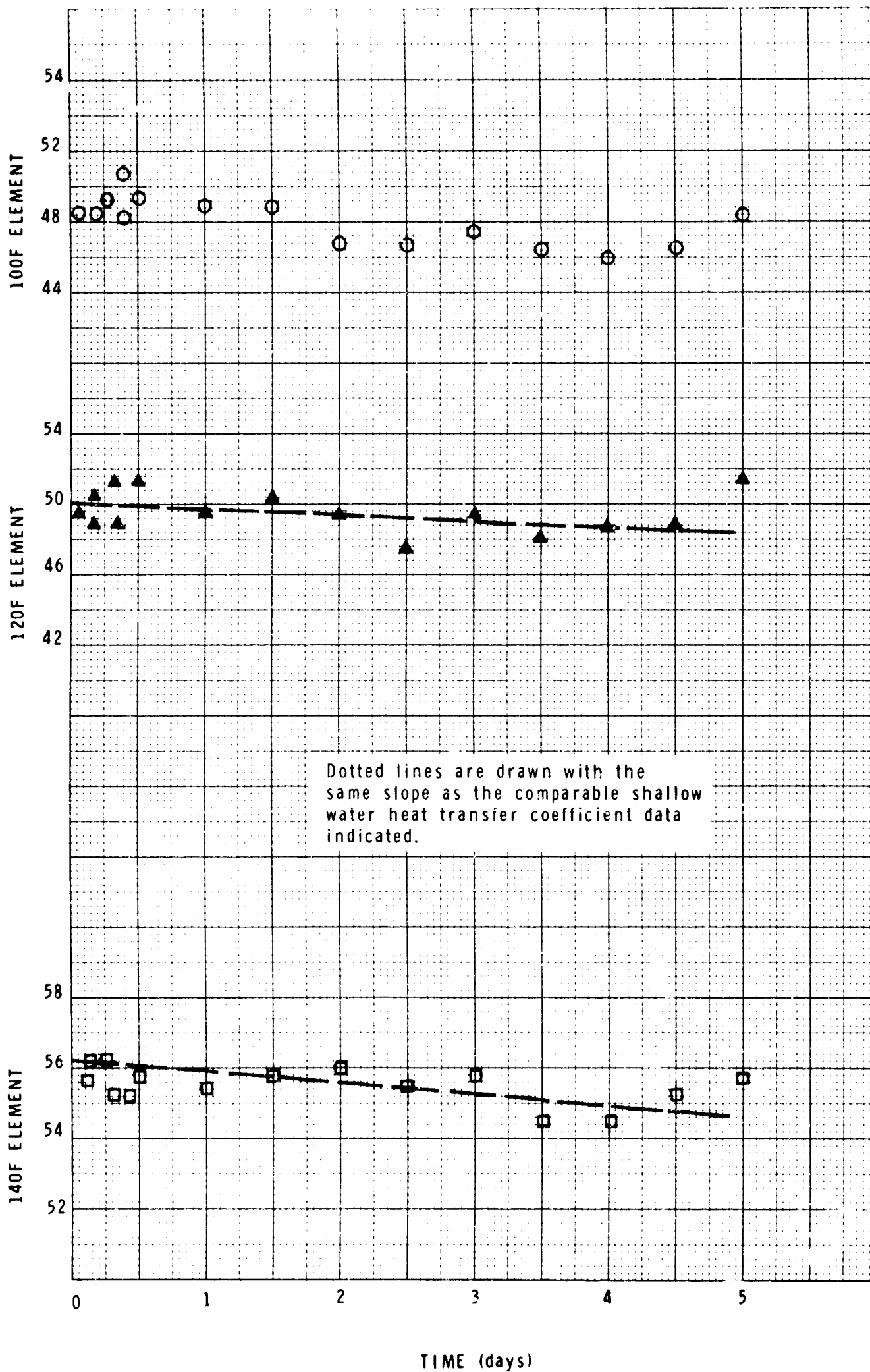


AL BR MONEL 70-30  
NO 11 Pot NO 3 NO 11

300-FOOT TEST HEAT TRANSFER  
COEFFICIENT VERSUS TIME

JEC

FIGURE 17

OVERALL HEAT TRANSFER COEFFICIENT (Btu/hr-ft<sup>2</sup>-F)

## 4,500-FOOT TEST

The 4,500-foot corrosion and fouling experiment was designed to determine the effects of varying metal surface temperature in deep ocean waters. A site was chosen southwest of the southern Coronado Island at 32-13 N, 117-19 W, where radar contact could be maintained with the island and the Mexican coastline. The 4,500-foot depth is below the photic zone where the commoner fouling organisms occur, and the dissolved oxygen content is lower than on the surface. We expected to find much less fouling and corrosion at these depths than in the shallow water tests.

The test began at 1900 hours May 27 and ended at 1900 hours June 1. Two boats were employed in the test, the 48-foot Sea Quest and the 66-foot ocean-going tug Laguna. The vessels are pictured in Figure 18.

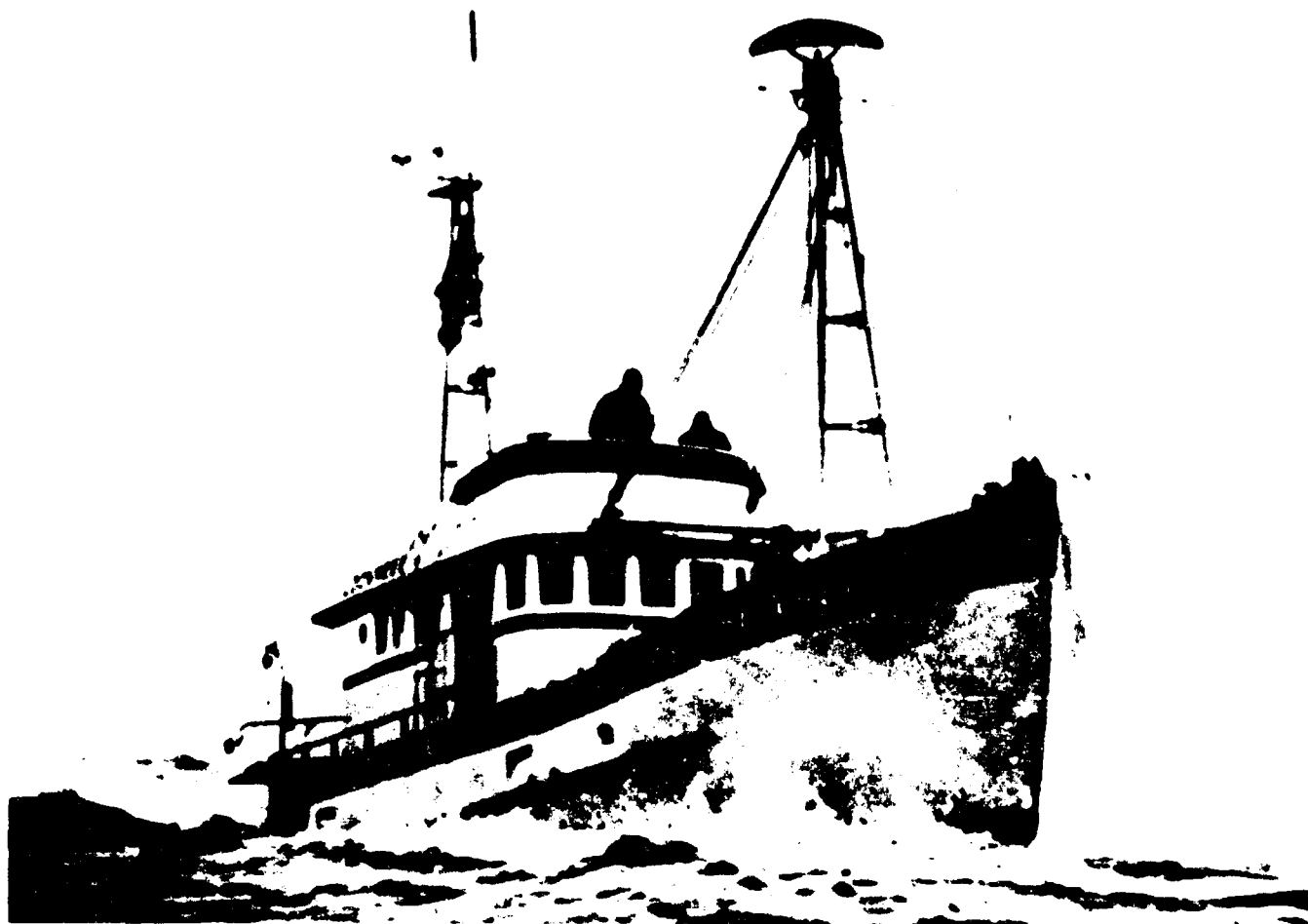
**EXPERIMENTAL APPARATUS** We used the same deep ocean test unit as in the 300-foot test, except for replacement of the metal specimens. Instrumentation was the same also. The instruments were mounted on the deck of the Laguna in a plywood box, because there wasn't room for them in the cabin. A 200-watt light globe burned inside the cabinet throughout the test to reduce corrosion of the instruments.

Twelve 2- by 2-inch glass slides were also exposed at the test depth to find out what kind of living bacteria were present. The slides were to be examined under a microscope after retrieval.

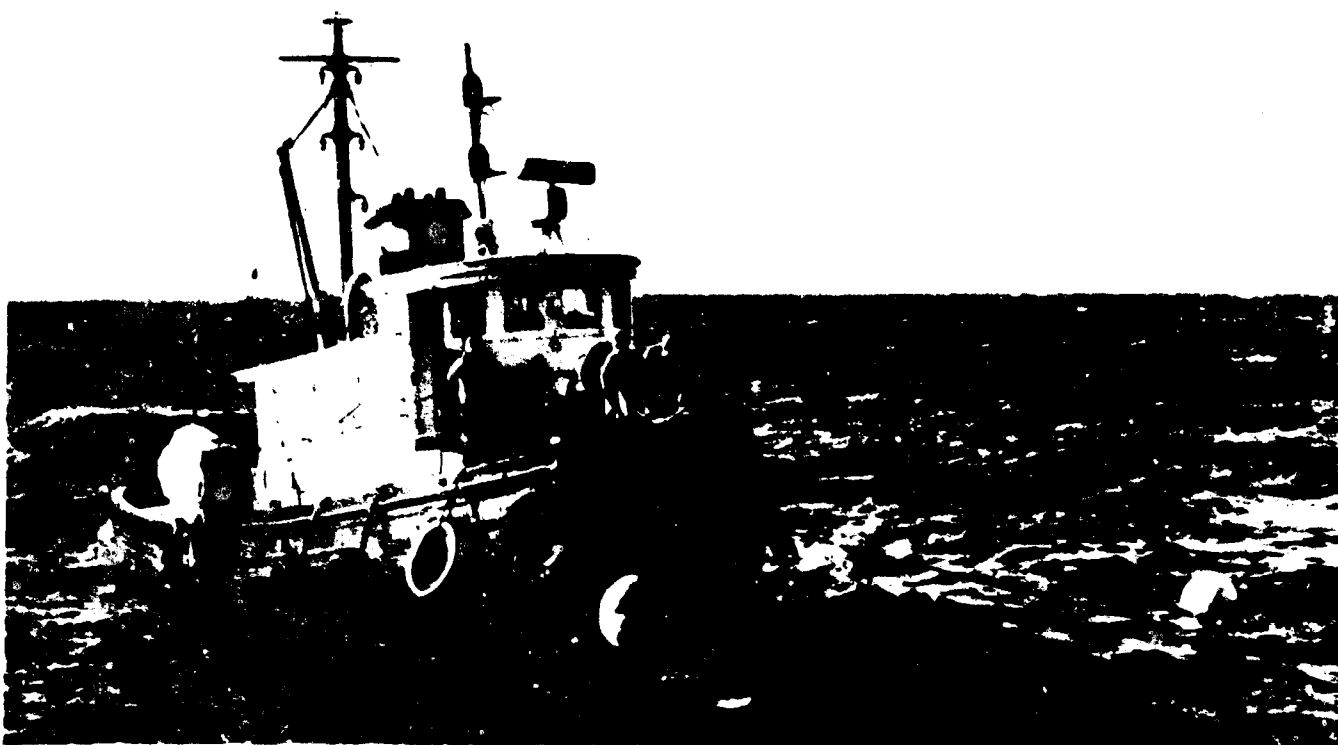
Cumulative power consumption of each element was measured by a Sangamo 480-volt, single-phase, 60-cycle, 15-amp, bottom-connected, watt-hour meter. As in the 300-foot test, correction had to be made for line power losses, but here the losses were much greater. Power and instrument cables were 5,300 feet long. This required a source voltage of 385 volts to maintain 120 volts across the heaters. A 3-phase, 30 kva diesel portable generator was used to power the unit. Each element was connected to a phase to provide a balanced load.

The 48-foot Sea Quest was used for bottom surveys, oceanographic measurements, and assistance in placing the equipment. Star and Crescent's 66-foot ocean-going tug, Laguna, transported the experimental gear and acted as the test platform. There was at least one Braun engineer aboard each boat.

FIGURE 18  
THE TUG LAGUNA AND THE SEA QUEST



48' Oceanographic Research Vessel - The Sea Quest



66' Ocean Going Tug - The Laguna

## 4,500-FOOT TEST Continued

**EXPERIMENTAL PROCEDURE** We first attempted the test in January at a depth of 6,000 feet, using a mooring scheme similar to the 300-foot test. See Figure 19. The location was 31-45.5 N, 117-43 W. A storm caused the mooring to fail and, once adrift, the test unit was destroyed by dragging on the bottom. Only the uppermost support plate and eye bolt were recovered. Because of the severe loading, the support cable and electrical wires were badly twisted.

Since weather and sea state were uncontrollable variables, we tried to minimize their effects by redesigning the mooring system. A novel taut line mooring scheme was developed in which the test unit support cable served also as the anchor line. See Figure 20.

In this design, the mooring cable was weighted by a 2,800-pound clump anchor at the bottom and held taut by two submerged buoys near the surface. A 350-foot pennant line separated the tugboat from the submerged buoys. Two surface buoys were placed along the line. One was designed to submerge when the wind velocity reached approximately 15 knots as a warning to the skipper. The second would submerge when the wind reached 25 knots, and the skipper could attempt to maneuver the vessel to keep this buoy above water. Figure 21 indicates the mooring configuration for the design conditions.

The test unit was placed approximately 50 feet above the bottom. A special weak link placed just below the unit would enable us to retrieve the test unit had the anchor stuck on the bottom. See Figure 22. Power and instrument leads were joined to the load cable every 200 feet with metal clamps and tied with nylon rope at 75-foot intervals in between. The mooring scheme is described in detail in Appendix C.

The 6,000-foot test was initiated again in early May at 32-1 N, 117-52 W. This time the weather was fine, but other complications forced us to discontinue the test. The recorder-controllers, which ran smoothly in the lab, performed erratically at sea. Also, one of the submerged buoys imploded. The resulting shock evidently caused the power lead to break.

Because a satisfactory 6,000-foot test location compatible with Naval operations could not be found and as a 4,500-foot test would still meet the objectives of the program, this requirement was changed. The final test site was ideal. It had a flat bottom and we could maintain radar contact with two points.

FIGURE 19  
SLACK LINE MOORING TEST SYSTEM

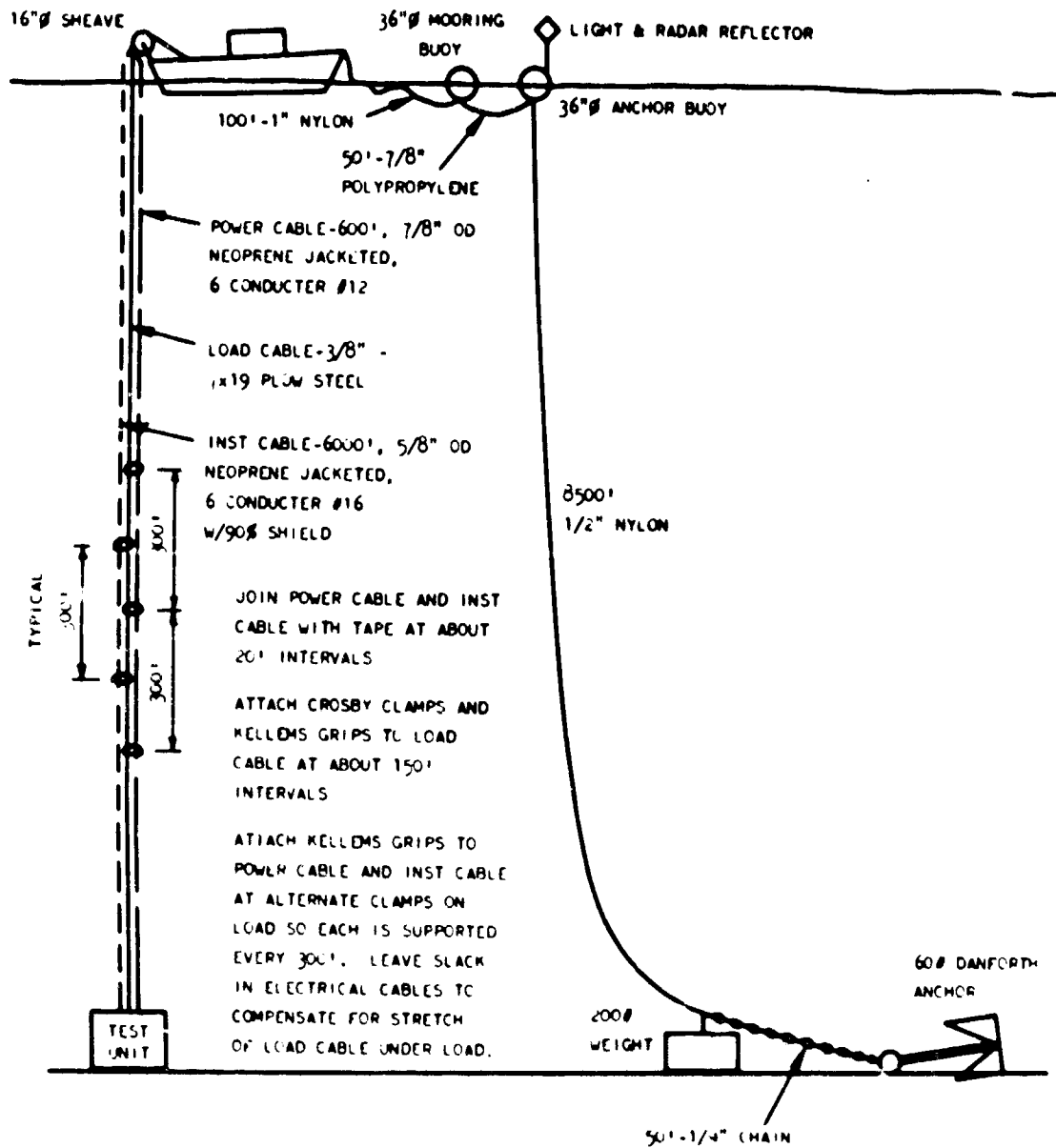


FIGURE 20  
TAUT LINE MOORING TEST SYSTEM

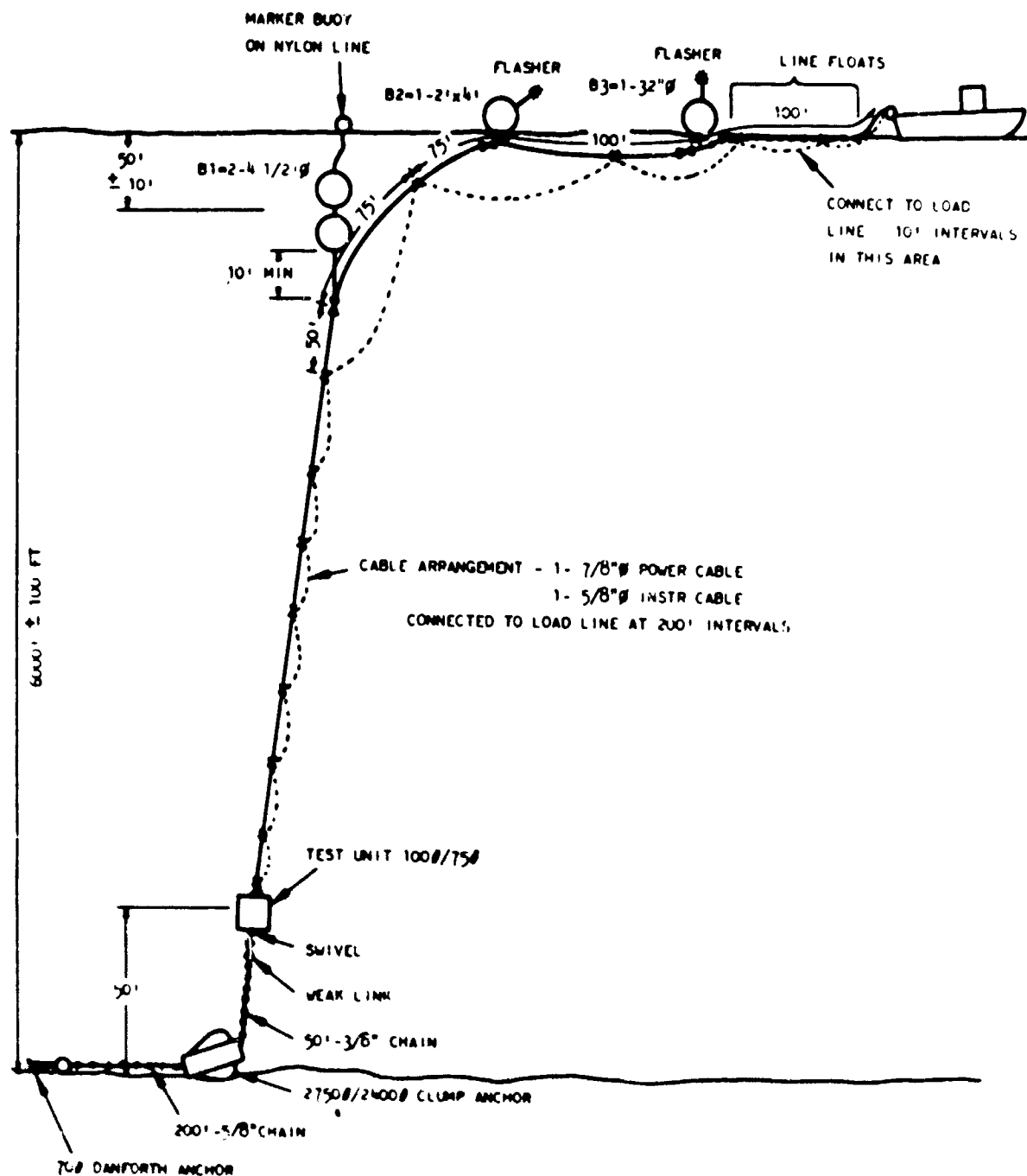


FIGURE 21  
MOORING CONFIGURATIONS FOR DESIGN CONDITIONS

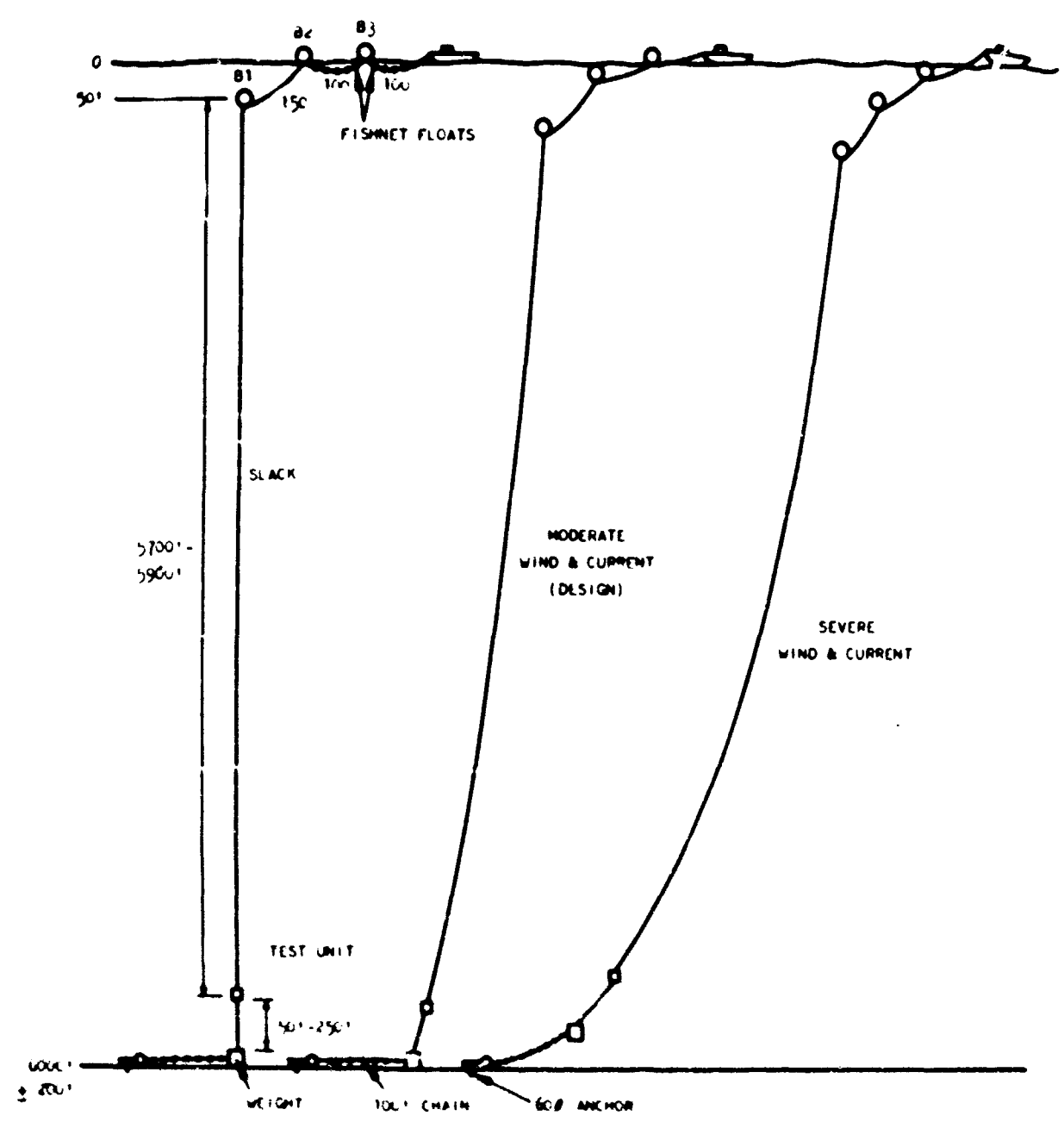
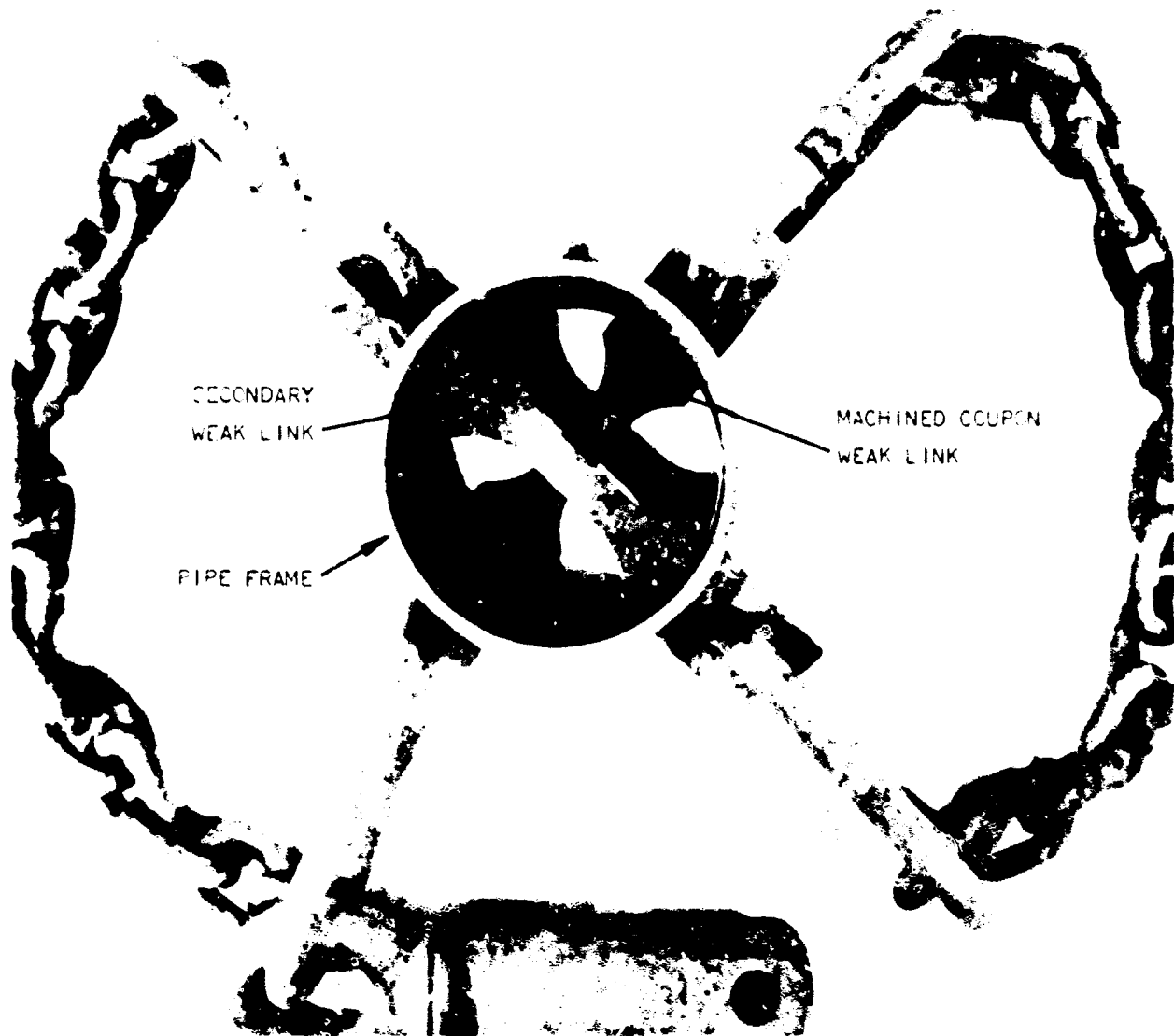




FIGURE 22  
WEAK LINK ARRANGEMENT



#### 4,500-FOOT TEST Continued

Upon arriving at the test site just after sunrise on May 27, the Sea Quest mapped the bottom in the vicinity and took the same oceanographic data as in the 300-foot test. Then the Laguna crew started placement of the experimental unit. The Laguna was secure and test operation started at 1900 hours that day. The Sea Quest departed for San Diego to return again at the completion of the test period to repeat the oceanographic readings.

After retrieval at 1900 hours on June 1, the unit was photographed, examined for biological fouling, and the corrosion measurements were made.

**FOULING RESULTS** No evidence of biological fouling was found on any part of the array. Glass slides exposed at the test depth showed evidence that living bacteria were present. Since bacteria initiate the fouling cycle, it is likely that in time a colony of microorganisms would have formed. In this instance, however, only limited reproduction took place. No other sessile organisms were evident.

Under 1,000 X magnification, the concentration was 10 to 20 bacteria per field (less than one square centimeter) on the average. These were not unique in any way. Ovoid rods 4 to 5 microns long were predominant. Next most abundant were long rods (10 microns), slender rods (less than 6 microns), and a similar number of vibrio. Also, cocci of a spherical shape were noted.

**CORROSION RESULTS** At 4,500 feet, oxygen content was in the range of 2.3 to 2.6 ppm, salinity ranged from 34.47 to 34.56, and ambient temperature remained constant at 38 F. Corrosion results are tabulated in Table VI.

**MONEL** The cylinder at ambient temperature had formed a large number of pit sites as shown in Figure 23. The heated cylinders were free of pits. No crevice corrosion was noted on any of the Monel specimens. In addition, the heated specimens retained a brighter metallic luster than the unheated specimen. See Figure 23 for the comparison.

**70 CU - 30 NI** In contrast with Monel, the ambient 70 Cu - 30 Ni cylinder showed less surface tarnish than the heated cylinders. See Figure 23 for comparison. The corrosion rates on 70 Cu - 30 Ni are significantly lower at 4,500 feet than at 300 feet. This may reflect the lower oxygen concentration at 4,500 feet.

TABLE VI

4500-FOOT TEST CORROSION

## CYLINDERS

<u>SPECIMEN</u>	<u>TEMPERATURE</u>	<u>CORROSION RATE</u> <u>MILS/YEAR</u>	
MONEL	AMBIENT	1.2	SURFACE HAS METALLIC APPEARANCE, BUT CORROSION
MONEL	100 F	- )	
MONEL	120 F	- )	SURFACES ARE BRIGHT AND SHINY. NO
MONEL	140 F	- )	
90 CU-10 NI	AMBIENT	1.5	SURFACE HAS A DULL YELLOW COLOR, NO
70 CU-30 NI	AMBIENT	1.7	AMBIENT SPECIMEN HAS SLIGHTLY MORE
70 CU-30 NI	100 F	3.3)	
70 CU-30 NI	120 F	1.4)	SUPERFICIAL SURFACE TARNISH, SLIGHT
70 CU-30 NI	140 F	3.4)	
AL BRONZE	AMBIENT	1.2)	
AL BRONZE	100 F	1.5)	ALL SPECIMENS HAVE MOTTLED APPEARANCE
AL BRONZE	120 F	1.6)	AREA UNDER SPACERS HEATED SAMPLE
AL BRONZE	140 F	1.2)	
SI BRONZE	AMBIENT	1.4	HEAVY SURFACE TARNISH PATCHES OF
NAVAL BRASS	AMBIENT	1.7	SURFACE LER. BLOTCH. YELLOW GREEN

## PLATES

BE COPPER	AMBIENT	0.9	LIGHT YELLOW SURFACE TARNISH, NO CR
AL BRONZE	AMBIENT	1.0	LOOKS THE SAME AS CYLINDERS
TITANIUM	AMBIENT	NIL	BRIGHT AND SHIN
70 CU-30 NI	AMBIENT	0.9	HAS BRIGHTER METALLIC APPEARANCE THAN
HC COPPER	AMBIENT	1.1	DULL COPPER MATTE TARNISH, FEW SPOT
HP BRASS	AMBIENT	1.5	YELLOW GREEN SURFACE TARNISH. FEW
SI BRONZE	AMBIENT	1.3	DULL MATTE TARNISH, VERY BLOTCHY.
CARBON STEEL	AMBIENT	34.7	HEAVY RUST SCALE

CONDITIONS OF EXPOSURE

 OXYGEN CONTENT  
 TEMPERATURE  
 TIME

 2.3 - 2.6 PPM  
 38 F  
 120 HOURS

A

TABLE VI

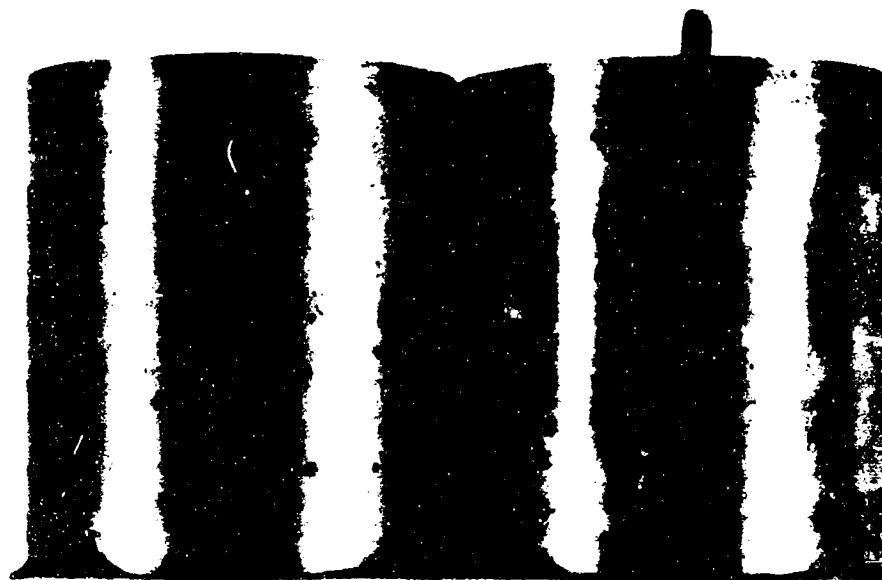
OT TEST CORROSION RESULTS

APPEARANCE AFTER EXPOSURE

...C APPEARANCE, BUT DULLER THAN HEATED SPECIMENS. MANY PIT SITES HAVE FORMED. NO MARINE GROWTH OR CREVICE  
AND SHINY. NO EVIDENCE OF PITTING OR CREVICE CORROSION. NO MARINE GROWTH  
... YELLOW COLOR, NO PITTING OR CREVICE CORROSION  
... S SLIGHTLY MORE METALLIC APPEARANCE THAN HEATED SPECIMENS. NO PITTING, CREVICE CORROSION OR MARINE GROWTH  
... TARNISH, SLIGHT DEPOSIT UNDER SPACER, NO PITTING, CREVICE CORROSION OR MARINE GROWTH  
... MOTTLED APPEARANCE. DULL MATTE TARNISH, YELLOW GREEN IN COLOR. AMBIENT SPECIMEN SHOWS COPPER COLORED  
... HEATED SAMPLES TEND TO FORM A DEPOSIT UNDER SPACERS. NO EVIDENCE OF PITTING  
... PISH. PATCHES OF BLUE-GREEN DEPOSITS. METAL UNDER SPACER IS COPPER COLORED IN SPOTS  
... YELLOW GREEN AREAS AND COPPER COLORED AREAS  
... ICE TARNISH, NO CREVICE CORROSION AND NO MARINE GROWTH  
... CYLINDERS  
... IC APPEARANCE THAN HEATED CYLINDERS  
... TARNISH, FEW SPOTS OF GREEN DEPOSIT. BRIGHT METAL UNDER SPACER, SOME DEPOSIT ADJACENT TO SPACER  
... ICE TARNISH. FEW SPOTS OF BLUE-GREEN DEPOSITS. SOME DEPOSIT ADJACENT TO SPACER  
... VERY BLOTCHY. SOME GREEN DEPOSIT. LESS DEPOSIT AROUND SPACER THAN HC COPPER

**B**

FIGURE 23  
APPEARANCE OF MONEL AND 70Cu-30Ni AFTER THE  
4500-FOOT TEST



MONEL - COLD

MONEL - 100 F

Dark spots on the ambient specimen are pit sites.  
Heated specimens retained more metallic luster  
as shown by the 100F cylinder.



70-30 Cu Ni  
Cold

70-30 Cu Ni  
100 F

#### 4,500-FOOT TEST Continued

**ALUMINUM BRONZE** All specimens developed a dark mottled surface tarnish. The corrosion rates obtained on both the unheated and heated specimens were nearly equal. The specimens showed some signs of dealuminization.

**TITANIUM** The plate specimen was bright and shiny with a negligible corrosion rate.

**MISCELLANEOUS** Appearance and corrosion rates obtained on the remaining ambient specimens approximated the results obtained in the 300-foot and shallow water tests.

**HEAT TRANSFER RESULTS** Overall heat transfer coefficients calculated from the power consumption and ambient and metal surface temperatures, are indicated on Figure 24. Overall coefficient did not appear to change with time and no fouling factors of  $h_D$ 's were calculated.

#### DISCUSSION

**MARINE GROWTH** Fouling by macroscopic species did not take place on any surface above 100 F. However, in the shallow water test, structures near and above the heated surfaces supported luxurious groups of soft-bodied organisms. Within four months there appeared stratified growths of bryozoan *Bugula*, tunicate *Chione*, and mat-like bryozoan *Holoporella*. The most prolific growths occurred near the 100 F element. The least, near the 140 F element. These growths were preceded by a layer of filamentous algae and slime algae, which was also observed on the unheated element.

These observations suggest that fouling may occur on structures exposed to warm water currents from undersea heat rejection surfaces. Future designs should eliminate such contact if possible. No geometry or substrate roughness effect on fouling was detected.

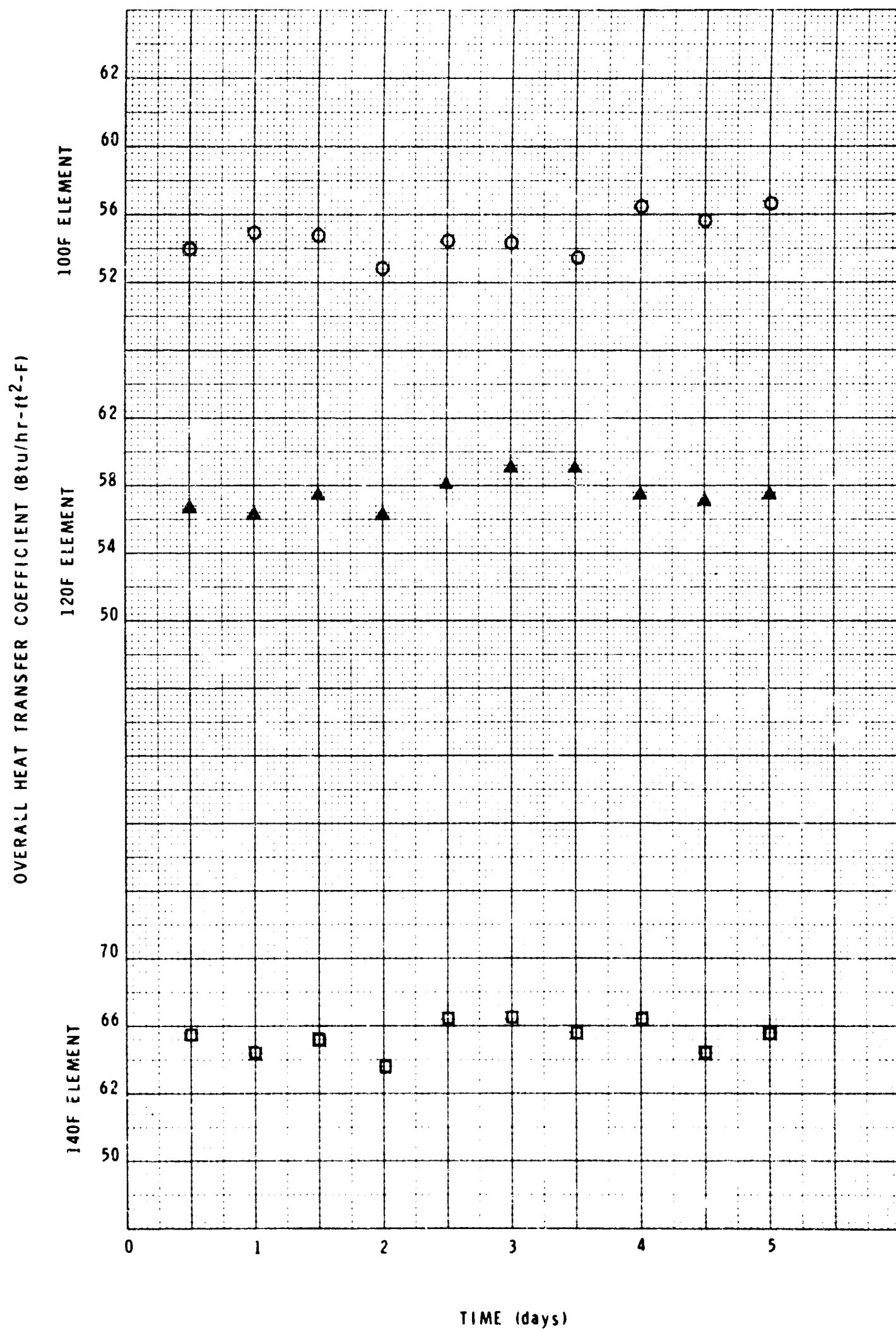
There were some differences between metals with respect to fouling. Normally, copper, silicon bronze, naval brass, and HH brass are considered nonfouling. No growth was observed on these metals. Titanium, on the other hand, is not considered antifouling, and it supported a large growth of tunicates. Monel and the cupronickel alloys also allowed marine growth.

During the sea experiments, we anticipated that no fouling would develop on the heated surfaces. However, there was a strong possibility that organisms might attach to areas in contact with heated water. Settling by cyprids, which normally occurs in three to four days, was chosen as a reference. There was no evidence of fouling by that species on the test unit.

4500-FOOT TEST HEAT TRANSFER  
COEFFICIENT VERSUS TIME

JEC

FIGURE 24



## DISCUSSION Continued

From the harbor results one might have assumed that no cyprids would have set on the deep ocean unit. In the shallow test, ample time passed without the appearance of mussels, of barnacles, or of any other hard-shelled fouler. Although the shallow water unit was in a severe fouling environment, no evidence of hard-shell fouling was seen on the heated metals. Thus, the metal surface temperature must have been in excess of environmental tolerances.

**CORROSION** The tendency to form scale does not seem to be affected greatly by temperature in shallow water. Monel formed a heavy gray scale at all temperatures. At 300 feet and 4,500 feet, heated Monel specimens retained a higher metallic luster than the ambient specimen. In contrast to this, the heated 70 Cu - 30 Ni specimens developed more tarnish than the ambient 70 Cu - 30 Ni specimen. In the shallow water test, the highest corrosion rate occurred at 120 F. The results from the 300- and 4,500-foot tests are somewhat erratic. The rate on 70 Cu - 30 Ni is relatively high at the 300-foot depth and is relatively constant over the temperature range.

**EFFECT OF DEPTH** Corrosion rates of the alloys high in copper are essentially the same at all depths. As noted previously, the relatively high corrosion rates on the 70 Cu - 30 Ni specimens at 300 feet are somewhat anomalous. This may be related to the higher oxygen content and temperature at 300 feet as compared to 4,500 feet. A striking difference was noted in the behavior of Monel at the different depths at ambient temperature. In the shallow water test, the ambient Monel cylinder showed severe crevice corrosion under the saran spacer. At 4,500 feet, the unheated Monel cylinder developed many pit sites and no crevice corrosion occurred. At 300 feet, no pitting or crevice corrosion was noted on the unheated Monel specimen.

**MONEL** Monel is a weak active-passive alloy. This class of alloy is characteristically susceptible to crevice corrosion or pitting where the passive film suffers a breakdown. At 4,500 feet, the supply of oxygen is apparently insufficient to prevent the tendency of chloride ions from locally perforating the passive film. These corrosion properties of Monel tend to make it a poor material for use in the deep ocean.

**CUPRONICKELS** The cupronickels are considerably less susceptible to crevice corrosion, pitting, or marine fouling than Monel. These alloys combine the desirable properties of copper and nickel. The 90 Cu - 10 Ni offers better resistance to marine fouling in shallow water and adequate corrosion resistance in deep water. It appears to offer the widest range of flexibility as a material for components submerged in the ocean.



## DISCUSSION Continued

**ALUMINUM BRONZE** The aluminum bronze alloy exhibited good resistance to corrosion under all conditions of test. However, in the 4,500-foot test there was some evidence of aluminum removal. Aluminum bronze has resistance to marine fouling and relatively high mechanical strength. Further deep ocean corrosion tests should be conducted with aluminum bronze before it is employed as a deep ocean construction material.

**TITANIUM** Under the nonfouling conditions in deep water, the corrosion resistance of titanium offers a decided advantage over other alloys. Even in shallow water, heated surfaces of titanium would probably be free of fouling as were the other alloys tested. Future test programs should include titanium heated specimens. Titanium has exceptionally good mechanical strength but a low thermal conductivity.

**HEAT TRANSFER** Overall coefficients of heat transfer obtained in the test can be compared on the basis of the first week's results only. While the 4,500-foot test coefficient did not change significantly with time, the shallow water and 300-foot test coefficients fell. In the 300-foot test, overall heat transfer coefficients calculated from experimental data appeared to follow the shallow water data trend. However, the decreases were within the limits of experimental error.

The percentage differences between shallow water coefficients derived from power consumption the first day and the first week are 5.1 (100 F), 2.0 (120 F), and 2.2 (140 F). These decreases cannot be considered very significant in view of the data scatter in succeeding weeks. However, it is important to note that all three shallow water coefficients did fall during the first week.

## CONCLUSIONS AND RECOMMENDATIONS

## SUMMARY OF CONCLUSIONS

- 1 Marine fouling did not occur on heated surfaces above 100 F.
- 2 Metal and plastic structures in contact with warmed water were severely fouled by soft-bodied organisms in the shallow water test. The most prolific marine growth occurred near the 100 F element, and the least, near the 140 F element.
- 3 No effect of geometry or substrate roughness was observed on marine growth.

## CONCLUSIONS AND RECOMMENDATIONS Continued

- 4 Future designs should eliminate, if possible, structures exposed to warm water currents from undersea heat rejection surfaces.
- 5 There were significant differences between metals in their ability to sustain marine growth.
- 6 No fouling occurred on the deep ocean test unit when exposed five days at 300 feet and five days at 4,500 feet. There was a low bacteria count on glass slides exposed at 4,500 feet.
- 7 The tendency to form corrosion scale was not greatly affected by temperature over the range 100 - 140 F.
- 8 Depth did not significantly affect corrosion rates of alloys high in copper content.
- 9 Because its passive film suffers a breakdown in low oxygen environment, Monel is not recommended as a deep ocean construction material.
- 10 Both 70 - 30 and 90 - 10 cupronickel were less susceptible to crevice corrosion, pitting, and marine fouling than Monel. The alloy 90 - 10 cupronickel is recommended as a construction material for heat rejecting components in the deep ocean.
- 11 Aluminum bronze exhibited good corrosion and marine fouling resistance, but showed slight evidence of aluminum removal in the 4,500-foot test. This effect should be further investigated before aluminum bronze is employed as a deep ocean construction material.
- 12 Titanium's very low corrosion rate in seawater makes it appear attractive as an undersea construction material. An unheated specimen was severely fouled in the shallow water test. Titanium's resistance to marine growth and corrosion characteristics under heated conditions remains to be tested.
- 13 Overall heat transfer coefficient of the shallow water 100 F element did not decrease with time. During the first four weeks of exposure, overall heat transfer coefficients of the shallow water 120 F and 140 F elements did decrease with time. Fouling coefficients at 200 and 310 Btu/hr-ft<sup>2</sup>-F were calculated for the 120 F and 140 F elements, respectively.

## CONCLUSIONS AND RECOMMENDATIONS Continued

- 14 There was no significant change in overall heat transfer coefficient with time for any of the elements in the 4,500-foot test. During a comparable period in the shallow water tests, the overall coefficients fell two to five percent.
- 15 The 300-foot test overall heat transfer coefficients appeared to follow the same trend as the shallow water test data. However, decreases with time were within the range of experimental error.

RECOMMENDATIONS FOR FUTURE WORK The results and conclusions of this initial investigation of corrosion and fouling of heated surfaces have suggested several areas of needed investigation. Although the two ocean tests have indicated that significant fouling does not occur, additional long-term data would be desirable to verify this extrapolation. Of course, such data would be expensive to obtain from a ship. However, an attractive alternative may be experimentation with bottom-mounted elements from a pier adjacent to a submarine canyon using shore-side power. Depths up to 500 feet (a region of low light intensity) could be reached with about a half-mile of electrical cable from several canyons along the Southern California coast.

Velocity along a heated surface appeared to be an important variable in marine fouling and in the heat transfer fouling coefficient  $h_D$ . According to literature data, marine fouling decreases and  $h_D$  increases as velocity is raised. We achieved velocities which were estimated at less than 0.5 feet per second with the test units. Greater velocities would probably be developed by turbulent natural convection along a full scale submerged heat rejection unit. Effect of this variable could be determined by testing longer elements with a greater heater capacity.

This investigation's results indicated that additional testing of certain metals would be desirable. The ambient titanium specimen had an extremely low corrosion rate which made it appear attractive as an undersea construction material. Additional tests are necessary to determine titanium's corrosion and biological growth characteristics when heated. Beryllium copper and silicon bronze, which showed promise at ambient temperature, could be tested along with the titanium. The deep ocean corrosion characteristics of aluminum bronze should be further investigated to determine the rate of dealuminization.

## TERMS AND SYMBOLS, CHAPTER II

A	Heat transfer area, $\text{ft}^2$
$h_D$	Fouling coefficient, $\text{Btu/hr-ft}^2\text{-F}$
Q	Heat transfer rate, $\text{Btu/hr}$
U	Overall heat transfer coefficient, $\text{Btu/hr-ft}^2\text{-F}$
$U_C$	Clean overall heat transfer coefficient, $\text{Btu/hr-ft}^2\text{-F}$
$U_D$	Overall heat transfer coefficient with scale, $\text{Btu/hr-ft}^2\text{-F}$
$\Delta t$	Temperature difference, F

## CHAPTER III, NATURAL CONVECTION HEAT TRANSFER

## ABSTRACT

In this chapter we present results of a literature survey of natural convection heat transfer from both single and multiple vertical surfaces to water and other fluids. The survey indicated that little would be gained by more investigation of the laminar region. However, additional experimentation is necessary in the turbulent region. We found no published experimental data for natural convection heat transfer from vertical finned surfaces at the high Rayleigh numbers expected in seawater.

A heat transfer mathematical analysis showed that a very small portion of an undersea heat rejection surface is likely to operate in the laminar region. A semiempirical mathematical model was proposed for the more pertinent turbulent region. It demonstrates that boundary layers can limit fin spacing or height of surface in turbulent natural convection heat transfer.

A new method was developed to optimize the geometry of a finned heat transfer surface with respect to gross heat transfer coefficient. This technique includes the effect of fin spacing in addition to generally accepted variables. It also takes into account nonuniformity of surface heat transfer coefficient over a finned configuration.

## LITERATURE SURVEY

In the literature search we emphasized the following topics - vertical cylinders and plates, parallel plates, banks of vertical tubes, effects of a perpendicular current on free convection, and mathematical techniques for solving the natural convection differential equations. The complete survey is listed in the bibliography. Only the works most pertinent to our study will be described in this section.

Natural convection heat transfer on vertical surfaces has been extensively studied from both theoretical and experimental standpoints. However, most of the experimental work and almost all theoretical attacks have dealt with the laminar rather than the turbulent flow region. Experimental studies have concentrated on air as a working fluid and only a few investigations have been performed with liquids. Multiple surface studies are very rare.

## LITERATURE SURVEY Continued

To achieve an idea of the magnitude of the Prandtl and Grashof numbers, which are the governing groups in natural convection heat transfer, we constructed the following example. Physical properties of seawater were obtained from Sverdrup et al (111).

## Assume

Metal surface temperature = 140 F  
Seawater temperature = 40 F  
Depth = 20,000 ft  
Pressure = 6,000 decibars (8,700 psia)  
Salinity = 35 o/oo

## Calculate

Film temperature = 90 F  
 $C_p = 0.945 \text{ Btu/lbm-F}$   
 $\rho = 66.7 \text{ lbm/ft}^3$   
 $\mu = 5.84 \times 10^{-4} \text{ lbm/ft-sec}$   
 $k = 0.35 \text{ Btu/hr-ft}^2\text{-F/ft}$   
 $\beta = 1.95 \times 10^{-4} \text{ F}^{-1}$   
 $Pr = 5.68$   
 $Gr_x = 8.20 \times 10^9 (x)^3$   
 $Ra_x = 4.66 \times 10^{10} (x)^3$

Notice that the Grashof and Rayleigh (Grashof times Prandtl) numbers can reach extremely high values, even at low values of height  $x$ . It is generally accepted that the transition from laminar to turbulent natural convection takes place at Rayleigh numbers between  $10^9$  to  $10^{10}$ . Thus, the majority of heat transfer would occur under turbulent rather than laminar conditions. Transition in the example would occur at vertical distances of 0.28 to 0.60 feet above the leading edge.

## LITERATURE SURVEY Continued

Because heat transfer will occur primarily under turbulent conditions on undersea heat rejection surfaces, we decided to devote most of our effort to this area. Prediction methods for laminar natural convection heat transfer on vertical surfaces are included for completeness.

**VERTICAL PLATES AND CYLINDERS** Possibly the first practical straightforward solution of the convection equation for vertical surfaces was due to Lorenz (86) in 1881. He derived an expression for the mean heat transfer coefficient for steady-state laminar natural convection in gases. The form of his equation, which is

$$Nu = C (Ra_x)^{1/4} \quad (1)$$

has persisted, and Lorenz's equation represents a triumph of the classical approach.

The laminar natural convection equation has been improved since, mainly from the standpoint of logic and elegance employed in the derivation. The most elaborate improvement was effected by E Schmidt and Beckman (103) in 1930, in cooperation with Pohlhausen (92). These workers succeeded in obtaining a solution of the laminar temperature and velocity boundary layer equations. Their derivation is given in many textbooks on heat transfer - for instance, Jakob (77). Schmidt and Beckman also measured temperature and velocity profiles in laminar natural convection with air and obtained excellent agreement with their theoretical results.

To generalize Schmidt and Beckman's approach for all fluids, Ostrach (90) in 1952 numerically solved the Navier-Stokes and flow energy equations for varying Prandtl number. He obtained the expression

$$Nu_{\text{mean}} = f(Pr) (Ra_x)^{1/4} \quad (2)$$

where  $f(Pr)$  is given below

<u>Pr</u>	<u>f(Pr)</u>
0.01	0.242
0.733	0.518
1.0	0.535
10	0.619
100	0.652
1,000	0.655

## LITERATURE SURVEY Continued

Thus, the difference between the Nusselt modulus in a liquid metal with  $Pr = 0.01$  and a viscous oil with  $Pr = 1,000$  is over 250 percent at equal Rayleigh numbers. Ostrach's theoretical results also agreed favorably with experimental data.

Sparrow and Gregg (107) theoretically explored the difference between laminar heat transfer coefficients obtained under constant surface temperature and constant heat flux. They concluded that the difference was only slight if the average Nusselt number for constant heat flux was calculated using the  $\Delta T$  at one-half the height of the plate. Even if end point  $\Delta T$ 's were employed, the maximum error would be less than 10 percent. Sparrow and Gregg's analysis has been substantiated by the experimental results of Libby (85), Hill (75), and Bartolsky (51).

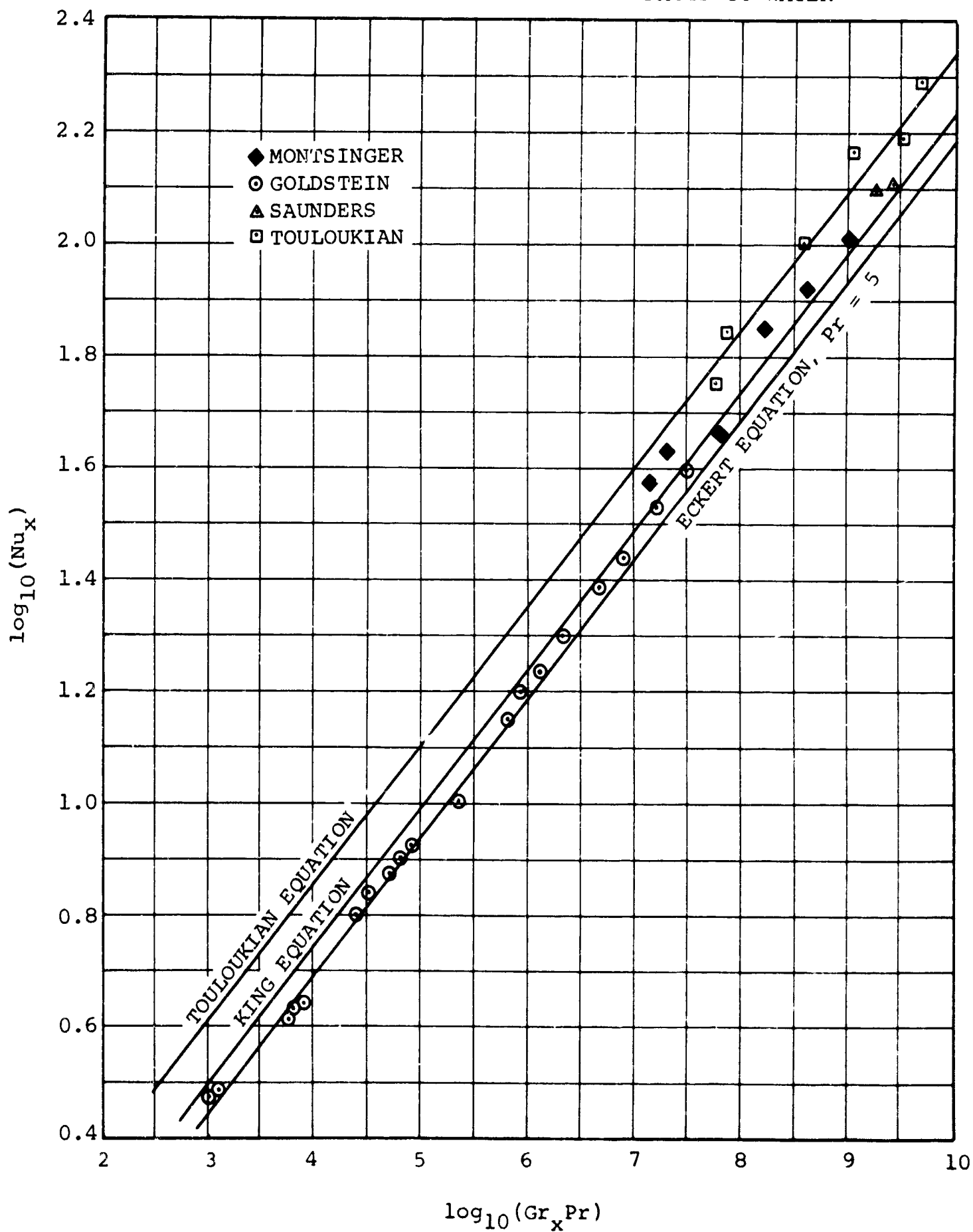
A compilation of experimental data on laminar natural convection heat transfer data with liquids from vertical plates is presented in Figure 25. Several authors have proposed empirical or semiempirical equations to fit observed data. The most common equations are listed below and are also indicated in Figure 25.

AUTHOR	LAMINAR NATURAL CONVECTION HEAT TRANSFER EXPRESSION	
King (81), 1932	$Nu_x = 0.555 (Ra_x)^{1/4}$	(3)
Touloukian (112), 1948	$Nu_x = 0.726 (Ra_x)^{1/4}$	(4)
McAdams (89), 1954	$Nu_x = 0.590 (Ra_x)^{1/4}$	(5)
Eckert (60), 1959	$Nu_x = 0.508 Pr^{1/4} (0.952 + Pr)^{-1/4} (Ra_x)^{1/4}$	(6)

As one might expect, turbulent natural convection heat transfer is on a far less firm theoretical basis than its laminar counterpart. Most prediction methods are based on dimensional analysis, where the constants are derived empirically from experimental data.

We found only a few experimental investigations which dealt with turbulent natural convection heat transfer in water from vertical plates and cylinders. Saunders (97) in 1939 experimented with two aluminum plates each 30.5 cm wide with lengths of 61 and 30.5 cm. Electric heating elements of resistance type, insulated on both sides by sheets of mica, were sandwiched between the aluminum sheets. The sandwich construction was framed with wood projecting 2.5 cm from the edge of the plates and made flush to the aluminum.



EXPERIMENTAL DATA ON LAMINAR NATURAL CONVECTION  
HEAT TRANSFER FROM VERTICAL SURFACES TO WATER

## LITERATURE SURVEY Continued

Saunders used four heating elements for the large plate and two for the smaller one. He embedded copper-eureka thermocouples into horizontal grooves cut into the front face of the aluminum and covered them with lead.

For the heat transfer tests, he suspended the plates in a tank 25 x 61 cm horizontal section and 1,600 cm high. The top of the plate remained 30 cm below the surface of the water. Saunders determined heat transfer coefficients from the equation

$$h = \frac{q/A}{(T_S - T_A)_{\text{mean}}} \quad (7)$$

When ambient temperatures differed more than 10 percent from the leading edge to the top of the plate, he rejected the data. Saunders' data are shown in Figure 26.

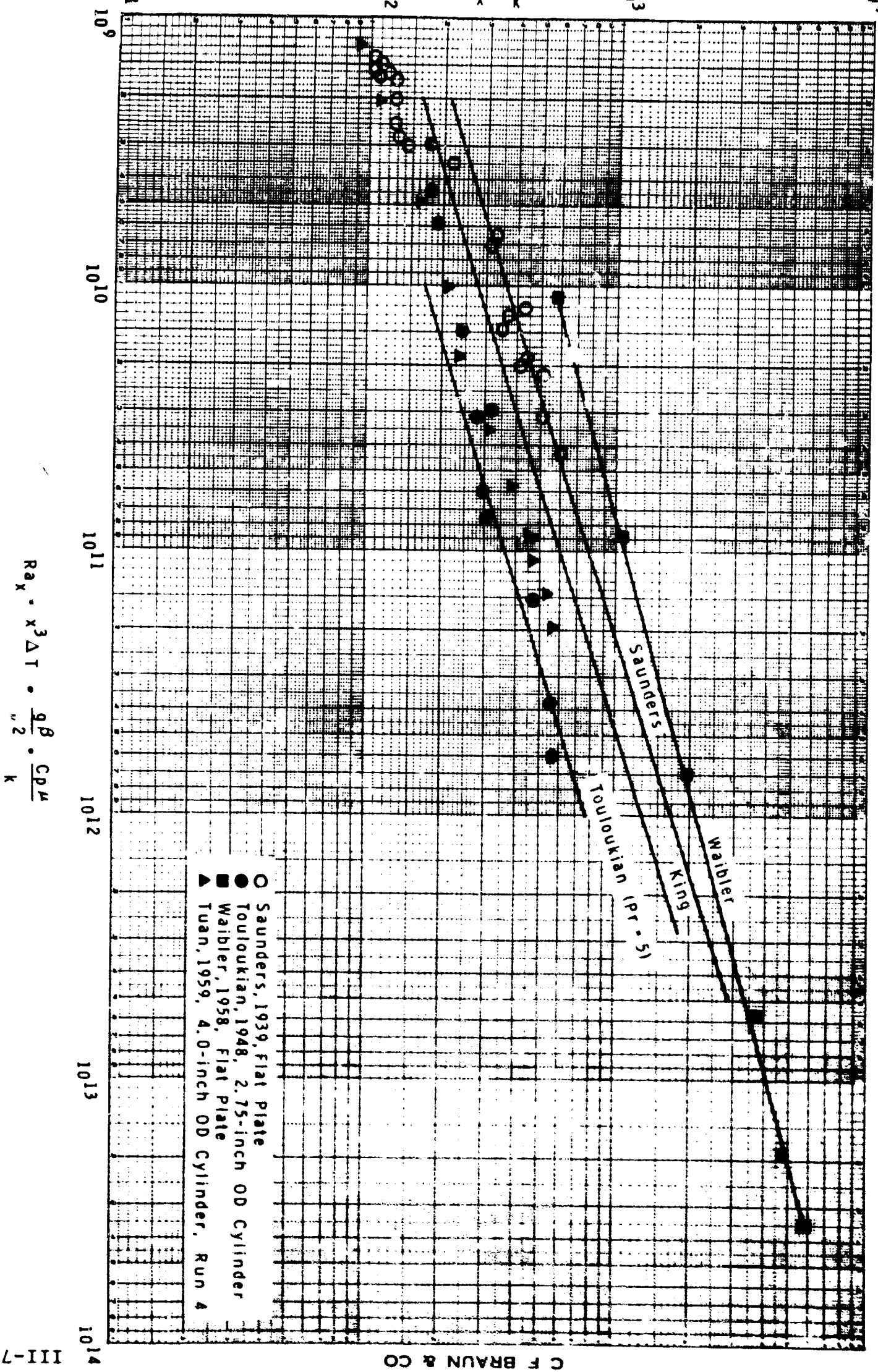
Touloukian (112) in 1948 presented turbulent natural convection heat transfer data on water and ethylene glycol from heated cylinders. He used 2.5-inch OD cylinders and heights of 6, 18, and 36.25 inches. Touloukian concluded that it is unlikely that the heat transfer coefficients obtained with the cylinders should differ significantly from those obtained with flat plates because of the relatively large diameter. He cited the experimental work of Carne (53) as proof.

Touloukian's test sections were heated by Chromel A electrical ribbons located in their interiors. To keep a constant surface temperature, it was necessary to vary the heat input along the test sections. Heat losses from the ends were deducted from the input power. Touloukian's data are plotted in Figure 26. Notice that Touloukian's and Saunders' data differ at Rayleigh numbers above  $10^{10}$ , indicating that more vertical flat plate natural convection heat transfer data are needed to better define the region above  $Ra_x = 10^{10}$ .

Waibler's (115) unpublished PhD thesis describes a thorough experimental and analytical effort in turbulent natural convection heat transfer from a 10-foot vertical plate to water. He used a condensing steam heat source. Traps were placed at various heights to collect condensate and thus determine the local heat flux. Width of the vertical passage was varied from 0.5 inches to 2.5 inches. Local Nusselt numbers were only slightly affected by changes in flow channel width. Experimental Rayleigh numbers ranged up to  $10^{14}$ .

# TURBULENT NATURAL CONVECTION HEAT TRANSFER DATA FOR WATER VERTICAL PLATES OR CYLINDERS

FIGURE 26



## LITERATURE SURVEY Continued

Waibler obtained velocities with small probes that measured both static and total pressure. Leads from the probe were connected to two chambers containing floats. The floats were rigidly supported by a cross-arm with a mirror. Differences in water level due to velocity head were determined precisely by sighting through a level on the image of a surveyor's rod seen in the mirror. By placing the rod and level some distance from the mirror, very small differences could be readily detected. He successfully correlated his velocity measurements using  $n$  equal to three near the plate and  $n$  equal to six at the outer edge of the boundary layer. The correlating expression was

$$\frac{U}{U_1} = (y/\delta)^{\frac{1}{n}} (1 - y/\delta)^2 \quad (8)$$

Waibler's experimentally determined Nusselt numbers fell 35 to 40 percent higher than those determined by Saunders and about 180 percent higher than those of Touloukian. See Figure 26.

Fujii (66) obtained experimental data on turbulent natural convection heat transfer to water and ethylene glycol from a 76 mm diameter 360 mm high vertical cylinder. He measured boundary layer temperature distributions in both the laminar and turbulent flow regions. According to Fujii's visual observation at  $Ra_x = 4 \times 10^9$ , the flow changes from laminar to vortex sheet and turbulent flow begins at  $Ra_x = 8.5 \times 10^9$ . Boundary layer temperature distributions were

$$\theta/\theta_w \approx (1 - y/\delta)^3 \quad \text{vortex sheet} \quad (9)$$

$$\theta/\theta_w \approx (1 - y/\delta)^6 \quad \text{fully turbulent} \quad (10)$$

Experimental Nusselt numbers, Fujii concluded, were proportional to  $Ra_x^{1/4}$  above  $Ra_x = 8.5 \times 10^9$ . However, his data range only extended to  $Ra_x \approx 7 \times 10^{10}$ , which is less than one order of magnitude. Because his experimental data were taken over a narrow range of Rayleigh numbers, determination of slope on a  $Nu_x$  versus  $Ra_x$  plot is extremely difficult.

## LITERATURE SURVEY Continued

Tuan (113) measured local turbulent natural convection heat transfer coefficients from a 4-inch outside diameter, essentially isothermal, 26-inch high vertical cylinder to water. The cylinder was mounted in a square tank 18.5 inches on a side and 48 inches high. He correlated his data by the equation

$$Nu_x = 0.0664 (Ra_x)^{0.39} \quad (11)$$

However, when we checked this expression against Tuan's data, it gave values much higher than his experimental points. A modified equation fits the data much better.

$$Nu_x = 0.0264 (Ra_x)^{0.39} \quad (12)$$

Van Dyke (114) used Tuan's apparatus to make additional heat transfer measurements. Employing an accurately positioned fine wire thermocouple, he obtained boundary layer temperature profiles. A typical turbulent profile could be represented by

$$a/a_w = (1 - y/\delta)^3 \quad (13)$$

Some of his profiles could be better represented by a higher power relation. However, none of his profiles gave the universal one-seventh power relation of forced convection.

Several empirical correlations have been proposed for turbulent natural convection heat transfer. King (81) in 1932 correlated the results of several investigators who experimented with air, water, and transformer oil. Water data by Colburn (56) used in the correlation is in some doubt since it was obtained under conditions of combined free and forced convection. Touloukian (112) represented his water and ethylene glycol data with an empirical equation having a stronger Prandtl number dependence. McAdams (89) recommends King's expression. Table VII lists the equations proposed for correlating turbulent natural convection heat transfer.

Eckert and Jackson (61) in 1951 developed a semiempirical expression for predicting turbulent natural convection heat transfer coefficients and boundary layer thicknesses. They represented velocity and temperature profiles by empirical fits of the experimental data of Griffith and Davis (72) and the one-seventh power law.

$$U = 1.87 \left(\frac{y}{\delta}\right)^{1/7} \left(1 - \frac{y}{\delta}\right)^4 \quad (14)$$

$$a = a_w \left[ 1 - \left(\frac{y}{\delta}\right)^{1/7} \right] \quad (15)$$

## LITERATURE SURVEY Continued

They assumed that, close to the wall, forced convection relationships are valid. The wall shear stress and heat flux are related by the Reynolds analogy corrected by a factor  $Pr^{-2/3}$ .

Substitution of Equations III-14 and III-15 into boundary layer momentum and energy relationships yielded the following set of boundary layer equations.

$$\delta/x = 0.565 Gr_x^{-1/10} Pr^{-8/15} \left( 1 + 0.494 Pr^{2/3} \right)^{1/10} \quad (16)$$

$$Re_{max} = \frac{U_{max} x}{\nu} = 0.636 Gr_x^{1/2} \left( 1 + 0.494 Pr^{2/3} \right)^{-1/2} \quad (17)$$

$$Nu_x = 0.0295 (Ra_x)^{2/5} Pr^{1/15} \left( 1 + 0.494 Pr^{2/3} \right)^{-2/5} \quad (18)$$

Equations III-16, III-17, and III-18 define the flow and heat transfer characteristics at a point on a vertical surface for the turbulent regime. The heat transfer coefficient is proportional to  $x^{1/5}$ , so that  $h_{avg} = h_x/1.2$ .

Bayley (49) attempted to treat the boundary layer flow on a vertical plate due to natural convection by a more realistic approach. He divided the boundary layer into two parts - a viscous sublayer and a turbulent outer layer. He assumed that the thermal sublayer thickness was

$$y^+ = \frac{y}{2} \left( \frac{g \tau_w}{\rho} \right)^{1/2} = 15 \quad (19)$$

From this assumption he calculated and related the temperature drops in each layer. Then the temperature relationships were substituted into integral forms of the boundary layer equations. The equations were solved for velocity and boundary layer thickness. Heat transfer coefficients were derived from these quantities.

Like Eckert and Jackson, Bayley assumed identical thicknesses for velocity and temperature boundary layers, employed the Reynolds analogy, and used the Blasius shear expression. He used the experimental velocity and temperature profiles of Griffith and Davis (72). Bayley numerically evaluated his expression for air and found good agreement with the experimental results of Saunders (97). For a Rayleigh number range of  $2 \times 10^9$  to  $10^{15}$ , his equation is

$$Nu_x = 0.183 (Ra_x)^{0.31}$$

## LITERATURE SURVEY Continued

Fujii (66) in 1959 derived several solutions for free convection at high Rayleigh numbers. In one of the solutions he used the laminar boundary layer equations where the wall shear stress was equal to

$$\tau_w = \frac{\mu}{g} \left( \frac{\partial U}{\partial y} \right)_{y=0} \quad (20)$$

Like Bayley, Fujii divided the boundary layer into two parts - a viscous sublayer and a turbulent outer layer. His solution indicated that the Nusselt number was proportional to  $Ra^{1/4}$ , instead of the usual one-third power relationship in turbulent flow.

Larson (84) published a PhD thesis on turbulent free convection in near critical water in late 1964. He studied heat transfer from a vertical flat plate, both analytically and experimentally. His analytical solution involved an integral technique similar to Eckert and Jackson (61). However, different velocity and temperature profiles were used. For velocity distribution in the boundary layer, Larson employed Waibler's (115) expression

$$\frac{U}{U_1} = (y/\delta)^{1/3} (1 - y/\delta)^2 \quad (21)$$

From the conclusions of Van Dyke (114) and Fujii (66), the boundary layer temperature distribution in free convection is

$$\frac{a}{a_w} = (1 - y/\delta)^3 \quad (22)$$

Larson developed two solutions, one for a variable property fluid and one for a constant property fluid. The latter solution, which fits the case considered in this work, is

$$Nu_x = 0.121 \left[ \frac{Gr_x}{1 + 0.976 Pr^{2/3}} \right]^{1/3} Pr^{5/9} \quad (23)$$

It gives values generally low as compared to the experimentally determined Saunders' equation

$$Nu_x = 0.17 (Ra_x)^{1/3} \quad (24)$$

## LITERATURE SURVEY Continued

Larson reasoned that the difference was caused by the choice of a value for  $C_n$ , the Blasius law constant used in the derivation of Equation III-23. He had extrapolated existing experimental data to obtain a value of 5.1 ( $n = 3$ ). By selecting  $C_n = 3.5$ , he obtained a result which compared well with the experimental data of Saunders (97).

$$Nu_x = 0.177 \left[ \frac{Gr_x}{1 + 0.978 Pr^{2/3}} \right]^{1/3} Pr^{5/9} \quad (25)$$

Larson's theoretical treatment appears to offer several improvements over the Eckert-Jackson approach. First, Nusselt number is proportional to Grashof number to the one-third power, while Eckert-Jackson predict a power of two-fifths. Existing experimental data are predicted better by a one-third power relationship. Second, Larson's equation, which shows that length  $x$  does not affect the heat transfer coefficient in the turbulent region, agrees with experimental results. Eckert and Jackson's method indicates that  $h$  is proportional to  $x^{1/5}$ . Table VII lists the turbulent natural convection equations proposed in the literature.

Transition from laminar to turbulent free convection flow on flat plates was studied by Eckert and Soehngen (62) in 1951. In air the change occurs at a critical Grashof number around  $Gr_x = 10^9$ . This corresponds to a critical Reynolds number based on boundary layer thickness  $Re_{x_c} = \frac{U_{max}}{\nu} = 550$ , thus indicating that in free convection transition takes place at lower Reynolds numbers than in forced convection. Saunders (97) observed transition from laminar to turbulent boundary layer flow at  $Gr_x Pr = 4 \times 10^9$ . Touloukian (112) stated that transition occurred at Rayleigh number of approximately  $8 \times 10^9$  in his experiments.



TABLE VII

## TURBULENT NATURAL CONVECTION EQUATIONS

1 Bayley (49) air

$$Nu_x = 0.10 Ra_x^{1/3}$$

2 Eckert-Jackson (61)

$$Nu_x = 0.0295 \left[ \frac{Ra_x}{1 + 0.494 Pr^{2/3}} \right]^{2/5} Pr^{1/15}$$

$$Nu_{avg} = \frac{Nu_x}{1.2}$$

3 King (81)

$$Nu_x = 0.13 Ra_x^{1/3}$$

4 Larson (84)

$$Nu = 0.178 \left[ \frac{Ra_x}{1 + 0.976 Pr^{2/3}} \right]^{1/3} Pr^{2/9}$$

for  $Cn = 3.5$

5 Saunders (97)

$$Nu_x = 0.17 Ra_x^{1/3}$$

6 Touloukian (112)

$$Nu_x = 0.0674 (Ra_x Pr^{1.29})^{1/3}$$

7 Tuan (113) (as corrected in Chapter III)

$$Nu_x = 0.0264 Ra_x^{0.39}$$

8 Waibler (115)

$$Nu_x = 0.795 Ra_x^{0.285}$$

## LITERATURE SURVEY Continued

Carne (53) conducted an experimental investigation on the influence of diameter of vertical cylinders on free convection heat transfer in air. He found almost no influence of diameter on heat transfer coefficient when the diameter was greater than 2 inches. The difference in heat transfer coefficient between a 1-inch and a 3-inch vertical cylinder was in the order of 0.5 percent. In a study of forced flow outside cylinders, Jakob and Dow (78) concluded that in turbulent flow the Nusselt number of a cylinder is higher than that of a flat plate by a percentage amount of  $30 \delta/r$ , where  $r$  is the cylinder radius. The difference in Nusselt number between a 1-inch diameter cylinder and a flat plate would be in the order of 20 percent by this approach.

Most investigators have ignored treatment of end effects in free convection. Touloukian (112) discussed the effect of unheated entering and exit lengths. Rutkowski (95) studied edge effects in air using a Mach-Zehnder interferometer. He found that the edge effect was almost independent of plate temperature, geometry, or inclination. Rutkowski presented a graphical correction curve.

**PARALLEL PLATES AND VERTICAL FINNED SURFACES** If end effects are neglected in natural convection flow and heat transfer from vertical finned surfaces, the system reduces to flow and heat transfer between parallel plates. The approximation is valid when fin height is large compared to fin spacing.

E Schmidt (101) in 1928 experimented with the spacing of two 6-inch square isothermal vertical parallel plates in air. He found that as the plates were brought together, the convection coefficient was not affected until the separation reached about 0.5 inch. As the spacing was reduced further, the convection coefficient rapidly fell off, until at a separation of 0.125 inch the heat loss was almost zero. King (80) in 1930 obtained similar results with somewhat larger plates.

In a series of articles, Elenbaas (63) theoretically attacked the problem of heat dissipation at parallel plates for laminar flow. For parallel plates of height  $b$  and spacing  $D$ , he derived the following heat dissipation formula for the laminar region.

$$Nu_D = \frac{1}{24} \frac{D}{b} (Gr_D Pr) \left[ 1 - e^{-24 \left( \frac{0.5 b}{D Gr_D Pr} \right)^{3/4}} \right] \quad (26)$$

## LITERATURE SURVEY Continued

All physical properties in the above equation are to be evaluated at the wall temperature rather than the film temperature. At large values of  $b$ , the expression reduces to the usual laminar flow vertical flat-plate equation.

Wordsworth (53) in 1953 published expressions for laminar free convection between heat producing vertical plates in a liquid. He developed an analytic expression for heat transfer coefficient for an array of parallel plates.

Siegel and Norris (105) published results of tests of free convection in the space between two heated vertical plates. They employed a constant heat flux, and the Grashof number based on plate height was  $1.8 \times 10^{10}$ . Hence, a good portion of the flow along the surface was turbulent. The top of the rectangular space between the plates was left open. During most of the tests the bottom and sides were closed. However, a few experiments were performed with open sides and bottom.

Siegel and Norris did not find a large effect of plate spacing on natural convection heat transfer. This was presumably because they only experimented at spacings above two percent of the plate height. Closing the sides with insulation, while leaving the bottom open, increased heat transfer significantly in the laminar region but insignificantly in the turbulent region. Clearance of the bottom edge of the plates above the floor did not significantly affect heat transfer, down to a clearance of one percent of the duct height.

Bodoia and Osterle (52) in 1962 presented results of a study of flow development between heated vertical plates. Confining their study to the laminar region only, they concluded that fully-developed flow is practically impossible for all but very viscous fluids. The height of channel with a 0.1 foot spacing necessary to produce a flow within 10 percent of full development is of the order of  $10^5$  feet for water. Their computations agreed well with the work of Elenbaas.

In 1963, Starner and McManus (110) reported results of an experimental investigation of free convection heat transfer from rectangular fin arrays. Four arrays were positioned with the plate vertical, 45 degrees, and horizontal, while dissipating heat to room air. It was discovered that the fins tested gave coefficients 10 to 30 percent below those of similarly spaced parallel plates. In all but the shortest fin array, the coefficients were maximum when the plate was vertical. It was found that an optimum combination of fin height and spacing existed for heat dissipation. Vertical fin array heat transmission was not strongly influenced by end effects or inflow.

## LITERATURE SURVEY Continued

Heat transfer in liquids confined by two parallel plates was investigated by Dropkin and Somerscales (58) in 1964. The plates were inclined at angles of 0, 30, 45, 60, and 90 degrees to the horizontal, and were confined on the sides and bottom. Water, silicone oil, and mercury were employed as test fluids. The experiments covered a range of Rayleigh numbers between  $5 \times 10^4$  and  $7 \times 10^8$  and Prandtl numbers between 0.02 and 11,560. Results were correlated by the usual dimensional groups with a multiplying constant that varied with inclination. Interestingly, the ratio of height to distance between plates did not affect the Nusselt number even though it varied from 4.41 to 16.56 in the tests.

At the 1964 Winter Annual ASME meeting, Welling and Wooldridge (117) presented results of a series of experiments on free convection heat transfer to air from rectangular vertical fins. All data were in the laminar region. They employed four levels of fin spacing, three fin heights, and three fin surface temperatures. The electrically heated aluminum base surface was 8.0 inches high and 2.61 inches wide. Thermocouples were placed at four elevations on the back of the base surface. The fins were thick enough that their surface temperature was essentially the same as the base surface. Experimental coefficients were corrected for radiation heat transfer and other losses to yield the natural convection coefficients.

Experimental results showed that a vertical rectangular fin section with the same vertical length and surface temperature as a vertical flat plate will not have as large a free-convection coefficient as a flat plate. The finned sections had greater coefficients than either parallel plates or a square duct. Welling and Wooldridge found that there was an optimum fin height for each fin spacing.

In 1965, Fairbanks and Mark (64) presented an optimization procedure for finning in free convection. They considered a horizontal tube with vertical fins and essentially extended isothermal solutions of Elenbaas (63) to the more practical case of nonuniform fin temperature. Optimum solutions were obtained for fin spacing, fin thickness, and fin base diameter by an iterative solution.

Hsu, Hsieh, and Vatsaraj (76) in 1965 described a new type of surface for free convection cooling. The surface consisted of a base covered with rows of round pins to which circular fins were attached. Installing fins on the pins definitely increased the heat transfer rate, and the weight increase over plain pins was insignificant. The authors also presented an analytical solution of heat transfer from a finned pin.

## LITERATURE SURVEY Continued

**NEEDED WORK** From the literature survey, we concluded that laminar natural convection on vertical flat plates had been well enough investigated, making additional investigation unnecessary. This is not true, however, for turbulent natural convection heat transfer in water from vertical plates. Because of the spread of existing data in the turbulent region and the lack of data above  $Ra = 10^{12}$ , additional experimental data are necessary. A theoretical model was also needed to predict boundary layer thicknesses for turbulent natural convection flow.

The literature survey yielded no experimental data for finned surfaces at the Rayleigh numbers one would expect in seawater. The laminar region has been well studied theoretically, but no theoretical prediction of the effects of fin height or spacing on heat dissipation was uncovered for the turbulent region.

The effect of cylinder diameter on heat transfer has not been studied experimentally in turbulent natural convection flow. Jakob's (78) expression needs to be experimentally verified.

No data appeared to have been published on the effects of multiple vertical finned surfaces, either flat or cylindrical. This topic needed experimental study.

## VERTICAL FLAT PLATE AND CYLINDER MATHEMATICAL MODELS

To deal mathematically with natural convection heat transfer from multiple surfaces, one must know the details of the boundary layers formed on the solid surfaces. In laminar flow, this problem has been approached in two ways. First, the Navier-Stokes equations may be simplified to fit the flow situation, and then integrated numerically. This was the method employed by E Schmidt (103), Ostrach (90), and Sparrow (106, 107, 108). It has the advantage that the solutions are nearly exact mathematically. The chief disadvantages are the cumbersome equations and the necessity of employing digital computation.

A second laminar flow approach is to approximate experimentally determined velocity and temperature profiles for use in the integral boundary layer equations. This semiempirical technique was employed by Eckert (60). Results are very close to the more exact approach of Ostrach (90). Reference (60) gives a comparison. The semiempirical approach yields equations that can be handled without use of a digital computer.

# VERTICAL FLAT PLATE AND CYLINDER MATHEMATICAL MODELS Continued

In the turbulent region, an exact solution is presently impossible. Therefore, one must resort to the semiempirical approach. Besides knowing velocity and temperature profiles in the boundary layer, one must determine the relationship between wall friction and heat flux.

**LAMINAR BOUNDARY LAYER** Eckert's (60) approach was employed to mathematically describe the laminar natural convection boundary layer on a vertical plate. A complete derivation is given in Appendix D and is summarized here.

The governing motion and energy equations are simplified by the following assumptions.

- 1 Steady state
- 2 Constant density except in the buoyancy term
- 3 Two dimensional flow, x and y direction
- 4 Viscous dissipation is neglected
- 5 Acceleration due to gravity acts in the minus x direction
- 6 Both thermal and velocity boundary layers end at  $\delta$
- 7 Constant wall temperature

Momentum and energy equations reduce to

$$d/dx \int_0^{\delta} U^2 dy = g\beta \int_0^{\delta} \theta dy - \nu \left( \frac{dU}{dy} \right)_w \quad (27)$$

$$d/dx \int_0^{\delta} U \theta dy = -\alpha \left( \frac{d\theta}{dy} \right)_w \quad (28)$$

Velocity and temperature profiles are represented by the following expressions.

$$U = U_1 \frac{Y}{\delta} \left( 1 - \frac{Y}{\delta} \right)^2 \quad (29)$$

$$\theta = \theta_w \left( 1 - \frac{Y}{\delta} \right)^2 \quad (30)$$

## VERTICAL FLAT PLATE AND CYLINDER MATHEMATICAL MODELS Continued

Substituting these equations into Equations III-27 and III-28 and considering  $U_1$  and  $\delta$  to be exponential functions of vertical distance, yields the following boundary layer equations.

$$\frac{\delta}{x} = 3.93 (Ra_x)^{-1/4} Pr^{-1/4} (0.952 + Pr)^{1/4} \quad (31)$$

$$Re_{max} = \frac{U_{max} x}{\nu} = 0.766 (0.952 + Pr)^{-1/2} Gr_x^{1/2} \quad (32)$$

$$Nu_x = 0.508 Pr^{1/4} (0.952 + Pr)^{-1/4} (Ra_x)^{1/4} \quad (33)$$

Equations III-31, III-32, and III-33 define the flow and heat transfer characteristics at a point on a vertical surface. Since  $h$  varies with  $x$  as  $x^{-1/4}$ , the average coefficient of a vertical plate of height  $x$  is  $4/3$  the local value at the point  $x$ .

Using a similar approach as that of Eckert, we have solved the laminar boundary layer equations for the constant heat flux case. For this condition, the heat transfer equation is

$$Nu_x = 0.547 Pr^{1/2} (0.8 + Pr)^{-1/4} Gr_x^{1/4} \quad (34)$$

Notice that there is little difference between Equations III-33 and III-34. At a Prandtl number of unity the difference in  $Nu_x$  is 7.2 percent, while at a Prandtl number of ten the percent difference is 7.0. Temperature difference at the wall varies as  $x^{1/5}$  at constant heat flux.

For flow between parallel plates, with no end effects, plate spacing will not influence the heat transfer coefficient if it is greater than twice the boundary layer thickness. If spacing is reduced below this limit, heat transfer is adversely affected as shown by experiments reported in the previous section. Thus, the boundary layer equations may be used directly to predict fin spacing, subject to the condition that end effects are negligible.

# VERTICAL FLAT PLATE AND CYLINDER MATHEMATICAL MODELS Continued

For the example presented on Page III-2, Equations III-31, III-32, and III-33 yield the following results.

$x(\text{ft})$	$\delta(\text{in})$	$Re_{x_{\max}}$	$U_{\max}(\text{ft/sec})$	$h_x(\text{Btu/hr-ft}^2\text{-F})$
0.01	$2.77 \times 10^{-3}$	$2.70 \times 10^1$	0.023	252
0.1	$4.93 \times 10^{-3}$	$8.65 \times 10^2$	0.076	142
1.0	$8.78 \times 10^{-3}$	$2.70 \times 10^4$	0.236	80

Transition to turbulent flow should occur between 0.28 to 0.60 feet above the leading edge, according to the observations of Saunders (97) and Touloukian (112).

The example indicates that boundary layer thicknesses are so small in laminar flow that fins may be very closely spaced without a reduction in heat transfer coefficient.

**TURBULENT BOUNDARY LAYER** We employed an approach very similar to Larson (84) and Eckert-Jackson (61) to mathematically describe the turbulent natural convection boundary layer on a flat plate. Appendix D contains a complete derivation which is summarized here.

The same assumptions are made to simplify the momentum and energy equations as in laminar flow. These equations reduce to

$$\frac{d}{dx} \left( \delta \int_0^1 U d\eta \right) = g\beta \int_0^1 \theta d\eta = g \frac{\tau_w}{\rho} \quad (35)$$

$$\left( q/A \right)_w = \rho C_p \frac{d}{dx} \left( \delta \int_0^1 U \theta d\eta \right) \quad (36)$$

Velocity and temperature profiles are represented by empirical fits of the data of Waibler (115), Fujii (66), and Van Dyke (114).

$$\theta = \theta_w (1 - \eta)^3 \quad (37)$$

$$U = U_1 \eta^{1/3} (1 - \eta)^2 \quad (38)$$



## VERTICAL FLAT PLATE AND CYLINDER MATHEMATICAL MODELS Continued

Shear stress on a flat surface is given by Schlichting (100) as

$$\tau_w = Cn^{-3/2} \frac{U_1^2 \rho}{g} \left( \frac{v}{U_1 y} \right)^{1/2} \quad (39)$$

Here  $Cn$  is the Blasius law constant which is given by the general power law velocity distribution equation for turbulent flow.

$$\frac{U}{v^*} = Cn \left( \frac{v^* y}{v} \right)^{1/n} \quad (40)$$

$$\text{where } v^* = \left( g/\rho \tau_w \right)^{1/2}$$

The value of the constant  $Cn$  is not known for turbulent natural convection flows. Therefore, we have included it as an additional variable to be evaluated from experimental heat transfer data.

Wall heat flux and shear stress are related by the Reynolds analogy corrected for variable Prandtl number by a factor  $Pr^{-2/3}$ .

Substituting Equations III-37 and III-38 into Equations III-35 and III-36, and considering  $U_1$  and  $\delta$  to be exponential functions of vertical distance yields the following boundary layer equations

$$Nu_x = 0.624 Cn^{-1} Pr^{2/9} \left[ 1 + 0.978 Pr^{2/3} \right]^{-1/3} Ra_x^{1/3} \quad (41)$$

$$\delta_x = 4.5 Cn^{-1} \left[ 1 + 0.978 Pr^{2/3} \right]^{1/6} Pr^{-5/18} Ra_x^{-1/6} \quad (42)$$

$$Re_{max} = \frac{U_{max} x}{v} = 0.676 Ra_x^{1/2} Pr^{-1/2} \left[ 1 + 0.978 Pr^{2/3} \right]^{-1/2} \quad (43)$$

We have solved the turbulent boundary layer equations for the constant heat flux case using a similar technique. The final heat transfer equation is

$$Nu_x = 0.626 Cn^{-1} (Ra_x)^{1/3} Pr^{2/9} \left( 1 + 0.962 Pr^{2/3} \right)^{1/3} \quad (44)$$

## VERTICAL FLAT PLATE AND CYLINDER MATHEMATICAL MODELS Continued

Note that Equations III-41 and III-44 are almost identical. This indicates that experimental data may be acquired under either constant temperature or constant heat flux conditions without introducing significant error. Wall temperature difference  $\theta_w$  varies as  $x^{-1/7}$  in the constant heat flux case.

Employing the same reasoning we used in the laminar region,  $2\delta$  is the minimum fin spacing under conditions of negligible end effects. For the example presented on Page III-2, Equations III-41, III-42, and III-43 yield the following results with  $C_n = 3.22$ .

<u>x(ft)</u>	<u><math>\delta</math>(in)</u>	<u>Re<sub>x</sub> max</u>	<u>U<sub>max</sub> (ft/sec)</u>	<u>h<sub>x</sub> (Btu/hr-ft<sup>2</sup>-F)</u>
1	0.157	$6.96 \times 10^4$	0.61	373
2	0.222	$1.98 \times 10^5$	0.87	373
5	0.350	$7.80 \times 10^5$	1.37	373
10	0.496	$2.19 \times 10^6$	1.92	373

This example indicates that boundary layer thickness in turbulent flow can limit the fin spacing. To aid the designer in boundary layer thickness prediction, Figure 27 was constructed, based on Equation III-42.

## OPTIMUM FIN GEOMETRY IN FREE CONVECTION

Optimization of fin geometry has received considerable attention in engineering literature. As in most engineering problems, economics is usually the optimizing criterion. Thus, there is no optimum fin mathematical expression that will fit all circumstances.

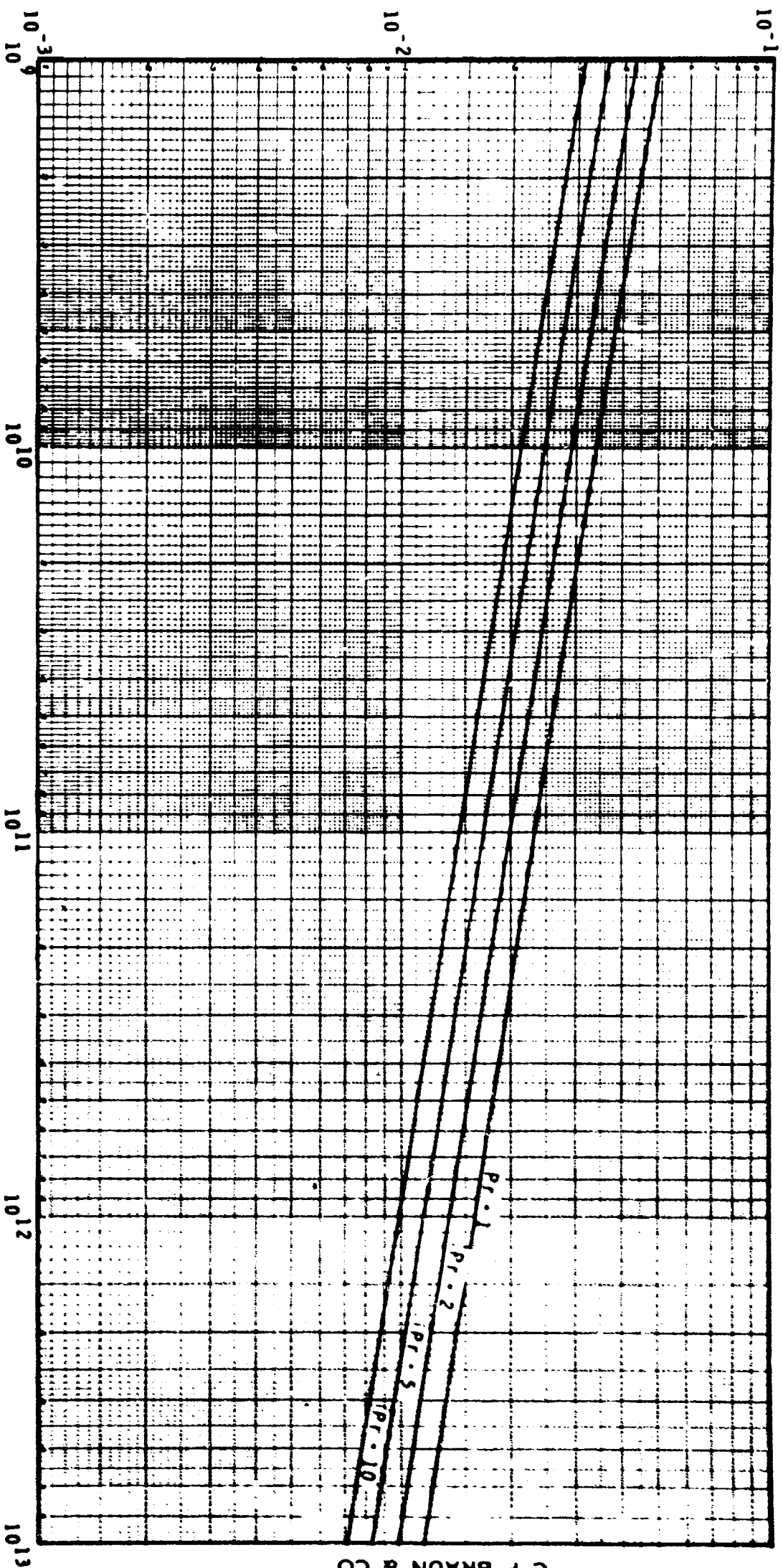
Since the true optimum fin geometry is usually determined by economics, this investigation will not yield it. Our purpose is to provide for the designer of future undersea heat transfer surfaces enough heat transfer information to determine the optimum point for each design.

Sometimes low cost is associated with the smallest amount of fin material required for a given heat dissipation. This would always be true if material costs greatly outweighed fabrication costs. For a given heat duty, minimum fin weight is associated with a concave parabolic fin profile. This was proved in an intuitive manner by E Schmidt (102) in 1926 and rigorously by Duffin (59) in 1959. Minimizing fin weight is of extreme importance in aircraft and space heat rejection applications.

JEC

# BOUNDARY LAYER THICKNESS IN TURBULENT NATURAL CONVECTION

figure 27



C F BRAUN & CO

$$Ra_x = \frac{x^3 g \beta \Delta T}{\nu^2} \cdot \frac{C_p \mu}{k}$$

## OPTIMUM FIN GEOMETRY IN FREE CONVECTION Continued

A recent investigation by Appl and Hung (47) indicated that optimum fin geometry for an individual fin is not necessarily optimum for a finned surface. Fin spacing, therefore, introduces additional complications. We will treat the entire finned surface in this optimization study.

Optimizing fin geometry on an undersea natural convection heat rejection surface involves other considerations besides fin weight. First, one must consider the power cycle and the base surface geometry. Efficiency of all thermal cycles is improved if unconverted heat is rejected at the lowest temperature possible. Usually the source temperature has an upper limit because of limitations caused by materials or working fluid thermodynamic properties. The sink temperature of an undersea device is fixed. Heat transfer base surface area would probably be expensive, especially with thermoelectric devices. Thus, a high gross heat transfer coefficient would be highly desirable on an undersea heat rejection surface. Gross heat transfer coefficient is defined as the base surface heat flux divided by difference between base surface and ambient temperatures.

Second, one must consider the effects of biological fouling and corrosion upon the surface heat transfer coefficient. These effects were treated in Chapter II. Their design implications will be presented in Chapter VI.

In this report we will optimize fin surface geometry with respect to gross heat transfer coefficient. These results will represent an upper limit for heat transfer rate per unit area from a base surface under a given temperature difference.

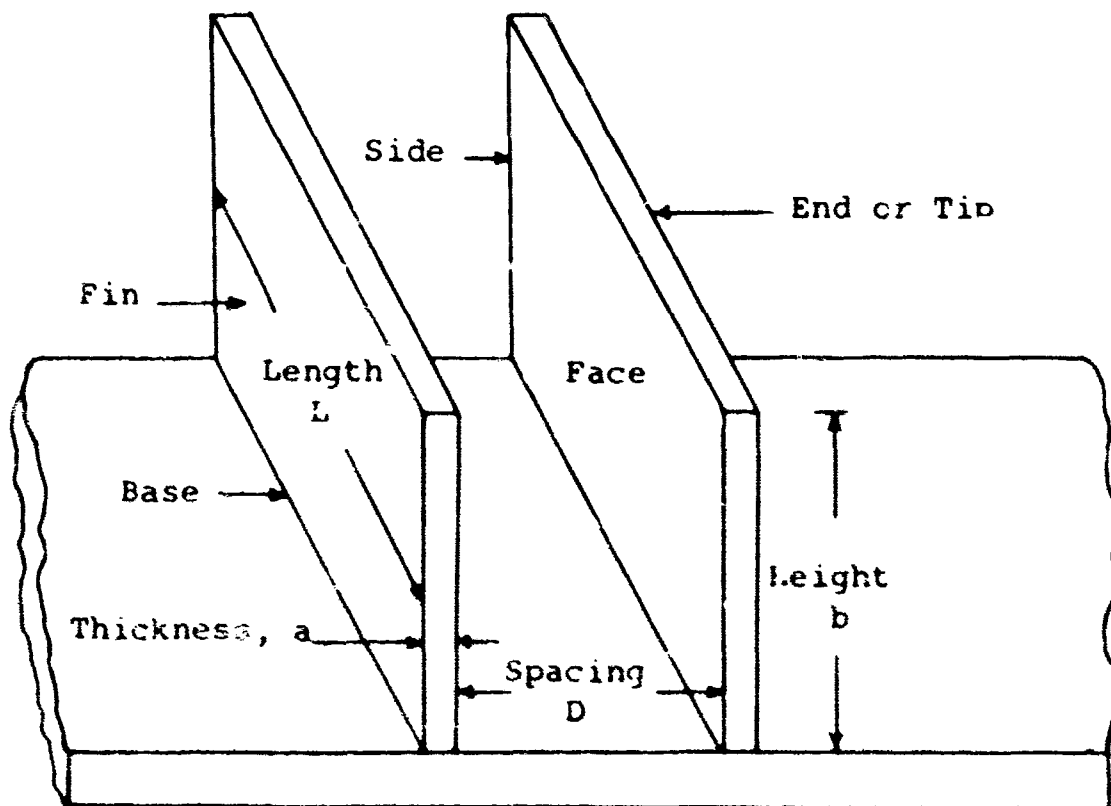
**REVIEW OF FIN THEORY** Many textbooks and journal articles present elementary fin theory in detail. Rather than repeat the same material, we refer the reader to the works of Jakob (77), Gardner (67), Kraus (83), and Chapman (54). Analysis is also limited here to rectangular fins, although much of the reasoning could also be applied to triangular, trapezoidal, and parabolic fins as well.

## OPTIMUM FIN GEOMETRY IN FREE CONVECTION Continued

Mathematical analyses of fins and finned surfaces are usually based upon the following assumptions.

- 1 Steady-state heat flow
- 2 Homogeneous fin material and constant fin thermal conductivity
- 3 Constant heat transfer coefficient over the face surface of the fin
- 4 Uniform temperature in the surrounding fluid
- 5 No temperature gradients occur along the length and across the thickness of the fin
- 6 Temperature at the fin base is uniform, and there is no contact resistance at the fin base
- 7 There are no heat sources within the fin itself
- 8 Heat transferred from the fin end and sides is negligible

The drawing below pictures a heat transfer surface composed of rectangular fins and base metal. Important variables include fin height, fin spacing, fin thickness, surface heat transfer coefficient, and metal thermal conductivity.



## OPTIMUM FIN GEOMETRY IN FREE CONVECTION Continued

All of these assumptions show some idealization of the real world, but a few of them are particularly objectionable for free convection in liquids. Assumption 3 is not true in turbulent free convection where  $h$  is proportional to  $(\Delta T)^{1/3}$ . Assumption 4 is valid for short, widely spaced fins but untrue for high, narrowly spaced ones. Assumption 5 requires that the height of the fin be great compared to the thickness and that the fin be long enough that the effect of heat transferred from the sides may be neglected. Usually, an average temperature based upon an average inside coefficient corrects for the inadequacy of Assumption 7. Assumption 8 is valid if the fin is long, thin, and high. A high surface coefficient tends to validate Assumption 8.

Harper and Brown (73) suggested a very practical way to eliminate the most objectionable part of Assumption 8 (an insulated fin tip). They recommended using a corrected fin height  $b_c = b + \frac{a}{2}$  in calculations. In this way, the fin problem is simplified greatly because heat which actually leaves the fin tip is assumed to leave through an added height. No heat is assumed to leave at the tip where  $y = b_c$ .

Cumo, Lopez, and Pinchera (57) eliminated the last part of Assumption 5, and Assumptions 6 through 8, and developed a Fortran computer program for solving the resulting two-dimensional differential equations. Input data to the program are as follows.

- 1 Finning profile
- 2 Maximum network spacing (optional) for the numerical solution
- 3 Heat transfer coefficient
- 4 Fin material thermal conductivity
- 5 Internal heat generation rate
- 6 Heat flux at the inner face of the base tube
- 7 A rough estimate of the mean fin temperature
- 8 An over-relaxation factor

The program, when run on the IBM 7094 computer, calculates the two dimensional temperature distribution in fin and base surface and the fin efficiency, fin effectiveness, and finning ratio.

The authors used the program to test the reliability of the Gardner and the Harper and Brown methods of determining temperature distribution and performance factors. Results showed that Gardner's method overestimated performance values for high, thin fins and underestimated for short, thick fins. Harper and Brown's curves were always one percent to five percent higher than those of the authors, and in general, roughly parallel. Therefore Cumo, Lopez, and Pinchera confirmed the simplified approach of Harper and Brown. The computer approach could be used if the precision in physical properties and surface coefficients could justify it.

## OPTIMUM FIN GEOMETRY IN FREE CONVECTION Continued

Simplified fin equations in the literature are based on a uniform surface coefficient. With turbulent natural convection heat transfer, this assumption is certainly untrue and is not on the conservative side either. Rather than employ the more complicated computer approach of Cumo, Lopez, and Pinchera, we chose an approach amenable to hand calculations.

According to simple fin theory (83), the basic differential equation for heat transfer in a fin is

$$\frac{d^2 \theta}{dy^2} - \frac{2h}{k_m a} \theta = 0 \quad (45)$$

All assumptions are retained here except Number 3. In turbulent natural convection heat transfer, the heat transfer coefficient is proportional to the cube root of the difference between surface and ambient temperature. Instead of using a constant coefficient, let

$$h = h_o (\theta/\theta_o)^{1/3}, \text{ and } v = \theta/\theta_o$$

Then the differential equation becomes

$$\frac{d^2 v}{dy^2} - \frac{2h_o}{k_m a} v^{4/3} = 0 \quad (46)$$

$$\text{Let } m^2 = \frac{2h_o}{k_m a}$$

Substituting this into the differential equations yields

$$\frac{d^2 v}{dy^2} - m^2 v^{4/3} = 0 \quad (47)$$

Boundary conditions are

- 1 Fin root  $y = 0$  ,  $v = 1$
- 2 Fin tip  $y = b$  ,  $\frac{dv}{dy} = 0$  (insulated)

We were not able to obtain an analytical solution to the equations. However, a partial solution was developed which indicated the limits of error caused by Assumption 3. This solution is outlined in the following paragraphs.

## OPTIMUM FIN GEOMETRY IN FREE CONVECTION Continued

Using first order differential equation solution methods, the first integration yields

$$\left(\frac{dv}{dy}\right)^2 = 6/7 m^2 v^{7/3} + C \quad (48)$$

Substituting Boundary Condition 2 into Equation III-48 gives the following expression for C.

$$C = -6/7 m^2 v_b^{7/3}$$

and the first order differential equation becomes

$$\frac{dv}{dy} = 0.924 m \left( v^{7/3} - v_b^{7/3} \right)^{1/2} \quad (49)$$

Rate of heat flow through the fin base is given by the expression

$$q_o = -k_m A \theta_o \left( \frac{dv}{dy} \right)_{y=0} \quad (50)$$

and  $A = aL$ . Substituting Equation III-49 into Equation III-50 yields

$$q_o = 0.924 m k_m a L \theta_o \left( 1 - v_b^{7/3} \right)^{1/2} \quad (51)$$

If we had not taken into account nonuniformity of heat transfer coefficient over the surface, the heat flow rate expression would have been

$$q_o = m k_m a L \theta_o \left( 1 - v_b^2 \right)^{1/2} \quad (52)$$



## OPTIMUM FIN GEOMETRY IN FREE CONVECTION Continued

Taking the special case of infinite height fins where  $v_b = 0$ , we find that 7.6 percent less heat is transferred due to nonuniform surface coefficient.

$$\frac{q_o \text{ nonuniform } h}{q_o \text{ uniform } h} = 0.924 \text{ at } v_b = 0$$

As fins become shorter in height, this ratio increases and approaches unity as  $v_b \rightarrow 1$ . Therefore, 7.6 percent is the maximum penalty caused by nonuniform surface coefficient under the given assumptions.

Simple fin theory with uniform surface coefficient shows that  $v_b$  is given by

$$v_b = \frac{1}{\cosh (mb)}$$

Thus the heat flow rate expression for uniform surface coefficient is

$$q_o = mk_m a L \theta_o \tanh (mb)$$

To be on the conservative side, we will penalize the heat flow rate as if the fins were infinitely tall. For nonuniform surface coefficient, heat flow rate is given then by

$$q_o = 0.924 mk_m a L \theta_o \tanh (mb) \quad (53)$$

## OPTIMUM FIN GEOMETRY IN FREE CONVECTION Continued

**OPTIMIZATION OF A FINNED SURFACE** A surface composed of rectangular fins and flat base surface will be optimized on the basis of achieving the maximum heat dissipation rate per unit temperature difference. This represents one limiting case. Its results can then be modified as desired to achieve the true, or economic, optimum. The following assumptions are made in this development.

- 1 Steady-state heat flow
- 2 Homogeneous material and constant metal thermal conductivity
- 3 Effects of nonuniform surface coefficient can be taken into account by reducing the fin base heat transfer rate by 7.6 percent.
- 4 Uniform temperature in the surrounding fluid
- 5 One-dimensional fin heat flow
- 6 Uniform fin base temperature and no fin contact resistance
- 7 No heat sources within the fin
- 8 Heat transfer from the fin sides is negligible and heat transfer from the fin tip may be approximated by the Harper-Brown modification.
- 9 Fins are spaced at a distance  $D$ , determined by hydrodynamics of natural convection flow on the base and fin surfaces.

Rate of heat flow through the fin base per unit base surface width is

$$q_o = 0.924 n m k_m a L \theta_o \tanh (m b_c)$$

$$= 0.924 n (2 h_o k_m a)^{1/2} L \theta_o \tanh \left[ \left( \frac{2 h_o b_c^2}{k_m a} \right)^{1/2} \right] \quad (54)$$

Rate of heat flow through the unfinned base surface per unit base surface width is

$$q_B = n h_o D L \theta_o$$

Total heat transferred per unit time per unit base surface width is the sum of  $q_o$  and  $q_B$

$$q = n L \theta_o \left\{ 0.924 (2 h_o k_m a)^{1/2} \tanh \left[ \left( \frac{2 h_o b_c^2}{k_m a} \right)^{1/2} \right] + h_o D \right\} \quad (55)$$

and heat transfer area per unit base surface width is

$$A = n L (D + a) \quad (56)$$

## OPTIMUM FIN GEOMETRY IN FREE CONVECTION Continued

Gross heat transfer coefficient is defined as  $q/\theta_o A$ . It is the amount of heat that can be transferred per unit base surface area per unit temperature difference between base surface and ambient fluid. The equation for gross heat transfer coefficient is

$$h_G = q/\theta_o A = \frac{0.924 (2h_o k_m a)^{1/2} \tanh \left[ \left( \frac{2h_o b_c^2}{k_m a} \right)^{1/2} \right] + h_o D}{D + a} \quad (57)$$

Gross heat transfer coefficient is a function of five variables,  $h_o$ ,  $k_m$ ,  $a$ ,  $b_c$ , and  $D$ . It increases monotonically with an increase in either  $h_o$ ,  $k_m$ , or  $b_c$ . However, with respect to fin thickness,  $a$ , and fin spacing,  $D$ , the gross coefficient reaches maximum values. The maximum  $h_G$  with respect to  $D$  occurs at such a low value of fin spacing that it is not of practical interest when dealing with water. However, the maximum  $h_G$  with respect to  $a$  is of great practical importance.

To maximize the gross coefficient with respect to fin thickness, we

set  $\frac{\partial h_G}{\partial a} = 0$ , checked the sign of the second partial for a maximum, and found the following implicit expression in  $a$ .

$$f(a) = B \left( \frac{D}{a} + 1 \right) \operatorname{sech}^2 \left( \frac{B}{a^{1/2}} \right) + \left( \frac{D-a}{a^{1/2}} \right) \tanh \left( \frac{B}{a^{1/2}} \right) - A = 0 \quad (58)$$

$$\text{where } A = \left( \frac{2h_o}{k_m} \right)^{1/2} \frac{D}{0.924}$$

$$B = \left( \frac{2h_o}{k_m} \right)^{1/2} b_c$$

## OPTIMUM FIN GEOMETRY IN FREE CONVECTION Continued

Equation III-58 was solved for  $a$  by an iterative interpolation method on a Burroughs B5500 Computer. An initial approximation of the root was given by a particular solution of the equation for infinite height fins.

$$a \text{ (at } b = \infty) = 1/4 \left[ -A + (A^2 + 4D)^{1/2} \right]^2 \quad (59)$$

The desired root for Equation III-58 always fell between the value for infinite height fins and zero.

Results of the computer solutions are presented in Figures 28 through

31. In each graph for a particular value of  $\left(\frac{2h_o}{k_m}\right)^{1/2}$ , optimum fin thickness is plotted versus fin spacing, with corrected fin height as a parameter. Notice that optimum fin thickness always increases with increasing fin height and increasing fin spacing. Figure 32

demonstrates the behavior of optimum fin thickness with  $\left(\frac{2h_o}{k_m}\right)^{1/2}$  at a specified fin spacing. Initially, optimum fin thickness increases with increasing  $\left(\frac{2h_o}{k_m}\right)^{1/2}$ . Then a maximum is reached. Afterwards, optimum fin thickness decreases with increasing  $\left(\frac{2h_o}{k_m}\right)^{1/2}$ .

Figures 33 through 36 indicate the effect of fin spacing, fin height, and  $\left(\frac{2h_o}{k_m}\right)^{1/2}$  upon  $\frac{h_G}{k_m}$ . Fins are at the optimum thickness in all cases.

Gross heat transfer coefficient increases with increasing fin height, metal thermal conductivity, and  $\left(\frac{2h_o}{k_m}\right)^{1/2}$ . It decreases as the fin spacing increases.

Figures 28 through 36 form the starting point for a design method. They enable one to calculate maximum gross heat transfer coefficient and optimum fin thickness for a surface - given values of base surface heat transfer coefficient, fin spacing, and metal thermal conductivity. Base surface coefficient is primarily a function of surface and ambient temperature and heat flux in the turbulent region of natural convection. Fin spacing is primarily a function of boundary layer thickness, which in turn can be related to the same variables.

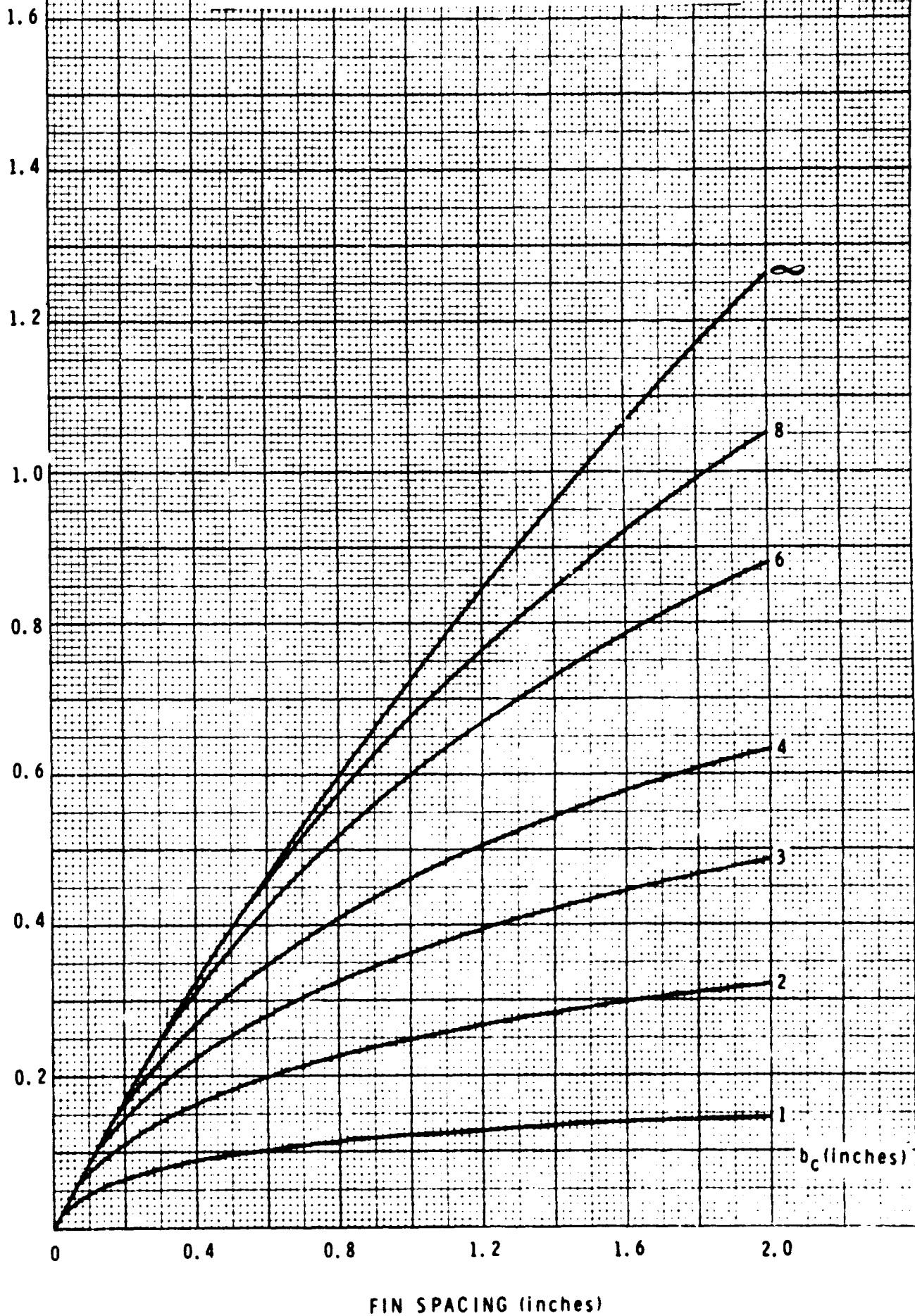
JEC

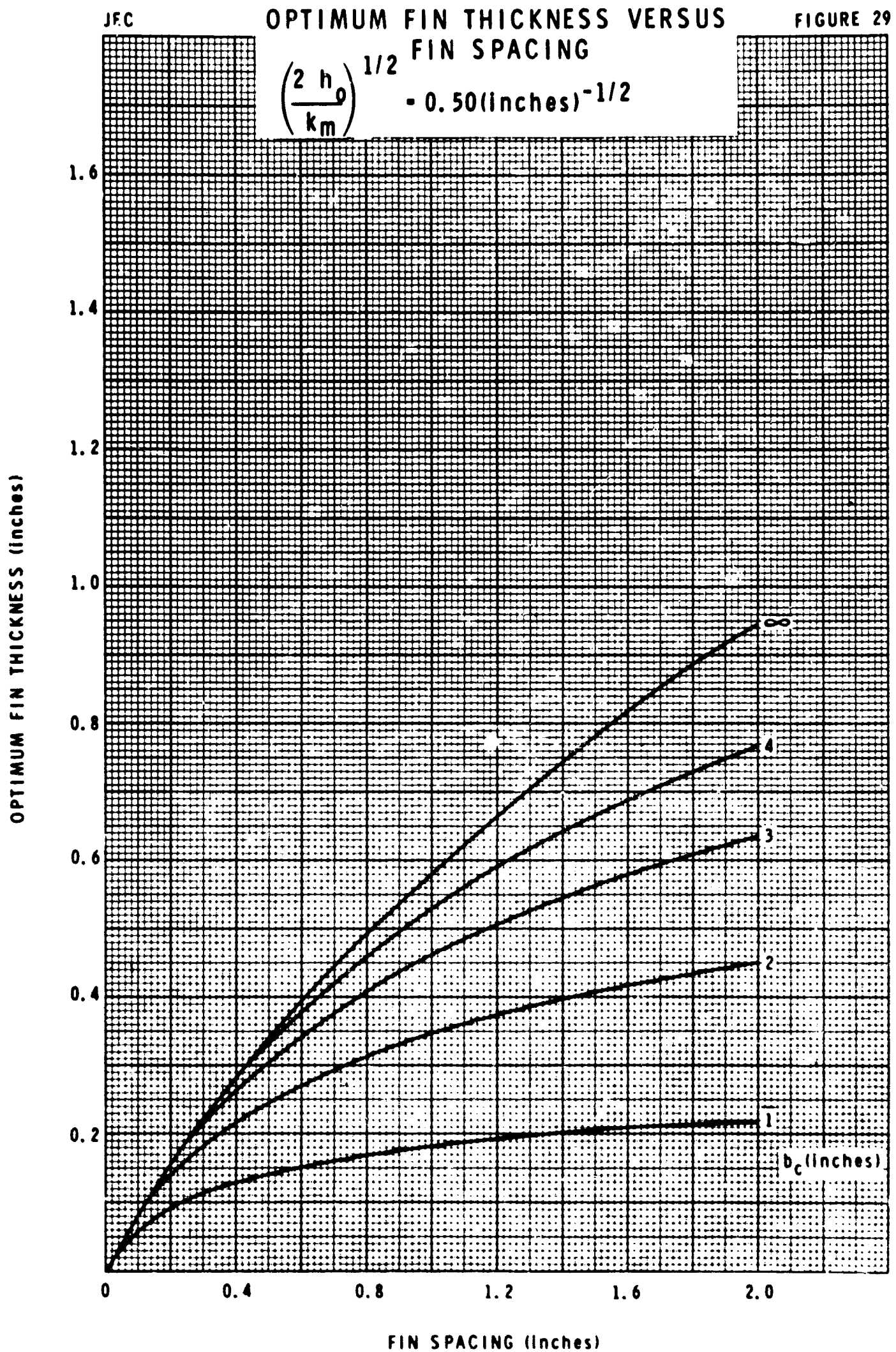
OPTIMUM FIN THICKNESS VERSUS  
FIN SPACING

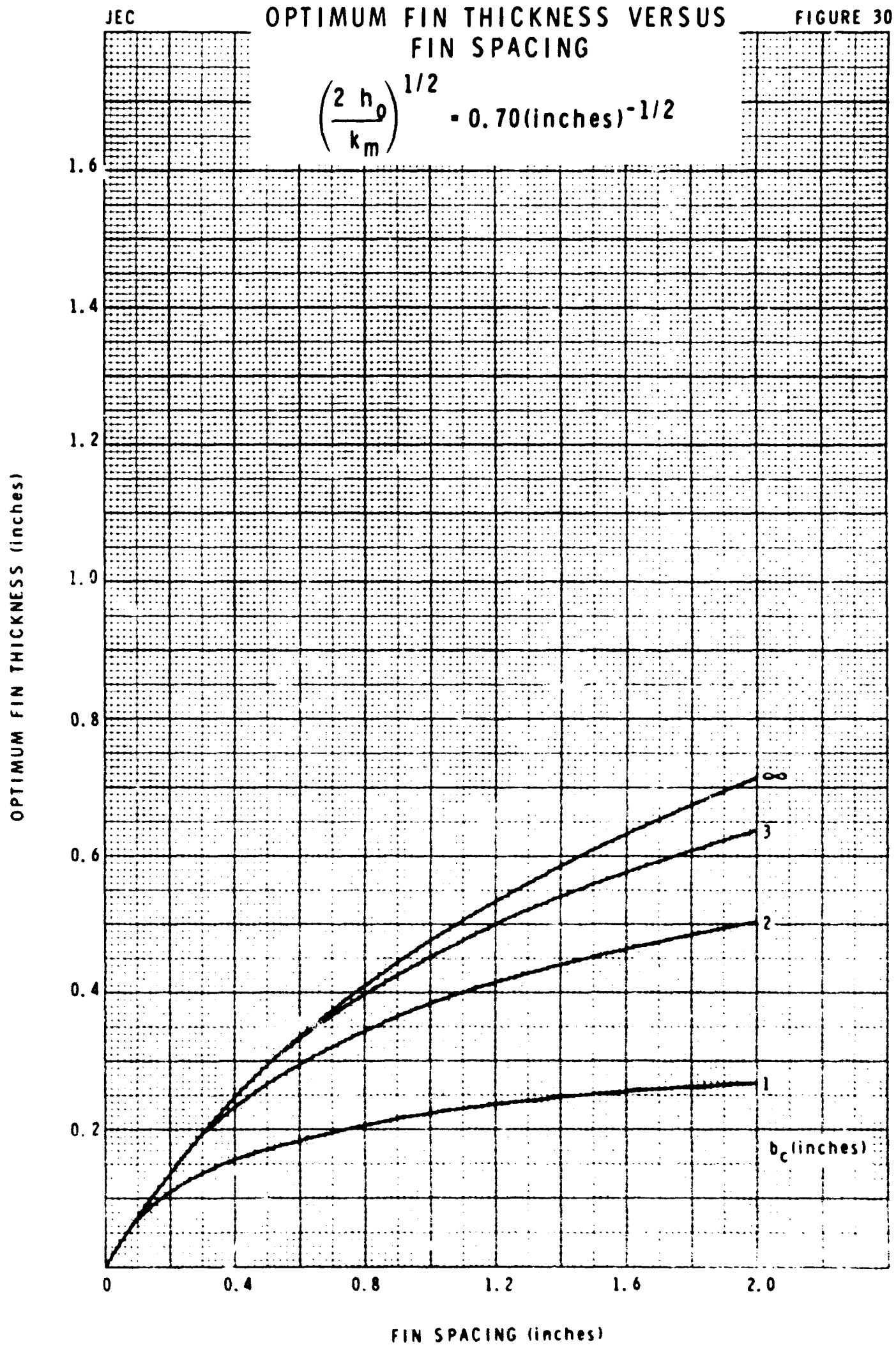
FIGURE 28

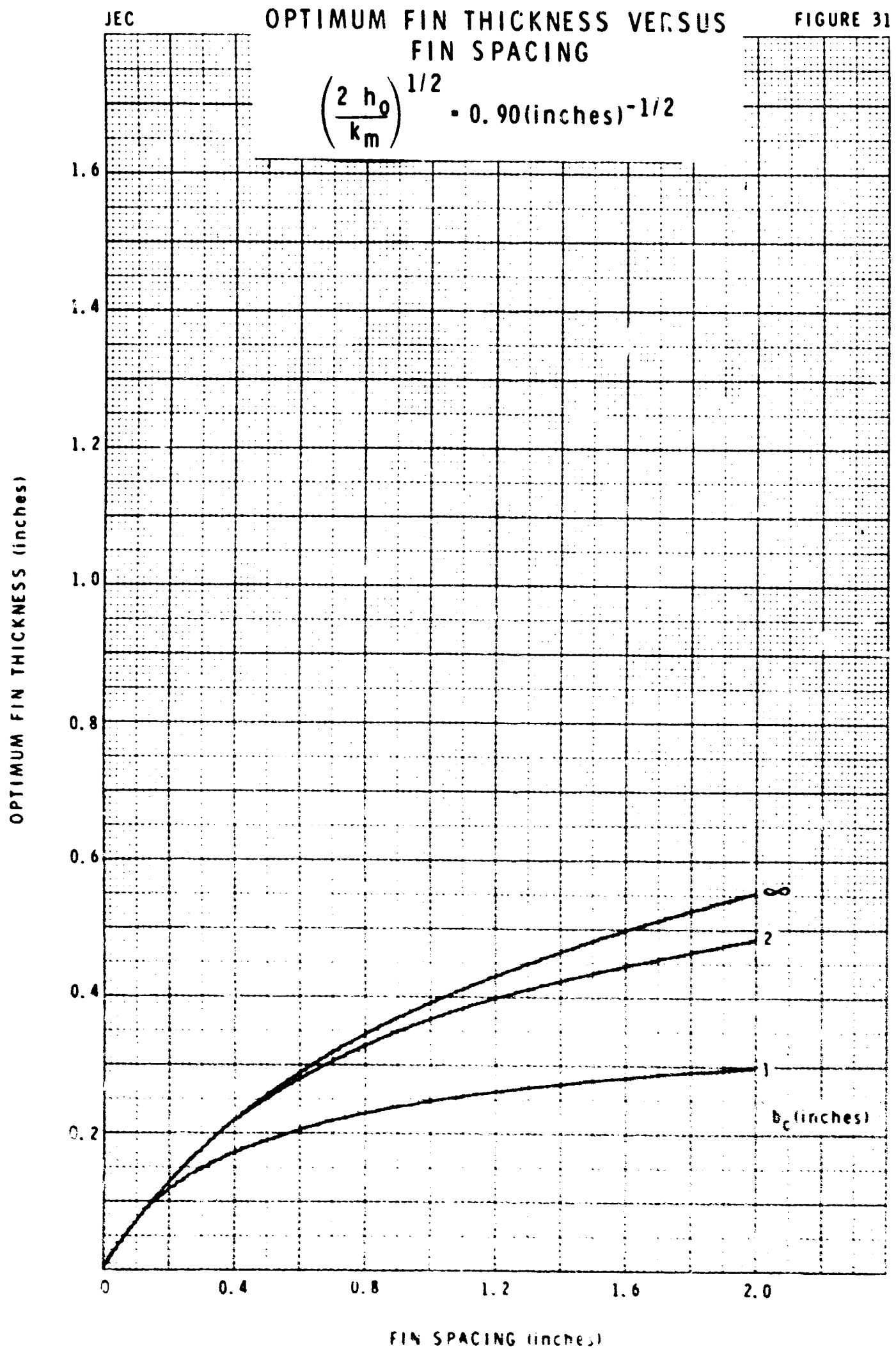
$$\left(\frac{2 h_0}{k_m}\right)^{1/2} = 0.30(\text{inches})^{-1/2}$$

OPTIMUM FIN THICKNESS (inches)

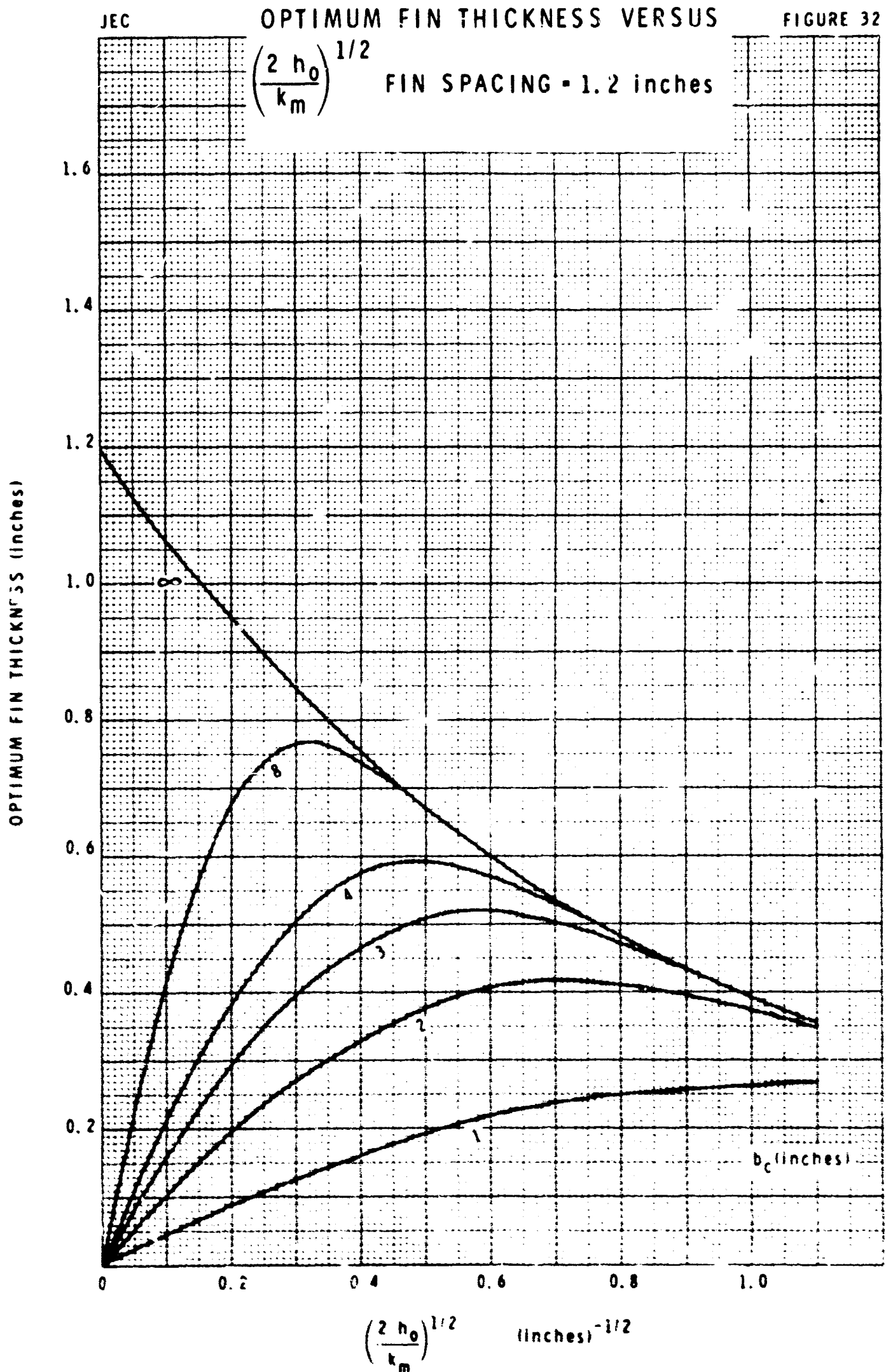


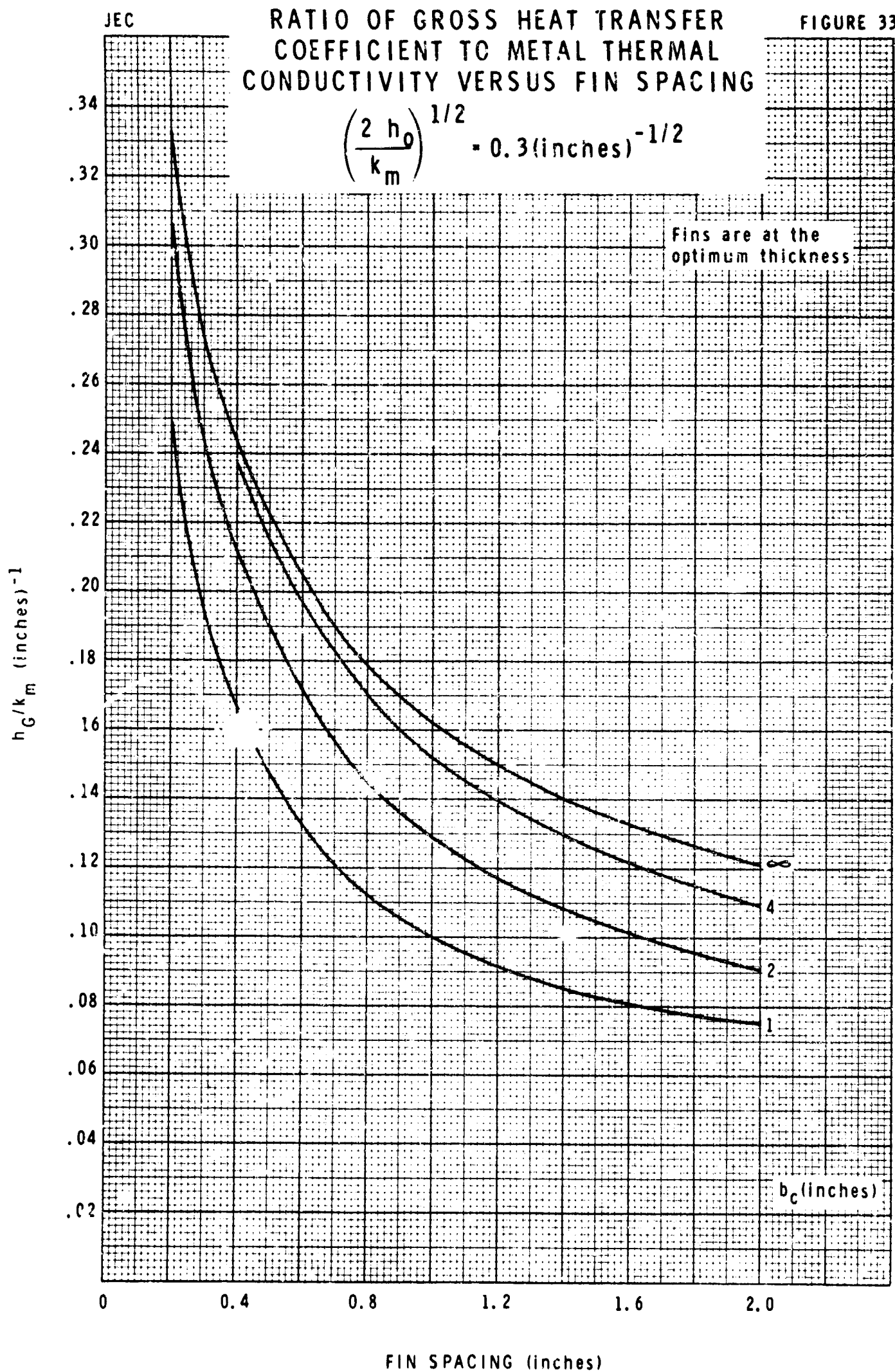


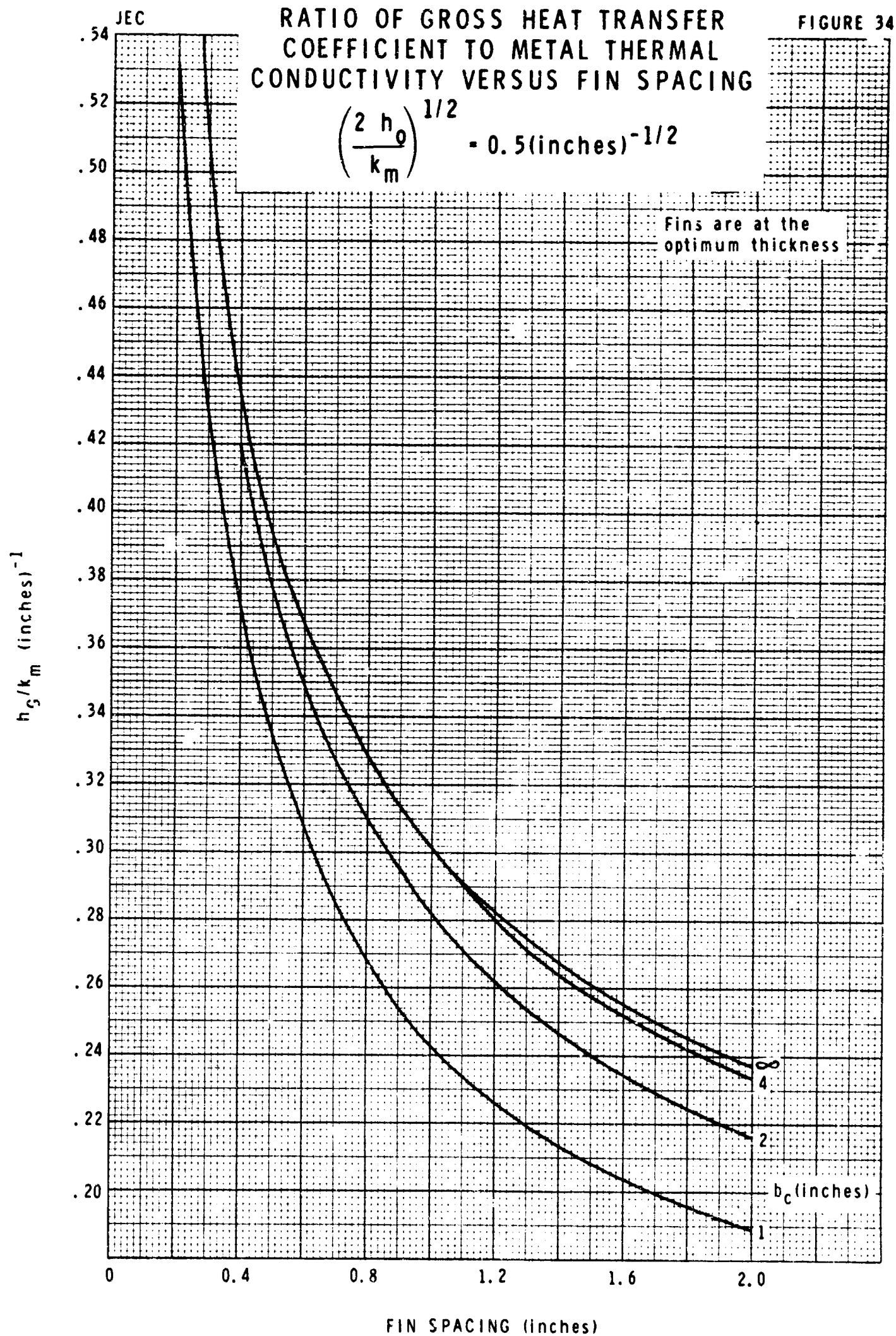


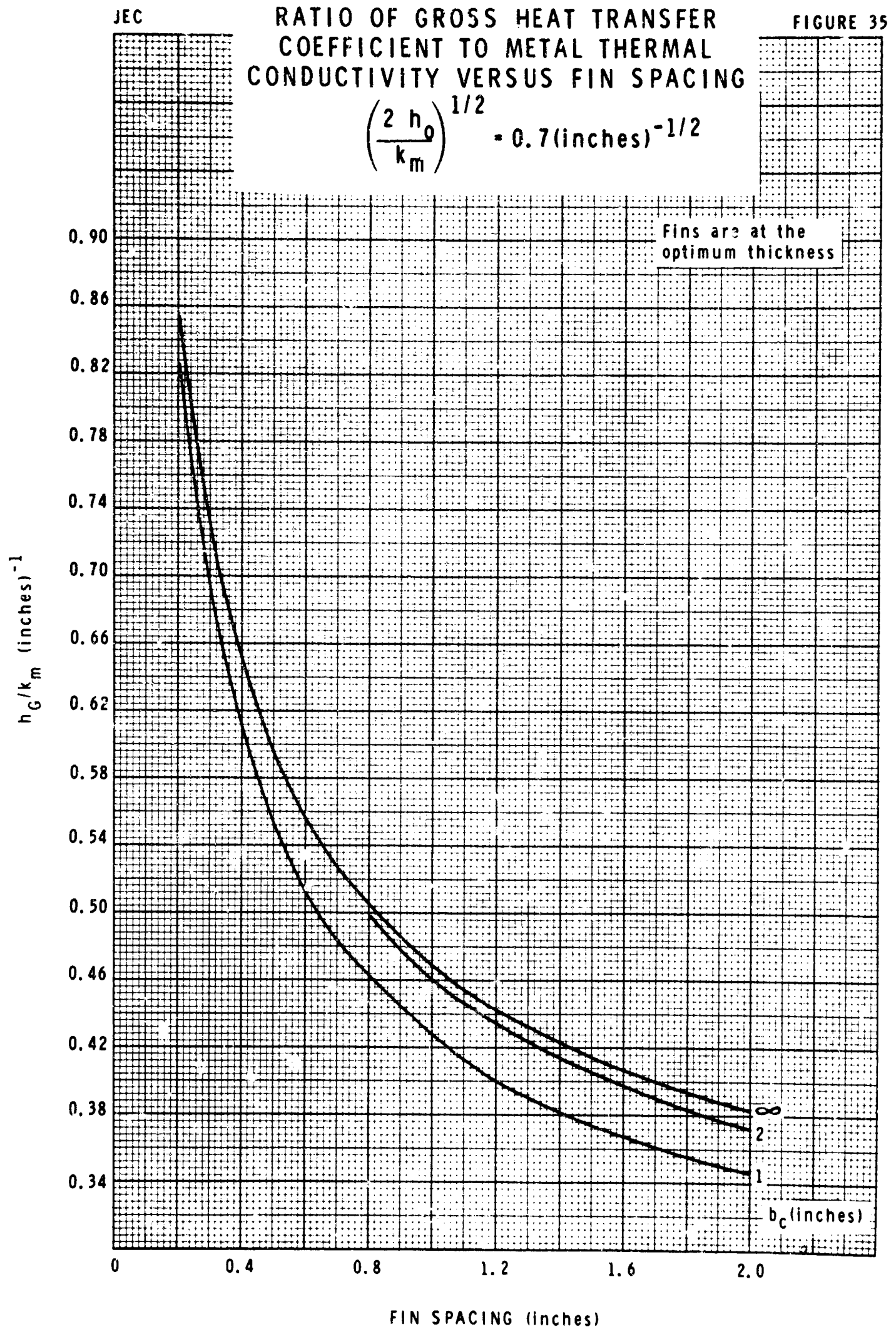












RATIO OF GROSS HEAT TRANSFER  
COEFFICIENT TO METAL THERMAL  
CONDUCTIVITY VERSUS FIN SPACING

FIGURE 36

$$\left(\frac{2 h_o}{k_m}\right)^{1/2} = 0.9(\text{inches})^{-1/2}$$

Fins are at the  
optimum thickness

$h_G/k_m (\text{inches})^{-1}$

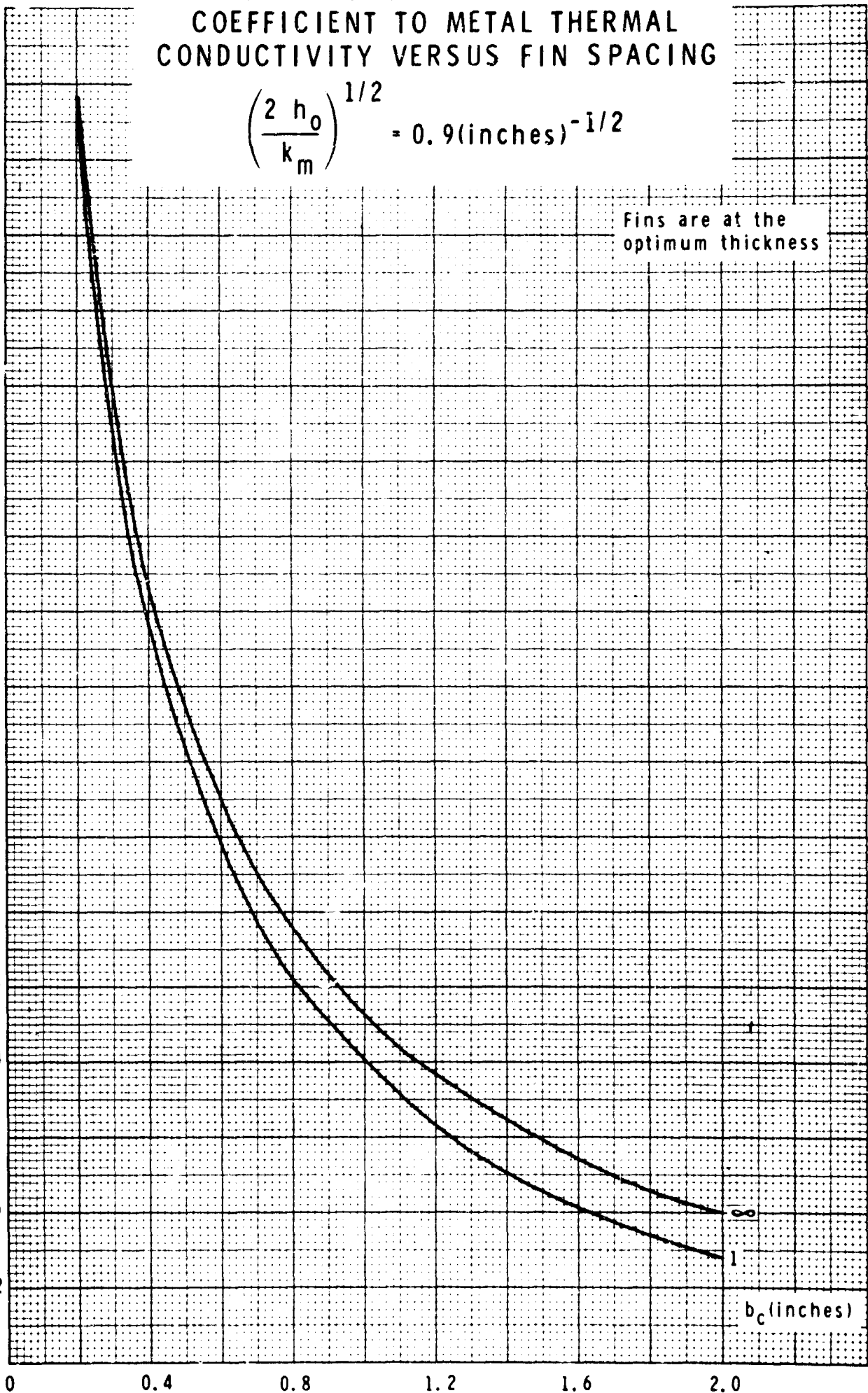
1.16  
1.12  
1.08  
1.04  
1.00  
0.96  
0.92  
0.88  
0.84  
0.80  
0.76  
0.72  
0.68  
0.64  
0.60  
0.56  
0.52

0 0.4 0.8 1.2 1.6 2.0

FIN SPACING (inches)

$b_c (\text{inches})$

8  
1



## TERMS AND SYMBOLS, CHAPTER III

a	Fin thickness, inches
A	Area, $\text{ft}^2$
b	Fin height, inches
Cn	Blasius law constant
Cp	Specific heat at constant pressure, Btu/lbm-F
D	Fin spacing, inches
f	Function
g	Acceleration of gravity
$\text{Gr}_x$	Grashof number based on x, $\frac{x^3 g \beta \Delta T}{\nu^2}$
h	Heat transfer coefficient, Btu/hr-ft <sup>2</sup> -F
k	Thermal conductivity, Btu/hr-ft-F
l	A length larger than the boundary layer thickness
L	Length, ft
m	Fin modulus $\left(\frac{2h_o}{k_m a}\right)^{1/2}$
n	Constant, or number of fins per foot width
$\text{Nu}_x$	Nusselt number based on x, $\frac{hx}{k}$
Pr	Prandtl number, $\frac{Cp \mu}{k}$
q	Heat rate, Btu/hr
$\text{Ra}_x$	Rayleigh number based on x, $\text{Gr}_x \text{Pr}$
$\text{Re}_x$	Reynolds number based on x, $\frac{Ux}{\nu}$
T	Temperature, F
U	Velocity, ft/sec
$U_1$	Constant employed in velocity profile expression

## TERMS AND SYMBOLS, CHAPTER III Continued

x, y, z Coordinates, feet

$y^+$  A modified Reynolds number involving friction velocity

## GREEK

$\alpha$  Thermal diffusivity,  $\frac{k}{\rho C_p}$ ,  $\text{ft}^2/\text{hr}$

$\beta$  Coefficient of thermal expansion,  $F^{-1}$

$\delta$  Boundary layer thickness, ft

$\Delta$  Signifies a change

$\eta$  Dimensionless temperature ratio  $\theta/\theta_w$

$\mu$  Viscosity,  $\text{lbm}/\text{ft}\cdot\text{hr}$

$\nu$  Kinematic viscosity,  $\mu/\rho$ ,  $\text{ft}^2/\text{hr}$   
Also, temperature difference ratio  $\theta/\theta_o$

$\rho$  Density,  $\text{lbm}/\text{ft}^3$

$\theta$  Temperature difference, F

$\tau$  Shear stress,  $\text{lbf}/\text{ft}^2$

## SUBSCRIPTS

a Ambient

avg Average

B Evaluated at the base surface

c Critical

C Corrected

D Based on plate or fin spacing

G Gross

m Metal

## TERMS AND SYMBOLS, CHAPTER III Continued

max	Maximum
S	Surface
o	Evaluated at the fin base
x	Based on length x
w	Evaluated at the wall



## CHAPTER IV, NATURAL CONVECTION HEAT TRANSFER TESTS

## ABSTRACT

Turbulent natural convection heat transfer from vertical surfaces to water was investigated both theoretically and experimentally. We performed the experiments in a 5.5-foot diameter 25-foot high column simulator filled with water in which electrically heated flat-plate and cylindrical modules were suspended.

Vertical flat plate experimental results verified the use of Saunders' equation over a Rayleigh number range of  $2.0 \times 10^9$  to  $3.6 \times 10^{12}$ . However, for vertical cylinders, experimental Nusselt numbers fell higher than Saunders' equation would predict at high-heat fluxes and fell lower at low-heat fluxes. A semiempirical equation of Larson closely predicted flat plate experimental heat transfer coefficients. Measured boundary layer temperature profiles, however, indicated that over 10 percent of the total temperature driving force is present at the boundary layer thickness predicted by Larson's method.

Agreement between predicted and observed gross heat transfer coefficients was quite good for finned vertical flat plates. For finned vertical cylinders, the predicted coefficients greatly exceeded the measured ones. Spacing between finned flat plates or finned cylinders did not greatly affect experimental gross heat transfer coefficients.

Chimney and inlet flow restriction experiments revealed a strong side flow effect which must be considered when extrapolating these data to larger units. Small crosscurrents significantly increased gross heat transfer coefficients of the finned units.

A conceptual design study was conducted for an undersea convector section of a 500 kw (e) fuel cell. We constructed a prototype unit and tested it in a shallow ocean basin for 54 hours. Experimental data in the ocean confirmed the laboratory test data and the design approach.

## EXPERIMENTAL EQUIPMENT AND METHODS

**APPARATUS** Heat transfer tests were performed in a 5.5-foot diameter, 25-foot high column simulator filled with tap water. A "pump-around" system was used to superimpose horizontal currents normal to the test sections for the combined forced and free convection experiments. Electrically heated test sections were suspended in quiescent water for the natural convection tests. Figure 37 is a flow diagram of the column simulator. A photograph of the simulator is shown in Figure 38.

In Chapter III, we stated that Grashof and Rayleigh numbers in seawater would likely range up to the following values.

$$Gr_x = \text{up to } 8.20 \times 10^9 (X)^3 \text{ at } \Delta T = 100 \text{ F}$$

$$Ra_x = \text{up to } 4.66 \times 10^{10} (X)^3 \text{ at } \Delta T = 100 \text{ F}$$

A 3 MW(e) thermoelectric power generator designed by Westinghouse (4) utilized surfaces 10 feet long by 2.5 feet high, mounted at a 45-degree angle to the horizontal. For this case the Grashof and Rayleigh numbers are

$$Gr_x = 3.65 \times 10^{11} \text{ at } \Delta T = 100 \text{ F}$$

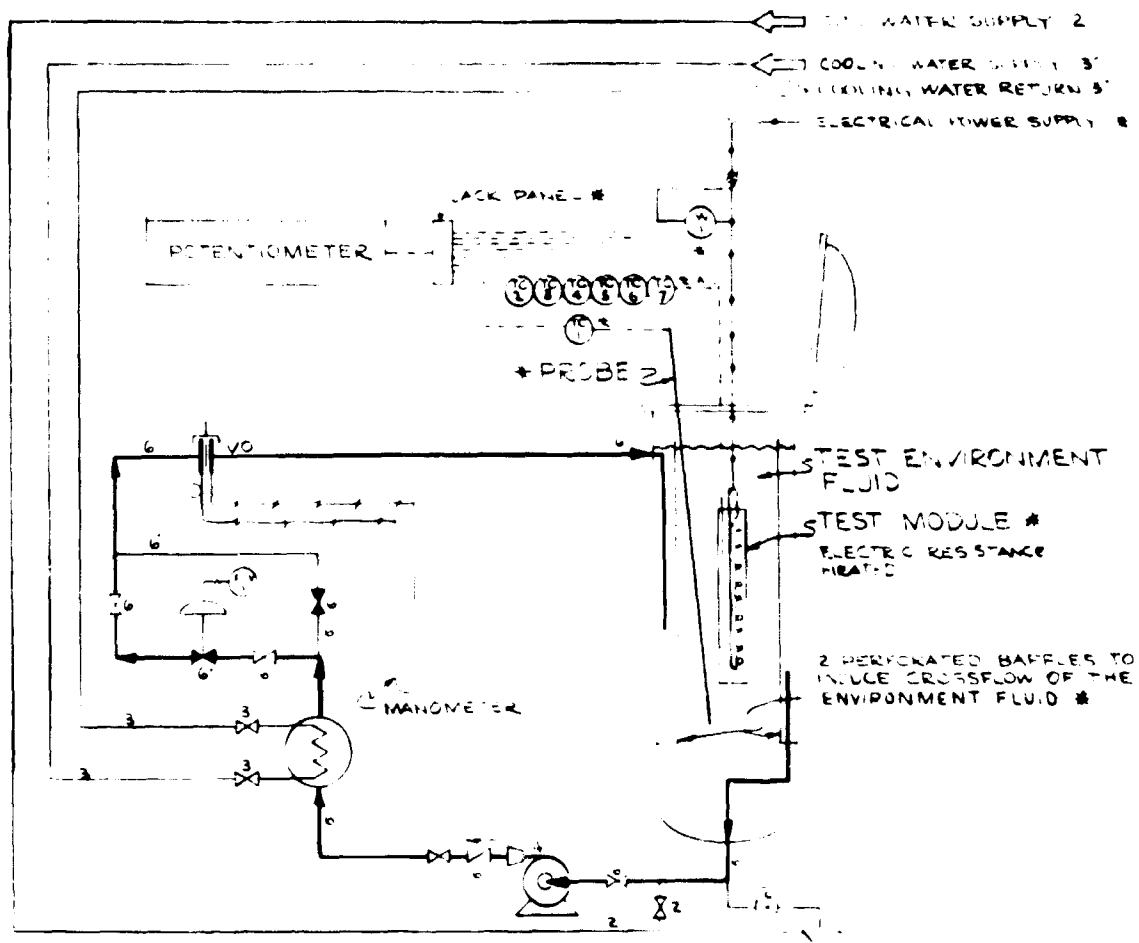
$$Ra_x = 2.08 \times 10^{12} \text{ at } \Delta T = 100 \text{ F}$$

Using these numbers as a guide, we designed two, identical, electrically heated, flat plate test sections.

Figure 39 is a drawing of one of the flat plate test sections. Heat generated by twelve 2,200-watt resistance heaters (25.4 kw total) flows through one face of a 5-inch wide by 36-inch high by 2-inch thick copper block. The heaters, divided into two rows of six each, were fitted into vertical, precision drilled holes in the block. Power level could be continuously controlled from zero to 25.4 kw by dividing the heaters into four banks of three each. Three of the banks were switched on or off and the fourth was controlled by a variable transformer.

All faces of the copper block, except the front, were insulated with 2-inch Foamglas insulation. The insulation was bonded to the block with Dow Corning RTV601 silicone rubber.

## COLUMN SIMULATOR



E-1 15-96 ET 39/50 P-1 1/2" GPM V-1 60 DIA X 25"

ALL EQUIPMENT EXISTING EXCEPT AS NOTED BY \*

## LEGEND OF SYMBOLS

- MAIN FLOW LINES
- AUXILIARY FLOW LINES
- ELECTRICAL POWER SUPPLY
- INSTRUMENT AIR
- INSTRUMENT ELECTRICAL
- - - - - INSTRUMENT TRANSMISSION LINE
- ⊗ GLOBE VALVE
- ⊕ AIR OPERATED CONTROL VALVE
- ⊖ AIR TO CLOSE
- ⌞ CHECK VALVE — FLOW DIRECTION
- ⌞ GATE VALVE
- ⌞ VARIABLE ORIFICE
- ⊙ SEAL POTS
- ⌞ OPEN DRAIN

## THERMOCOUPLES, COPPER CONSTANTAN, METAL SHEATH

- TC 1 PROBE FOR ENVIRONMENT FLUID
  - TC 2
  - TC 3
  - TC 4
  - TC 5
  - TC 6
  - TC 7
- LOCATED IN TEST MODULE

## WATERMETER

- WM 1 WATERMETER CONTROL HOUSE MOUNTED
- WM 2 OF FULL RANGE ACCURACY

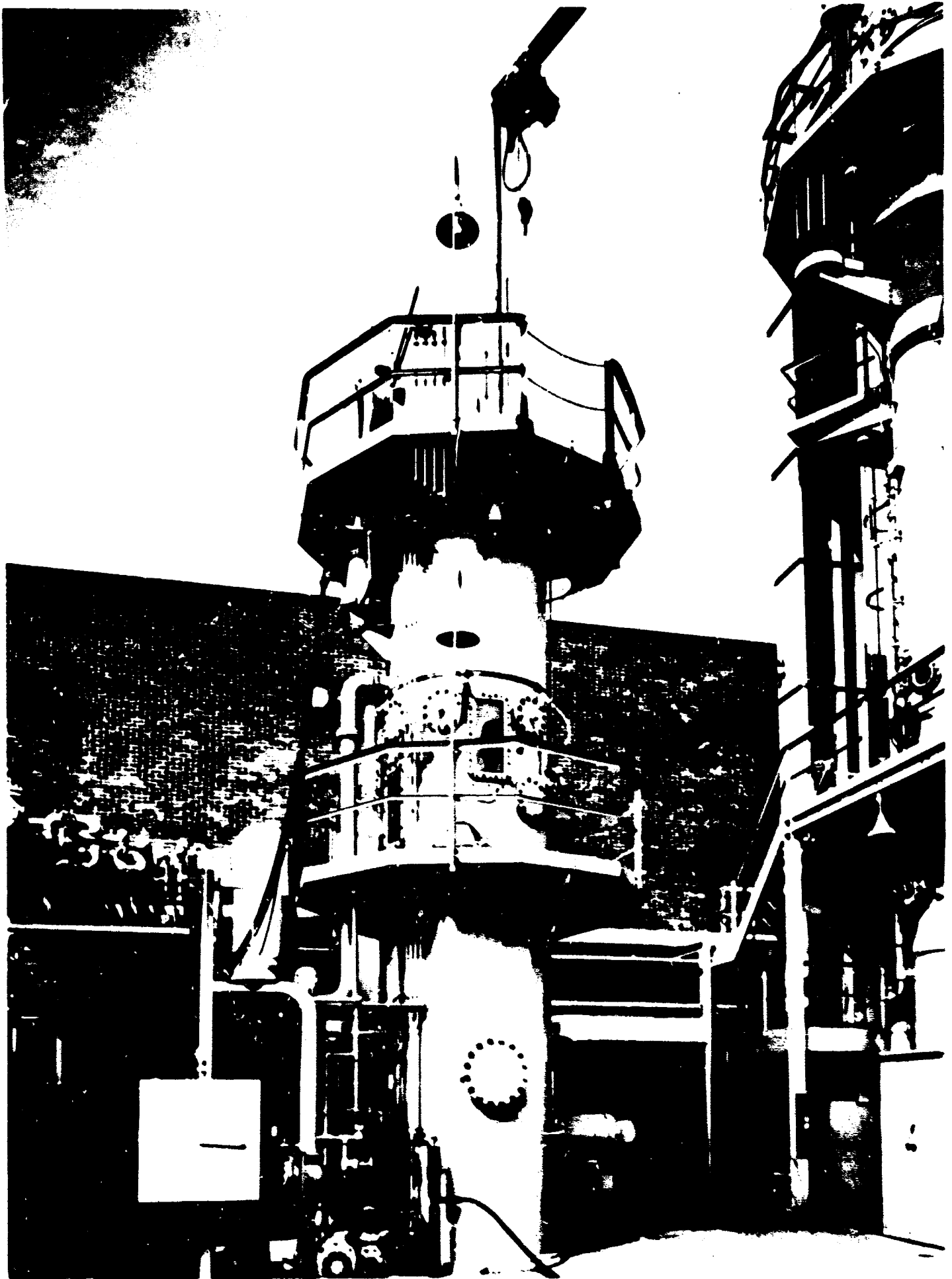
## ELECTRIC CONTROL VALVE

- ECV 1 INSTRUMENT AIR OPERATED VALVE
- ECV 2 CONTROL HOUSE

P&I FLOW DIAGRAM

COLUMN SIMULATOR

FIGURE 38



FOAM LASS INSULATION

2 6 CONDUCTOR AWG 4 TYPE 33  
600 VOLT HEAT RESISTANT CABLE  
100 SAMPLES NO 3222

1. 2 6 CONDUCTOR AWG 4 TYPE 33  
600 VOLT HEAT RESISTANT CABLE

2. SUPPORT FRAME

3. THERMOCOUPLE LEAD  
TUBE & SUPPORT FRAME

4. STAINLESS

5. SUPPORT ROLL 1/2 IN DIA  
ATTACHED 2 ROLLER 1/2 IN DIA  
LEATH ROLLERS  
COLD 2 IN DIA

6. PLATED COPPER ROLL  
2 IN DIA 1/2 IN DIA

7. COPPER ROLL

8. FOAM LASS INSULATION  
2 IN THICKNESS 3 IN DIA  
TOP 4 IN DIA

A

A

ATTENTION: 1. 2 6 CONDUCTOR  
600 VOLT HEAT RESISTANT CABLE  
100 SAMPLES NO 3222

FOAM LASS INSULATION

2 6 CONDUCTOR AWG 4 TYPE 33

A

TERMINAL BOX OF 2  
VALVE 1/2 IN DIA

2 6 CONDUCTOR AWG 4 TYPE 33

TERMINAL BOX OF 2  
VALVE 1/2 IN DIA

2 6 CONDUCTOR AWG 4 TYPE 33

2 6 CONDUCTOR AWG 4 TYPE 33

2 6 CONDUCTOR AWG 4 TYPE 33

2 6 CONDUCTOR AWG 4 TYPE 33

2 6 CONDUCTOR AWG 4 TYPE 33

2 6 CONDUCTOR AWG 4 TYPE 33

2 6 CONDUCTOR AWG 4 TYPE 33

2 6 CONDUCTOR AWG 4 TYPE 33

2 6 CONDUCTOR AWG 4 TYPE 33

2 6 CONDUCTOR AWG 4 TYPE 33

2 6 CONDUCTOR AWG 4 TYPE 33

2 6 CONDUCTOR AWG 4 TYPE 33

2 6 CONDUCTOR AWG 4 TYPE 33

2 6 CONDUCTOR AWG 4 TYPE 33

2 6 CONDUCTOR AWG 4 TYPE 33

2 6 CONDUCTOR AWG 4 TYPE 33

2 6 CONDUCTOR AWG 4 TYPE 33

2 6 CONDUCTOR AWG 4 TYPE 33

2 6 CONDUCTOR AWG 4 TYPE 33

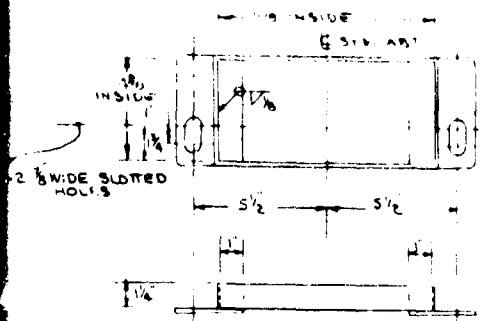
2 6 CONDUCTOR AWG 4 TYPE 33

2 6 CONDUCTOR AWG 4 TYPE 33

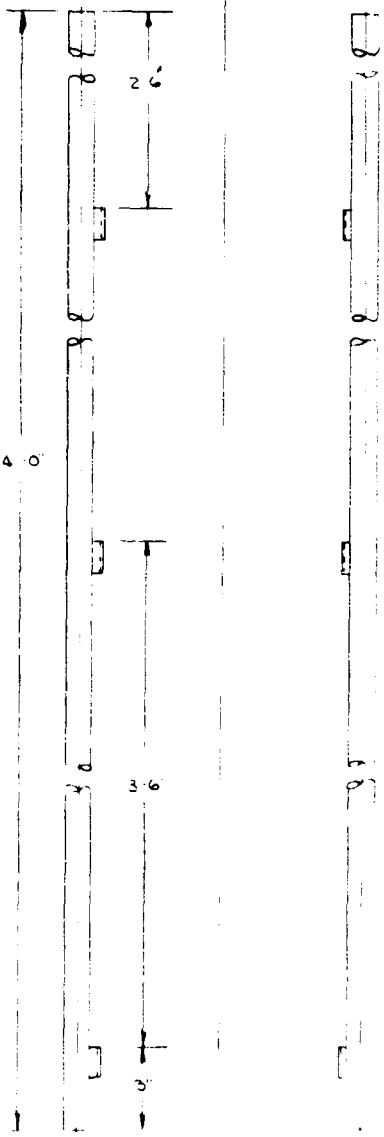
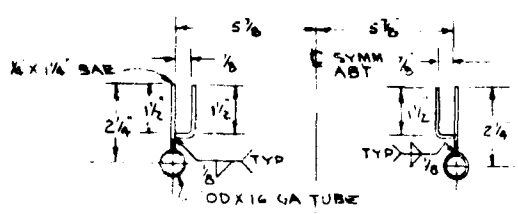
2 6 CONDUCTOR AWG 4 TYPE 33

2 6 CONDUCTOR AWG 4 TYPE 33

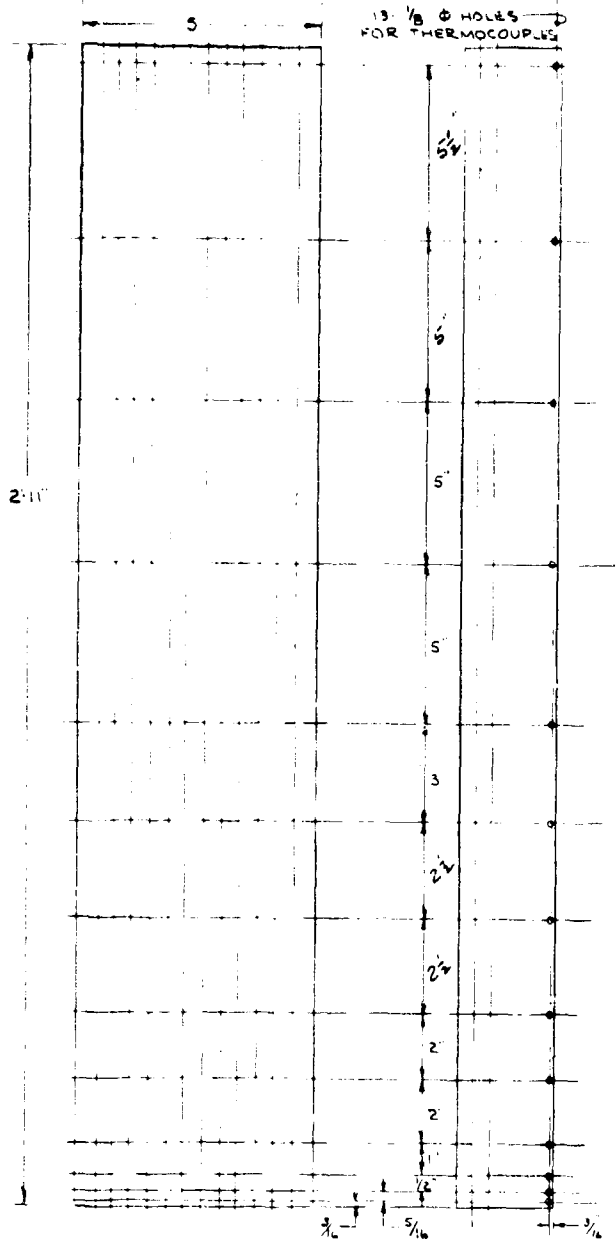
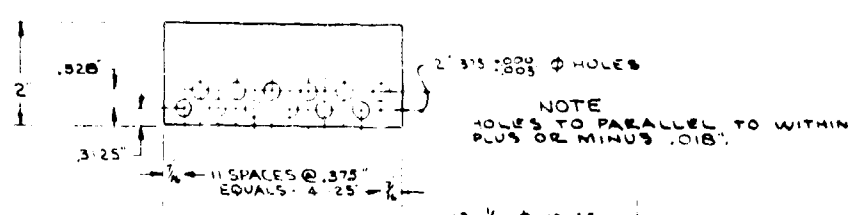
A



(2) SUPPORT FRAME  
MAKE 4 - 3/16" THK C STL



(3) TC SUPPORT FRAME  
MAKE 2 C STL



(4) HEATED COPPER BLOCK  
MAKE 2 HARD DRAWN BASS BAR COPPER

REV	DATE	DESCRIPTION	APPROVED
<p>NOTICE</p> <p>THIS DRAWING HAS NOT BEEN RELEASED. IT IS THE SOLE PROPERTY OF C F BRAUN &amp; CO. IT IS LOANED TO THE RESEARCH DEPT. OF THE CALIFORNIA INSTITUTE OF TECHNOLOGY AND IS TO BE USED ONLY FOR THE RESEARCH PROJECT FOR WHICH IT WAS LOANED. IT IS NOT TO BE REPRODUCED, COPIED, OR OTHERWISE USED IN ANY MANNER WITHOUT THE WRITTEN CONSENT OF C F BRAUN &amp; CO.</p>			
DESIGNED FOR CONSTRUCTION		CUSTOMER APPROVAL	
BY	DATE		
DESIGNED	DRAWN	REVIEWED	APPROVED
RJGAIL	RJGAIL		
FOR C F BRAUN & CO RESEARCH DEPT AT ALHAMBRA CALIFORNIA			
<p>PLATE NATURAL CONVECTION HEAT TRANSFER UNIT HEATER BLOCK ASSEMBLY &amp; DETAILS</p>			
ALHAMBRA C F BRAUN & CO CALIFORNIA			
SCALE	DRAWING NUMBER		REVISION
NONE	2650-100-RD-3		3
DATE	12-2-64		

B

## EXPERIMENTAL EQUIPMENT AND METHODS Continued

Thirteen copper-constantan thermocouples measured the surface temperature of one of the flat plate test sections, while the other section had seven thermocouples. The couples were mounted in 0.125-inch diameter horizontal holes drilled 0.25 inches back from the front face. Seven thermocouples were placed along the vertical centerline of each section. Six were placed near the edges of the first section only to detect end effects, if any. Figure 39 shows the thermocouple locations.

Fins were soldered to the front face of the copper blocks with 430 F (melting point) solder, which has a relatively high thermal conductivity and flows extremely well. Because of the high fluidity of the solder there appeared to be very little contact resistance between the fins and the base metal. Figure 40 is a photograph of one of the finned vertical flat plates. After fabrication, the flat-plate units were suspended 13 feet below the top of the column simulator by all-thread rods. One of the units was anchored to the column wall and the other was fastened to it by two small rods during the parallel plate tests.

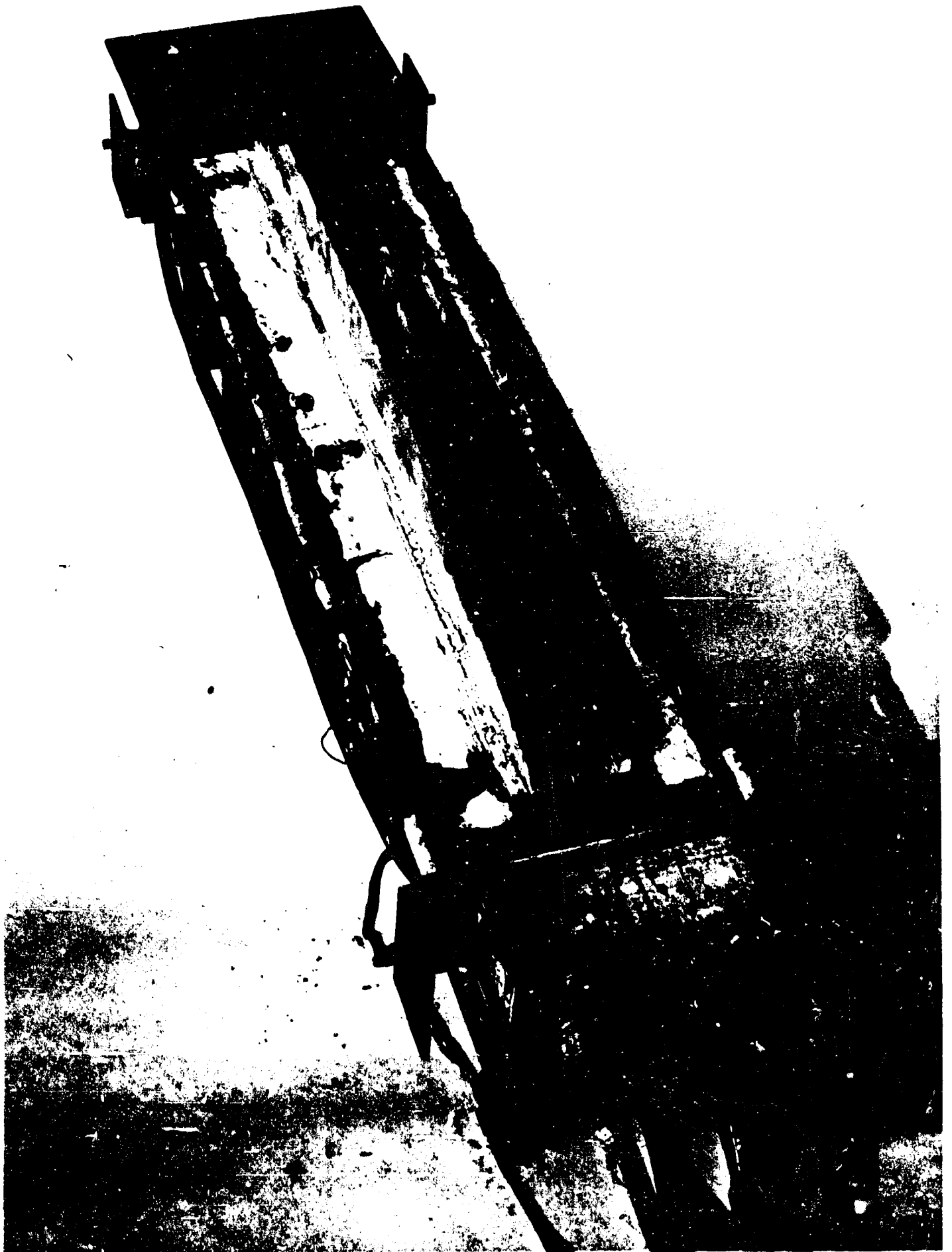
Before experimentation began, we determined the temperature profile in the block and fins by an electrical analog device manufactured by the Carlson Computer Company, Poway, California. With this technique, a cross section of the block and fins is cut out of electrically conductive paper and is glued to cardboard or a similar nonconducting material. The twelve heaters were represented by full-scale circles of high electrical conductivity (essentially infinite compared to the paper) silver paint. A strip of lower conductivity paper attached to the outer surfaces of block and fins simulated the surface heat transfer coefficient. Slits were cut in this paper to ensure electric current flow (analogous to heat flow) perpendicular to the fin or base outer surfaces. The heat sink was a stripe of silver paint at the outer edge of the surface conductance paper.

The machine was adjusted so that the heaters were at a higher voltage (analogous to temperature) than the ambient water sink. Then by determining intermediate voltages, we were able to map the temperature distribution in the block. Figure 41 pictures a typical temperature map.

Results of the analog study showed that the temperature profile at the surface was fairly uniform and that little temperature variation across the fin width existed. With these results in mind, we interpreted experimental surface temperature variations as evidence of variations in the surface coefficient - not as the characteristics of heater placement.

VERTICAL FINNED FLAT PLATE TEST UNIT

FIGURE 40



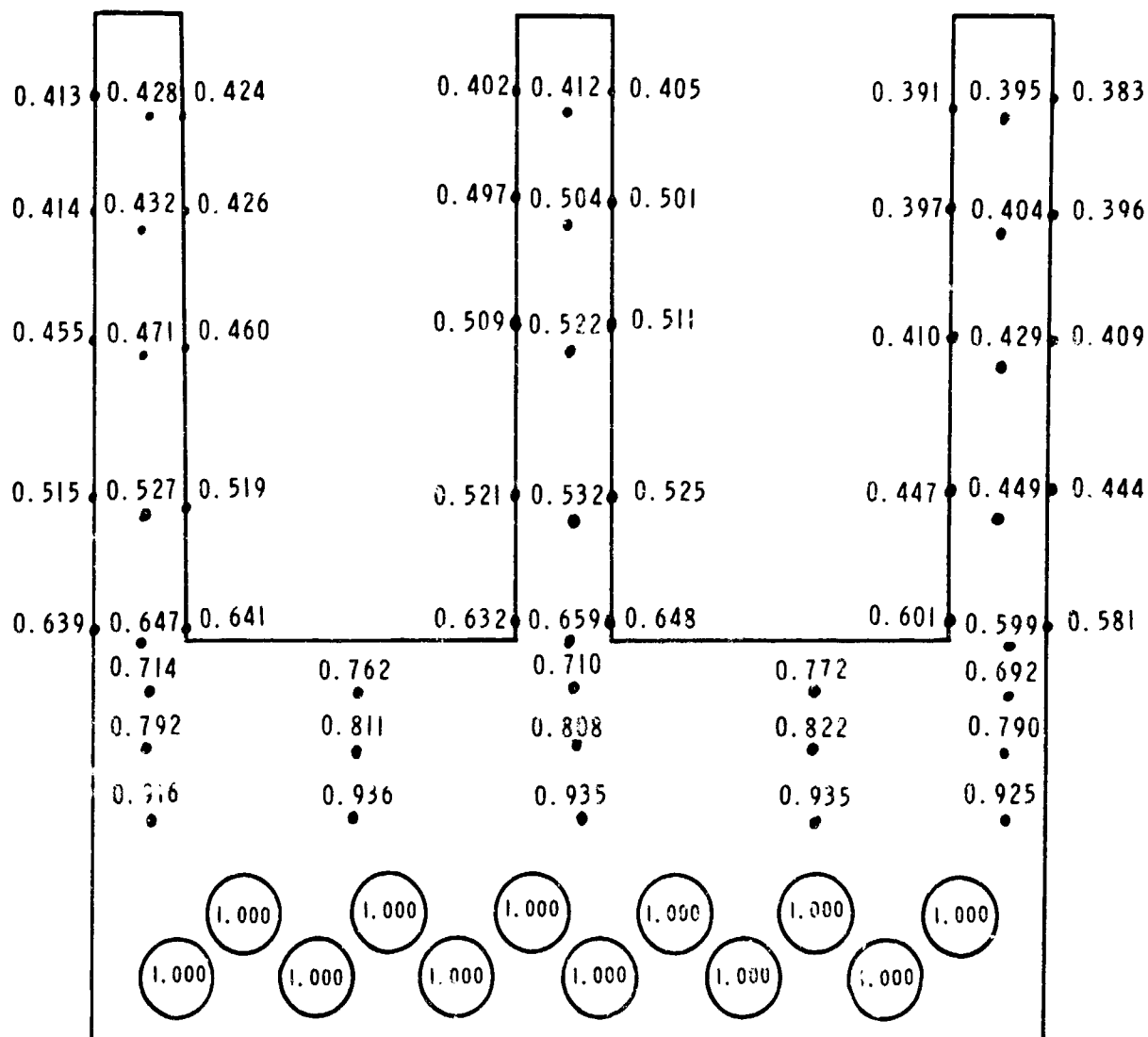


# ANALOG MAP OF TEMPERATURE DISTRIBUTION IN VERTICAL FINNED FLAT PLATE

Material - Electrolytically Pure Copper

Thermal Conductivity - 220 Btu/hr-ft-F

Surface Coefficient - 183 Btu/hr-ft<sup>2</sup>-F



Numbers represent the fractional temperature driving force. At the heater surface, temperature difference is unity. It is zero in the ambient fluid.

## EXPERIMENTAL EQUIPMENT AND METHODS Continued

Cylindrical test units were also made of copper. Figure 42 is a drawing of one of the seven 2-inch OD cylinders. Each 4-foot long cylinder contained two 3.75 kw resistance heaters, which were fitted into precision drilled holes through the copper rod. Centerless grinding of the heater sheath was necessary to achieve a proper fit ( $\pm 0.001$  inch).

Eight thermocouples were installed on one of the cylinders as shown in Figure 42. A long groove was machined for each thermocouple. The thermocouples were placed in 0.125-inch OD copper tubes, which in turn were put into the grooves. They were covered with solder with a melting point of 509 F. Fins were attached in the same manner as with the flat-plate units.

Each cylinder end was insulated by a 6-inch long, 2-inch OD phenolic cylinder filled with Dow Corning RTV601 silicone rubber. Calculated heat losses were negligible. The phenolic spacers also provided unheated flow development entry and exit regions.

Cylinders were suspended from a plate above by 1-inch pipes, 5 feet long. Figure 43 is a photograph of the 2-inch OD cylindrical test unit.

After experimentation with the 2-inch OD cylindrical unit was complete, fins were removed, and the outside diameters of the cylinders were reduced to 1 inch. This diameter was too small to accommodate thermocouple grooves. Therefore, we strung lead wires from copper-constantan thermocouples soldered to the copper cylinder  $3/16$  inch below the outer surface, at right angles to the cylinder. This created some flow disturbance in the boundary layer. However, the thermocouple junctions were placed upstream of the flow disturbance, so it is unlikely that their readings were affected. Six surface thermocouples were mounted at distances of 2.0, 6.0, 11.0, 23.0, 35.0, and 46.0 inches from the leading edge. Only the center cylinder was instrumented. Figure 44 shows the 1-inch diameter cylinder unit.

The ends of each cylinder were insulated by a 6-inch long (minimum), 1-inch OD phenolic cylinder filled with epoxy resin. Phenolic spacers provided unheated flow development entry and exit regions and served as a means of supporting the cylinders.

ARTER TYPE ELECTRICAL  
RESISTANCE HEATER 240 VAC  
7.5 KW. PRECISION 42 NO. 00 75  
HONED HOLE IN COPPER BAR WITH  
.001 INCH MAXIMUM ANGULAR DEVIANCE

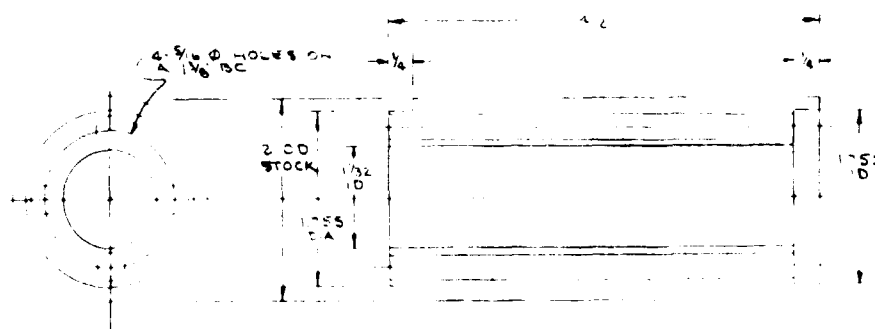
1/2" COPPER BAR, INTERLESS  
GROUND ON ONE END A RMS 63 FINISH

4 .125 DIA. KEYS  
ON A .125 INCH SPACING

.125 DIA

3 1/4" HEATED LENGTH  
ABOUT 4" OVERALL

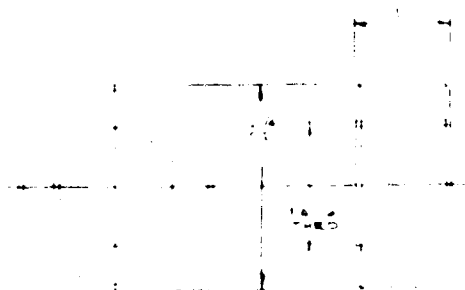
HEATER DETAIL  
MAKE ONE AS SHOWN  
MAKE SIX WITHOUT THE THERMOCOUP



THERMO BARRIER  
MAKE 14 MATERIAL PHENOLIC

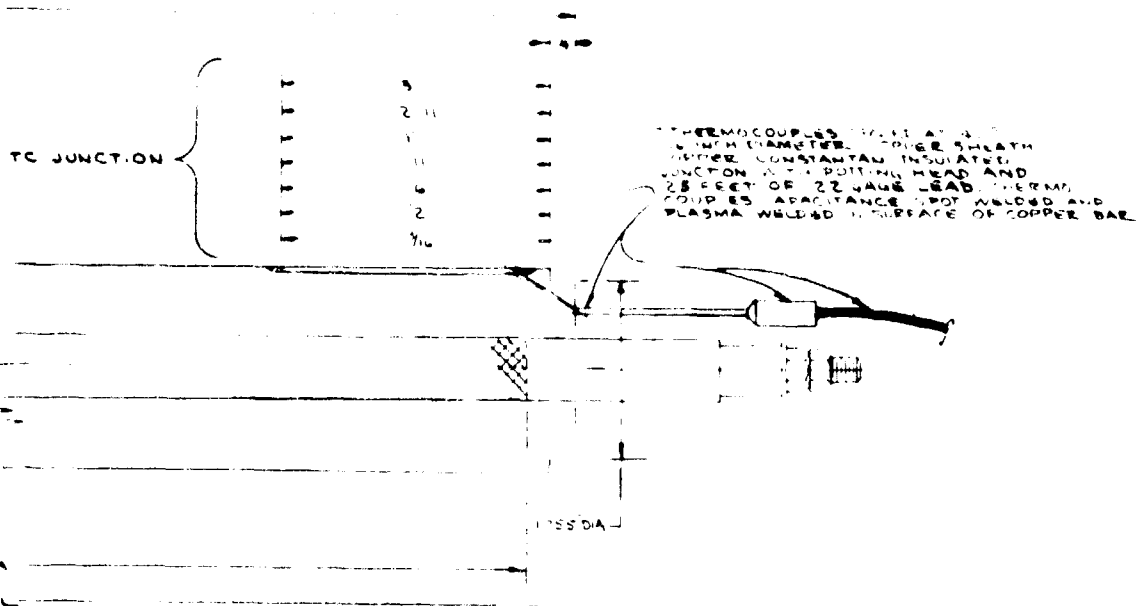


SUS  
MAKE  
END 9

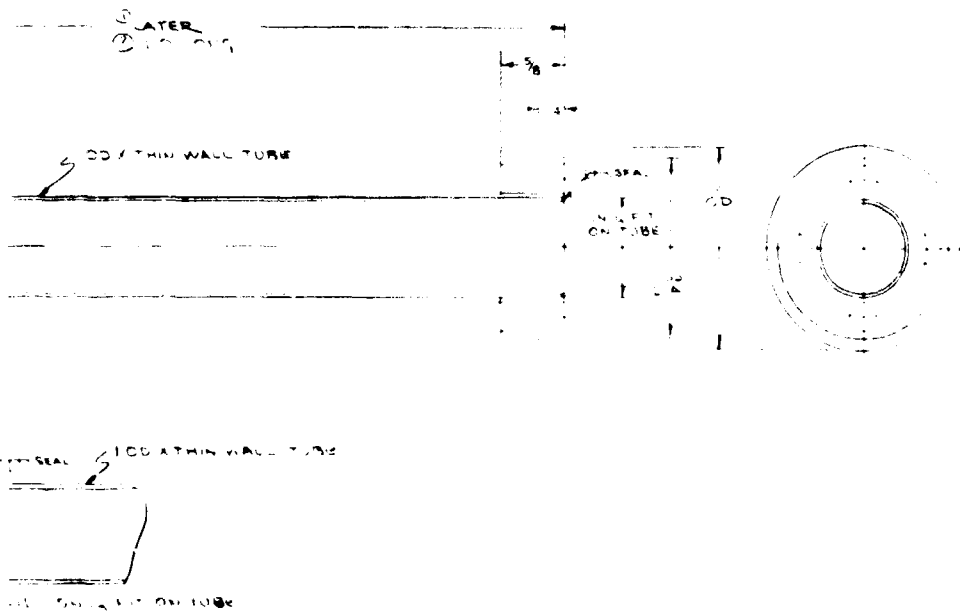


SUPPORT NUT  
MAKE 1 MATERIAL C STL

A



# UP COUPLES



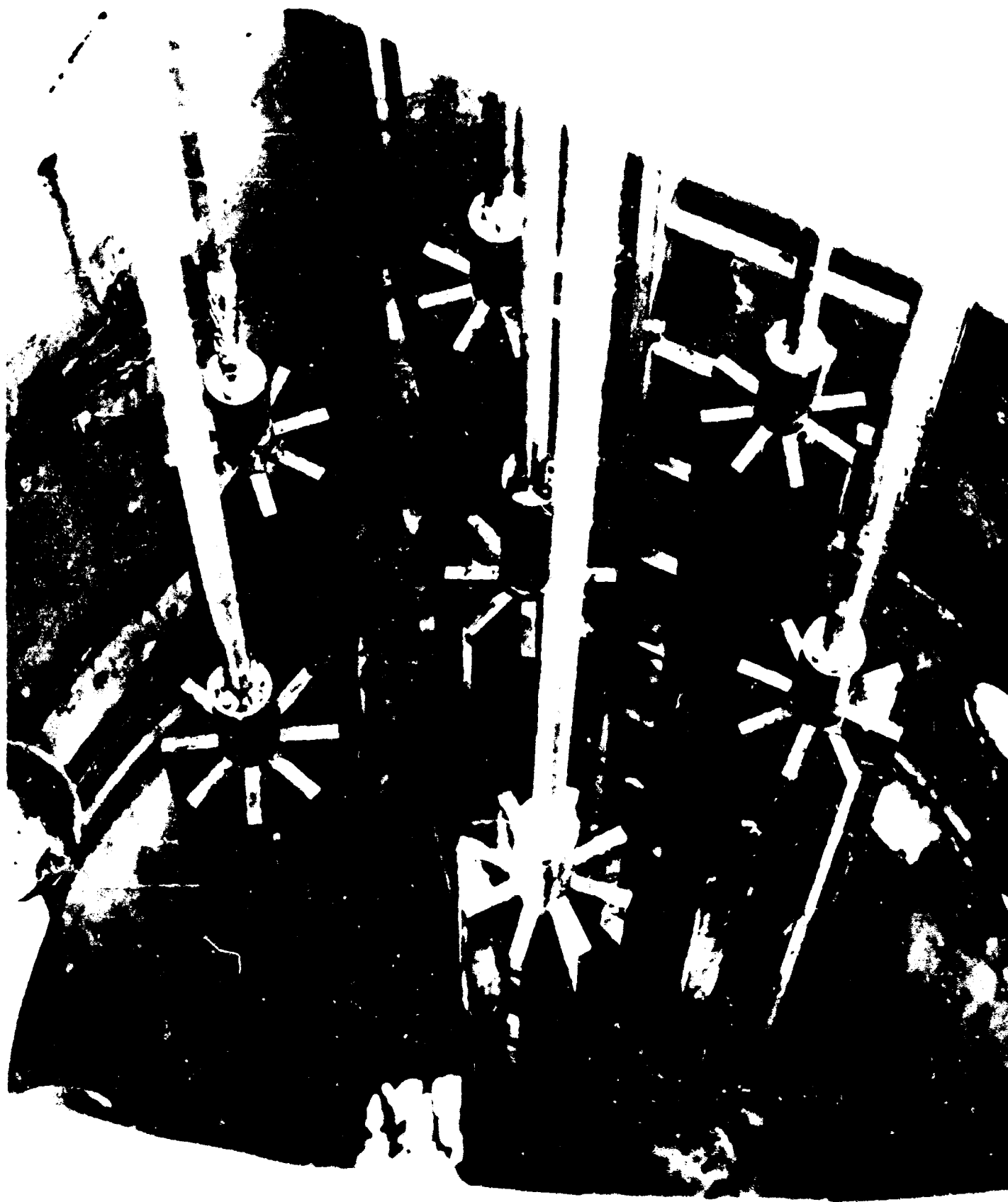
SUPPORT AND CONDUIT TUBES  
1/4" O.D. END & 1" O.D. END 1/4" O.D. END  
SHOWN ON RIGHT END MATERIAL 1/4" O.D. END

B

REV	DATE	DESCRIPTION	APP
NOTICE			
THIS DRAWING IS THE PROPERTY OF C. F. BRAUN & CO. AND IS NOT TO BE REPRODUCED OR USED IN ANY MANNER WITHOUT THE WRITTEN PERMISSION OF C. F. BRAUN & CO. ANY VIOLATION OF THIS NOTICE WILL BE PROSECUTED TO THE FULL EXTENT OF THE LAW.			
DESIGNED FOR CONSTRUCTION		CUSTOMER APPROVAL	
BY	DATE		
DESIGNED	DATE	REVIEWED	APPROVED
C. F. BRAUN & CO. RESEARCH DEPARTMENT AT ALHAMBRA, CALIFORNIA			
CYLINDER NATURAL CONVECTION HEAT TRANSFER UNIT HEATER DETAIL			
ALHAMBRA C. F. BRAUN & CO. CALIFORNIA			
SCALE	DRAWING NUMBER		
NONE	2650-100-RD-6		
DATE	2-23-65		

TWO INCH DIAMETER CYLINDRICAL TEST UNIT

FIGURE 43



NOV 1964

ONE INCH DIAMETER  
CYLINDRICAL TEST UNIT

FIGURE 44



## EXPERIMENTAL EQUIPMENT AND METHODS Continued

Flat plywood baffles were positioned at several distances below the leading edges of the units for the inlet clearance tests. The cylindrical unit baffle was a 26.3-inch diameter circle and flat-plate unit baffle was a 5.0-inch by 9.0-inch rectangle. The flat-plate unit chimneys were 3-foot high plywood boards placed parallel to the outside fin on each side. They blocked entrainment of ambient water to the unit. A 4-foot high piece of sheet metal was formed into several circular chimneys of different diameters for the cylindrical unit. It was formed into several circular chimneys.

**INSTRUMENTATION** All temperatures were measured by copper-constantan thermocouples with an ice reference junction and a Leeds and Northrup No 9662 precision portable potentiometer. Each thermocouple was carefully calibrated against a precision thermometer prior to use in the tests. Several 0.0625-inch OD thermocouple probes were constructed to determine boundary layer temperatures and temperature distribution in the channels between fins. Figure 45 shows one of the probes.

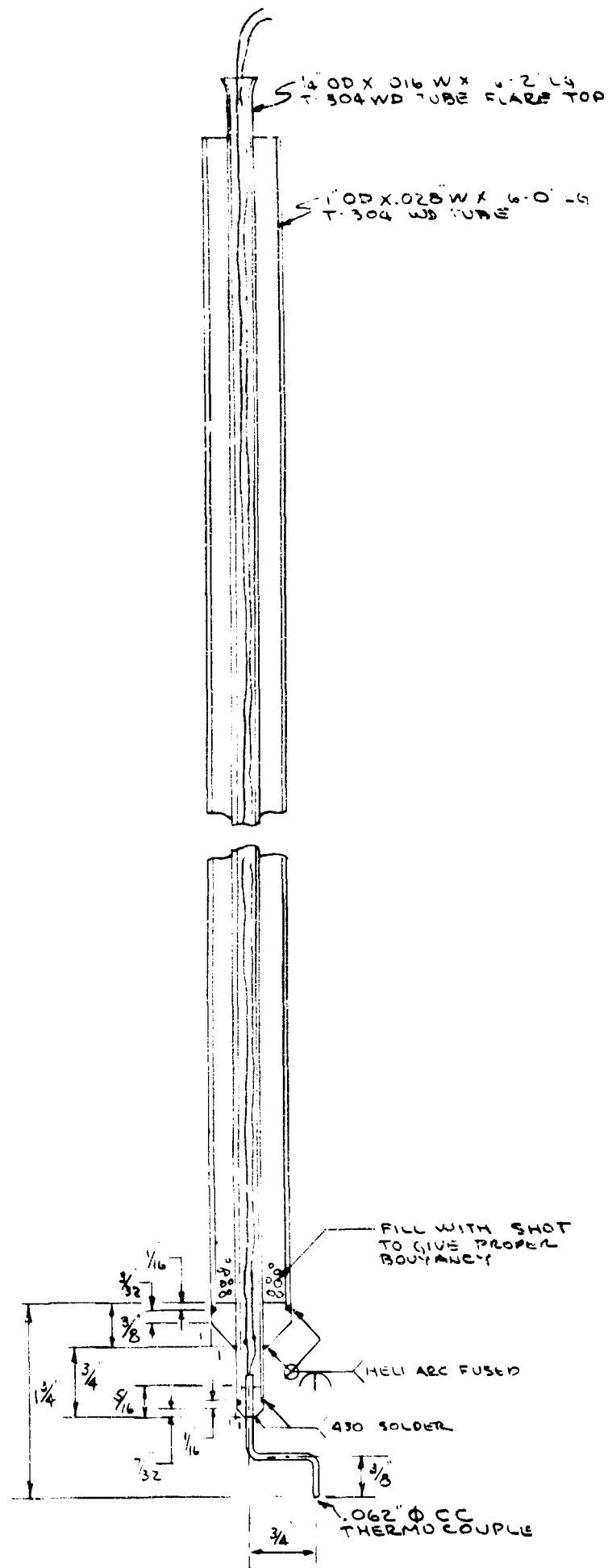
Three-phase AC power to the units was measured by two Westinghouse Pa 5 voltmeters and two ammeters, a Weston Model 904 and a Westinghouse Pa 5. All meters had a rated accuracy of 1/2 percent of full range. Two Esterline-Angus current transformers set at a ratio of 40:1 were mounted in series with the ammeters. The product of the voltmeter and ammeter readings multiplied by the transformer setting was compared to a wattmeter reading and found to be equal. This showed that the load was essentially resistive and that the power factor was unity. Deductions for lead wire resistance were negligible in all cases.

**PROCEDURE** Before beginning an experimental run, the proper test section was installed and the column simulator was filled with Alhambra city water. We then turned on the required amount of electric power and waited for a steady state heat transfer condition. We defined steady state as a condition when the block thermocouple readings did not change with time. Usually, about one to two hours were required to achieve time-invariant operation.

The following data were recorded upon reaching steady state.

- 1 Voltmeter and ammeter readings
- 2 Block thermocouple readings
- 3 Ambient water temperature
- 4 Boundary layer temperatures as required

Data recording required from 30 minutes to over 2 hours depending on the experiment.



1" OD X .028" WALL 6-0' LG  
T-304 WD TUBE

FILL WITH SHOT  
TO GIVE PROPER  
BOUANCY

## HELIX ARC FUSED

430 SOLDIER

1.062"  $\phi$  CC  
THERMOCOUPLE

# BOUNDARY LAYER TEMPERATURE PROBE



## EXPERIMENTAL EQUIPMENT AND METHODS Continued

We found initially, while performing vertical flat plate experiments, that ambient water temperature varied significantly from the bottom to the top of the test section. This stratification made experimental data treatment cumbersome and destroyed the simulation of conditions in the deep ocean. However, we discovered that stratification could be eliminated by introducing a limited upward flow of fresh water (0.001 feet/second) by the test sections. Since this velocity was much smaller than the boundary layer velocities, the flow did not affect boundary layer momentum and heat transfer significantly.

**PRECISION AND ACCURACY OF MEASUREMENTS** Because we employed large test units, power consumption was known very accurately on a percentage basis. The estimated maximum error in power measurement was  $\pm 850$  Btu/hr for both the flat plate and cylindrical units. Thermocouples not located in the boundary layer were estimated to be accurate to  $\pm 0.2$  F. In the boundary layer, turbulence caused temperature fluctuations, which lowered the estimated accuracy to  $\pm 0.5$  F.

Heat losses from the flat-plate units were very small. According to the manufacturer, Foamglas has a thermal conductivity of 0.41 Btu/hr-ft<sup>2</sup>-F/in at 100 F and 0.485 Btu/hr-ft<sup>2</sup>-F/in at 225 F. Assuming that the copper block is never warmer than 225 F and the ambient water is never colder than 40 F, the maximum heat loss is 107.5 Btu/hr (0.0314 kw). This is only 0.124 percent of the total heat load. An order of magnitude was verified during the experimentation by readings of thermocouples attached to the Foamglas.

Another source of heat loss, namely conduction of heat through the supports and electric lead wires, was present in both flat-plate and cylindrical test units. We embedded thermocouples in the phenolic supports for the cylinders and taped thermocouples to the metal supports for the flat plates. In all cases, temperatures were essentially ambient. Thus, we concluded that this heat loss was not significant.

We estimated that heat transfer coefficients calculated from experimental data would have a maximum error range of +1.6 and -1.5 percent for the flat-plate runs. Because the cylinders were run at lower temperature differences, the error range in heat transfer coefficient was estimated at  $\pm 3.2$  percent.

## RESULTS AND DISCUSSION

**VERTICAL FLAT PLATE** Results of the vertical flat-plate tests conducted at twelve power levels are presented in Figure 46. This plot shows the relationship between the experimental Nusselt and Rayleigh numbers. Correlations of Saunders (97), Waibler (115), King (81), Eckert-Jackson (61), and Larson (84) are also indicated on the graph.

Notice that our experimental data follow Saunders' correlation almost exactly. This is truly remarkable, because Saunders developed the expression from experimental data covering only a little more than one order of magnitude of Rayleigh number. He did not experiment with Rayleigh numbers above  $4.6 \times 10^{10}$ . These additional data show that his correlation holds for water having Rayleigh numbers up to  $3.62 \times 10^{12}$ .

Waibler's correlation predicts Nusselt numbers about 70 percent higher than those obtained experimentally at low Rayleigh numbers. At Rayleigh numbers over  $10^{12}$ , Waibler's prediction is much closer. This discrepancy may be due to a "chimney effect" in Waibler's experiment, in which he had a vertical cold surface located 2.5 inches from the heated one.

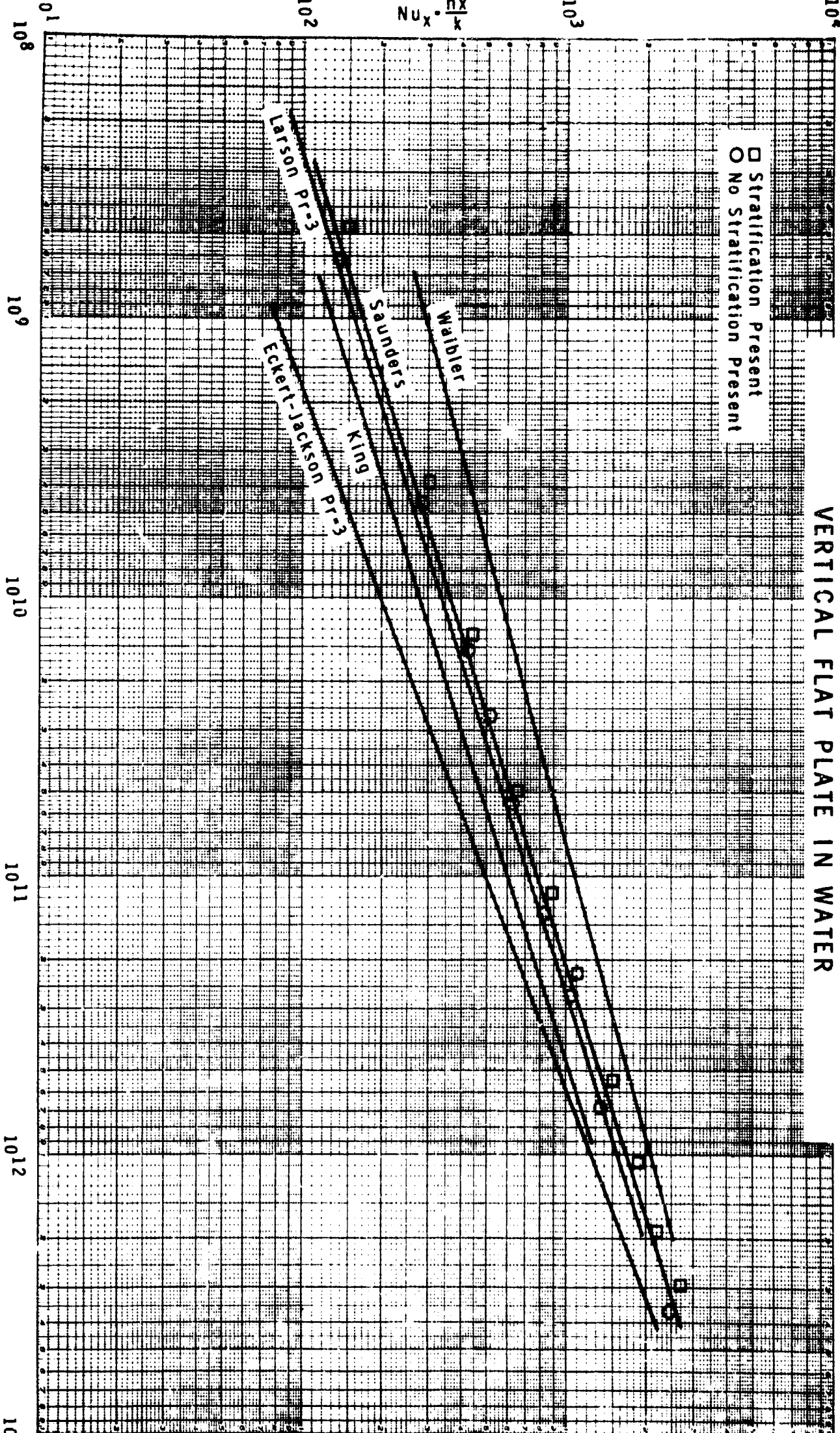
King's equation predicts 23.5 percent lower Nusselt numbers than the Saunders correlation. This expression, essentially a compromise of several natural convection relationships for different fluids, is recommended by McAdams (89) and Jakob (77) for general use. Air Nusselt numbers, which conform well with the Bayley (49) and Eckert-Jackson relationships, fall lower than the King equation prediction and water Nusselt numbers fall higher.

The semiempirical relationship of Larson (taking  $C_n = 3.5$ ) closely predicts the experimental data, while the Eckert-Jackson equation underpredicts considerably. This evidence and the reasons given in Chapter III indicate Larson's method is preferable to the Eckert-Jackson method.

Using the approach similar to Larson and Eckert-Jackson presented in Chapter III, we calculated boundary layer thicknesses from the experimental Nusselt numbers. We assumed that the deviation between Larson's prediction and Saunders' correlation was caused by an improper Blasius law constant in the boundary layer shear stress equation. Before calculating boundary layer thicknesses, we first determined  $C_n = 3.22$  from the experimental Nusselt-Rayleigh number relationship (Figure 46) and Equation III-41. Then boundary layer thicknesses were calculated by Equation III-42.

# NATURAL CONVECTION HEAT TRANSFER TEST RESULTS VERTICAL FLAT PLATE IN WATER

FIGURE 46



## RESULTS AND DISCUSSION Continued

We attempted to measure thermal boundary layer thickness as a function of vertical position by mapping the boundary layer temperatures. Measurements were taken in the outer portion of the boundary layer only. Figure 47 shows the correlated results as a dimensionless temperature ratio plotted against a dimensionless distance.

The temperature ratio  $\theta/\theta_w$  represents fractional temperature driving force in the boundary layer. It is unity at the heat transfer surface and should drop to zero at the outer edge of the boundary layer. The distance ratio  $y/\delta$ , the fractional boundary layer thickness, is zero at the heat transfer surface and increases to unity at the boundary layer thickness.

Experimental temperature ratio data points from all the turbulent vertical flat-plate runs are plotted in Figure 47. They appear to be well correlated by the dimensionless distance and temperature ratios. Boundary layer thickness was calculated from Equation III-42 using  $C_n = 3.22$ . Notice that slightly over 10 percent of the total temperature driving force is present at the predicted boundary layer thickness. At a distance of  $2y/\delta$  from the flat plate, about 6 percent of the total temperature driving force remains. Figure 47 demonstrates the arbitrary nature of the boundary layer concept.

Equation III-42, which was proposed by Van Dyke, is shown in Figure 47. Curves are drawn for dependent variables  $y/\delta$  and  $2y/\delta$ . The experimental data points do not follow this relationship.

**VERTICAL FINNED FLAT PLATES** Results of nine vertical finned flat plate experiments are presented in Table VIII and Figure 48. The flat-plate section was run at full power. Heat flux, based upon base surface area, varied from  $7.12 \times 10^4$  to  $7.34 \times 10^4$  Btu/hr-ft<sup>2</sup> during experimentation. Fin thicknesses and heights were predetermined by the fin analysis methods outlined in Chapter III. Experimentally measured boundary layer thicknesses guided selection of fin spacing.

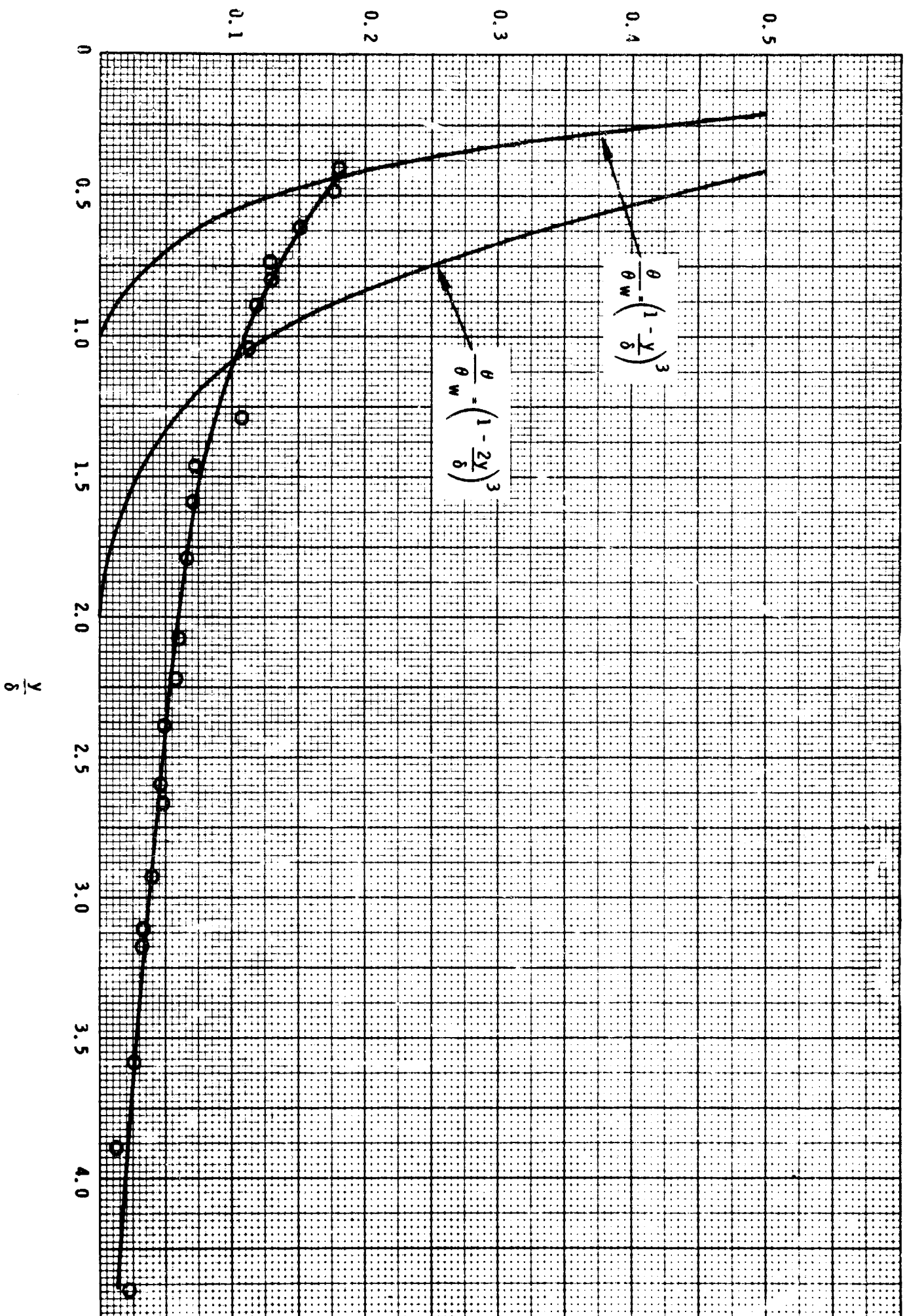
Fin thickness was fixed during the tests at 0.5 inches. It was a compromise between optimum values for the different spacings for 4-inch high fins. Since this height, theoretically, gave the highest heat transfer coefficients, heights of one and two inches were added to test this prediction.

Experimental results indicated that a 4-inch fin height with 1-inch spacing gave the highest coefficient. Figure 49 and Table VIII compare predicted and observed gross heat transfer coefficients. Equation III-57 yielded the predicted values.

JEC

# VERTICAL FLAT PLATE BOUNDARY LAYER TEMPERATURE PROFILE

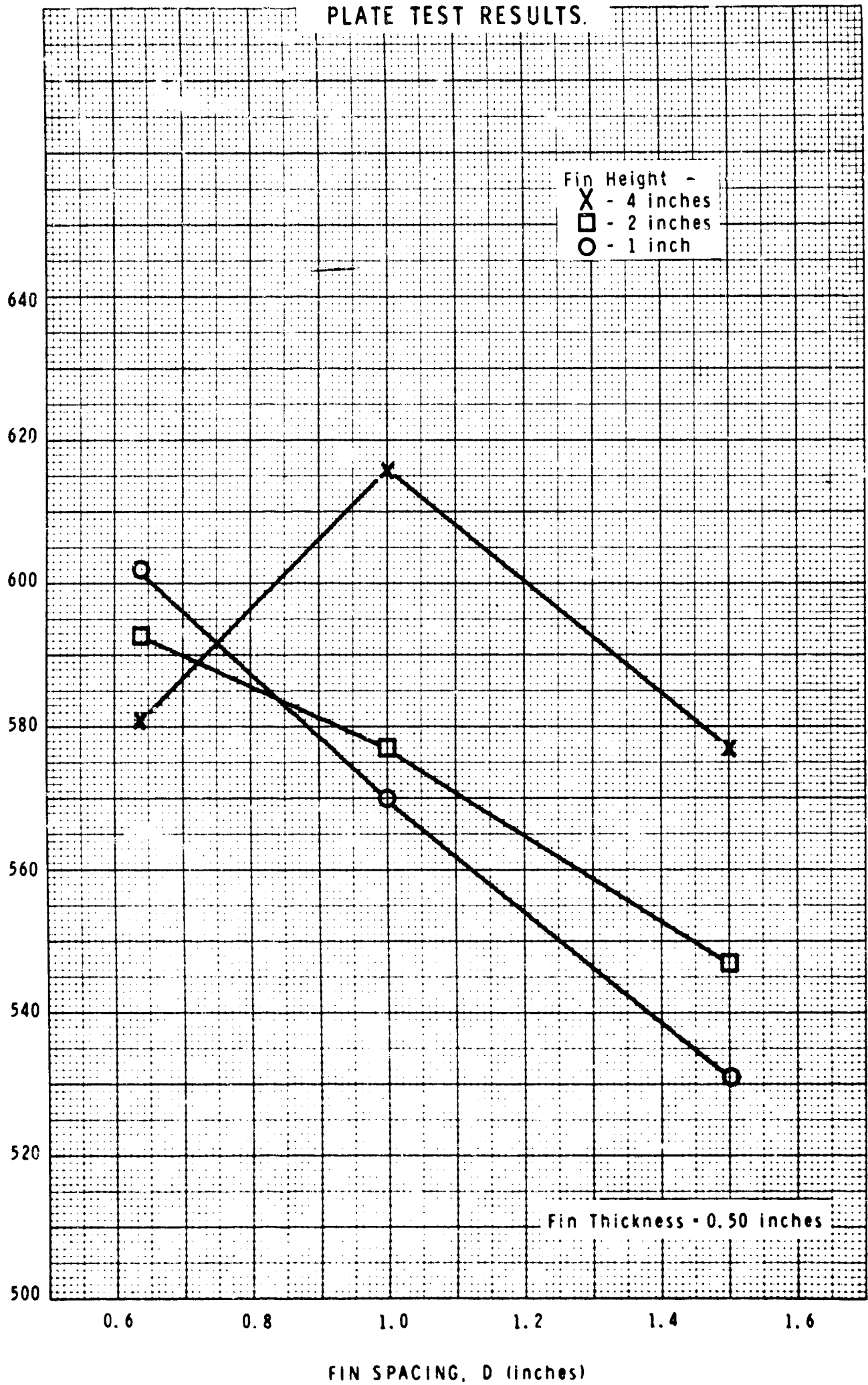
FIGURE 47



JEC

VERTICAL FINNED FLAT  
PLATE TEST RESULTS.

FIGURE 48

GROSS HEAT TRANSFER COEFFICIENT,  $h_g$  (Btu/hr-ft<sup>2</sup>-F)FIN SPACING,  $D$  (inches)

JEC

COMPARISON OF OBSERVED AND  
PREDICTED GROSS HEAT TRANSFER  
COEFFICIENTS - FINNED VERTICAL PLATES

FIGURE 49

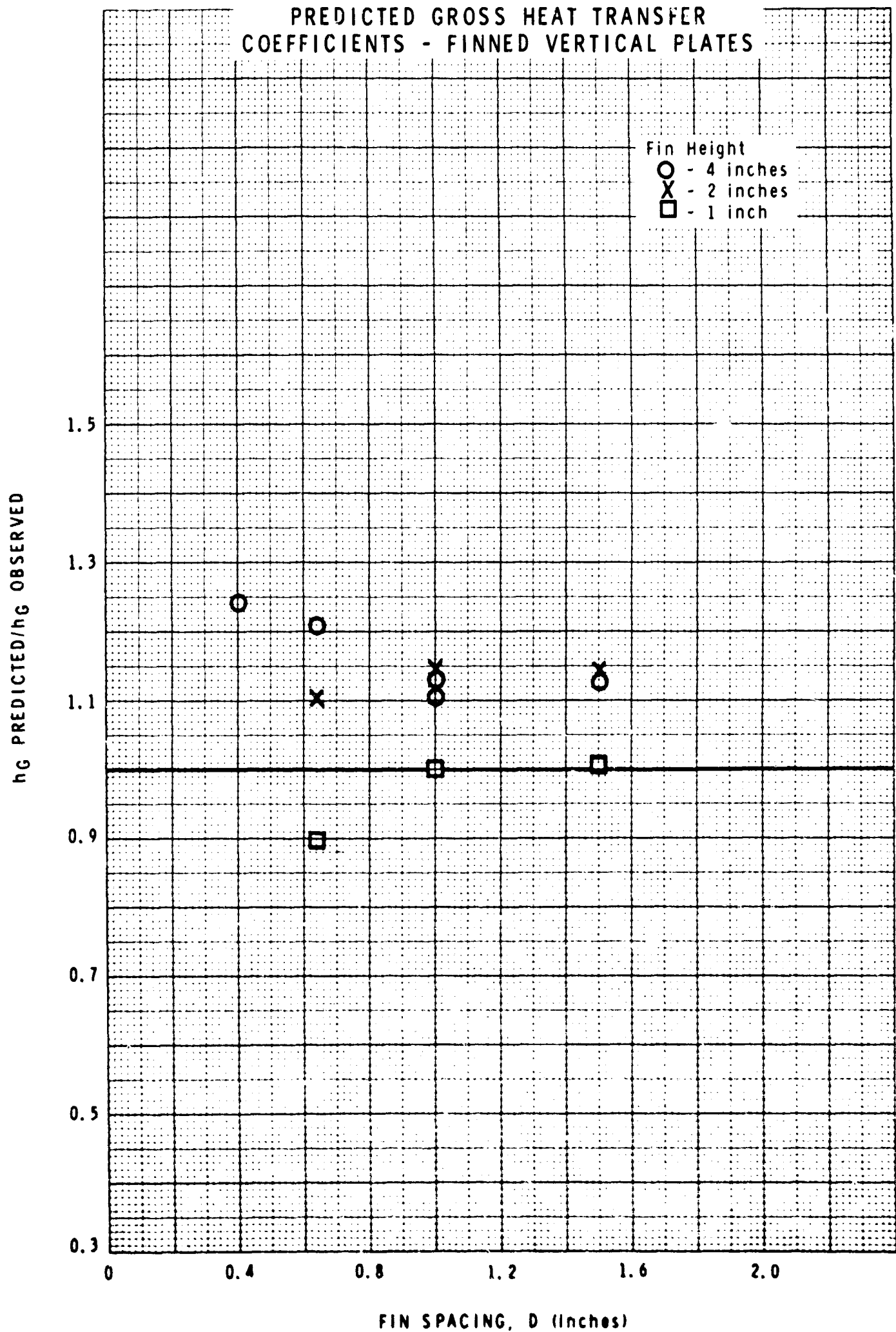




TABLE VIII

## VERTICAL FINNED FLAT PLATE RESULTS

Fin thickness = 0.5 inches

Base Surface Heat Flux =  $7.12$  to  $7.34 \times 10^4$  Btu/hr-ft<sup>2</sup>

<u>FIN SPACING INCHES</u>	<u>FIN HEIGHT INCHES</u>	<u>OPTIMUM FIN THICKNESS INCHES</u>	<u><math>h_G</math> OBSERVED BTU/HR-FT<sup>2</sup>-F</u>	<u><math>h_G</math> PREDICTED BTU/HR-FT<sup>2</sup>-F</u>	<u>PERCENT DIFFERENCE</u>
0.64 three fins	4	0.40	581	701	20.7
	2	0.28	593	663	10.6
	1	0.16	602	541	-10.1
1.00 three fins	4	0.53	616	682	10.7
	2	0.35	577	678	14.9
	1	0.18	570	571	0.2
1.50 three fins	4	0.64	577	650	12.6
	2	0.40	547	626	14.4
	1	0.20	531	533	0.4
0.40 four fins	4	0.28	658	816	24.0
1.00 four fins	4	0.53	639	720	12.7



## RESULTS AND DISCUSSION Continued

Because the same base surface width was used throughout the tests, it was distributed differently at small fin spacings than at large spacings. This effect causes lower gross coefficients as fin spacing narrows, and was accounted for in gross coefficient prediction.

We performed two additional experiments with four 4-inch high fins spaced at 0.40 inches and 1.00 inches. Deviations between predicted and observed values of  $h_g$  followed the same pattern with these tests as with the experiments employing three fins. The gross heat transfer coefficient for a spacing of 0.40 inch was higher than that for a spacing of 1.00 inch.

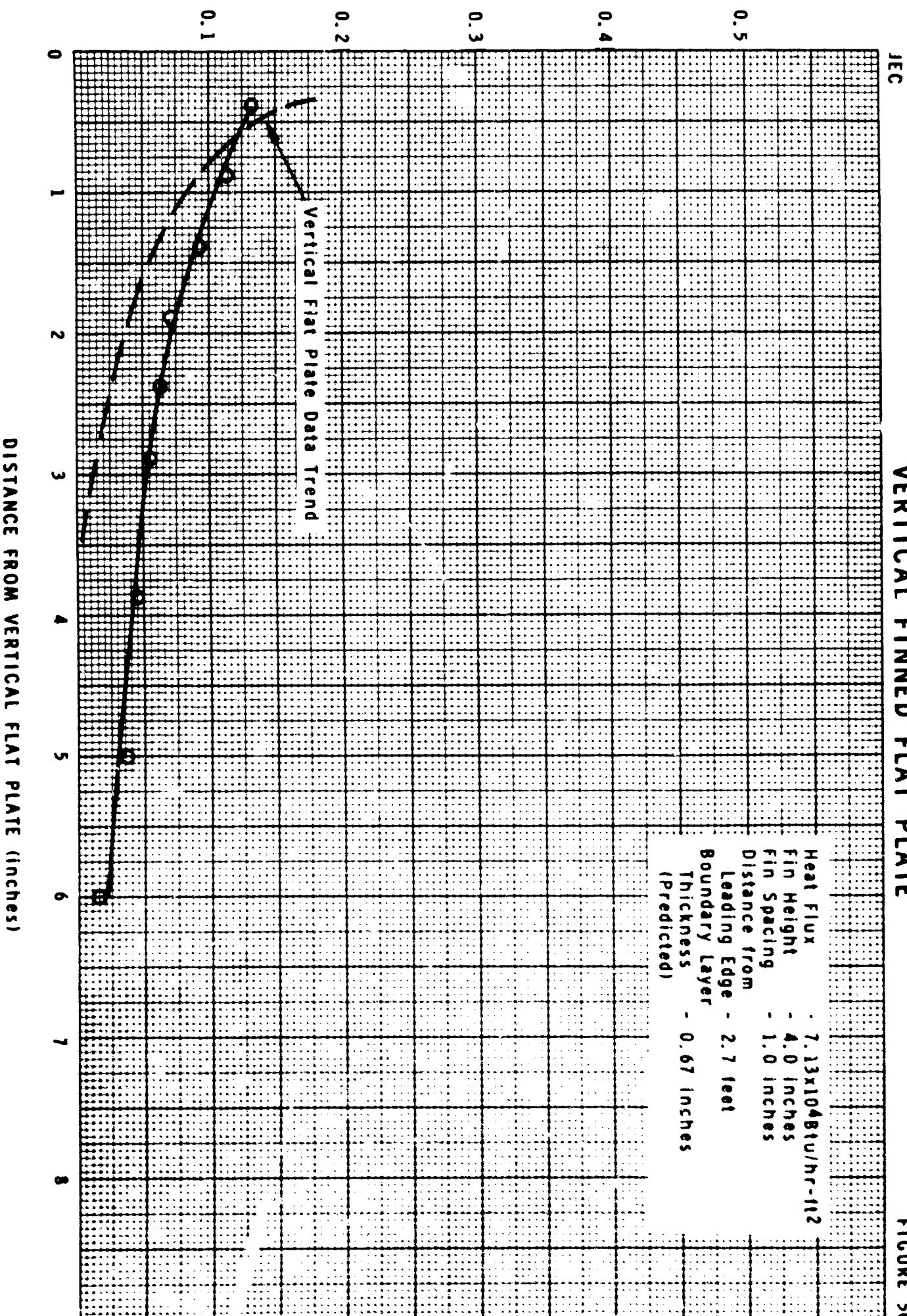
Agreement between predicted and observed gross heat transfer coefficients was quite good considering that a rather simplified model was used for the prediction. In all but one run (1-inch height, 0.64-inch spacing), the predicted  $h_g$  was higher than the observed. Deviations appeared to be a function of both fin height and fin spacing. Gross heat transfer coefficients for 1-inch fins were very closely predicted. At wider fin spacings, predicted  $h_g$ 's were from 10 to 15 percent higher than those observed for 2-inch and 4-inch fins. The deviation rose to 24 percent for 4-inch fins at 0.40-inch spacing.

Temperatures in the centers of the channels between the fins were sometimes much higher than ambient. High channel center temperatures were closely associated with large deviations between experimental and predicted gross heat transfer coefficients. Figure 50 depicts a typical channel center temperature profile. The model proposed in Chapter III does not take into account temperature variations such as these. Higher temperatures in the channel reduce the effective heat transfer driving force, and thus reduce the gross coefficient.

We suspect that by taking into account the higher channel temperatures in the model, one would be able to reduce the deviation between predicted and observed gross heat transfer coefficients.

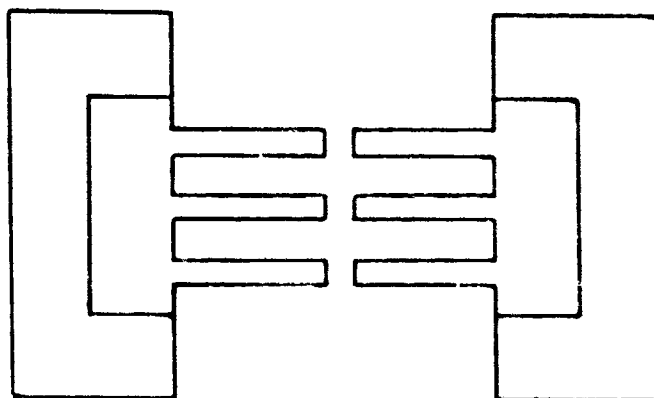
# CHANNEL TEMPERATURE PROFILE FOR VERTICAL FINNED FLAT PLATE

FIGURE 50



## RESULTS AND DISCUSSION Continued

Figure 51 shows the effect of spacing between vertical finned flat plate heat transfer surfaces on gross heat transfer coefficient. The graph indicates that spacings between fin tips in the range 0.5 and 5.0 inches have little effect on  $h_G$ . There is an apparent maximum at a spacing of 3.0 inches. However, the difference between this value of  $h_G$  and the one at a spacing of 0.5 inches is only 3.4 percent - about twice the estimated experimental error. The units were placed as shown in the sketch below.



Chimney tests were performed by blocking the sides of the flat-plate unit with two plywood boards. Figure 52 is a plot of the gross heat transfer coefficient versus distance of the plywood board chimney from the unit. Notice that placing the chimney close to the unit severely reduced the gross heat transfer coefficient. These results indicate that entrainment of water from the sides of the unit is considerable.

Figure 53 graphically presents the inlet clearance test results. According to experimental data, the gross heat transfer coefficient was not affected by placing the inlet clearance baffle against the leading edge of the test unit. At a distance of 1.0 inch below the leading edge,  $h_G$  reached a maximum and then decreased as the baffle was lowered more. These results seemed puzzling. One would expect  $h_G$  to steadily decrease as the clearance baffle was positioned closer to the leading edge. We checked our experimental technique and repeated three of the runs, with the same results. These data seem to further point out the importance of entrainment from the side.

To check the importance of side entrainment, we performed a run with the chimney positioned 2.63 inches from the sides of the unit and the inlet clearance baffle 1.0 inch below the leading edge. The average gross coefficient dropped from 617 Btu/hr-ft<sup>2</sup>-F to 583 Btu/hr-ft<sup>2</sup>-F, a decrease of 5.8 percent. This indicates that reducing the inlet clearance does have some effect if side flow is restricted, as would be the case if the unit were wider.

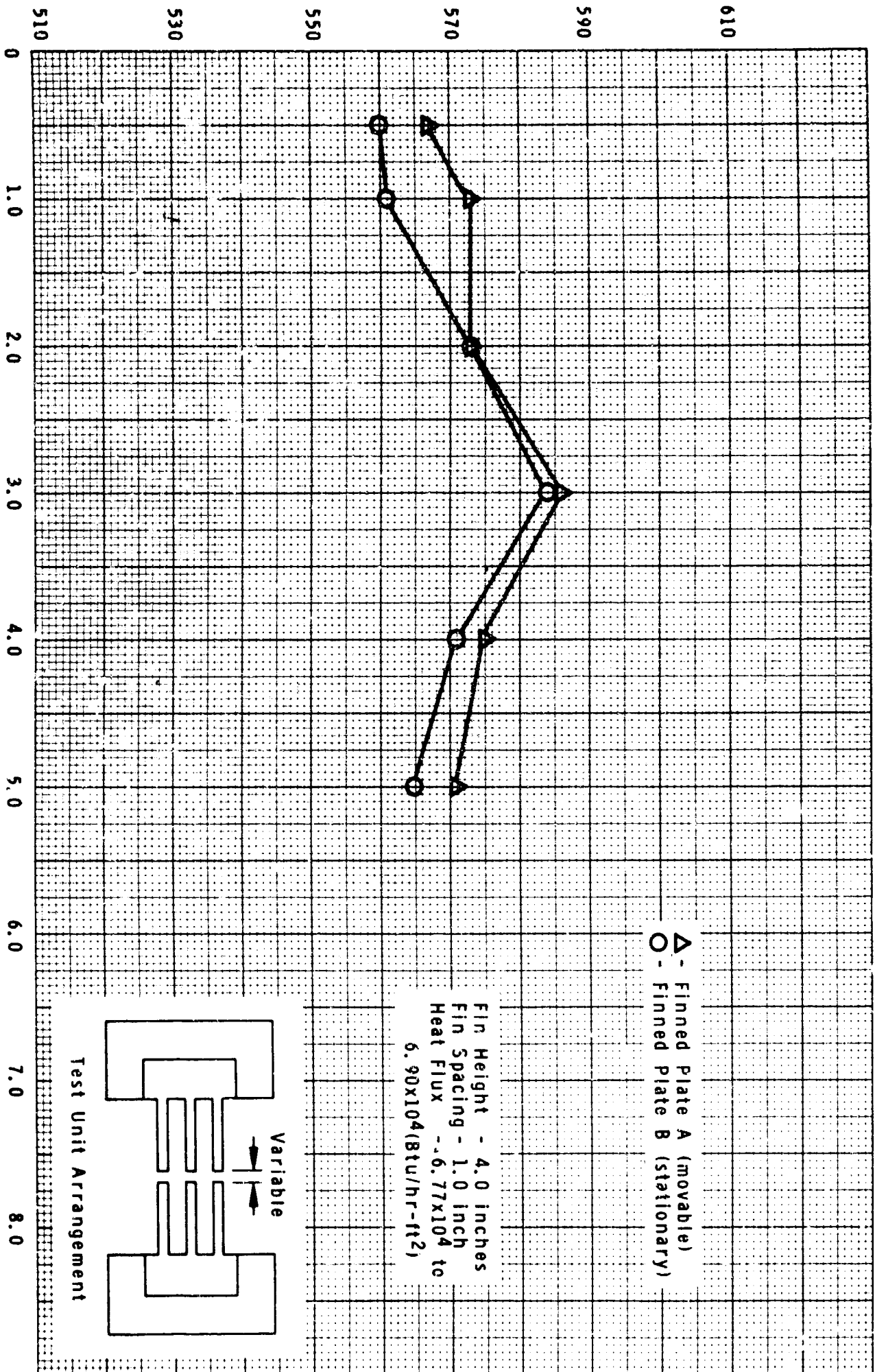
GROSS HEAT TRANSFER COEFFICIENT,  $h_g$  (Btu/hr-ft<sup>2</sup>-F)

JEC

EFFECT OF SPACING BETWEEN TWO  
VERTICAL FINNED FLAT PLATES ON  $h_g$

FIGURE 51

SPACING BETWEEN FIN TIPS (inches)

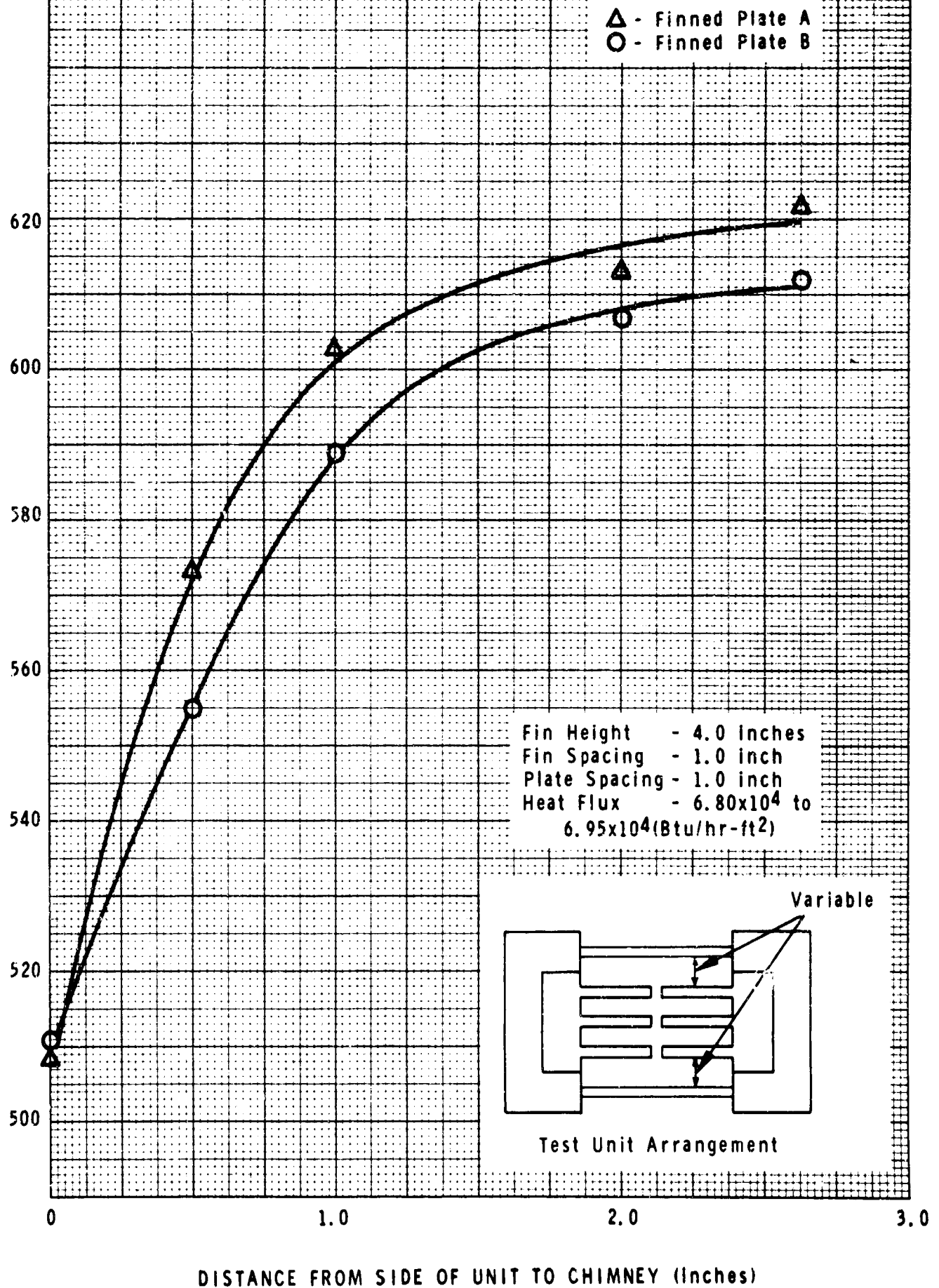


JEC

## CHIMNEY TEST RESULTS

FIGURE 52

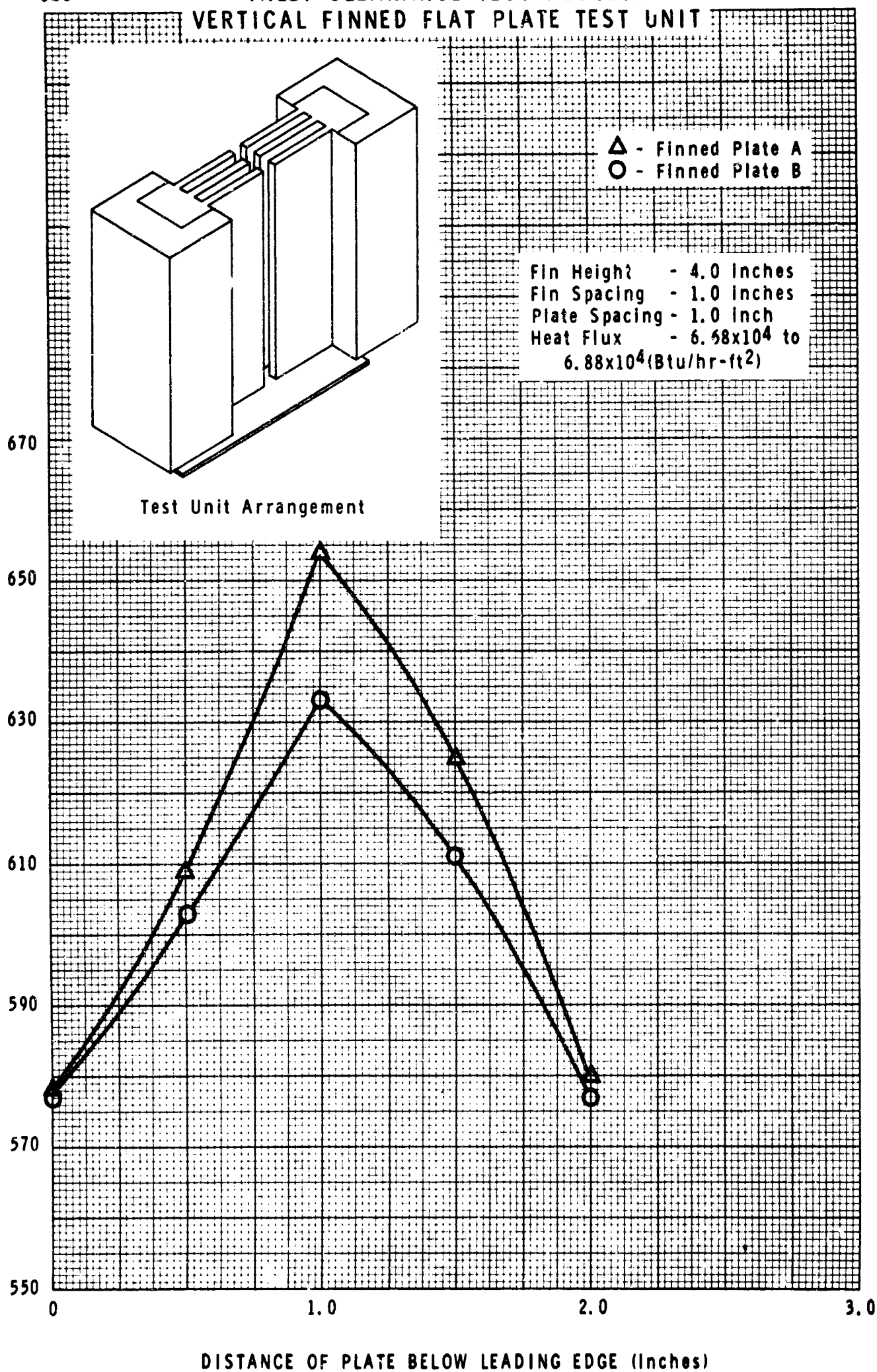
## VERTICAL FINNED FLAT PLATE TEST UNIT

GROSS HEAT TRANSFER COEFFICIENT,  $h_g(\text{Btu/hr-ft}^2\text{-F})$ 

JEC

INLET CLEARANCE TEST RESULTS  
VERTICAL FINNED FLAT PLATE TEST UNIT

FIGURE 53

GROSS HEAT TRANSFER COEFFICIENT,  $h_g$  (Btu/hr-ft<sup>2</sup>-F)

## RESULTS AND DISCUSSION Continued

We placed the inlet clearance baffle directly above the unit to determine the effect of an outlet restriction on the gross heat transfer coefficient. There was no discernible effect.

Flow restriction experiments pointed out a substantial effect of side flow into the unit. The contribution of side flow to these data must be recognized when extrapolating these results to a wider unit where large entrainment from the sides is not possible.

**VERTICAL CYLINDERS** Figure 54 shows the results of natural convection experiments with a 2-inch diameter cylinder, 4 feet long, at five heat fluxes. Saunders' equation is shown as a dotted line. Notice that, at high-heat fluxes the experimental points fall above Saunders' equation but fall lower at low-heat fluxes. However, the  $1/3$  power Nusselt-Rayleigh number relationship seems to hold for all heat fluxes except perhaps the lowest.

Generally, the same behavior was exhibited by the 1-inch diameter cylinder turbulent natural convection data, which are presented in Figure 55. A significant heat flux effect took place over the 11-fold experimental heat flux range.

Taking the liberty of drawing lines of slope 1:3 through data points of equal heat flux and cross-plotting the smoothed Nusselt numbers versus heat flux, led to Figure 56. It shows the effect of heat flux on the ratio  $\frac{Nu_x \text{ (cylinder)}}{Nu_x \text{ (flat plate)}}$ . Smooth curves can be drawn through the points for each cylinder. The 1-inch cylinder gives slightly lower Nusselt number ratios than does the 2-inch cylinder.

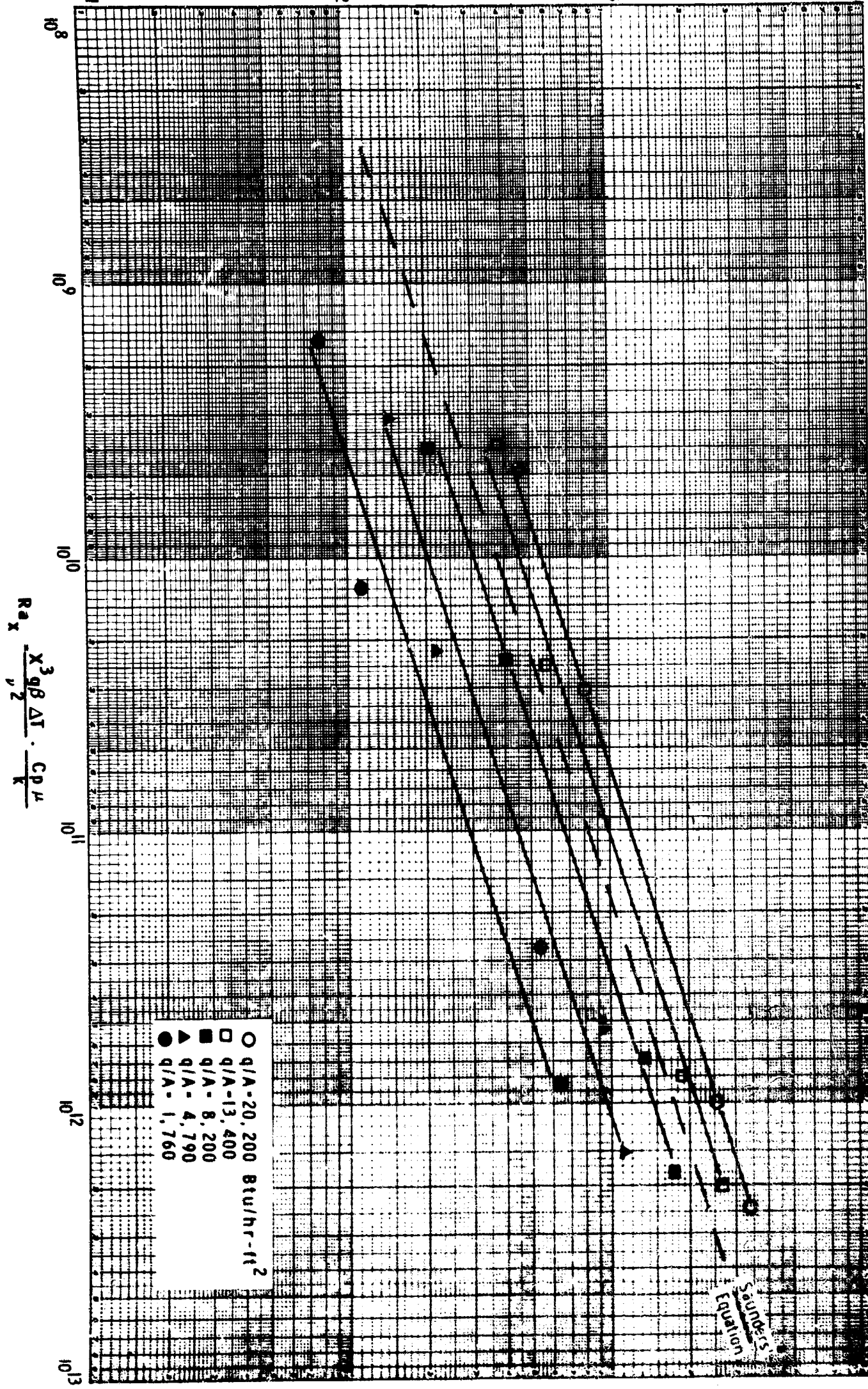
We have included in Figure 56 the data of Touloukian (112), who experimented with a 2.75-inch OD cylinder over a heat flux range of 625 to 1,880 Btu/hr-ft<sup>2</sup>. His data appear to conform to the same pattern.

Behavior of the data with respect to heat flux was somewhat puzzling. Jakobs prediction (78) for forced convection indicates that cylinder Nusselt numbers exceed those of a flat plate by a percentage amount of  $30 \delta/r$ . Boundary layer thickness for a given geometry varies directly with heat flux. Thus, at high-heat fluxes cylinder Nusselt numbers should exceed those for a flat plate, with the difference decreasing as  $q/A$  is lowered. Experimental data at high-heat fluxes follow this behavior. But at lower fluxes, experimental Nusselt numbers are lower than the corresponding flat plate values. Cylinder diameter did not have a great effect in the range studied.



# VERTICAL 1-INCH DIAMETER CYLINDER TEST RESULTS

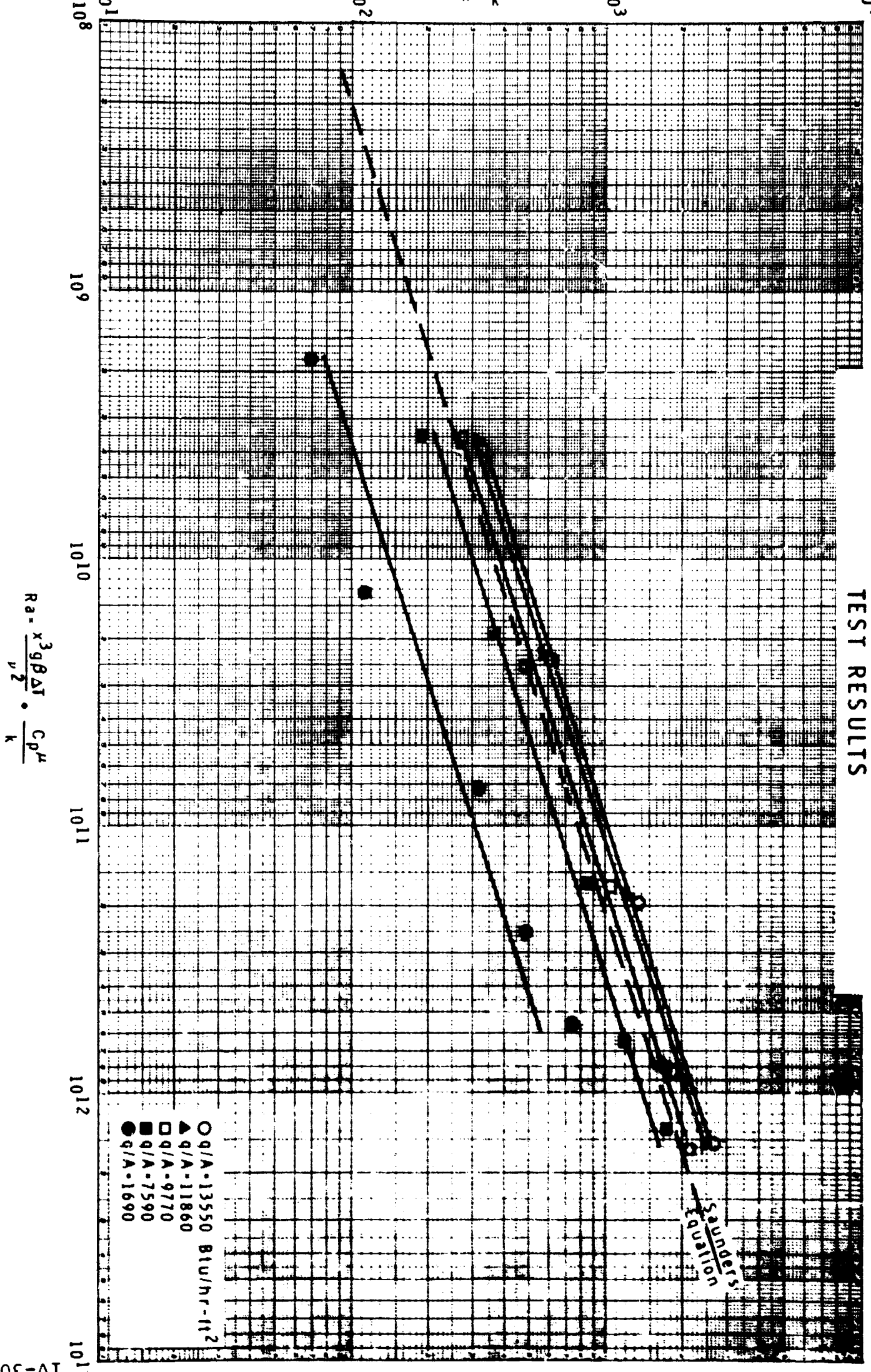
FIGURE 55





# VERTICAL 2-INCH DIAMETER CYLINDER TEST RESULTS

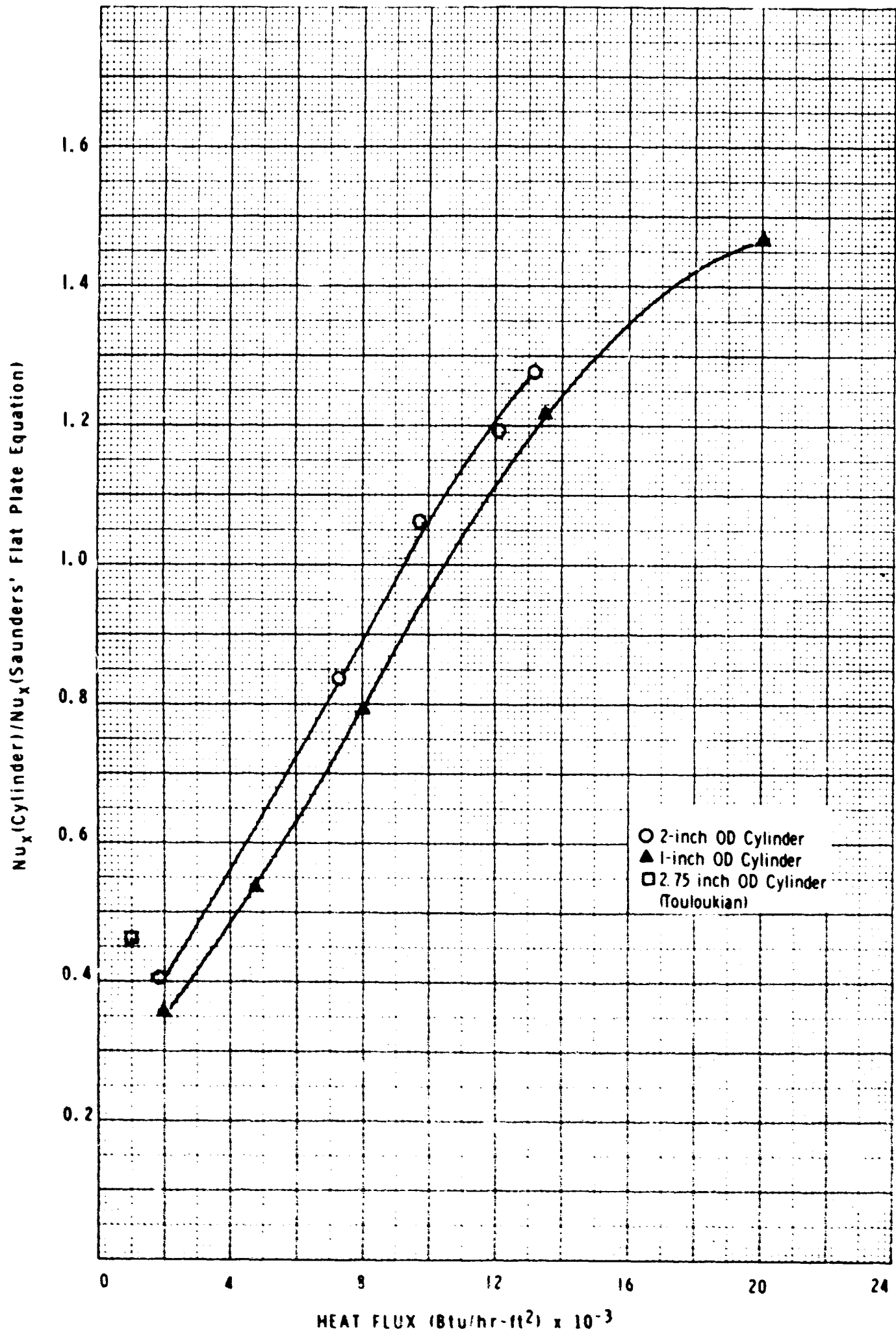
FIGURE 54



EFFECT OF HEAT FLUX ON NUSSELT  
NUMBER - VERTICAL CYLINDER

JEC

FIGURE 56



## RESULTS AND DISCUSSION Continued

A possible explanation for this behavior may be a delayed laminar-turbulent transition at the lower heat fluxes. It is well known that the laminar-turbulent transition may take place over a considerable range of Reynolds numbers in forced convection flow. This behavior may be evidence of the same phenomenon in natural convection. On the other hand, the flat-plate data did not exhibit this trend. However, the minimum heat flux was 10,800 Btu/hr-ft<sup>2</sup>, 6.4 times larger than the minimum 2-inch diameter cylinder heat flux. Additional experimental data, preferably with more than one fluid, are necessary to clarify this behavior.

Saunders' flat-plate equation and Figure 56 may be used to predict heat transfer coefficients for the cylinders. This procedure should be employed only within the experimental data heat flux and cylinder diameter range.

**VERTICAL FINNED CYLINDERS** With the 2-inch OD cylinders, experimental gross heat transfer coefficient data were obtained for three fin heights (1.0, 1.88, and 4.0 inches) and three circumferential fin spacings (0.285, 1.07, and 2.60 inches) at a constant fin thickness of 0.50 inches. Data were collected at three levels of heat flux for each height-spacing combination. There was a total of 27 experiments. Complete results are presented in Table IX. Experimental data for the highest heat flux only are displayed graphically in Figure 57. Gross heat transfer coefficient varied directly with fin height and heat flux, and varied inversely with fin spacing.

Table IX also presents predicted values of  $h_G$  by Equation III-56. In the equation,  $h_0$  was given by Saunders' equation - for curved surfaces, it was corrected by Figure 56. Percent difference between predicted and observed gross heat transfer coefficients ranged from 22.0 to 102.0 percent. In general, predicted and observed values of  $h_G$  agreed more closely at higher heat fluxes than at lower ones.

Since deviations between predicted and observed gross heat transfer coefficients do not strongly depend upon fin spacing, high-channel temperatures cannot explain the discrepancy. It seems likely that the primary cause of the discrepancy is a nonuniform base surface temperature. If the temperature of the base metal was lower in the vicinity of the fins, heat dissipation of the fins would be greatly reduced.

A fin spacing of 0.285 inches and a fin height of 1.88 inches was chosen as the best combination for the 2-inch diameter cylindrical unit. A 4-inch fin height would give a larger value of  $h_G$ . However, the cylinders could not be closely placed into a compact configuration.

TABLE IX

## VERTICAL FINNED 2-INCH DIAMETER CYLINDER RESULTS

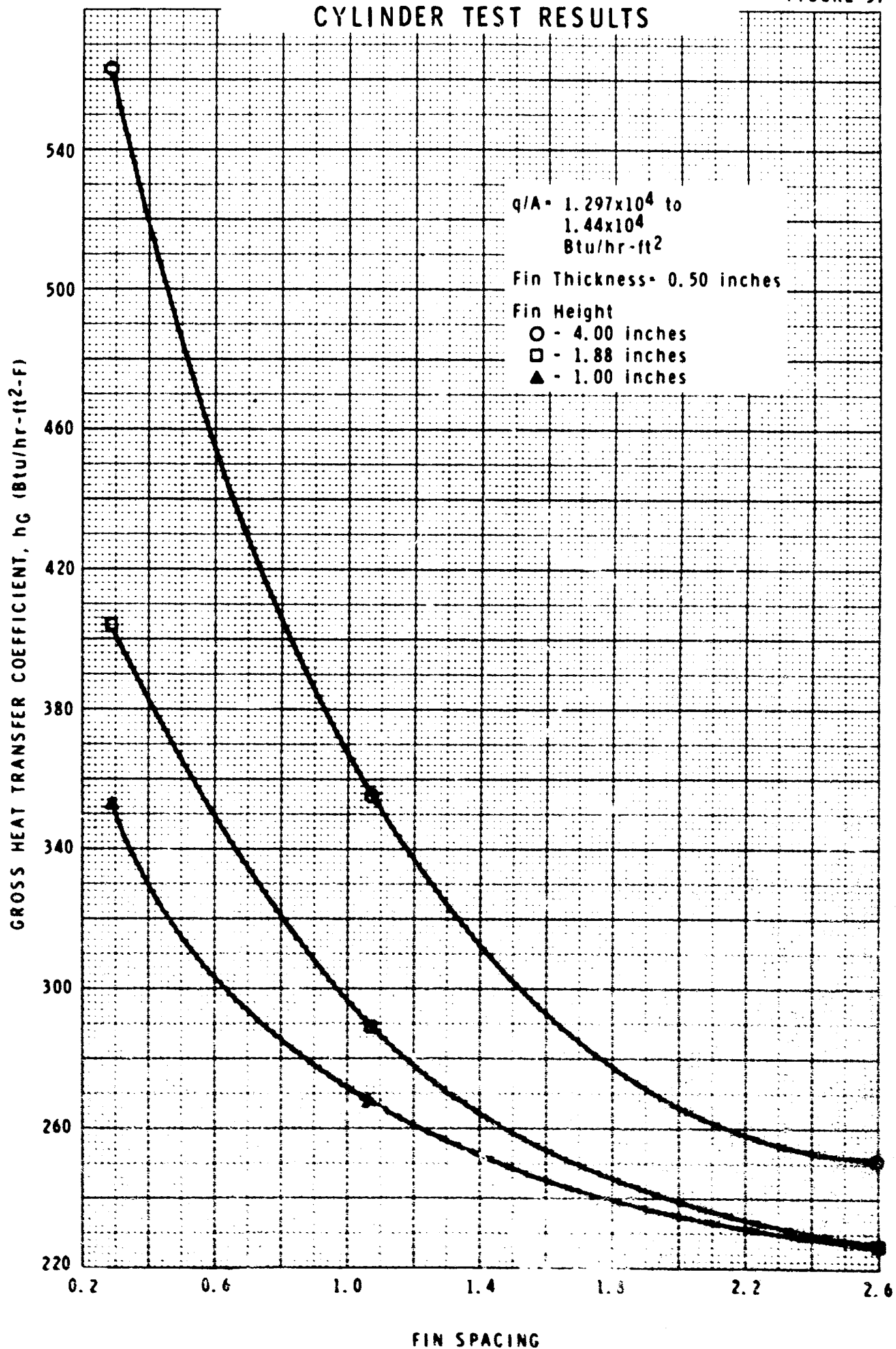
Fin thickness = 0.5 inches

<u>FIN SPACING INCHES</u>	<u>FIN HEIGHT INCHES</u>	<u>HEAT FLUX BTU/HR-FT<sup>2</sup></u>	<u>h<sub>G</sub> OBSERVED BTU/HR-FT<sup>2</sup>-F</u>	<u>h<sub>G</sub> PREDICTED BTU/HR-FT<sup>2</sup>-F</u>	<u>PERCENT DIFFERENCE</u>
0.285	4.00	13,200	563	687	22.0
		7,630	435	617	41.8
		4,020	287	568	98.0
1.07		13,700	355	488	37.5
		8,090	259	426	64.5
		4,230	190	360	89.5
2.64		14,100	251	409	63.0
		8,040	183	262	43.0
		4,150	140	234	67.2
0.285	1.88	13,600	404	618	53.0
		7,860	305	535	75.0
		4,150	235	325	91.5
1.07		13,700	289	472	63.0
		7,890	215	372	73.0
		4,200	152	310	104.0
2.64		13,000	227	378	66.6
		7,530	164	273	66.5
		4,120	116	218	88.0
0.285	1.00	13,600	353	484	37.1
		7,920	254	407	60.2
		5,000	176	350	99.0
1.07		13,600	267	382	43.1
		8,070	210	296	41.0
		4,100	136	233	71.4
2.64		13,600	227	341	50.2
		8,070	164	250	52.4
		4,050	112	170	51.0

JEC

VERTICAL FINNED 2-INCH DIAMETER  
CYLINDER TEST RESULTS

FIGURE 57



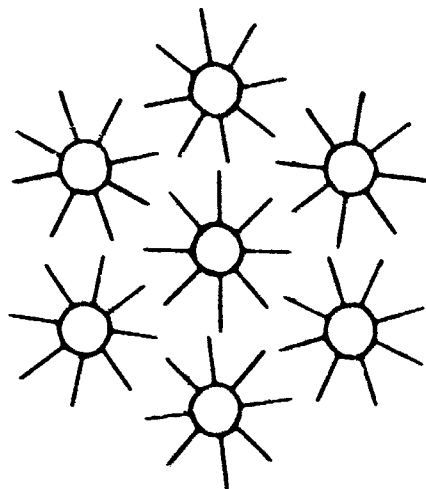
## RESULTS AND DISCUSSION Continued

Experimental gross heat transfer coefficient data were obtained for one finned, 1-inch diameter cylinder. Fin thickness was 0.5 inches, spacing was 0.285 inches, and fin height was 1.88 inches.

<u>HEAT FLUX<sub>2</sub></u> <u>BTU/HR-FT<sup>2</sup></u>	<u><math>h_G</math></u> <u>OBSERVED</u> <u>BTU/HR-FT<sup>2</sup>-F</u>	<u><math>h_G</math></u> <u>PREDICTED</u> <u>BTU/HR-FT<sup>2</sup>-F</u>	<u>PERCENT</u> <u>DIFFERENCE</u>
19,000	586	599	2.2
13,500	491	571	16.3
7,890	389	470	20.8
4,140	257	443	72.4

The difference between predicted and observed gross heat transfer coefficients appeared to follow the same pattern as with the 2-inch diameter cylinders. However, at high-heat fluxes, agreement between predicted and experimental  $h_G$  was much closer.

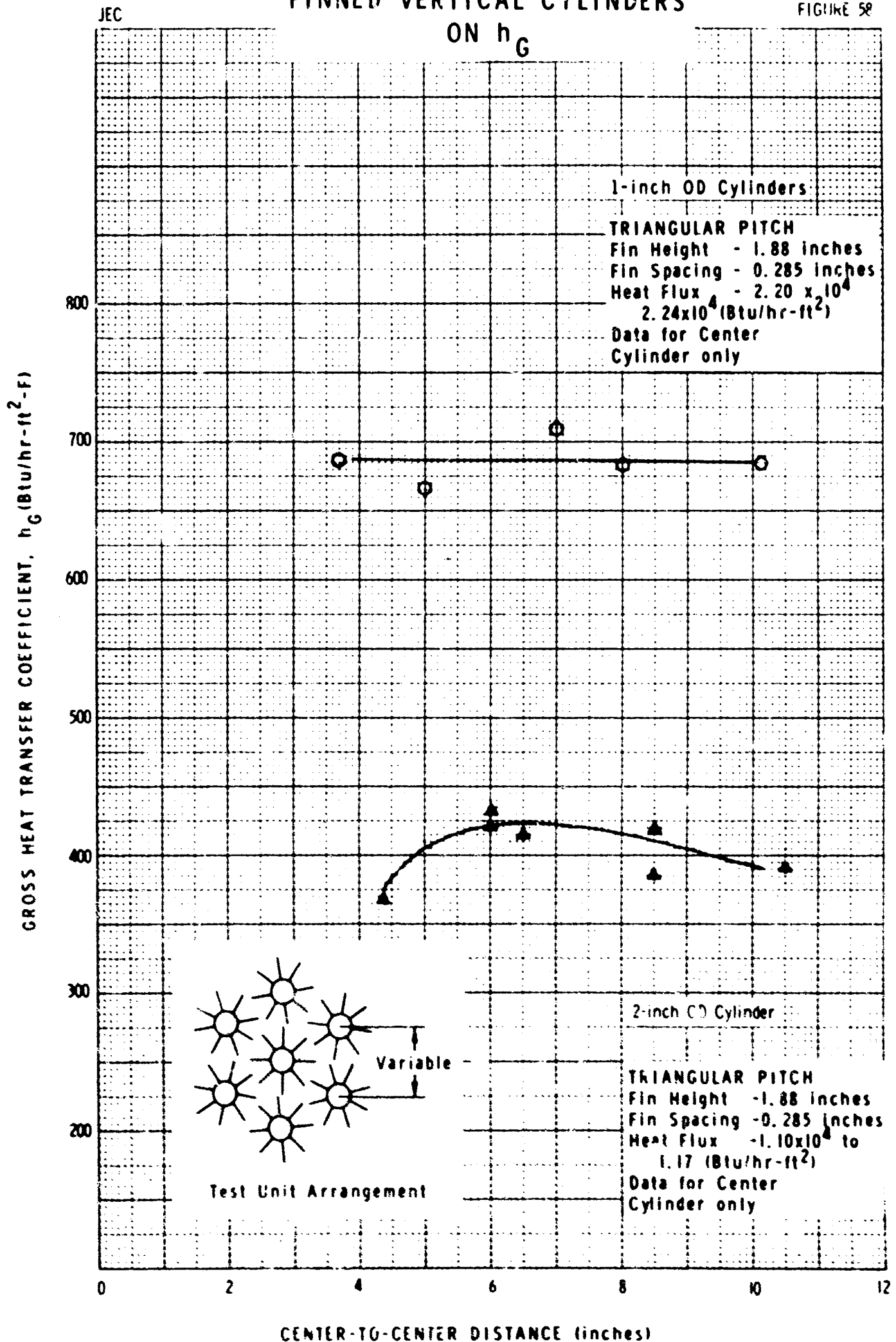
Figure 58 shows the effect of spacing between seven finned, 2-inch diameter vertical cylinders on the gross heat transfer coefficient. Varying center-to-center distances from 4.4 inches (the closest possible packing) to 10.5 inches had very little effect upon  $h_G$ . The optimum center-to-center distance appeared to be 6.0 inches. Cylinders were spaced as shown in the sketch below.



Effect of spacing between seven finned, 1-inch diameter vertical cylinders on the gross heat transfer coefficient is also shown on Figure 58. Center-to-center spacings, varying from 3.75 inches to 10.125 inches had virtually no effect upon  $h_G$ .

EFFECT OF SPACING BETWEEN  
FINNED VERTICAL CYLINDERS

FIGURE 58



## RESULTS AND DISCUSSION Continued

Chimney test results for the 2-inch OD cylinder unit are graphed in Figure 59. The effect of side clearance on  $h_G$  was very small. Placing the chimney against the side of the unit reduced  $h_G$  14 percent below the value obtained when the chimney was 3.0 inches away. The chimney did not appear to enhance the heat transfer coefficient significantly in the distance range investigated.

Figure 60 presents inlet clearance test results for the vertical 2-inch diameter finned cylinder test unit. Obstructing the inlet flow appeared to enhance  $h_G$  as was the case with the flat-plate unit. However, the total variation in  $h_G$  with distance below the leading edge was small (12 to 13 percent).

When we performed a run with the chimney positioned 1.5 inches from the outer edge of the fins and the inlet clearance baffle against the leading edges of the cylinders,  $h_G$  dropped 5.6 percent. Lowering the baffle 0.5 inches reduced the gross coefficient 3.7 percent. This indicates that diminishing inlet clearance lowers the gross heat transfer coefficient if the side flow is restricted. However, this effect was less with the cylindrical than with the flat-plate unit.

COMBINED FORCED AND FREE CONVECTION Both the finned flat-plate and 2-inch diameter cylinder units were subjected to horizontal currents normal to the natural convection flow direction. Figure 61 presents the experimental gross heat transfer coefficients as a function of current magnitude and orientation angle of the finned flat-plate unit. Current velocity was based upon the cross-sectional area of a 10.5 ft<sup>2</sup> channel built around each of the units.



JEC

# CHIMNEY TEST RESULTS VERTICAL 2-INCH DIAMETER FINNED CYLINDER TEST UNIT

FIGURE 59

GROSS HEAT TRANSFER COEFFICIENT,  $h_G$  (Btu/hr-ft<sup>2</sup>-F)**TRIANGULAR PITCH**

Fin Height - 1.88 inches

Fin Spacing - 0.285 inches

Heat Flux -  $1.10 \times 10^4$  to  
 $1.12 \times 10^4$  (Btu/hr-ft<sup>2</sup>)

Cylinder Spacing - 6.0"

Center-to-center

Data for Center

Cylinder only

600

500

400

300

200

100

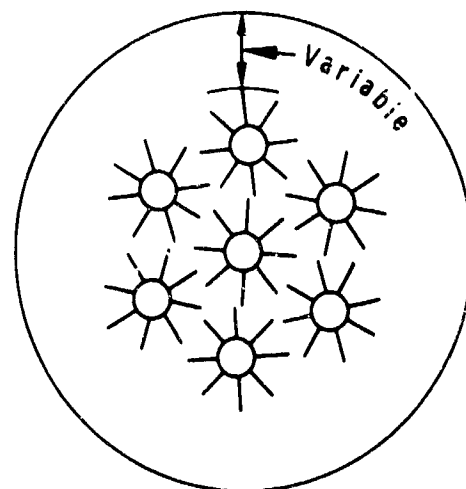
0

1.0

2.0

3.0

DISTANCE FROM SIDE OF UNIT TO CHIMNEY (Inches)



Test Unit Arrangement

JEC

# INLET CLEARANCE TEST RESULTS VERTICAL 2-INCH DIAMETER FINNED CYLINDER TEST UNIT

FIGURE 60

GROSS HEAT TRANSFER COEFFICIENT,  $h_G$  (Btu/hr-ft<sup>2</sup>-F)

## TRIANGULAR PITCH

Fin Height - 1.88 inches  
Fin Spacing - 0.285 inches  
Heat Flux -  $1.10 \times 10^4$  to  
 $1.19 \times 10^4$  (Btu/hr-ft<sup>2</sup>)  
Cylinder Spacing - 6.0"  
Center-to-center  
Data for Center  
Cylinder only

600

500

400

300

200

100

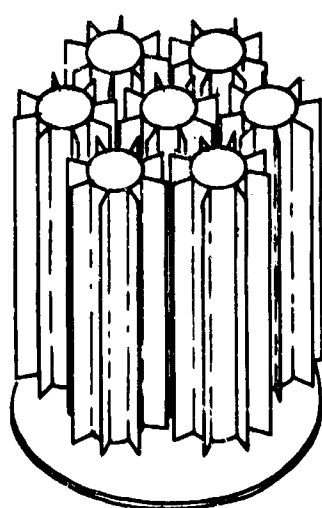
0

1.0

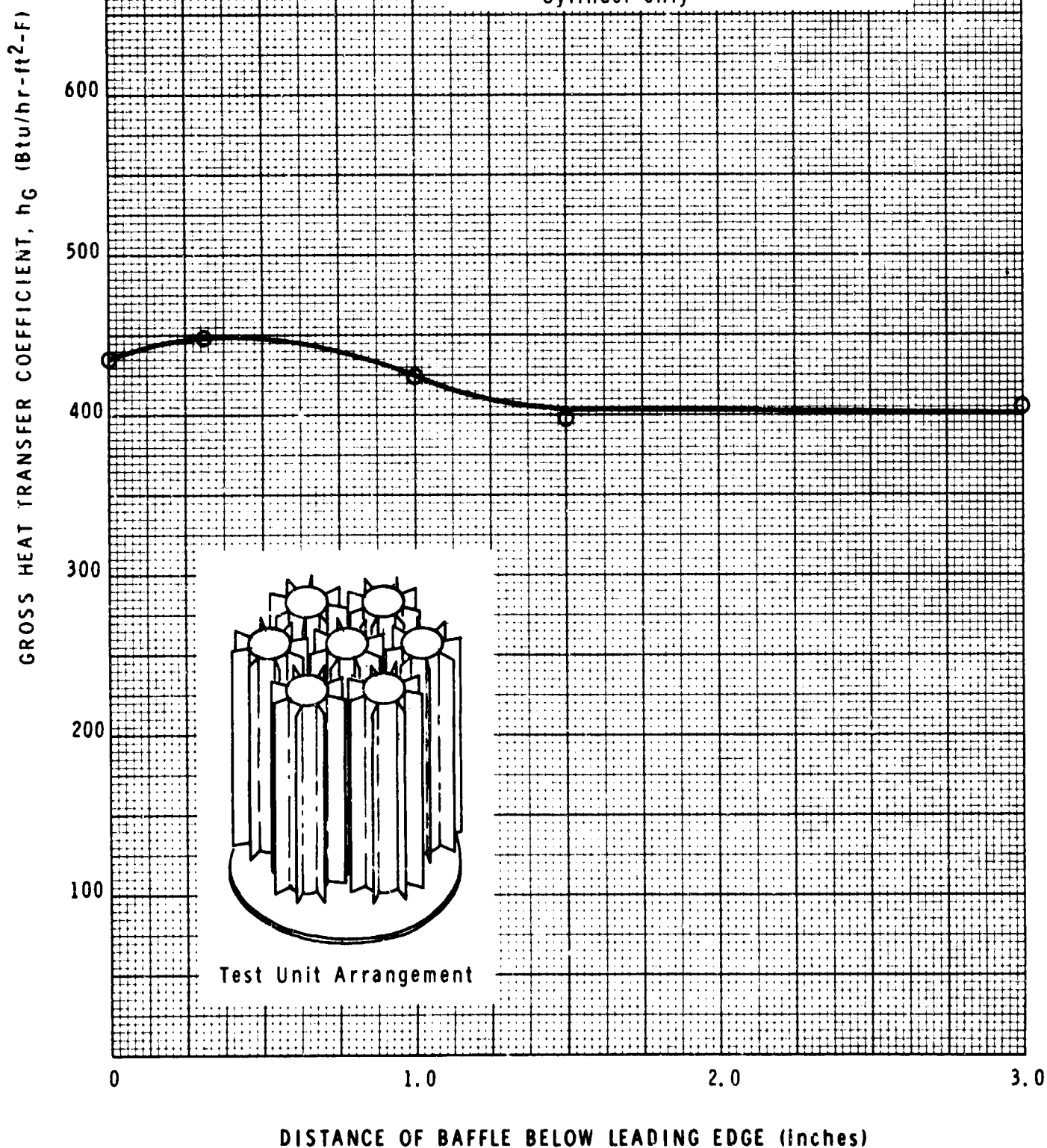
2.0

3.0

DISTANCE OF BAFFLE BELOW LEADING EDGE (inches)

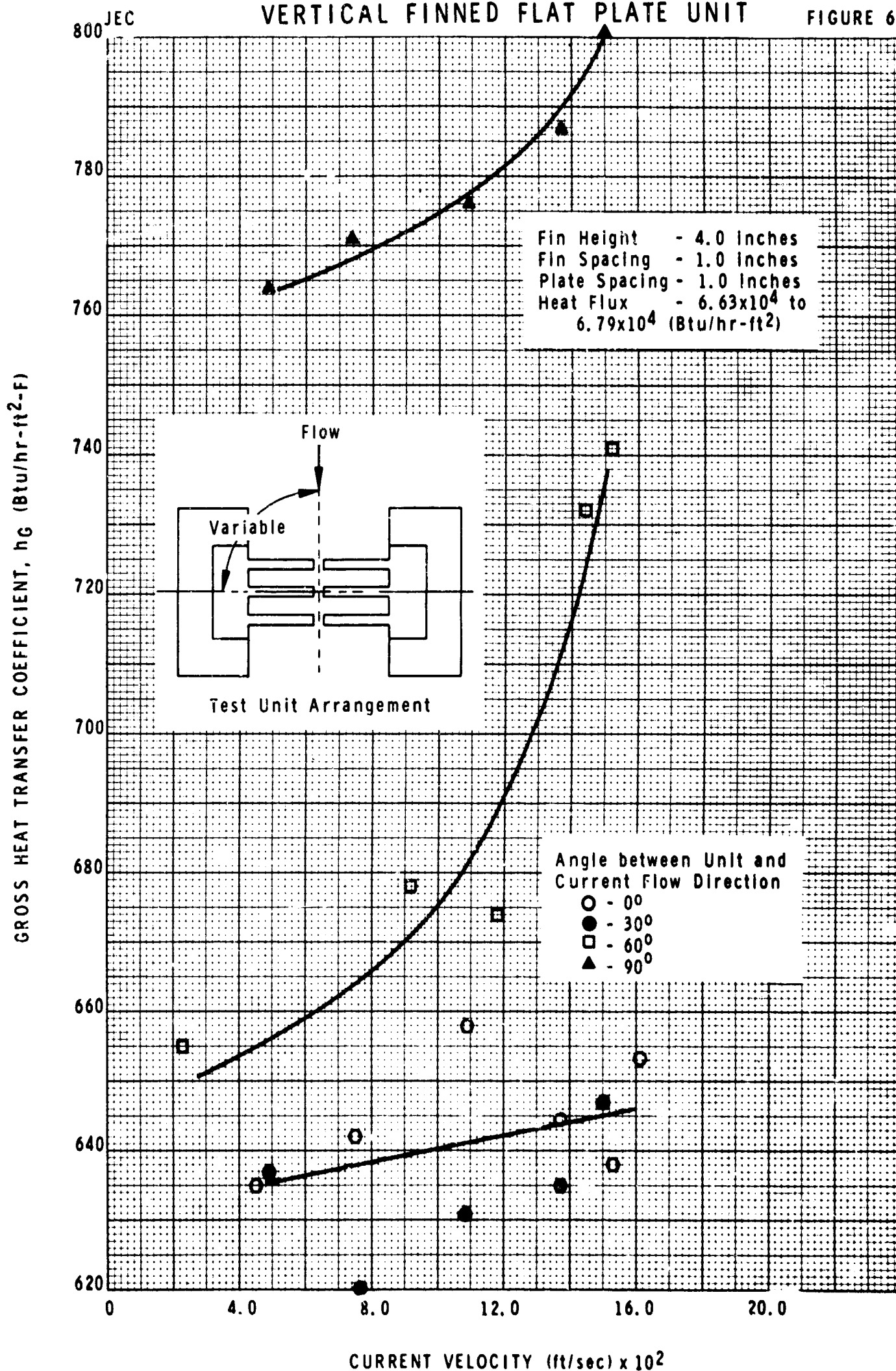


Test Unit Arrangement



# CURRENT TEST RESULTS VERTICAL FINNED FLAT PLATE UNIT

FIGURE 61



## RESULTS AND DISCUSSION Continued

Generally,  $h_g$  increased with current velocity for the finned flat-plate unit. However, magnitude of the rise was highly dependent upon the angle between the unit and the current direction. When the current direction was toward the insulated backside of the unit (0-degree angle),  $h_g$  was scarcely affected by a velocity increase. An angle of 90 degrees (current direction perpendicular to the fins) gave the highest coefficients. Coefficients for a 60-degree orientation fell between the ones for 0-degree and 90-degree angles. Gross heat transfer coefficients obtained for a 30-degree angle were approximately the same as for a 0-degree angle.

Figure 62 shows gross heat transfer coefficients for the cylindrical unit. Here again,  $h_g$  increased with current velocity. Because this unit was geometrically symmetrical, orientation variations were not necessary.

An undersea heat rejection unit would probably not be designed to take advantage of prevailing ocean currents, because they change unpredictably. However, knowledge of the increase in gross heat transfer coefficient with current velocity is helpful to estimate what the actual performance characteristics of the unit will be in operation. Our tests show that even small crosscurrents can significantly raise the gross heat transfer coefficient of a finned heat rejection surface.

**SHALLOW OCEAN BASIN TEST** After completion of the laboratory experimental program, we conducted a conceptual design of an undersea convector section for a 500 kw (e) fuel cell. See Appendix E. We concluded that a section composed of a bank of vertical finned tubes would be best for this service. The 2-inch diameter vertical finned cylinder elements were used to assemble a prototype heat rejection unit for testing in a shallow ocean basin. Port Hueneme harbor was chosen as the test site (34-09.1N, 119-12.5W).

The purpose of the shallow ocean test was to gather additional heat transfer data to check the laboratory data correlations and to test the turbulent plume mathematical model. Chapter V discusses the turbulent plume data and conclusions. Gross heat transfer coefficient data recorded as a function of time during the 54-hour test are tabulated in Appendix G. Figure 63 shows the prototype unit.

The maximum  $h_g$  was 424 Btu/hr-ft<sup>2</sup> F and the minimum was 267 Btu/hr-ft<sup>2</sup>-F. Fluctuations in  $h_g$  appeared to be due to variations in supply power, small currents in the harbor, and ambient temperature. These data essentially confirmed the laboratory test data. There was no visible corrosion or marine fouling on the unit. Dissolved oxygen concentration ranged from 6.56 to 6.74 parts per million and salinity ranged from 33.31 to 33.39 parts per thousand.

JEC

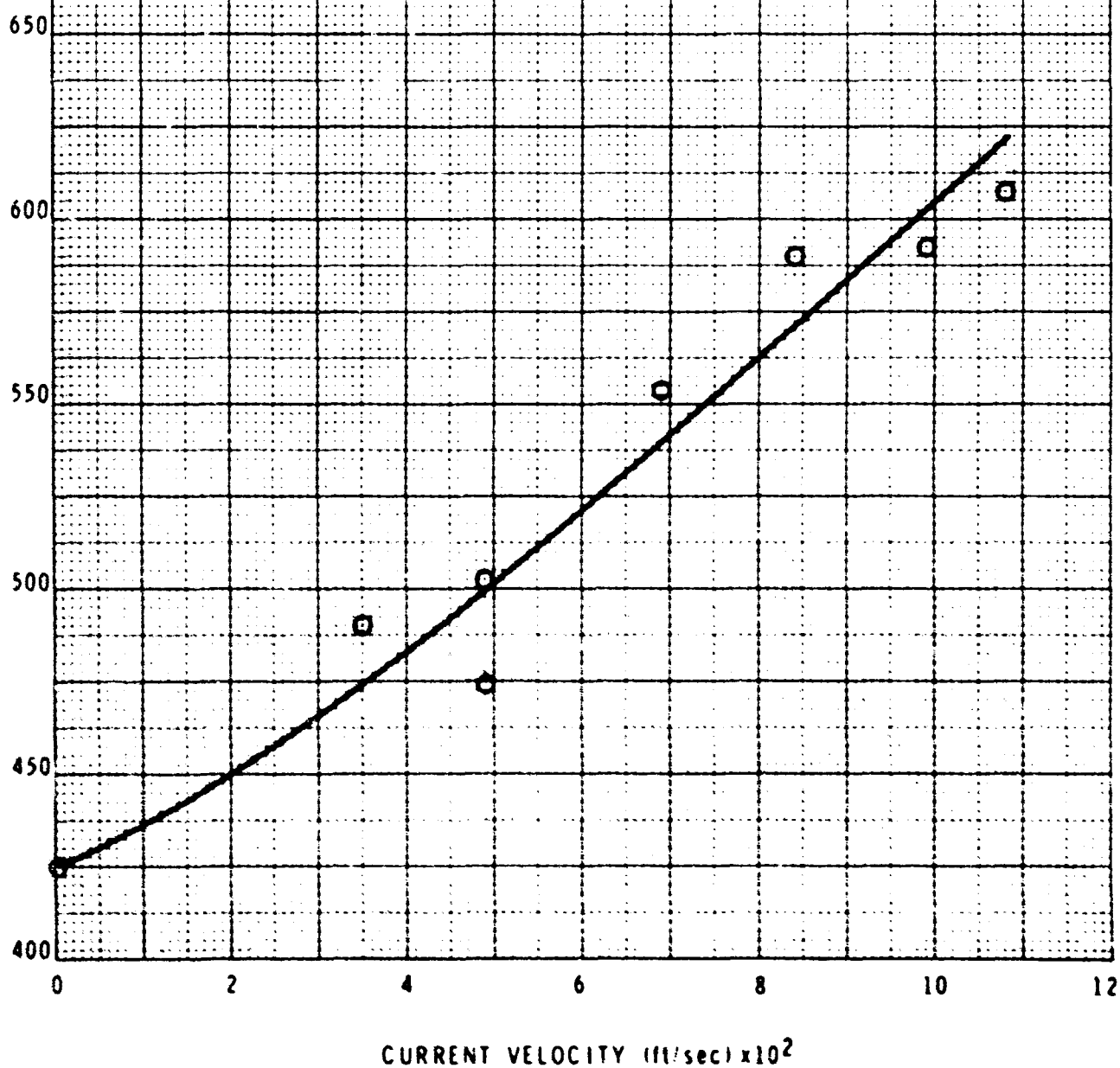
# CURRENT TEST RESULTS VERTICAL 2-INCH DIAMETER FINNED CYLINDER TEST UNIT

FIGURE 62

GROSS HEAT TRANSFER COEFFICIENT,  $h_g$  (Btu/hr-ft<sup>2</sup>-F)

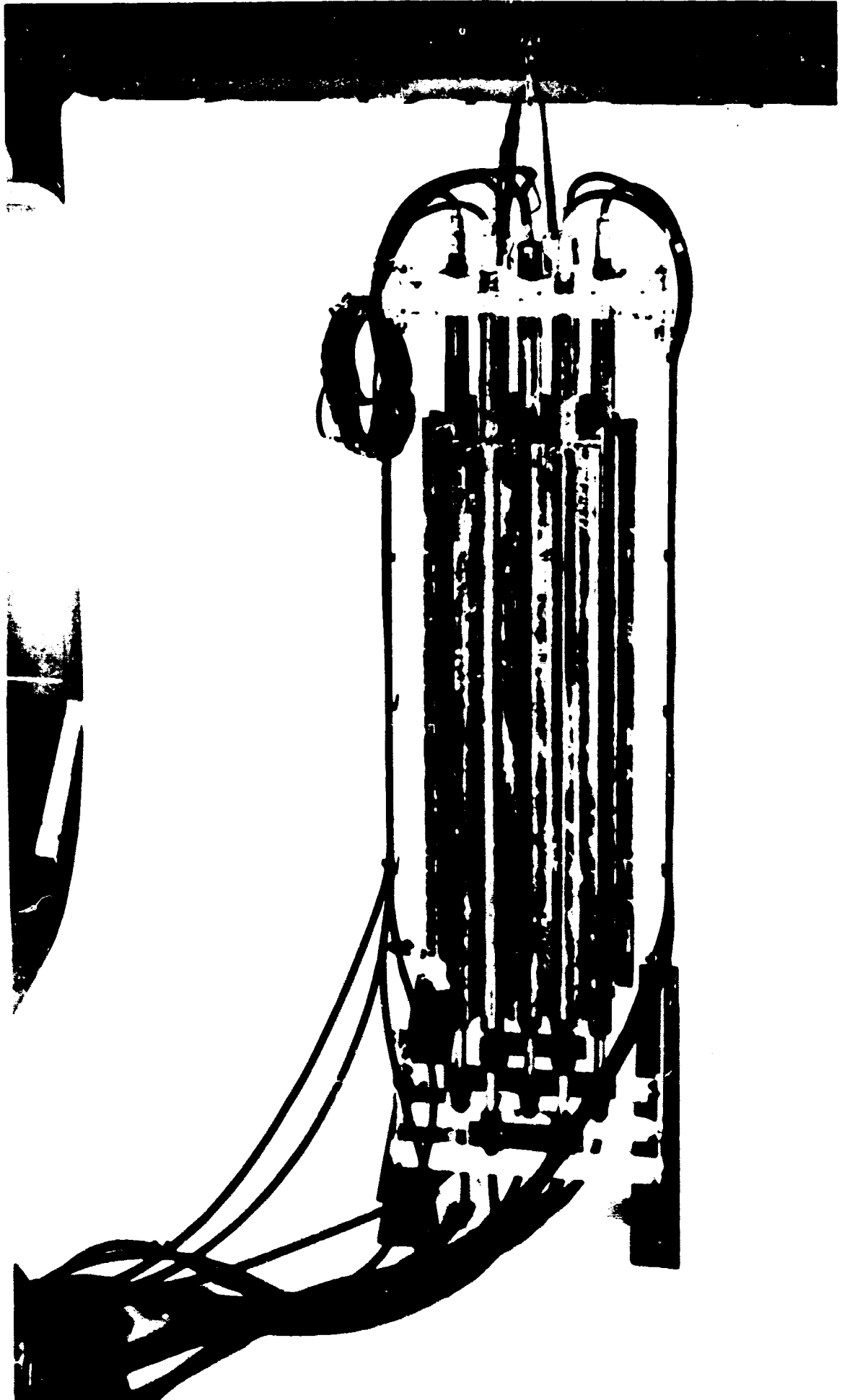
## TRIANGULAR PITCH

Fin Height - 1.88 inches  
Fin Spacing - 0.285 inches  
Heat Flux -  $1.09 \times 10^4$  to  
 $1.13 \times 10^4$  (Btu/hr-ft<sup>2</sup>)  
Cylinder Spacing - 6.0"  
Center-to-center  
Data for Center  
Cylinder only  
Current Flow Area - 10.45 ft<sup>2</sup>



PROTOTYPE NATURAL CONVECTION  
HEAT TRANSFER UNIT

FIGURE 63



## CONCLUSIONS AND RECOMMENDATIONS

## SUMMARY OF CONCLUSIONS

- 1 Vertical flat-plate turbulent natural convection heat transfer to water data showed that Saunders' equation holds for water having a Rayleigh number range of  $2.0 \times 10^9$  to  $3.6 \times 10^{12}$ .
- 2 The semiempirical approach of Larson closely predicts vertical flat plate experimental data while the Eckert-Jackson equation underpredicts considerably.
- 3 Measured boundary layer temperature profiles demonstrated that over 10 percent of the total temperature driving force is present at the predicted boundary layer thickness. These data pointed out the arbitrary nature of the boundary layer concept.
- 4 Vertical finned flat-plate experimental results indicated that a 4-inch fin height, with 1-inch spacing, yielded the highest gross heat transfer coefficient, for a fin thickness of 0.5 inches and a vertical length of three feet.
- 5 Agreement between predicted and observed gross heat transfer coefficients was quite good for finned vertical flat plates. The larger deviations were closely associated with high temperatures in the channels between the fins, which the prediction does not account for.
- 6 Spacings of 0.5 to 5.0 inches between the fin tips of two vertical finned plates had little effect upon gross heat transfer coefficient. A spacing of 1.0 inch was considered optimum.
- 7 Placing a chimney close to the vertical flat-plate unit severely reduced the gross heat transfer coefficient. This showed that entrainment of ambient water from the sides of the unit was considerable.
- 8 Without a chimney present, restricting inlet flow to the finned flat-plate test unit increased the gross heat transfer coefficient. The gross heat transfer coefficient did drop when inlet flow was restricted with a chimney in place. These data further point out the importance of side entrainment.
- 9 The contribution of side flow to the chimney and inlet clearance data must be recognized when extrapolating the data to a wider unit where large side entrainment is not possible.

## CONCLUSIONS AND RECOMMENDATIONS Continued

- 10 With a 2-inch diameter vertical cylinder, experimental Nusselt numbers fell higher than Saunders' equation at high-heat fluxes and fell lower at low-heat fluxes. Specification of heat flux and Rayleigh number is necessary to determine the Nusselt number.
- 11 Vertical finned 2-inch diameter cylinder experimental results indicated an optimum combination of a 0.285-inch fin spacing and a 1.88-inch fin height, for a fin thickness of 0.5 inch.
- 12 Predicted gross heat transfer coefficients greatly exceeded experimentally measured ones for vertical finned 2-inch diameter cylinders. This discrepancy could have been caused by a nonuniform base surface temperature.
- 13 The optimum center-to-center distance between finned 2-inch diameter cylinders appeared to be 6.0 inches.
- 14 Chimneys did not seem to appreciably enhance heat transfer from the vertical finned 2-inch diameter cylinders.
- 15 Obstructing inlet flow to the 2-inch diameter cylindrical unit raised the gross heat transfer coefficient slightly.
- 16 Small crosscurrents (below 0.15 ft/second) significantly increased gross heat transfer coefficients of the finned test units.
- 17 A bank of vertical finned tubes was selected as a heat rejection exchanger for a 500 kw (e) fuel cell.
- 18 Gross heat transfer coefficients obtained from the prototype heat rejection unit test in Port Hueneme harbor confirmed the laboratory test data.

RECOMMENDATIONS FOR FUTURE WORK Results and conclusions of this investigation suggest several areas of desirable experimental work. In the first place, more fundamental data are necessary to adequately describe the turbulent natural convection boundary layer flow. Velocity profile data are needed to confirm Waibler's empirical expression. Measurement of the wall shear stress would enable one to determine the proper Blasius law constant for turbulent natural convection flow. Since fin spacing is determined by the boundary layer thickness, these data would have immediate practical significance.



## CONCLUSIONS AND RECOMMENDATIONS Continued

We experimented with only one fin thickness which was optimum for only one height, spacing, and  $(2h_o/k)^{1/2}$  combination. It would be useful to gather additional gross heat transfer coefficient and temperature profile data for finned flat plates and cylinders at other fin spacings, fin heights, and fin thicknesses. This would impose a wider range of experimental conditions to test our prediction methods. Because the units are already fabricated, and the fin soldering technique has been perfected, such data could be obtained inexpensively.

Some improvement could be made upon the heat transfer model proposed in Chapter III by correlation of channel temperature data obtained in the experiments, in our opinion. Additional correlating effort should be spent on the vertical finned cylinder experimental data. Electrical analog studies, similar to those performed for flat plates, should be able to yield the effect of nonuniform base surface temperature upon  $h_G$  for vertical finned cylinders.

Additional data are necessary to elucidate the natural convection mechanism for vertical cylinders and to develop a generalized prediction. A wider range of cylinder diameters should be tested. Because physical properties of the fluid may also be a factor, additional experimentation should include more than one fluid.

## TERMS AND SYMBOLS, CHAPTER IV

A	Area, $\text{ft}^2$
b	Plate spacing, in
C	Constant
C <sub>n</sub>	Blasius law constant
C <sub>p</sub>	Specific heat at constant pressure, Btu/lbm-F
f	Function
g	Acceleration of gravity, $\text{ft/sec}^2$
Gr <sub>x</sub>	Grashof numbers based on x, $\frac{x^3 g \Delta T \rho}{\nu^2}$
h	Heat transfer coefficient, Btu/hr-ft <sup>2</sup> -F
k	Thermal conductivity Btu/hr-ft <sup>2</sup> -F/ft
l	A length larger than the boundary layer thickness
m	Constant
n	Constant
Nu <sub>x</sub>	Nusselt number based on x, $\frac{hx}{k}$
Pr	Prandtl number $\frac{C_p \mu}{k}$
q	Heat flow rate, Btu/hr
r	Radius, ft
Ra	Rayleigh number, Gr <sub>x</sub> Pr
Re <sub>x</sub>	Reynolds number based on x, $\frac{Ux}{\nu}$
St	Stanton number, $\frac{q/A}{\rho C_p U \theta}$
T	Temperature, F
U	Velocity, ft/sec
U <sub>1</sub>	Constant employed in velocity profile expression
x, y, z	Coordinates, ft

## TERMS AND SYMBOLS, CHAPTER IV Continued

## GREEK

$\alpha$	Thermal diffusivity, $\frac{k}{\rho C_p}$ , ft <sup>2</sup> /hr
$\beta$	Coefficient of thermal expansion, F <sup>-1</sup>
$\delta$	Boundary layer thickness, ft
$\Delta$	Signifies a change
$\mu$	Viscosity, lbm/ft-hr
$\nu$	Kinematic viscosity, $\mu/\rho$ , ft <sup>2</sup> /hr
$\rho$	Density, lbm/ft <sup>3</sup>
$\theta$	Temperature difference, F
$\tau$	Shear stress, lbf/ft <sup>2</sup>

## SUBSCRIPTS

a	Ambient
avg	Average
b	Based on plate spacing
c	Critical
max	Maximum
S	Surface
x	Based on length x
w	Evaluated at the wall
Q	Free stream

## CHAPTER V, FLOW OF A TURBULENT PLUME

## ABSTRACT

The thermal upwelling from an underwater heat source will penetrate into the surrounding seawater to dissipate its thermal energy and its momentum. The dynamics of the free jet flow depends on the initial velocity and temperature of the jet, the temperature of the surrounding water, the rate of entrainment, and the magnitude of the prevailing ocean currents. A survey of the literature indicates the fundamental fluid dynamics of jet or plume flow is well known. Applications of the theoretical correlations have been made in the case of gases, particularly air. Very little experimental work is available on the propagation of liquid plumes.

We investigated various factors affecting thermal upwelling in the ocean. Experimental results indicate the flow of the plume will be turbulent. Adiabatic cooling tends to slightly reduce plume penetration. The effect of the Coriolis force in reducing the plume penetration varies with the prevailing ocean currents and latitude. Ocean currents greatly enhance the dissipation of the plume and reduce the penetration to less than half the anticipated height. Vertical temperature stratification in the ocean will reduce plume penetration.

We developed a mathematical model for the turbulent plume in the absence of currents. Equations are given to predict the mass flow rate, mean bulk and maximum temperature differences, mean vertical velocity, and the plume radius. Comparison of experimental results obtained in the shallow ocean generally show the predicted results to be conservative. Predictions for two underwater heat sources located at 300- and 1,000-foot depths indicate the plume will not reach the ocean surface.

## LITERATURE SURVEY

An underwater heat source will cause the upwelling of warm water. This upwelling is referred to as a plume. For a variety of reasons, it is necessary to predict the characteristics and the penetration of the plume generated by a given heat source. This section of the chapter presents the results of the literature survey on the turbulent flow of free jets. Theoretical and experimental results are utilized to develop a procedure for the solution of the plume problem. In subsequent sections, the recommended model of the turbulent plume is applied to three typical cases and compared with test results from the heat transfer experiments.

## LITERATURE SURVEY Continued

The extent to which the plume expands and penetrates into the surrounding water depends on the momentum of the free jet leaving the heat exchanger, the temperature of the surrounding water, the rate of entrainment, and the magnitude of the prevailing ocean currents. The initial momentum of the free jet will be affected by the geometry and the heat dissipation rate from the source. As the buoyancy force gradually disappears, the vertical momentum of the free jet of warm water is dissipated and the flow in the vertical direction finally ceases. In almost all cases, the plume will be in turbulent rather than in laminar flow.

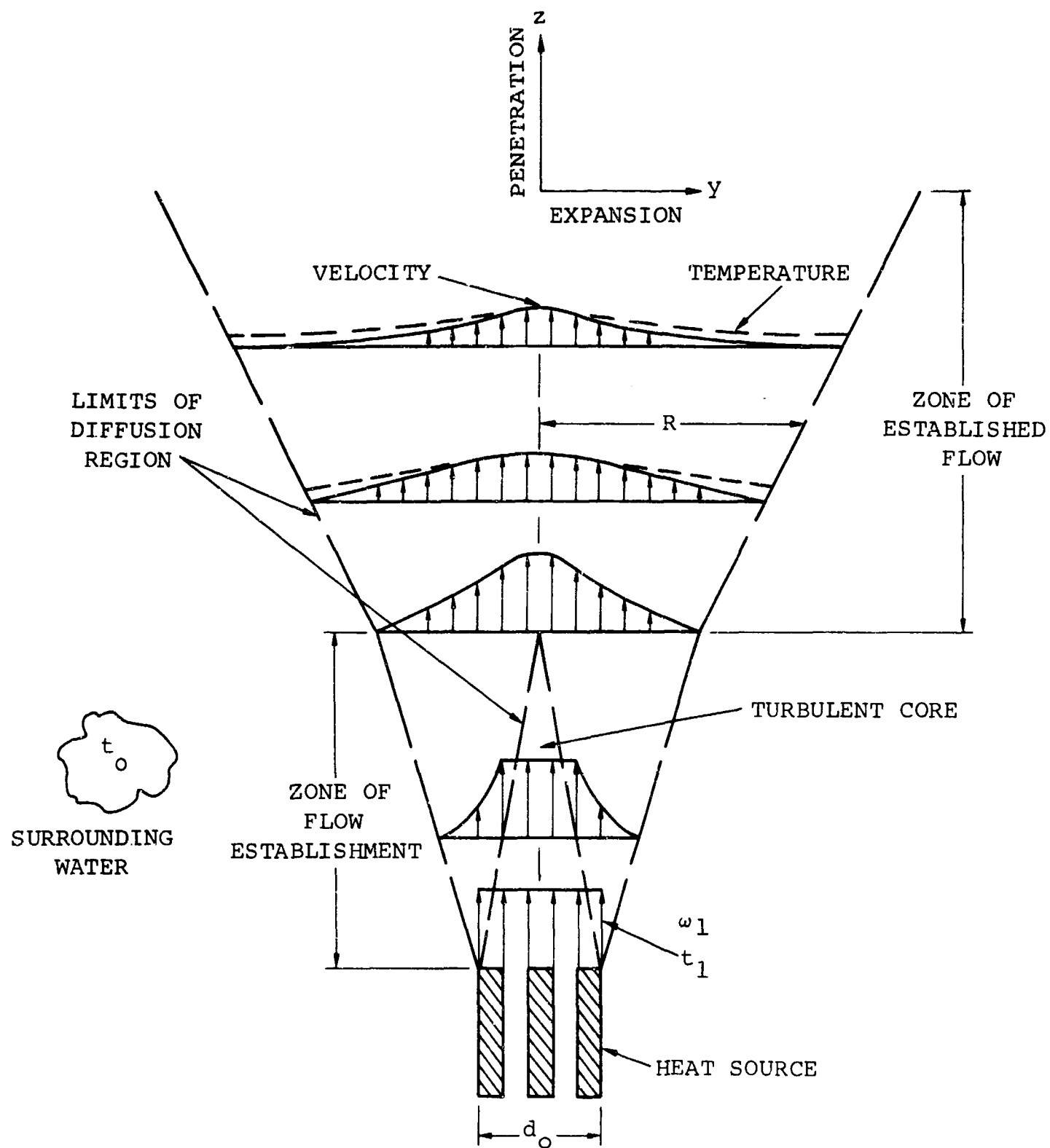
**PLUME FORMATION** Plume flow can originate from a point source, a line source, or a heat source of finite diameter. The initial flow can be laminar or turbulent and transient or steady. This analysis considers the axisymmetric plume with steady turbulent flow due to a finite heat source. In the ideal case, the effect of lateral movements due to currents is neglected. Figure 64 presents the free convection plume in the ideal ocean. The ideal plume can be divided into two zones. (1) Zone of flow establishment. And (2) the zone of established flow. The turbulent core which represents the initial flow is penetrated by entrainment.

The initial momentum of the plume is primarily dissipated by entrainment which causes the plume to expand as it penetrates vertically. The flow is fully established when diffusion reaches the vertical axis of the plume. Experimental data give the following clues about the dynamics of the plume flow. (1) The pressure distribution throughout the fluid in motion is hydrostatic and the only force accounting for the deceleration of the plume is the tangential shear between the layers of flowing fluid. Since this force acts wholly within the plume system, this characteristic of the plume flow leads to the assumption that the horizontal momentum flux at various elevations from the plume source is constant. And (2) the flow of the viscous fluid apparently does not affect the diffusion characteristics and the mixing process. Therefore, the same velocity function must characterize the horizontal profile at various elevations from the plume source.

## IDEALIZED PLUME DEVELOPMENT

GB

FIGURE 64



## LITERATURE SURVEY Continued

Experimental velocity data follow the trend of the Gaussian probability function.

$$\frac{w}{w_{\max}} = e^{-y^2/2\sigma^2} \quad (1)$$

Therefore, Equation V-1 characterizes the velocity profiles in Figure 64. The proportions of the curve are defined by two constants - the maximum velocity  $w_{\max}$  and the standard deviation  $\sigma$ .

Penetration of the plume terminates when the excess momentum in the vertical direction is fully dissipated. In Figure 64, the temperature profile at a given cross section is flatter than the velocity profile. This is due to the greater energy diffusivity compared to the diffusivity of momentum when the Prandtl number of the fluid is greater than about one. When diffusion reaches the vertical axis, the rate of diameter expansion is faster than in the zone of flow establishment. This is shown in Figure 64 by the break in the outer limit of the diffusion region.

**CIRCULAR JET** The classical problem of diffusion in a circular jet has been investigated both theoretically and experimentally. Different solutions of the problem have utilized Prandtl's mixing length theory, Taylor's theory of vorticity transport, dimensional analysis, and the equations of continuity, momentum, and buoyancy.

The velocity, radius, and mass flow of a jet varies with the vertical penetration from the heat source. The mass flow rate,  $W$  pounds per second, is the key variable of interest at any given cross section. Equation V-2 defines the mass flow rate at any height  $z$  as a function of the radial velocity distribution.

$$W = \int_0^{\infty} 2\pi\rho wydy \quad (2)$$

Solution of Equation V-2 for  $W$  requires a relation for the rate of entrainment or the variation of the vertical velocity  $w$  and radius  $y$  as a function of penetration  $z$ .

**TOLLMIEEN** The first theoretical solution of the circular jet problem was offered by Tollmien (172). Using the Prandtl mixing length hypothesis and constant momentum flux of the jet, he obtained a series solution for the axial velocity distribution through the jet. This solution indicates that the width of the jet varies linearly with penetration, and the vertical velocity varies inversely with penetration.

$$R \sim z$$

$$w \sim z^{-1}$$

## LITERATURE SURVEY Continued

For use in a given application, the generalized solution of Tollmien requires experimental determination of one constant. From this constant and the tabulated numerical solution, the velocity distribution and the plume expansion can be calculated. Determination of the single constant is equivalent to evaluating a constant eddy diffusivity for momentum throughout the plume. Schlichting (157) compares the velocity distribution predicted from the momentum transport theory of Tollmien with various sets of experimental results from isothermal air jets. Agreement is reasonably good when the value of  $z$  is relatively large.

Cleeves and Boelter (126) compared experimental velocity and temperature profiles for nonisothermal air jets with the Tollmien model. Whereas the velocity distribution shows reasonably good agreement, the temperature distribution shows agreement only after using the appropriate experimentally evaluated thermal eddy diffusivity. This indicates the thermal diffusivity can be 1.2 to 1.6 times as much as momentum diffusivity. Experimental results show the vertical velocity varies with  $z^{-1}$  when the penetration to initial diameter ratio,  $z/d_0$ , is greater than 8.

SCHMIDT Another theoretical solution of the free jet based on turbulent mixing according to Prandtl's mixing length theory was obtained by Schmidt (157,158). For line and point sources of heat, the variables of plume radius, velocity, and temperature vary with the penetration in the following manner.

	<u>LINE SOURCE</u>	<u>POINT SOURCE</u>
Plume radius, $R$	$z$	$z$
Vertical velocity, $w$	independent of $z$	$z^{-1/3}$
Temperature, $t$	$z^{-1}$	$z^{-5/3}$

YIH-ROUSE The problem of free convection of heat from a point source in air was investigated by Yih (177). For laminar flow of the plume, direct analytical solutions were obtained for fluids with Prandtl numbers of 1 and 2. The experimental data indicate the flow of the air plume to be actually turbulent. At a given distance above the source, the velocity and temperature distribution data follow the Gaussian probability distribution. Using dimensional analysis, Yih correlated the data for symmetrical turbulent flow above a point source by Equations V-3 and V-4.

$$\text{Velocity } w = 4.7 \left( \frac{gW}{\rho} \right) z^{-1/3} e^{-96 y^2/z^2} \quad (3)$$



## LITERATURE SURVEY Continued

## Buoyancy or temperature difference

$$(\rho_0 - \rho) = -11.0 \left( \frac{\rho W^2}{g} \right)^{1/3} z^{-5/3} e^{-71 y^2/z^2} \quad (4a)$$

$$\text{or } g \left( \frac{\rho_0 - \rho}{\rho} \right) = -11.0 \left( \frac{g^2 W^2}{\rho^2} \right)^{1/3} z^{-5/3} e^{-71 y^2/z^2} \quad (4b)$$

In Equations V-3, V-4a, and V-4b,  $w$  is in feet per second,  $y$  and  $z$  in feet,  $\rho_0$  and  $\rho$  in pound per cubic foot,  $g$  is 32.2 feet per second<sup>2</sup>, and  $W$  is in pound per second.

Subsequent to the work with the point source, Rouse, Yih, and Humphreys (155) extended the same approach to free convection of heat above a line source. The experimental work was based on air. The corresponding equations are the following (155,170).

$$\text{Velocity } w = 1.80 \left( \frac{gW}{\rho_0 L} \right)^{1/3} e^{-32 y^2/z^2} \quad (5)$$

## Buoyancy or temperature difference

$$(\rho_0 - \rho) = -2.6 \left( \frac{\rho_0 W^2}{gL^2} \right)^{1/3} \frac{1}{z} e^{-41 y^2/z^2} \quad (6)$$

In Equations V-5 and V-6,  $L$  is the length of the horizontal heat source in feet.

It is important to note that the variation of the important parameters such as velocity and buoyancy in Equations V-3 to V-6 is in agreement with the theoretical predictions of Schmidt. These studies indicate that the shape of the plume is a cone for a point or finite circular heat source and a wedge for a line source.

Digital computer simulation of buoyant convection from a line source was investigated by Lilly (143). The theoretical equations solved numerically allow for turbulent eddy exchange and give results which resemble the experimental results of Scorer (159). Batchelor (122) gives a general survey of most of the work done on plumes up to 1954 with different heat sources, laminar and turbulent, steady and unsteady flows.

## LITERATURE SURVEY Continued

PRIESTLEY AND BALL In an effort to build a generalized model of the air plume, Priestley and Ball (151) derived the continuity, momentum, and energy conservation equations and integrated them for any cross section at height  $z$  from the heat source. The momentum and energy equations integrated at any cross section from  $y = 0$  at the vertical axis of the plume to  $y = \text{infinity}$  give the following differential equations relating  $R$ , the radius of the plume,  $w$  and  $\Delta t$  variation along the vertical  $z$ -axis.

$$\text{Momentum } \frac{d}{dz} (R^2 w^2) = a R^2 \frac{\Delta t}{T_0} g \quad (7)$$

$$\text{Energy } \frac{d}{dz} (R^2 w^3) = b R^2 w \frac{\Delta t}{T_0} g - c R w^3 \quad (8)$$

$$\text{Buoyancy } \frac{d}{dz} (R^2 w \Delta t) = -d R^2 w \frac{\partial t_0}{\partial z} \quad (9)$$

In the above equations,  $a$ ,  $b$ ,  $c$ , and  $d$  are constants. Equations V-7 and V-8 can be utilized to derive the necessary characteristics of the plume. In Equation V-9, if the surrounding fluid is assumed to be at constant temperature,  $\partial t_0 / \partial z = 0$ , and the constant flow of heat across the plume is defined by the following equation.

$$R^2 w \Delta t = \text{constant}, A' \quad (10)$$

Substituting for  $\Delta t$  from Equation V-10 into Equations V-7 and V-8, the momentum and energy equations become

$$w \frac{d}{dz} (R^2 w^2) = \frac{a A' g}{T_0} \quad (11)$$

$$\frac{d}{dz} (R^2 w^3) = \frac{b A' g}{T_0} - c R w^3 \quad (12)$$

Substituting for  $A' g / T_0$  from Equation V-11 into Equation V-12, the differential equation relating velocity and radius with penetration is the following.

$$(3a-2b) \frac{1}{w} \frac{dw}{dz} + 2(a-b) \frac{1}{R} \frac{dR}{dz} = - \frac{ac}{R} \quad (13)$$

## LITERATURE SURVEY Continued

The solution of Equation V-13 and the significance of any specific solution depend on the values of the constants a, b, and c. For the case corresponding to

$$3a - 2b = 0 \quad (14)$$

Equation V-13 becomes

$$\frac{dR}{dz} = c$$

$$\text{and } R = cz + \text{constant} \quad (15)$$

The corresponding general solution for the velocity w and temperature difference  $\Delta t$  is obtained from Equations V-7, V-8, V-10, and V-15. Priestley and Ball obtained the following general solutions for  $a = 2$  and  $b = 3$  in Equation V-14.

$$w = \left( \frac{3A'g}{2T_0c^2 z} + \frac{B}{z^3} \right)^{1/3} \quad (16)$$

$$\Delta t = \frac{A'}{c^2 z^2} \left( \frac{3A'g}{2T_0c^2 z} + \frac{B}{z^3} \right)^{-1/3} \quad (17)$$

In Equations V-16 and V-17, B is an additional constant of integration and is fixed by a boundary condition. For  $B = 0$ , the variation of velocity w, buoyancy  $\Delta t$  and radius R is given by

$$w \sim z^{-1/3}$$

$$\Delta t \sim z^{-5/3}$$

$$R \sim z$$

These results are similar to Schmidt's solution and the results of Rouse and co-workers. In order to apply Equations V-16 and V-17, the spreading coefficient c must be obtained either from aerodynamic theory or experimental results.

Priestley and Ball have used Equations V-16 and V-17 to refute other models of the plume. They argue that the formation of the jet is originally dependent on the acceleration of a body of warm water which must, therefore, reach a maximum velocity and then decay according to some power law. They offer equations which solve for the maximum velocity and the position where this occurs.

## LITERATURE SURVEY Continued

TAYLOR While performing dye experiments with rotating liquids, Taylor (167,168) studied the formation and properties of vortices. Since a plume rising in a stably stratified fluid does not rigorously follow the assumption of similarity for velocity and temperature distribution, Taylor proposed the theory of vorticity transfer (169) to arrive at a relatively simple solution of the plume problem. Based on this theory, Morton, Taylor, and Turner (145) relate the inflow or entrainment at the edge of a convective plume to some characteristic velocity in the plume. Thus, the equations of conservation of mass, momentum, and heat are used to study convection currents in stably stratified as well as uniform incompressible fluids.

The equations developed by Morton, Taylor, and Turner use buoyancy as one of the dependent variables. If the density ( $\rho_o$ ) and the temperature ( $T_o$ ) of the fluid surrounding the plume are used as the reference, then buoyancy is defined by Equations V-18 and V-19.

$$\text{For gases} \quad \frac{\rho_o - \rho}{\rho} = \frac{T - T_o}{T_o} = \frac{\Delta t}{T_o} \quad (18)$$

$$\text{For liquids} \quad \frac{\rho_o - \rho}{\rho} = \beta(t - t_o) = \beta \Delta t \quad (19)$$

For gases, the coefficient of thermal expansion,  $\beta$ , is equal to the reciprocal of the absolute temperature ( $1/T_o$ ). For the case when the ocean is stably stratified, the surrounding liquid density at the heat source ( $\rho_{o1}$ ) will be generally higher than at positions above the heat source ( $\rho_o$ ). Similarly, the surrounding liquid temperature at the source ( $T_{o1}$ ) will be lower than at positions of increasing  $z$ .

From the theory of vorticity transport, the rate of entrainment is proportional to the mean vertical velocity,  $w$ . The following equations can then be derived for any position  $z$  above the heat source.

$$\text{Volumetric flow rate} = \pi R^2 w \quad (20)$$

$$\text{The rate of inflow or entrainment} = 2\pi R a w \quad (21)$$

In the above equations,  $a$  is the entrainment proportionality constant. From Equations V-20 and V-21, the continuity relation is the following.

$$\frac{d}{dz} (\pi R^2 w) = 2\pi R a w \quad (22)$$

The corresponding momentum and buoyancy equations are the following.

$$\frac{d}{dz} (\pi R^2 w^2) = \pi R^2 g (\rho_o - \rho) \quad (23)$$

$$\frac{d}{dz} [\pi R^2 w (\rho_{o1} - \rho)] = 2\pi R a w (\rho_{o1} - \rho_o) \quad (24)$$

## LITERATURE SURVEY Continued

In Equation V-24, buoyancy is measured relative to the fluid at the level of the heat source. The final working differential equations are obtained by the following manipulation. Substituting for  $(2\pi R w)$  from Equation V-22 into V-24

$$\begin{aligned} \frac{d}{dz} [\pi R^2 w (\rho_{01} - \rho)] &= (\rho_{01} - \rho_0) \frac{d}{dz} (\pi R^2 w) \\ &= \frac{d}{dz} [\pi R^2 w (\rho_{01} - \rho_0)] - \pi R^2 w \frac{d}{dz} (\rho_{01} - \rho_0) \\ &= \frac{d}{dz} [\pi R^2 w (\rho_{01} - \rho_0)] + \pi R^2 w \frac{d\rho_0}{dz} \\ (\rho_{01} - \rho) \frac{d}{dz} (\pi R^2 w) + \pi R^2 w \frac{d}{dz} (\rho_{01} - \rho) &= (\rho_{01} - \rho_0) \frac{d}{dz} (\pi R^2 w) \\ &\quad + \pi R^2 w \frac{d}{dz} (\rho_{01} - \rho_0) + \pi R^2 w \frac{d\rho_0}{dz} \end{aligned}$$

Collecting terms in the above equation

$$(\rho_0 - \rho) \frac{d}{dz} (\pi R^2 w) + \pi R^2 w \frac{d}{dz} (\rho_0 - \rho) = \pi R^2 w \frac{d\rho_0}{dz} \quad (25)$$

Since the variation of plume density with height is actually very small, the factor  $\rho$  on the left side of Equation V-23 can be assumed constant. Then Equations V-22, V-23, and V-25 give the following differential equations for the plume.

$$\frac{d}{dz} (R^2 w) = 2aRw \quad (26)$$

$$\frac{d}{dz} (R^2 w^2) = R^2 w \frac{(\rho_0 - \rho)}{\rho} \quad (27)$$

$$\frac{d}{dz} [R^2 w (\rho_0 - \rho)] = R^2 w \frac{d\rho_0}{dz} \quad (28)$$

Equation V-27 is similar to the momentum Equation V-7 derived by Priestley and Ball, and Equation V-28 is similar to the buoyancy Equation V-9. The different forms follow the definition of buoyancy.

Exact solutions for Equations V-26, V-27, and V-28 can be obtained for the case of uniform surrounding liquid density, that is

$$\rho_0 = \rho_{01} \text{ and } \frac{d\rho_0}{dz} = 0.$$

## LITERATURE SURVEY Continued

From Equation V-28

$$R^2 w (\rho_0 - \rho) = \text{constant}, A' \quad (29)$$

Equation V-29 shows that the vertical flux of buoyancy remains the same at all heights. The solution to the two remaining Equations V-26 and V-27 are obtained by eliminating  $(\rho_0 - \rho)$  in Equation V-27 and assuming the following boundary conditions.

At  $z = 0$ ,  $R = 0$  and  $R^2 w^2 \rho = 0$  (momentum flux)

The following solutions are given by Morton, Taylor, and Turner (145).

$$Rw = \left( \frac{9}{10} aA' \right)^{1/3} z^{2/3}, \quad R^2 w = \frac{6a}{5} \left( \frac{9}{10} aA' \right)^{1/3} z^{5/3}$$

$$R = \frac{6a}{5} z \quad (30)$$

$$w = \frac{5}{6a} \left( \frac{9}{10} aA' \right)^{1/3} z^{-1/3} \quad (31)$$

$$g \frac{\rho_0 - \rho}{\rho} = \frac{5A'}{6a} \left( \frac{9}{10} aA' \right)^{-1/3} z^{-5/3} \quad (32)$$

The variation of  $R$ ,  $w$ , and buoyancy have the same form as the results of Schmidt from mixing length theory and the results of Rouse, Yih, and Humphreys from dimensional analysis. The basic forms of the equations are comparable with the results of Priestley and Ball when  $B = 0$ . However, as in the case of  $c$  in Equations V-15, V-16, and V-17, the constant  $a$  in Equations V-30, V-31, and V-32 must be experimentally verified.

Morton, Taylor, and Turner obtained a generalized solution for the more real plume problem with a point source of heat in a stably stratified fluid, that is,  $d\rho_0/dz$  is not equal to zero. Assuming normal distribution curves for velocity and buoyancy profiles, the generalized numerical solution is tabulated for dimensionless penetration values from 0 to 2.8. These results are also given as Figure 5 in the 1961 reference of Taylor (170). Two conclusions from this generalized solution are important.

## LITERATURE SURVEY Continued

- 1 Although the velocity decay law from the simple model where  $d\rho_0/dz = 0$  follows the power law of  $z^{-1/3}$ , the true decay seems to follow this pattern up to a certain penetration after which velocity decay accelerates and results in the flat top of the typical plume. The simple model suggests the vertical velocity approaches zero asymptotically. The generalized solution indicates that during the top 20 percent of the penetration, velocity decay increases sharply until all vertical momentum is dissipated.
- 2 There is a finite distance which the plume penetrates to dissipate its momentum after buoyancy or temperature difference forces are completely dissipated. The additional penetration is equivalent to about one-third of the distance required for buoyancy dissipation.

**ENTRAINMENT** Instead of calculating the plume flow from experimentally determined velocity profiles and Equation V-2, Ricou and Spalding (153) devised an experimental technique whereby the plume flow and entrainment were measured directly. The experimental results with jets of air, propane, carbon dioxide, and hydrogen in air were correlated by Equation V-33.

$$\frac{W}{z(M_{\rho_0})^{1/2}} = 0.282 \quad (33)$$

The momentum flux,  $M$ , in Equation V-33 is defined as follows.

$$M = \frac{\pi d_0^2}{4} \rho w^2 \quad (34)$$

$M$  represents the rate of change of momentum or the total force associated with the moving free jet of the plume. Values of the constant in Equation V-33 vary from 0.22 to 0.404 for different studies reported in the literature. The work of Ricou and Spalding indicates that the value of 0.282 is currently the most reliable in as much as it is based on directly measured values of  $W$  and  $z$ , rather than on the numerical and graphical integration of velocity and temperature profile data.

## LITERATURE SURVEY Continued

For relatively small values of  $z$ , the momentum flux  $M$  is essentially constant and equal to the value at the jet or heat source. For large values of  $z$ , preceding theoretical approaches indicate  $W$ , which is related to buoyancy  $(\rho_o - \rho)/\rho$ , and  $\Delta t$  vary as  $z^{5/3}$ . Therefore, at large values of  $z$ ,  $M$  increases along with  $W$ . To obtain a solution of the plume problem, the following differential equation can be used as the valid entrainment or momentum exchange law for the region where  $M$  is relatively constant.

$$\frac{1}{(M\rho_o)^{1/2}} \frac{dW}{dz} = 0.282 \quad (35)$$

From Equation V-34

$$M = M_1 = \frac{\pi d_o^2}{4} \rho_1 w_1^2 = \frac{w_1^2}{\left[ \frac{\pi d_o^2}{4} \rho_1 \right]} \quad (36)$$

Substituting for  $M$  from Equation V-36 into V-35

$$\begin{aligned} \frac{dW}{w_1} &= 0.282 \left( \frac{4}{\pi} \right)^{1/2} \left( \frac{\rho_o}{\rho_1} \right)^{1/2} \frac{dz}{d_o} \\ \frac{W}{w_1} &= 0.32 \frac{z}{d_o} \left( \frac{\rho_o}{\rho_1} \right)^{1/2} + 1 \end{aligned} \quad (37)$$

Ricou and Spalding have developed a correlation for the rate of entrainment in a plume for the region of pure forced convection as well as free. The forced convection plume corresponds to a jet injected into the ambient fluid. This correlation is based on Equation V-35 with the assumption of normal distribution of velocity and temperature profiles, and the ratio of the widths of the temperature profile to the velocity profile equal to 1.17 for all  $z$ . This correlation is shown by the solid curve in Figure 65. The Froude number at the heat source in the absence of chemical reaction is defined by Equation V-38.

$$F_1 = \frac{w_1^2}{g d_o \left( \frac{\rho_o}{\rho_1} - 1 \right)} \quad (38)$$



# ENTRAINMENT BY BUOYANT JETS AND FLAMES RICOU & SPALDING, J FLUID MECH, 11, 21-32 (1961)

$W$  = MEAN VERTICAL MASS FLOW AT  $z$

$W_1$  = MEAN VERTICAL MASS FLOW AT  $z = 0$

$z$  = HEIGHT ABOVE JET SOURCE

$d_o$  = DIAMETER OF JET SOURCE

$\rho_1$  = MASS DENSITY OF JET FLUID AT SOURCE

$\rho_{o1}$  = MASS DENSITY OF SURROUNDING FLUID AT SOURCE

$F_1$  = FROUDE NUMBER AT SOURCE IN THE ABSENCE OF CHEMICAL REACTION

$w_1$  = VERTICAL VELOCITY AT SOURCE

$g$  = ACCELERATION OF GRAVITY

$$F_1 = \frac{w_1^2}{gd_o \left( \frac{\rho_{o1}}{\rho_1} - 1 \right)}$$

$$Y = \left( \frac{W_1}{W} \right)^{1/3}$$

THEORETICAL CURVE  
FOR PURE FORCED  
CONVECTION  $X \leq 1$

$$\frac{W}{W_1} = 0.32 \frac{z}{d_o} \left( \frac{\rho_o}{\rho_1} \right)^{1/3}$$

ASYMPTOTE FOR PURE  
FORCED CONVECTION

CORRELATION USED FOR MODEL

FOR  $X \geq 3$   $Y = 0.150 (X)^{1.67}$

FOR  $X < 3$   $\frac{W}{W_1} = 0.32 \frac{z}{d_o} \left( \frac{\rho_o}{\rho_1} \right)^{1/3}$

$$X = \frac{z}{d_o} \left( \frac{\rho_o}{\rho_1} \right)^{1/3} \frac{1}{F_1} \approx 0.5$$

DATA OF CLEEVES &  
BOELTER CHEM ENG  
PROG, 43, 123 (1947)

ASYMPTOTE FOR  
PURE NATURAL  
CONVECTION

DARK POINTS INDICATE  
TREND OF RICOU AND  
SPALDING, AND  
YIH DATA

DATA OF YIH  
PROC FIRST U S CONG  
APPL MECH, p.941 (1951)

PLUME ENTRAINMENT CORRELATION

## LITERATURE SURVEY Continued

In Figure 65, the experimental data of Ricou and Spalding are shown approximately along with the nonisothermal jet data of Cleeves and Boelter (126) and Yih (177). The theoretical correlation agrees with data in the forced convection region but tends to predict low entrainment in the free convection region. The theoretical equation in the forced convection region is the following.

$$\frac{W}{W_1} = 0.32 \frac{z}{d_o} \left( \frac{\rho_o}{\rho_1} \right)^{1/2} \quad (39)$$

It is apparent from Equation V-39 that the Froude number is not a significant parameter in forced convection, and  $F_1^{1/2}$  in Figure 65 is really redundant for this region. Equation V-39 implies that the plume will begin to expand and  $W/W_1$  will exceed unity when the ratio  $z/d_o$  is greater than about 3. That is, the penetration will reach a distance of about three times the diameter of the heat source before momentum transfer and entrainment of the surrounding liquid will become significant.

Other studies of the plume problem and related literature are listed in the bibliography at the end of this report. The basic concepts and experimental results presented above are utilized for the plume model recommended in the next section.

## MODEL OF TURBULENT PLUME

In this section we develop the basic procedure for the computation of the penetration and expansion of a liquid plume. In addition, the relative effect of the following factors on the idealized plume are discussed - flow instability and turbulence criteria, temperature and density gradient for stably stratified ocean, adiabatic cooling, Coriolis force, and ocean currents.

**LIQUID PLUME LITERATURE** Relatively few studies have been published in the literature concerning the transfer of momentum and energy in liquid jets. In a lengthy study of the theory and experiments with air, Albertson, Dai, Jensen, and Rouse (120) presented results useful for design purposes. The consensus is that the basic fundamentals valid for gases, and primarily air, are also applicable to liquid systems.

## MODEL OF TURBULENT PLUME Continued

Forstall and Gaylord (131) studied the transfer of momentum and mass in a submerged water jet. Their results are very important because a direct comparison is made between the relative diffusion rates of momentum, energy, and mass. (1) The shape of the liquid plume is basically the same as that in Figure 64. (2) The velocity and concentration profiles show the Gaussian probability distribution observed with gaseous plumes. The velocity distribution profile agrees with the momentum transfer model of Tollmien (172). And (3) as previously indicated, mass diffusion is faster than momentum diffusion. The axial decay of mass by radial diffusion follows the temperature and buoyancy decay observed by Corrsin and Uberoi (128) with air jets. Forstall and Gaylord concluded the behavior of the water jet is the same as that found by others for an air jet issuing into air, and constants obtained from measurements in air can be applied to water.

Kristmanson and Danckwerts (141) studied the mixing of a turbulent jet into an unlimited liquid environment. Measurements of the concentration as volume fraction jet fluid showed the mean concentration decaying as  $z^{-1}$ . The point on the axis at which all the jet fluid has been diluted to a specified concentration is 1.34 times as far from the orifice as the point where the mean concentration of the jet is reduced to the same specified value.

An experimental study of the downward convection of discrete masses of heavy liquid, called thermals, has been made by Saunders (156). Theoretical work to account for the oceanic thermocline and the temperature distribution in the thermocline region were carried out by Robinson and Stommel (154).

**ENTRAINMENT CORRELATION** Theoretically the transport phenomena for the dissipation of a liquid jet are similar to those in the gaseous jet. Limited experimental data with liquids indicate the validity of this approach. Ricou and Spalding provide the only simple and experimentally valid correlation for entrainment and the dissipation of jets. Therefore, this correlation is recommended as the basis for the computation of the liquid plume. With the entrainment correlation, the mass flow rate at any cross section of the plume is the single most important variable.

## MODEL OF TURBULENT PLUME Continued

The original correlation of Ricou and Spalding shown in Figure 65 is modified in the natural convection region to account for the appreciably higher entrainment, diffusion, or dissipation rates obtained for nonisothermal buoyant plumes. The data of Yih and Cleaves and Boelter indicate this trend in Figure 65. The correlating line in this region corresponds to values of the abscissa equal to or greater than 3. This line is drawn with a slope of 1.67 to follow the trend of the data by Ricou and Spalding and by Yih. The following equations represent the entrainment correlation for the plume model.

$$\text{For } X < 3 \quad \frac{W}{W_1} = 0.32 \frac{z}{d_o} \left( \frac{\rho_o}{\rho_1} \right)^{1/2} \quad (40)$$

$$\text{For } X \geq 3 \quad Y = 0.150 X^{1.67} \quad (41)$$

$$X = \frac{z}{d_o} \left( \frac{\rho_o}{\rho_1} \right)^{1/2} \frac{1}{F_1^{1/2}} \quad (42)$$

$$Y = \left( \frac{W}{W_1} \right) \frac{1}{F_1^{1/2}} \quad (43)$$

$$F_1 = \frac{w_1^2}{g d_o \left( \frac{\rho_{o1}}{\rho_1} - 1 \right)} \quad (44)$$

Equations V-40 and V-41 give the mass flow ratio at any cross section from the heat source of the plume. The density ratio term in Equations V-40 and V-42 is generally close to unity. X represents primarily the penetration at which the entrainment is to be evaluated. The Froude number defined by Equation V-44 is valid only for the heat source in the absence of chemical reaction. This condition is satisfied except for plumes generated by the combustion of fuel at the heat source. In the following paragraphs we show how various plume parameters are evaluated.

**MEAN  $\Delta t$**  The mean bulk temperature difference between the plume and the surrounding ocean decreases with entrainment and distance from the heat source. For the unstratified ocean with uniform ambient temperature, the following heat balance is valid.

$$W C_p (t_n - t_{o1}) = W_1 C_p (t_1 - t_{o1}) = \text{Constant} \quad (45)$$

## MODEL OF TURBULENT PLUME Continued

For most applications the variations of the mean  $C_p$  with temperature of the plume liquid can be neglected. The temperature difference for the case of uniform surrounding liquid is then given by Equations V-46a and V-46b.

$$t_n - t_{o1} = \frac{t_1 - t_{o1}}{(W/W_1)} \quad (46a)$$

$$\text{or } \Delta t_n = \frac{\Delta t_1}{(W/W_1)} \quad (46b)$$

For the case of the stably stratified ocean where  $t_o$  varies with distance from the heat source, the heat balance equation is the following.

$$\begin{aligned} W_n C_p (t_n - t_{on}) + (W_{n+1} - W_n) C_p \left( \frac{t_{on} + t_{on+1}}{2} - t_{on} \right) \\ = W_{n+1} C_p (t_{n+1} - t_{on}) \end{aligned} \quad (47)$$

The mean plume temperature solved from Equation V-47 is defined as follows.

$$t_{n+1} = \frac{t_n - \frac{t_{on} + t_{on+1}}{2}}{(W_{n+1}/W_n)} + \frac{t_{on} + t_{on+1}}{2} \quad (48)$$

For the case of the stratified ocean, the following procedure gives the mean bulk  $\Delta t$ .

- 1 Calculate  $W_{n+1}/W_1$  from the entrainment Equation V-40 or V-41 and V-43.
- 2 Calculate  $W_{n+1} = (W_{n+1}/W_1) (W_1)$
- 3 Calculate  $(W_{n+1}/W_n)$
- 4 Calculate  $t_{n+1}$  from Equation V-48. Then by definition

$$\Delta t_{n+1} = t_{n+1} - t_{on+1} \quad (49)$$

For the general case when  $(dt_o/dz)$  is practically constant, the stratified ocean temperature at any distance above the heat source is obtained from Equation V-50.

$$t_{on} = t_{o1} + \Delta z (dt_o/dz) \quad (50)$$

## MODEL OF TURBULENT PLUME Continued

**OCEAN TEMPERATURE GRADIENT** The temperature of the surrounding liquid at the heat source and the ambient temperature gradient ( $dt_o/dz$ ) are required for the computation of the model plume profiles. Figure B-1 in Appendix B gives a typical temperature profile for the model ocean. This temperature profile is based on curves presented by Von Arx (175) and Sverdrup, Johnson, and Fleming (163).

**DENSITY RATIO** The density ratio  $\rho_o/\rho_1$  must be evaluated with high precision for the computation of the Froude number  $F_1$  in Equation V-44. The following procedure is used.

- 1 Calculate the approximate absolute pressure at the heat source from Equations V-51a or V-51b.

$$\text{Approximate } P_1, \text{ decibars} = 10 + \text{depth in meters} \quad (51a)$$

$$\text{Approximate } P_1, \text{ decibars} = 10 + \frac{\text{depth in feet}}{3.3} \quad (51b)$$

- 2 From Table B-1 in Appendix B, determine the specific volume for a salinity of 35 parts per thousand, reference temperature of 0 C (32 F) and  $P_1$ . The value of  $\alpha_{35,0,P}$  from Table B-1 is in cu cm per g.
- 3 From Figure B-2 in the Appendix, determine the coefficient of thermal expansion  $\beta$  at the mean temperature between 0 C (32 F) and  $t_o$  or  $t$ . This value of  $\beta$  corresponds to  $t_o/2$  or  $t/2$  when the temperature unit is the centigrade. The specific volume or weight at the desired conditions are calculated from Equation V-52.

$$\alpha_{35,t,P} = \frac{1}{\rho} = \alpha_{35,0,P} (1 + \beta t) \quad (52)$$

In Equation V-52,  $\beta$  is evaluated at  $t/2$  C but multiplied by the temperature range  $(t - 0) = t$  C. Table B-2 in the Appendix gives the values of  $\beta$  corresponding to the values used in Figure B-2.

- 4 Calculate the density or specific weight ratio from Equation V-53.

$$\frac{\rho_o}{\rho_1} = \frac{\alpha_{35,t_1,P_1}}{\alpha_{35,t_o,P_1}} = \frac{\alpha_{35,0,P_1} (1 + \beta_1 t_1)}{\alpha_{35,0,P_1} (1 + \beta_o t_o)} = \frac{1 + \beta_1 t_1}{1 + \beta_o t_o} \quad (53)$$

## MODEL OF TURBULENT PLUME Continued

- 5 Calculate the actual absolute pressure at the heat source from Equations V-54a or V-54b.

$$P_1, \text{ decibars} = 10.13 + 0.9807 \rho_o \times \text{depth in meters} \quad (54a)$$

$$P_1, \text{ decibars} = 10.13 + 0.2989 \rho_o \times \text{depth in feet} \quad (54b)$$

$$P_1, \text{ psia} = 1.4503 \times P_1 \text{ in decibars} \quad (54c)$$

In Equations V-54a and V-54b,  $\rho_o$  is in g per cu cm.

**MEAN VELOCITY** The laws that govern velocity decay are related to those for entrainment and mean  $\Delta t$  decay. The entrainment correlation, Equations V-40 to V-44, was applied to three plumes with heat sources at 1,000-, 300-, and 25-foot depths. These applications will be discussed later on in more detail. Figure 66 shows a plot of the calculated mean bulk  $\Delta t$  versus penetration  $z$ . The results indicate that the slope of  $-\frac{5}{3}$  is valid for buoyancy and temperature decay for the case of uniform ocean temperatures. For the stratified ocean, such as in Case 2, the buoyancy decay curve follows the  $-\frac{5}{3}$  law initially and then becomes steep until the  $\Delta t$  difference disappears. This accelerated deterioration of plume buoyancy is due to the combined effects of (a) increasing plume density and decreasing temperature due to entrainment, and (b) decreasing ambient ocean density and increasing temperature due to stratification.

For the uniform temperature case, Figure 66 indicates the slope of  $-\frac{5}{3}$  is valid beyond a distance of about 1.5 to 4 times the diameter of the heat source. Extrapolation of the straight line representing the  $z^{-5/3}$  region to the  $\Delta t_1$  value gives the fictitious penetration  $z^*$  beyond which the  $-5/3$  law for buoyancy decay is valid. The slope of  $-5/3$  is important because it is identical to the theoretical results derived for turbulent plumes by Schmidt (158), Rouse, Yih and Humphreys, Priestley and Ball, and Morton, Taylor, and Turner (145, 155, 170).

These observations lead to the conclusion that the other dependent variables of the plume - mean velocity and radius - should also follow the theoretical results predicted by Equations V-30 and V-31. The mean velocity at any distance from the heat source is calculated from Equation V-55.

$$w = w_1 (z - z^*)^{-1/3} \quad (55)$$

## MODEL OF TURBULENT PLUME Continued

**ZERO BUOYANCY AND VELOCITY** The point at which the mean bulk temperature difference is less than 0.1 degree C is selected as the realistic limit for the buoyancy  $(\rho_0/\rho) - 1$  to be zero. This point is obtained by calculation or extrapolation of the temperature decay plot as shown in Figure 66.

The point at which the vertical velocity of the plume decays completely corresponds to a distance 33 percent greater than the point for buoyancy dissipation. This criterion is based on the generalized results of Morton, Taylor, and Turner (145,170).

**PLUME RADIUS** At a given penetration, the plume radius is calculated from the mass flow rate,  $W$ , and the mean velocity,  $w$ .

$$R = \sqrt{\frac{W}{\pi w \rho}} \quad (56)$$

For  $W$  in g per sec,  $w$  in cm per sec,  $\rho$  in g per cu cm and  $R$  in feet, Equation V-56 is equivalent to the following relation.

$$R, \text{ feet} = \frac{1}{54} \sqrt{\frac{W}{w \rho}} \quad (57)$$

Equations V-55 and V-56 can be combined to give the following relationship between the plume radius and penetration.

$$R = \sqrt{\frac{W}{\pi w_1 \rho}} \frac{\sqrt[3]{z - z^*}}{\sqrt[3]{z - z^*}} \quad (58)$$

In Equations V-56 through V-58,  $\rho$  is the specific weight of the plume fluid. Since variation of  $\rho$  with temperature, pressure, and penetration is relatively negligible, a constant value of  $\rho$  evaluated at the mean temperature  $(t_{01} + t_1)/2$  can be used. From simple dimensional analysis the variation of  $R$  with  $(z - z^*)$  is found as follows.

$$R \sim \sqrt{\frac{W}{w}} \sim \sqrt{\frac{(z - z^*)^{5/3}}{(z - z^*)^{-1/3}}} \sim (z - z^*) \quad (59)$$

**MAXIMUM  $\Delta t$**  The plume model in Figure 64 indicates the temperature difference at the vertical axis is unchanged throughout the zone of flow establishment. The maximum  $\Delta t$  will always prevail along the axis of the plume. In the zone of established flow, the maximum  $\Delta t$  can be approximated from the characteristic shape of the temperature distribution at any cross section. Since the temperature distribution has the shape of the Gaussian probability curve, the effective radius can be used to calculate the maximum  $\Delta t$ .



## MODEL OF TURBULENT PLUME Continued

For the Gaussian temperature distribution, the following equation gives the  $\Delta t$  at any radial distance from the vertical axis.

$$\sigma \Delta t = \frac{1}{\sqrt{2\pi}} e^{-(y/\sigma)^2/2} \quad (60a)$$

$$\text{or } \sigma \Delta t = 0.40 e^{-(y/\sigma)^2/2} \quad (60b)$$

The mean  $\Delta t$  can be evaluated for the plume extending from the vertical axis up to any effective radius along the horizontal axis. The horizontal distance is measured in units of standard deviation given by the ratio  $(y/\sigma)$ . For the circular cross section Equation V-61 defines mean  $(\sigma \Delta t)$ .

$$\text{mean}(\sigma \Delta t) = \frac{0.80 \int_0^{y/\sigma} e^{-(y/\sigma)^2/2} (y/\sigma) d(y/\sigma)}{(y/\sigma)^2} \quad (61)$$

Integration of Equation V-61 gives the following result.

$$\text{mean}(\sigma \Delta t) = \frac{0.80 (1 - e^{-(y/\sigma)^2/2})}{(y/\sigma)^2} \quad (62)$$

The maximum value of  $\Delta t$  at the vertical axis of the plume is  $\max(\sigma \Delta t) = 0.40$ . Therefore, the ratio of maximum  $\Delta t$  to the mean  $\Delta t$  is given by Equation V-63.

$$\frac{\max \Delta t}{\text{mean } \Delta t} = \frac{(y/\sigma)^2}{2 (1 - e^{-(y/\sigma)^2/2})} \quad (63)$$

Equation V-63 indicates that the ratio of max  $\Delta t$  to mean  $\Delta t$  increases with the effective plume radius defined by the ratio  $(y/\sigma)$ . Definition of the plume boundary in terms of the effective radius is arbitrary and depends on the remaining  $\Delta t$  at the periphery of the plume. The ratio of the remaining  $\Delta t$  at the effective radius to the max  $\Delta t$  at the vertical axis is given in standard Gaussian distribution tables.

## MODEL OF TURBULENT PLUME Continued

The following results based on Equation V-63 show the effect of  $(y/\sigma)$  on the two ratios,  $\max \Delta t / \text{mean } \Delta t$  and  $(\Delta t \text{ at } y/\sigma) / \max \Delta t$ .

Effective radius, $R^* = y/\sigma$	$\frac{\max \Delta t}{\text{mean } \Delta t}$	$\frac{\Delta t \text{ at } y/\sigma}{\max \Delta t}$
1	1.27	0.607
2	2.32	0.135
2.45	3.16	0.050
2.5	3.27	0.044
3	4.55	0.011

Based on these results, we have defined the effective radius at  $R^* = 2.45$  which corresponds to a peripheral  $\Delta t$  equal to 5 percent of the maximum  $\Delta t$ . The maximum  $\Delta t$  is calculated from the mean  $\Delta t$  defined previously and Equation V-64.

$$\max \Delta t = 3.16 (\text{mean } \Delta t) \quad (64)$$

**FLOW INSTABILITY AND TURBULENCE** In the discussion of the plume problem, we have stated that the flow of the plume is primarily turbulent. This assumes the transfer of momentum and energy by molecular diffusion are negligible as compared to the transport by lateral eddy diffusion. The basic entrainment correlation and plume model are valid for turbulent flow. What are the criteria for laminar or turbulent flow of the plume?

Instability of laminar flow of a free jet is an important factor which determines the nature of the flow at any given point along the path. As evidenced by the pattern of cigarette smoke, the flow at the heat source is laminar and distinct streamlines can be seen parallel to the flow path. Beyond a certain height instability and eddying set in, the flow becomes turbulent, and the plume is finally dissipated. Yih (177) obtained the following criterion for this type of instability.

$$\frac{g_1 z^2 w_1}{1^3} \cdot 9 \times 10^9 \quad (65)$$

## MODEL OF TURBULENT PLUME Continued

For the initial plume flow rate  $W_1$ , specific weight  $\rho_1$ , and viscosity  $\mu_1$ , Equation V-65 gives the height beyond which the flow is turbulent. The constant in Equation V-65 is approximately the cube of the laminar to turbulent transition Reynolds number for flow inside a pipe. The transition point  $z$  calculated from Equation V-65 for the plume applications discussed in the next section is a fraction of a foot. Therefore, the liquid plume flow is almost completely turbulent. The units in Equation V-65 are  $W_1$  lb per sec,  $\rho_1$  lb per cu ft,  $z$  feet,  $\mu_1$  lb per (ft-sec), and  $g$  32.2 feet per sec<sup>2</sup>. Table B-3 in the Appendix B gives the viscosity of seawater with 35 parts per thousand salinity as a function of temperature.

Another important laminar-turbulent transition instability is that investigated by Viilu (174). By simple colorimetric experiments, Viilu determined the Reynolds number of the original jet which would not upon entry into the stagnant liquid environment undergo a transition from steady streamline flow to ripple or ring vortex and finally turbulent flow. This criterion was found to correspond to a Reynolds number of about 10 to 12. For the practicable heat sources under consideration, the initial Reynolds numbers are of the order of 20,000 to 100,000.

The above discussion provides the basis for limiting the present study to the turbulent plume.

**ADIABATIC COOLING** As the warm water flows upward adiabatically from the heat source to the lower hydrostatic pressure region, its temperature diminishes due to the increasing specific enthalpy of the liquid at the lower pressure. This adiabatic cooling effect was shown by Lord Kelvin (175) to be approximately defined by Equation V-66.

$$-\left(\frac{\partial t}{\partial z}\right)_H = \left(\frac{\beta T}{J C_p}\right) \left(\frac{g}{g_c}\right), \text{ F per foot} \quad (66)$$

When  $\beta$  has the unit 1/F,  $T$  in degrees R,  $J = 778$  (ft-lb<sub>f</sub>) per Btu and  $C_p$  in Btu per (lb<sub>m</sub>-F), the adiabatic cooling effect is obtained from Equation V-66 in degrees F per foot. The following results are obtained as a typical calculation for Case 1 application presented in the next section.

At  $t_{ave} = 70$  F = 21.1 C,  $T = 460 + 70 = 530$  R,  $P_1 = 316.5$  decibars.

From Figure B-2, at  $t = 70$  F,  $\beta = 150 \times 10^{-6}$  1/F.

## MODEL OF TURBULENT PLUME Continued

Table B-4 in Appendix B gives  $C_p$  values for 35 parts per thousand salinity seawater as a function of temperature and pressure. For the above conditions,  $C_p = 0.932$  Btu per (lb-F). From Equation V-66,

$$-\left(\frac{\partial t}{\partial z}\right)_H = \frac{(530)(150 \times 10^{-6})}{(778)(0.932)} = 110 \times 10^{-6} \text{ F/ft}$$

For Case 1 where the warm waters penetrate about 213 feet, the effect of adiabatic cooling is approximately  $213 \times 110 \times 10^{-6} = 0.023$  F or 0.013 C. This would have a negligible effect upon the plume characteristics.

For a parcel of water at temperature  $t$  under hydrostatic pressure, the potential temperature is defined as the temperature this parcel of water would attain if it were brought adiabatically from the given depth to the surface of the ocean. Potential temperature is equal to the actual temperature of the parcel of water under hydrostatic pressure minus the adiabatic cooling. Tables 11 through 14 in Sverdrup, Johnson, and Fleming (163) give values of the adiabatic temperature gradient as a function of temperature, depth, and salinity. The effect of adiabatic cooling on the turbulent plume can be neglected.

**CORIOLIS FORCE** In this section, we shall determine the magnitude of the Coriolis force to estimate its effect on the penetration and characteristics of the turbulent plume. A particle traveling on the surface of a rotating body undergoes a force which acts to direct the particle into the rotating body. In the case of the rotating earth, particles of liquid with east-west current component  $u$  or north-south current component  $v$  will be affected by the Coriolis force. The general vectorial equation of motion for a viscous fluid including the Coriolis effect is defined as follows.

$$\frac{\partial}{\partial t} \rho \bar{c} = \underbrace{(-2\Omega \times \rho \bar{c})}_{(1)} - \underbrace{\nabla \cdot \rho \bar{c} \bar{c}}_{(2)} - \underbrace{\nabla \cdot \bar{\tau}}_{(3)} - \underbrace{\nabla p}_{(4)} + \underbrace{(\rho_0 - \rho) g}_{(5)} \quad (67)$$

Equation V-67 is the application of Newton's second law which states the force accelerating a body is equal to the sum of all the acting forces. The various terms in this equation represent the following forces.

- 1  $\frac{\partial}{\partial t} \rho \bar{c}$  = the net force per unit volume accelerating the particle
- 2  $(-2\Omega \times \rho \bar{c})$  = Coriolis force per unit volume

## MODEL OF TURBULENT PLUME Continued

- 3  $-\nabla \cdot \rho \bar{c} \bar{c} =$  rate of momentum gain by convection per unit volume
- 4  $-\nabla \cdot \bar{\tau} =$  rate of momentum gain by viscous shear per unit volume
- 5  $-\nabla p =$  pressure force per unit volume
- 6  $(\rho_0 - \rho)g =$  buoyancy force in gravitational field per unit volume

To estimate the relative importance of the Coriolis effect, Equation V-67 must be expressed in a more practicable form. The Coriolis force affecting motion in the x (east-west) and y (north-south) directions is defined as follows.

$$x - \text{direction C.F.} = (2\Omega \sin \phi) \rho v \quad (68)$$

$$y - \text{direction C.F.} = (-2\Omega \sin \phi) \rho u \quad (69)$$

In Equations V-68 and V-69,  $\Omega$  is the angular velocity of rotation of the earth and  $\phi$  is the latitude. It follows for a given current intensity  $u$  or  $v$ , the Coriolis force is a maximum at the poles and zero at the equator. The value of  $(2\Omega)$  is  $1.5 \times 10^{-4}$  radians per sec.

The acceleration (1) and convection (3) terms in Equation V-67 give the following equations for the substantial derivative in the three coordinate directions.

$$\frac{\partial}{\partial \theta} \rho \bar{c} + \nabla \cdot \rho \bar{c} \bar{c} =$$

$$x \text{ direction } \rho \frac{Du}{D\theta} = \rho \left( \frac{\partial u}{\partial \theta} + u \frac{\partial u}{\partial x} + v \frac{\partial u}{\partial y} + w \frac{\partial u}{\partial z} \right) \quad (70)$$

$$y \text{ direction } \rho \frac{Dv}{D\theta} = \rho \left( \frac{\partial v}{\partial \theta} + u \frac{\partial v}{\partial x} + v \frac{\partial v}{\partial y} + w \frac{\partial v}{\partial z} \right) \quad (71)$$

$$z \text{ direction } \rho \frac{Dw}{D\theta} = \rho \left( \frac{\partial w}{\partial \theta} + u \frac{\partial w}{\partial x} + v \frac{\partial w}{\partial y} + w \frac{\partial w}{\partial z} \right) \quad (72)$$

## MODEL OF TURBULENT PLUME Continued

The viscous shear term (4) in Equation V-67 can be defined for a fluid of constant density and viscosity by  $\mu \nabla^2 u$ ,  $\mu \nabla^2 v$ , and  $\mu \nabla^2 w$  for the x, y, and z coordinates, respectively. Substituting for the various components in the three coordinate directions from Equations V-68 through V-72 into Equation V-67, the generalized equations of motion for constant density and viscosity are defined as follows. For constant  $\rho$  and  $\mu$

$$\text{x direction } \rho \frac{Du}{D\theta} = (1.5 \times 10^{-4} \sin \theta) \rho v + \mu \nabla^2 u - \frac{\partial p}{\partial x} \quad (73)$$

$$\text{y direction } \rho \frac{Dv}{D\theta} = (-1.5 \times 10^{-4} \sin \theta) \rho u + \mu \nabla^2 v - \frac{\partial p}{\partial y} \quad (74)$$

$$\text{z direction } \rho \frac{Dw}{D\theta} = \mu \nabla^2 w - \frac{\partial p}{\partial z} + (\rho_o - \rho)g \quad (75)$$

To arrive at working relations, Equations V-73, V-74, and V-75 are further simplified. The substantial derivatives  $Du/D\theta$ , and so on, consist of the time dependent term  $\partial u/\partial \theta$ , and so on, and the advective terms  $(u\partial u/\partial x + v\partial u/\partial y + w\partial u/\partial z)$ , and so on. For steady-state conditions the time derivatives are equal to zero. Away from solid boundaries and gas-liquid interfaces, the local advective terms can be assumed to be negligible compared to other force terms in the equations of motion. Therefore, as a first approximation, Equation V-76 can be assumed to be valid.

$$\rho \frac{Du}{D\theta} = \rho \frac{Dv}{D\theta} = \rho \frac{Dw}{D\theta} = 0 \quad (76)$$

Equations V-73, V-74, and V-75 then lead to the following simplified flow equations.

$$\alpha \frac{\partial p}{\partial x} = (\mu/\rho) \nabla^2 u + (1.5 \times 10^{-4} \sin \theta) v \quad (77)$$

$$\alpha \frac{\partial p}{\partial y} = (\mu/\rho) \nabla^2 v - (1.5 \times 10^{-4} \sin \theta) u \quad (78)$$

$$\alpha \frac{\partial p}{\partial z} = (\mu/\rho) \nabla^2 w + \left( \frac{\rho_o - \rho}{\rho} \right) g \quad (79)$$

## MODEL OF TURBULENT PLUME Continued

Equations V-77, V-78, and V-79 are helpful to estimate the relative magnitude of the Coriolis force versus the buoyancy force. The recommended plume model assumes a stagnant body of water with  $u = v = 0$ . It also assumes the vertical shear stress due to viscosity  $(\mu/\rho)\nabla^2 w$  to be negligible. In the absence of rigorous data for the flow of free jets, assuming  $(\mu/\rho)\nabla^2 w$  term to be negligible is currently considered valid.

We can now apply Equations V-77, V-78, and V-79 to compare the Coriolis acceleration with the buoyancy acceleration, that is

$$(1.5 \times 10^{-4} \sin \phi) v \quad \text{versus} \quad \left( \frac{\rho_o - \rho}{\rho} \right) g$$

EXAMPLE Consider  $v = 1$  knot at the north pole,  $v = 51.48$  cm per sec or 1.689 ft per sec. Coriolis acceleration =  $(1.5 \times 10^{-4} \sin \phi) v = 1.5 \times 10^{-4} \times 1 \times 51.48 = 0.00772$  cm/sec<sup>2</sup>. The buoyancy acceleration is calculated for the plume of Case 1 discussed in the next section. From Table X at the heat source,  $\rho_o/\rho_1 = 1.001533$ ,

$$\text{buoyancy acceleration} = \left( \frac{\rho_o - \rho}{\rho} \right) g = (1.001533 - 1)(980.7) = 1.503 \text{ cm/sec}^2$$

At the heat source the ratio  $\frac{\text{buoyancy acceleration}}{\text{Coriolis acceleration}} = \frac{1.503}{0.00772} = 195$

For this example the buoyancy force is about 200 times larger at the heat source than the Coriolis force exerted by a current of 1 knot at the pole. Above the source this ratio will decrease, but the Coriolis force will not play a major role because of its small magnitude.

Coriolis acceleration diminishes as the latitude goes to zero at the equator. Buoyancy acceleration diminishes as the buoyancy of the plume is dissipated and  $\rho_o/\rho$  approaches unity. From a practical viewpoint, neglecting the Coriolis effect on the plume would make the predicted penetration more conservative. However, the effect of currents  $u$  and  $v$  on the plume can be very significant. This factor is discussed in the following paragraphs.

OCEAN CURRENTS The plume model does not account for the effect of ocean currents on buoyancy or temperature difference dissipation. The calculated penetration from the plume model would, therefore, be quite conservative in the presence of currents. A simple explanation of the effect of currents is bending of the plume axis at an angle from the vertical approximated by  $(\arctan \frac{v}{w})$ .

# MODEL OF TURBULENT PLUME Continued

Several references on the intensity of ocean currents are listed in the bibliography. Specific information on the effect of currents on liquid plumes is lacking.

In a study of various solutions of the plume problem, Meade (144) has applied the general equations for velocity and temperature decay to predict plume penetration in the presence of currents. The particular problem tackled is the penetration of warm air from two stacks in the presence of wind. Atmospheric measurements (119) were used to evaluate the constants in the generalized equations. The atmospheric measurements show considerable scatter on a plot of penetration versus wind velocity. The following trends can be observed for the two stack applications.

First stack  $d_o = 14$  feet

Air  $w_1 = 20.5$  feet per second,  $F_1 = 1.76$

As the wind velocity increases to 15 feet per second, the plume penetration is about 20 to 25 percent of the stagnant atmosphere case.

Second stack  $d_o = 9$  feet

Air  $w_1 = 7.3$  feet per second,  $F_1 = 0.30$

For wind velocities of 5 to 15 feet per second, the plume penetration is about 30 percent of the stagnant atmosphere case.

A rigorous solution of the interaction between ocean currents and a plume requires consideration of the two major forces acting on an element of the plume. The force of a current acting perpendicular to an element of volume of the plume is given by Equation V-80.

$$\frac{\text{Current force}}{\text{Unit volume}} = \rho u^2 (\text{elemental surface}) \quad (80)$$

The buoyancy force acting vertically on an element of volume of the plume is given by Equation V-81.

$$\frac{\text{Buoyancy force}}{\text{Unit volume}} = g(\rho_o - \rho) \quad (81)$$



## MODEL OF TURBULENT PLUME Continued

A rigorous solution of the plume shape requires definition of the surface as a function of height above the heat source. The shape of this surface depends on all factors already incorporated into the plume model as well as the deformation and bending caused by currents. Semiempirical solution of the force equations have been made by Bryant and Cowdrey (124) for the effect of wind on smoke plumes. The analytical solution for the ocean problem remains to be developed.

Ocean currents are slower than atmospheric winds. On the other hand, estimated initial plume velocities are also much smaller than gases leaving a stack. In the presence of ocean currents, the plume penetration could be conceivably only 20 to 50 percent of that calculated from the idealized model.

## APPLICATIONS

The plume model developed in the preceding section is illustrated for three different applications. The specific problems and the calculated results are summarized in Tables X, XI, and XII.

Case 1 represents a 4,940 kw heat source with a diameter of 10 feet located 1,000 feet below the surface. The initial temperature difference between the plume and its surroundings is 10 F. The solution is based on constant ambient temperature of 65 F.

Case 2 represents a problem similar to Case 1. A heat source of 4,930 kw and 10 feet diameter is located at a depth of 300 feet. The initial temperature difference is 10 F. The vertical temperature gradient of the surrounding water is 0.00333 F per foot.

Case 3 approximates the plume anticipated from the prototype model which was tested in the shallow ocean as part of the last phase of this study. The intensity of the heat source for Case 3 application is 556 kw with 1.5 feet diameter located 25 feet below the surface. The initial temperature difference is 10 F with a constant surrounding temperature of 60 F. Appendix F illustrates the plume calculations for Case 3.

**RESULTS** The calculated results for the three plumes are summarized in Tables X, XI, and XII. The variation of the important parameters with penetration and depth are shown for Cases 1 and 3 in Figures 66 through 70. The plotted variables are mass flow ratio, temperature difference, plume radius, and mean velocity.

## CASE 1 SUMMARY OF CALC

Exchanger Depth = 1,000 ft

 $P_1$  Pressure = 316.5 Decibars (459.0) $t_o$  Surrounding Water Temperature = 18 $t_1$  Bulk Water Leaving Exchanger = 23 $w_1$  Vertical Velocity Leaving Exchanger $R$  Radius of Exchanger = 5.00 ft $z^*$  (From Plot) = 14 ft $(z-z^*) \Big|_{w \approx 0} = 1.333 (z-z^*) \Big|_{\Delta t = 0.1 \text{ C}}$  $\Delta t_{\max}$  at Plume Axis  $\Delta t_{\max} = 3.16 \Delta t$ Intensity of Heat Source  $Q = 16.861$  $F_1 = 0.020, \sqrt{F_1} = 0.142$ 

	<u>DESCRIPTION</u>	TOP OF EXCHANGER	
		<u>POINT 1</u>	<u>POINT 2</u>
1	$z$ Distance above Exchanger, ft	0	30
2	$(z-z^*)$ ft	-14	16
3	Depth from Surface, ft	1,000	970
4	Mean Bulk $\Delta t$ , C	5.556	1.611
5	Max $\Delta t$ at Plume Axis, C	5.556	5.091
6	$w$ Mean Vertical Velocity cm/sec	3.048	1.210
7	Mass Flow Ratio, $W/W_1$	1.000	3.448
8	$(i_o/i)$ Ambient/Plume	1.001533	1.000403
9	$R$ Radius of Plume, ft	5.0	14.8
10	$(z-z^*)^{1/3}$	-	2.52
11	$W$ g/sec	228,000	786,000

**A**

X TABLE X

## CALCULATED RESULTS

0 psia (459.0 psia)

18.333 C (65 F)  $dt_o/dz = 0$ 

23.889 C (75 F)

Exchanger = 3.048 cm/sec (0.1 ft/sec)

00 ft

 $C_{\infty} = 0.1 C_{\infty} = 1.333 \times 160 = 213 \text{ ft}$  $\Delta t = 3.16 \Delta t_{\text{Mean}}$  $Q = 16.861 \times 10^6 \text{ Btu/hr (4,940 kw)}$ 

<u>P 2</u>	<u>POINT 3</u>	<u>POINT 4</u>	<u>POINT 5</u>
	60	100	200
	46	86	186
	940	900	800
.611	0.510	0.217	0.068
091	1.612	0.686	0.215
210	0.851	0.691	0.534
448	10.90	25.65	82.08
000403	1.000102	1.000035	1.000001
8	31.3	53.2	108.2
52	3.58	4.41	5.71
2,484,000		5,846,000	18,709,000

B

TABLE XI

## CASE 2 SUMMARY OF CALCULATIONS

Exchanger Depth = 300 ft

 $P_1 = 102.0$  Decibars (147.9 psia) $t_o$  SurroundingAt top of Exchanger  $t_{o1} = 20.556$  C

$$dt_o/dz = \frac{21.111 - 20.556}{300} = 0.0018$$

 $t_1$  Leaving Exchanger = 26.111 C (79 F) $w_1$  Vertical Velocity Leaving Exchanger $R$  Radius of Exchanger = 5.0 ft $z^*$  (From Plot) = 14. ft

$$(z-z^*) \Big|_{w \approx 0} = 1.333 (z-z^*) \Big|_{t = 0.1 \text{ C}}$$

 $\Delta t$  max at Plume Axis  $\Delta t$  max = 3.16 CIntensity of Heat Source  $Q = 16.833$  MW

$$F_1 = 0.019, \quad \sqrt{F_1} = 0.139$$

DESCRIPTION	TOP OF EXCHANGER	
	POINT 1	POINT 2
1 $z$ , ft	0	15
2 $(z-z^*)$ ft	-14	1
3 Depth, ft	300	285
4 Mean $t$ , C	5.555	5.046
5 Max $t$ , C	5.555	5.555
6 $w$ , cm/sec	3.048	3.048
7 $w/w_1$	1.000	1.095
8 $(t_o/t_1)$	1.001602	1.001575
9 $R$ , ft	5.0	5.2
10 $(z-z^*)^{1/3}$	-	1
11 $W$ q/sec	228,000	249,000

A

# TABLE XI

## SUMMARY OF CALCULATED RESULTS

psia)

5 C - 20.556 C (69 F)

83 <sup>6</sup> = 0.00185 C/ft

F) 111 C (79 F)

Exchanger = 3.048 cm/sec (0.1 ft/sec)

0 ft

C:  $\Delta t = 0.1 C \approx 0 = 1.333 \times 110 = 147$  ft

$\Delta t_{max} = 3.16 \Delta t_{mean}$

3 Q =  $16.833 \times 10^6$  Btu/hr (4.930 kw)

### POINT 3

30

16

270

1.544

4.879

1.210

3.536

1.000521

14.9

2.52

### POINT 4

60

46

240

0.449

1.419

0.851

11.26

1.000245

31.6

3.58

### POINT 5

100

86

200

0.141

0.446

0.891

26.86

1.000154

81.7

4.41

500,000

2,563,000

5,000,000

**B**

TABLE XII

## CASE 3 SUMMARY OF CALCUL

Exchanger Depth = 25 ft

 $P_1$  Pressure = 17.6 Decibars (25.5 psia) $t_o$  Surrounding = 15.556 C (60 F) $t_1$  Leaving Exchanger = 21.111 C (70 F) $w_1$  Vertical Velocity Leaving Exchanger $R$  Radius of Exchanger = 0.75 ft $z^*$  (From Plot) = 6 ft $(z-z^*)|_{w \approx 0} = 1.333 (z-z^*)|_{\Delta t = 0.1 \text{ C} \approx 0.1 \text{ F}}$  $\Delta t$  max at Plume Axis  $\Delta t$  max = 3.16  $\Delta t$ Intensity of Heat Source  $Q = 1.898 \times 10^6$  W $F_1 = 3.735$ ,  $\sqrt{F_1} = 1.933$ 

DESCRIPTION	TOP OF EXCHANGER		
	POINT 1	POINT 2	POINT 3
1 $z$ , ft	0	5	10
2 $(z-z^*)$ ft	-6	-1	4
3 Depth, ft	25	20	15
4 Mean $\Delta t$ , C	5.555	5.206	2.427
5 Max $\Delta t$ , C	5.555	5.555	5.555
6 $w$ , cm/sec	15.240	$\approx 15$	9.585
7 $W/W_1$	1.000	1.067	2.289
8 $(f_o/f)$	1.001387	1.001287	1.00057
9 $R$ , ft	0.75	$\approx 0.78$	1.436
10 $(z-z^*)^{1/3}$	-	-	1.59
11 $W$ g/sec	25,700	27,400	58,700

A

## I TABLE XII

## SUMMARY OF CALCULATED RESULTS

iairs (25.5 psia)

(60 F)

F) .111 C (70 F)

er ng Exchanger = 15.240 cm/sec (0.5 ft/sec)

1.75 ft

$\Delta t_o = 0.1 C_{\infty} = 1.333 \times 68 = 91$  ft

$\Delta t_{\max} = 3.16 \Delta t_{\text{mean}}$

$Q = 1.898 \times 10^6$  Btu/hr (556 kw)

<u>POINT 3</u>	<u>POINT 4</u>	<u>POINT 5</u>	<u>POINT 6</u>
10	15	20	25
4	9	14	19
15	10	5	0
2.427	1.236	0.766	0.528
5.555	3.906	2.421	1.668
9.585	7.327	6.324	5.697
2.289	4.494	7.249	10.525
1.000567	1.00273	1.000179	1.000110
1.436	2.297	3.141	3.993
1.59	2.08	2.41	2.675
1,700	115,000	186,000	270,000

**B**

## APPLICATIONS Continued

Cases 1 and 2 differ in the ocean depth and the ambient temperature gradient. The results in Tables X and XI indicate even a relatively small ambient temperature gradient appreciably reduces penetration of the plume. The initial buoyancy is the same for the two cases. At a penetration of 100 feet above the heat source, the mean bulk  $\Delta t$  is 0.141C for Case 2 against 0.217 C for Case 1. Figure 66 shows the mean bulk  $\Delta t$  or buoyancy decay for all cases. For Case 2, the calculated results are shown for both constant ambient temperature and a vertical gradient of 0.00333 F per foot.

For a given heat source geometry and intensity, Figure 66 shows the ideal plume does not vary significantly over a depth of a few thousand feet. With a vertical ocean gradient, buoyancy decay is initially the same as for the constant temperature case. Beyond a penetration of about 40 feet, buoyancy decay accelerates and becomes very steep for Case 2. Since momentum and velocity decay follow a similar increasing pattern, the velocities calculated in Table XI are only approximate for Case 2. The actual velocities can be estimated from Figure 68 since momentum decay is complete at about 150 feet for Case 2 and essentially the same as for Case 1 up to a penetration of about 40 feet.

The temperature difference or buoyancy decay plot in Figure 66 serves as the basis for two plume parameters. The first is the fictitious distance  $z^*$  above which the  $-5/3$  decay law becomes valid. The second is the distance where the mean bulk  $\Delta t$  is 0.1 degree C and can be assumed fully dissipated. The following results are obtained from Figure 66.

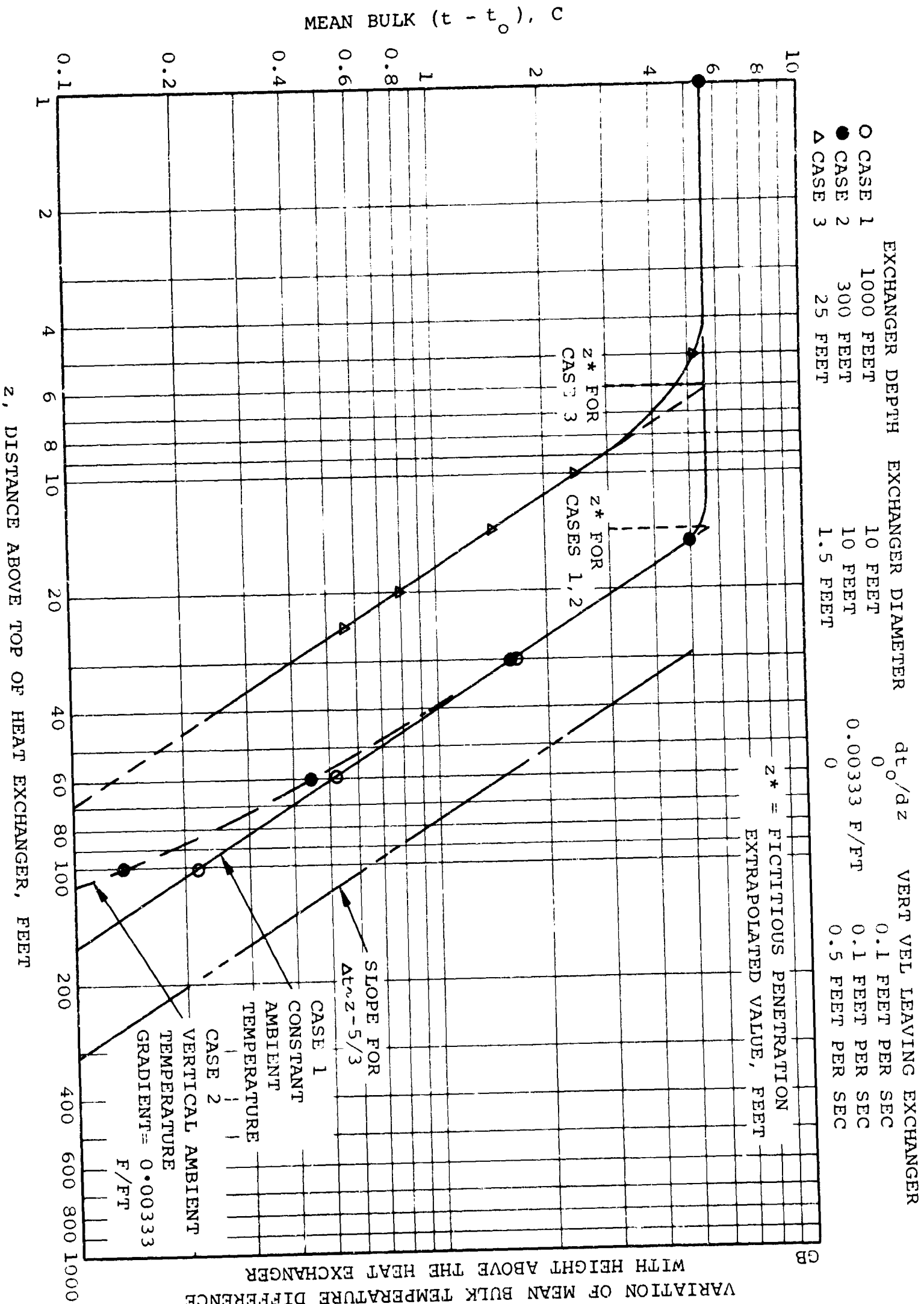
	<u>CASE 1</u>	<u>CASE 2</u>	<u>CASE 3</u>
Fictitious distance $z^*$ , feet	14	14	6
Distance at $\Delta t = 0.1$ C, feet	160	110	68
Maximum penetration, feet	213	147	91
Ratio $z^*/d$ .	1.4	1.4	4
$\sqrt{F_1}$	0.142	0.139	1.933

The maximum penetration is 1.333 times the distance at  $\Delta t$  equal to 0.1 C. In Figure 68, the accelerated decay of velocity beyond 200 feet penetration is shown to emphasize the fact that the simple  $-1/3$  power law is valid up to some 80 percent of the total penetration. For Case 3 this point cannot be shown in Figure 70 since the velocity profile is not complete at 25 feet penetration and disappears abruptly when the air-water interface is reached.



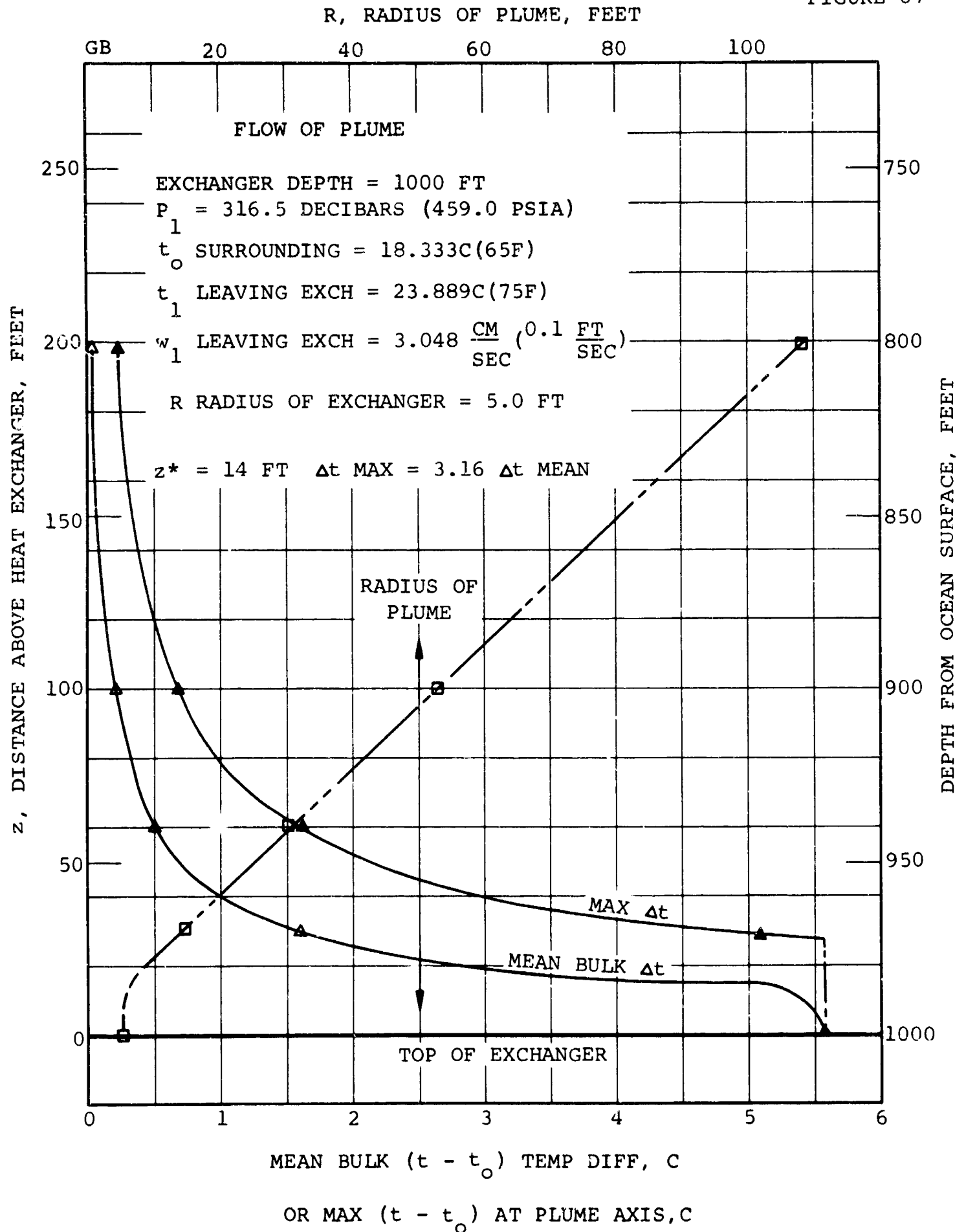
FIGURE 66

VARIAION OF MEAN BULK TEMPERATURE DIFFERENCE WITH HEIGHT ABOVE THE HEAT EXCHANGER



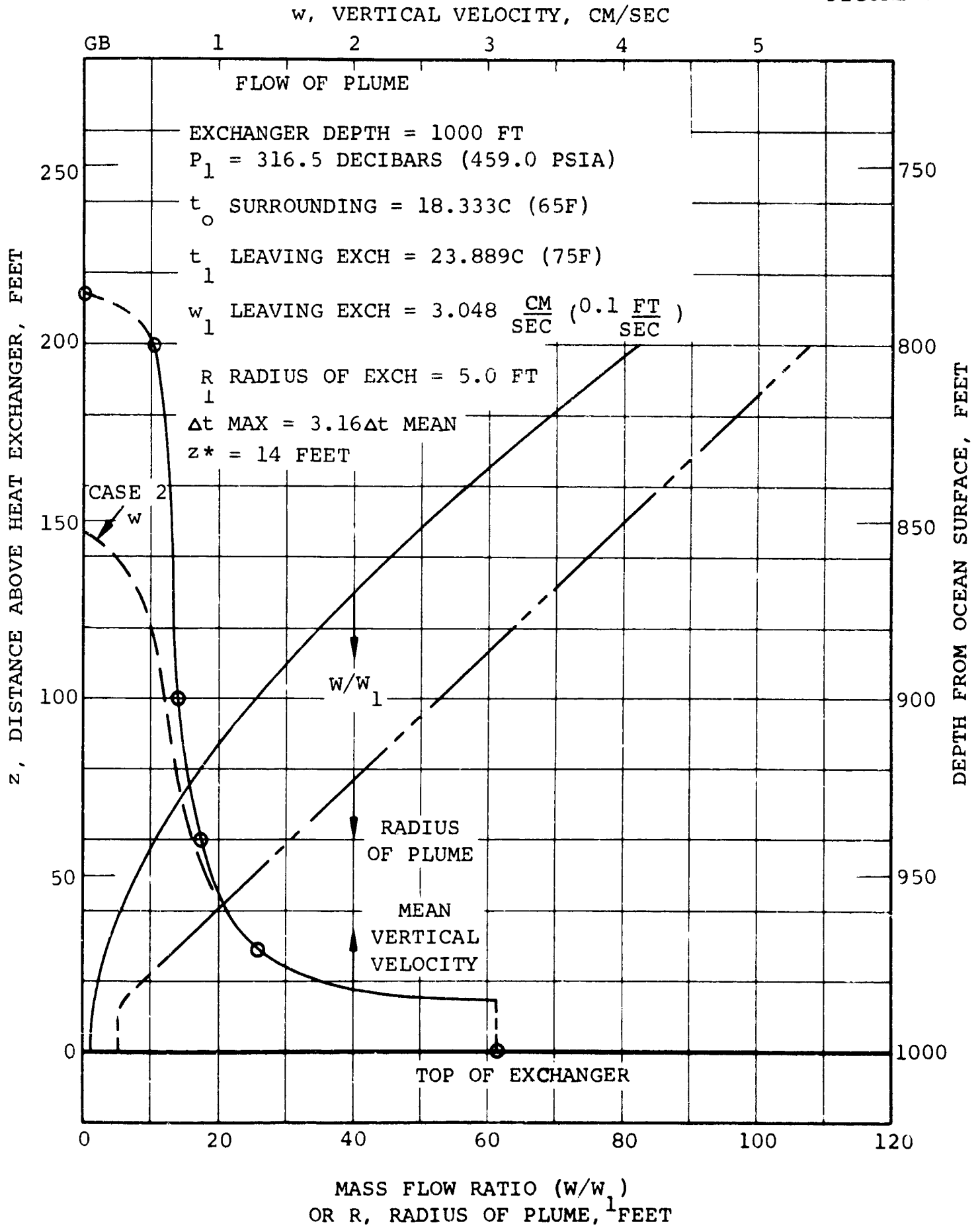
CASE 1 EXCHANGER DEPTH 1000 FEET  
 VARIATION OF TEMPERATURE  
 DIFFERENCE AND RADIUS OF PLUME WITH HEIGHT

FIGURE 67



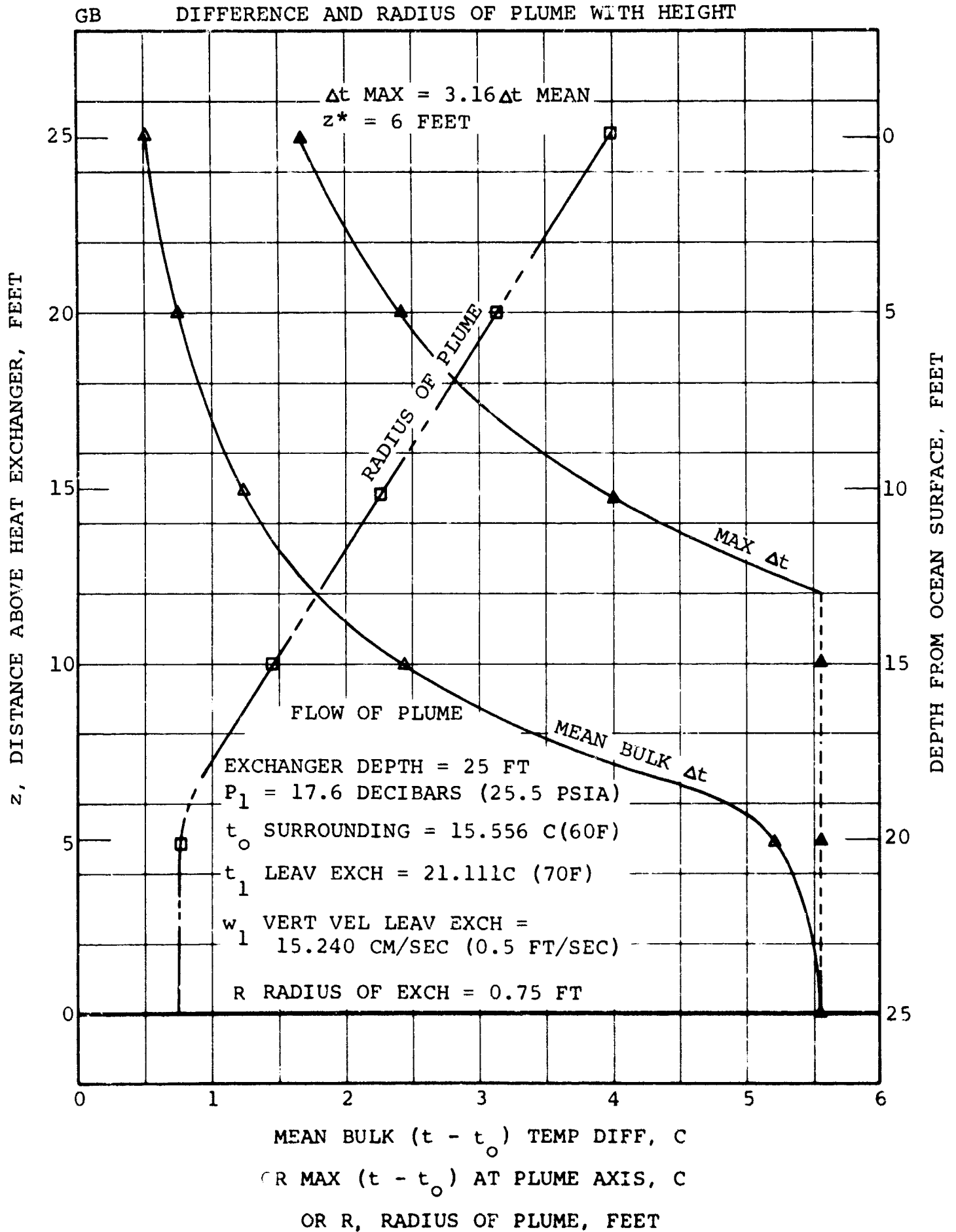
CASE 1 EXCHANGER DEPTH 1000 FEET  
 VARIATION OF MASS FLOW RATIO, VERTICAL  
 VELOCITY AND RADIUS OF PLUME WITH HEIGHT

FIGURE 68



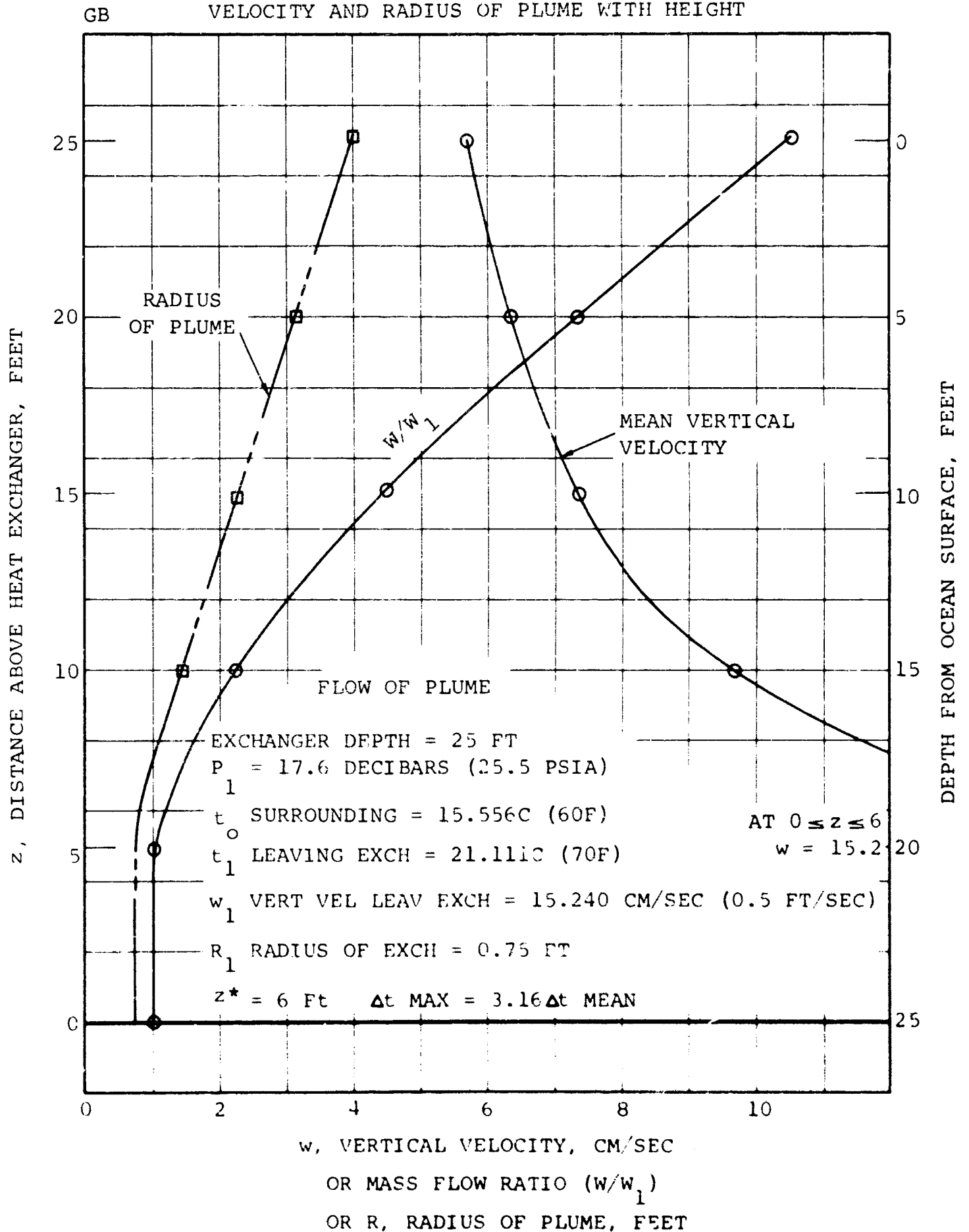
CASE 3 EXCHANGER DEPTH 25 FEET  
VARIATION OF TEMPERATURE

FIGURE 69



CASE 3 EXCHANGER DEPTH 25 FEET  
 VARIATION OF MASS FLOW RATIO, VERTICAL  
 VELOCITY AND RADIUS OF PLUME WITH HEIGHT

FIGURE 70



## APPLICATIONS Continued

Cases 1 and 2 indicate for the anticipated depth limits of 300 to 20,000 feet the plume penetration cannot reach the ocean surface. Relatively strong currents generally prevail in the surface layer due to external forces, such as wind and tidal effects. These currents would actually dissipate the plume much faster than, for instance, the calculated value of 147 feet for Case 2 (Table XI). A rough estimate would be a penetration 30 percent that of the value from the idealized model, or about 44 feet.

The diameter and intensity of the heat source are two design parameters which affect the distance required for development and temperature profile of the ideal plume. The initial intensity of the plume is characterized by the dimensionless function  $\sqrt{F_1}$ . For the three cases represented in this section, 1.4 diameters are required to initiate development of the plume when  $\sqrt{F_1}$  is 0.14 and 4 diameters when  $\sqrt{F_1}$  is 1.93.

## EXPERIMENTAL RESULTS AND DISCUSSION

Temperature measurements for the liquid plume and the surrounding water were made during the course of the natural convection heat transfer experiments. The apparatus, instrumentation, and procedure for the heat transfer tests are described in Chapter IV. The temperature data used for analysis of the turbulent plume and comparison with the predicted model plume are classified into four sets. Table XIII identifies the four groups of data.

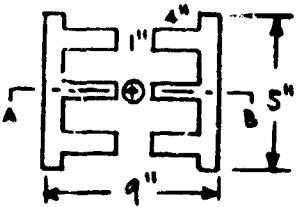
- Set 1 Vertical finned flat plate in simulator
- Set 2 Vertical finned cylinder in simulator
- Set 3 Vertical finned cylinder in shallow ocean without shroud
- Set 4 Vertical finned cylinder in shallow ocean with shroud

**VERTICAL FINNED FLAT PLATE** Set 1 data were obtained with the vertical finned flat plate in the simulator. The simulator test facility is shown in Figures 37 and 38. The vertical finned flat plate is illustrated in Figures 39, 40, and 41. The plume temperatures were measured with the temperature probe shown in Figure 45. The test unit was submerged 9 feet below the surface.

One set of vertical temperatures were measured at a distance of 3/4 inch from the vertical axis of the unit up to a distance of 7.3 feet from the top of the heat source. The horizontal profile data consisted of nine measurements symmetrically spaced from the vertical axis of the heat source, along the axis AB in Table XIII. The horizontal profile of the plume was measured at 0.5 foot intervals starting at the top of the heat source and extending 9 feet above the heat source.

TABLE XI

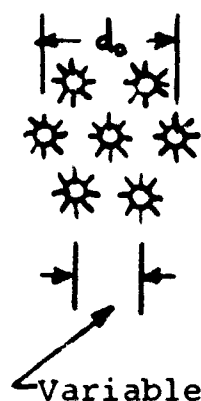
## PLUME HEAT SOURCE

<u>ITEM</u>		DATA SET 1 <u>TOP VIEW</u>	
1	Heat source geometry		
2	Test conditions		Vertical finned flat plate in simulator
3	Overall dimensions of source, inches		5 x 9
4	Cross sectional area, A sq ft		0.312
5	Equivalent circle radius, R ft	0.316	0.365
6	Equivalent circle diameter, $d_o$ ft	0.632	0.730
7	Heat flow, Q Btu per sec	46.0	
<u>BASIS FOR PREDICTED PLUME</u>			<u>At</u>
8	Ambient temperature at source, $t_o$ F	72.2	
9	Plume temperature at source, $t_1$ F	85.4	
10	Initial temperature difference, $\Delta t_1$ F	13.2	
11	Initial mass flow rate, $w_1$ lb/sec	3.48	
12	Initial velocity, $w_1$ ft/sec	0.179	
13	Froude number, $F_1$	0.800	
14	Plume intensity parameter, $\sqrt{F_1}$	0.894	
15	Distance for plume development, $z^*$ ft	1.88	
16	Ratio $z^*/d_o$ , diameters	3.0	

A

TABLE XIII

## HEAT SOURCE DIMENSIONS

DATA SET 2  
TOP VIEW

Vertical finned 2-inch cylinders in simulator

8.75- to 10.5-inch diameter

0.419 to 2.41

0.365 to 0.875

0.730 to 1.750

46.4

At  $d_o = 1.0$  ft

74.6

84.9

10.3

4.50

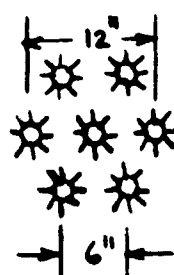
0.092

0.167

0.409

2.1

2.1

DATA SET 3  
TOP VIEW

Vertical finned 2-inch cylinders in shallow ocean without shroud

12-inch diameter

0.5

1.0

0.785

47.2

58.5

64.5

6.0

7.87

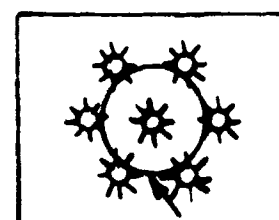
0.160

0.397

0.630

2.6

2.6

DATA SET 4  
TOP VIEW

Shroud hole  
10-inch diameter

Vertical finned 2-inch cylinders in shallow ocean with shroud

10-inch diameter

0.417

0.834

0.545

47.2

58.5

64.5

6.0

7.87

0.231

0.993

0.996

2.6

3.1

**B**



## EXPERIMENTAL RESULTS AND DISCUSSION Continued

The mean bulk plume temperature at a given elevation was calculated by graphical integration of the point temperature data. Typical plots showing the temperature averaging technique are shown in Figures 71 and 72 at elevations of zero and 0.5 feet above the heat source. Similar figures were prepared at the other elevations.

Figure 73 shows two vertical axis profiles of the plume temperature along with the profile of the mean bulk plume temperature. The sharp rise in the vertical axis profiles indicates the boundary layers of hot water leaving the vertical fins require about 1 to 2 feet to attain a uniform plume core temperature. The white dots representing the profile closer to the boundary layer leaving the flat faces of the fins indicate faster mixing than the black dots representing the profile between the fin ends.

In Figure 73, the mean bulk plume temperature initially drops sharply from 85.4 to about 79 to 80 F, remains constant for about 3.5 foot elevation, and then rises sharply to a final uniform temperature of about 87 F. The most plausible explanation for this trend is that over the 1-foot height above the heat source, there is appreciable entrainment of cold ambient water available at the periphery of the plume. Beyond a height of 1 foot the entrainment and buoyancy decay rate is virtually zero. We believe the cause of reduced entrainment is stratification of the ambient water in the simulator and the relative diameters of the plume and the simulator.

Fresh water flow rate of 15 gpm was maintained during all tests. The vertical velocity of this flow is 0.001 feet per second. Apparently, in spite of the elimination of vertical stratification, a simulator to heat source diameter ratio of  $(5.5/0.632)$  or 8.7 is nowhere adequate for the normal propagation of the plume. In the ocean, this ratio is infinite. The trend of the mean bulk temperature in Figure 73 beyond  $z = 5$  feet can be due to calorimetric mixing of the water towards the top of the simulator. The data show definitely the presence of the warmer water at distances greater than 5 feet above the heat source.

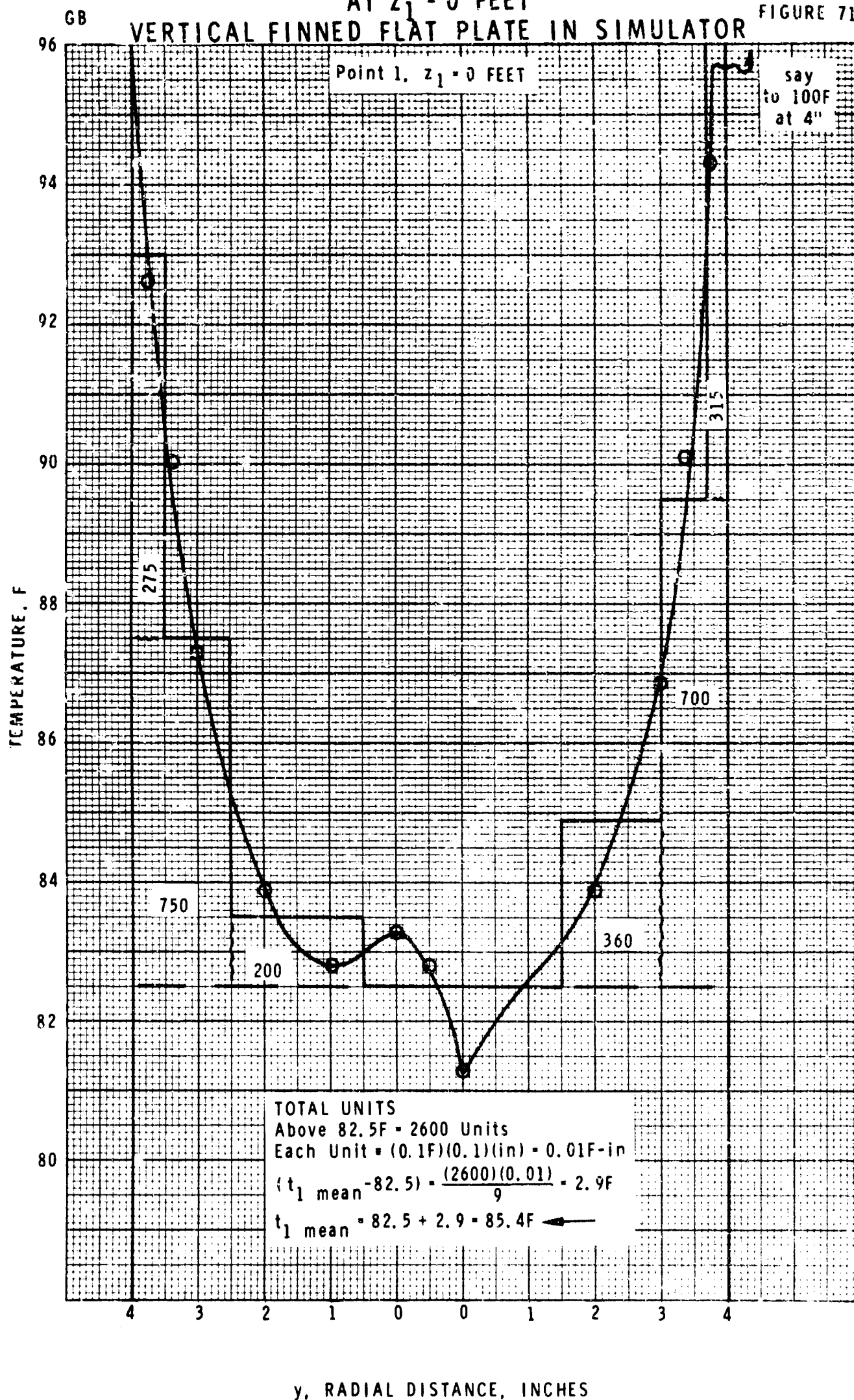
Figure 74 shows the mean bulk temperature difference between the plume and its surroundings. The experimental results are based on the initial ambient temperature of 72.2 F. If the true effective ambient temperature were known as a function of  $z$ , then it could be shown that the  $\Delta t$  actually approaches zero at distances above 5 feet. The predicted buoyancy or  $\Delta t$  profile is based on the known initial source conditions. In general, the predicted and experimental results seem comparable in the region up to  $z = 2$  feet where evidence of entrainment is shown also by the mean bulk temperature in Figure 73.

## SET 1 MEAN PLUME TEMPERATURE

AT  $z_1 = 0$  FEET

## VERTICAL FINNED FLAT PLATE IN SIMULATOR

FIGURE 71

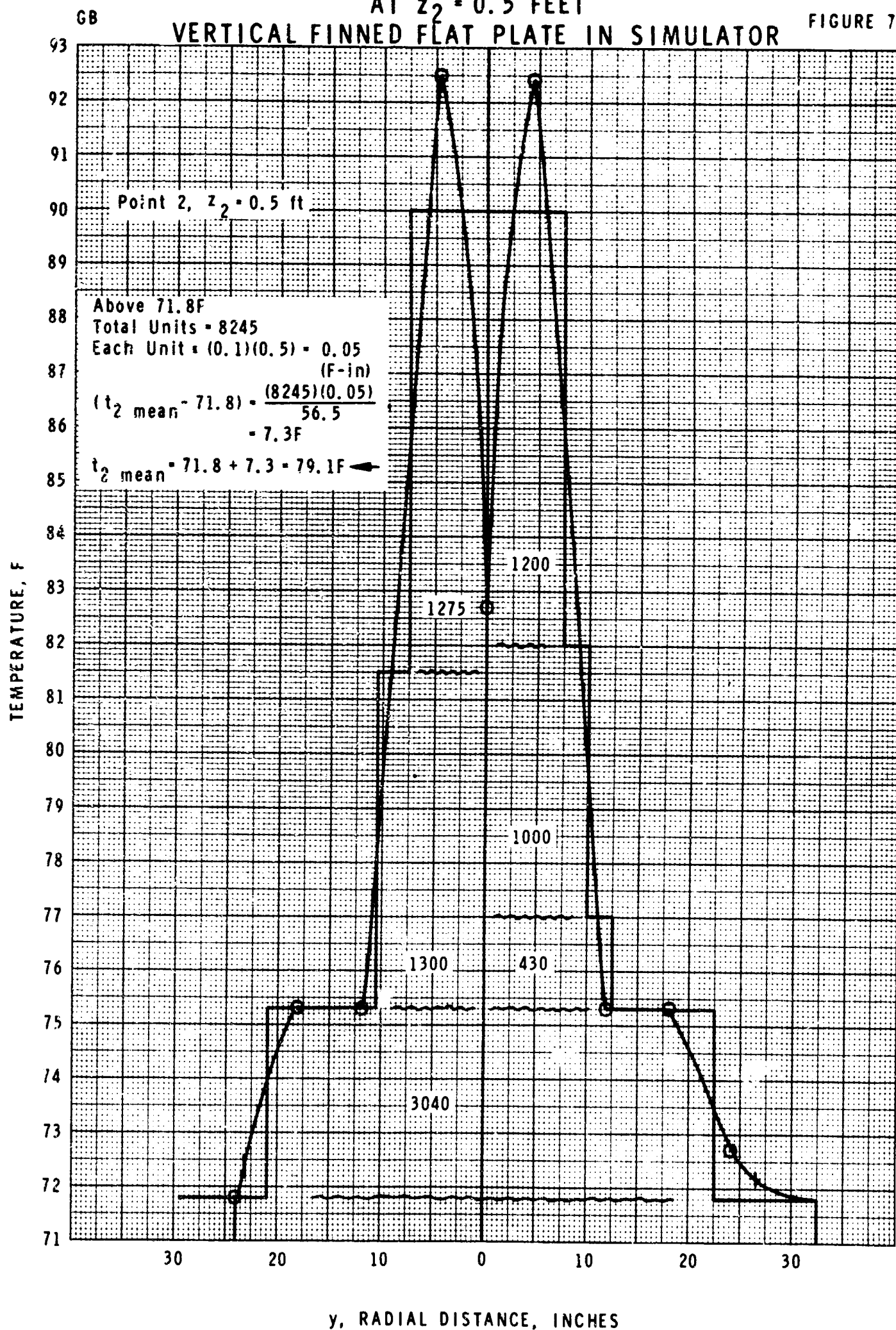


## SET 1 MEAN PLUME TEMPERATURE

AT  $z_2 = 0.5$  FEET

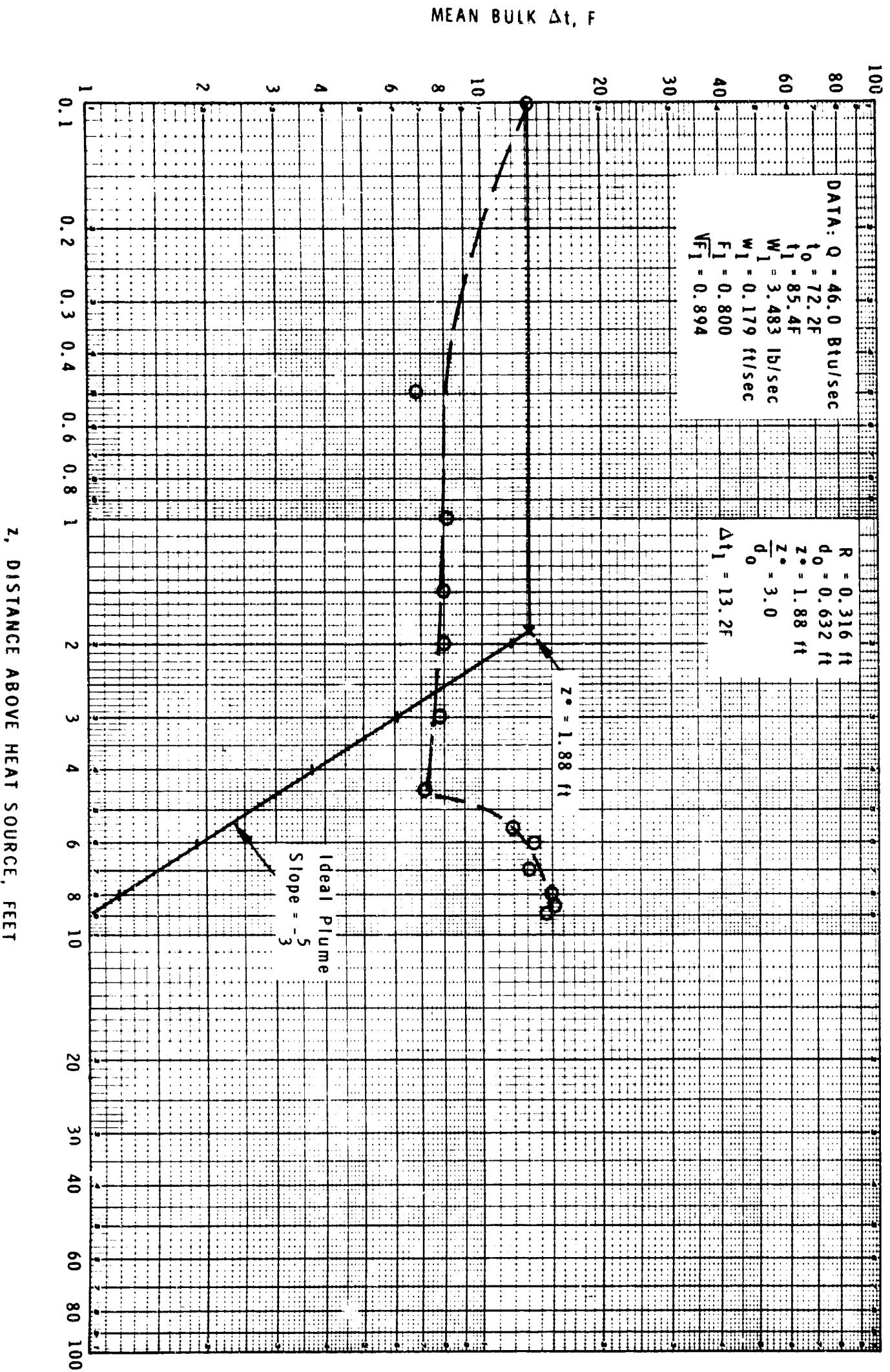
## VERTICAL FINNED FLAT PLATE IN SIMULATOR

FIGURE 72



# SET 1 PLUME BUOYANCY DECAY VERTICAL FINNED FLAT PLATE IN SIMULATOR

FIGURE 74



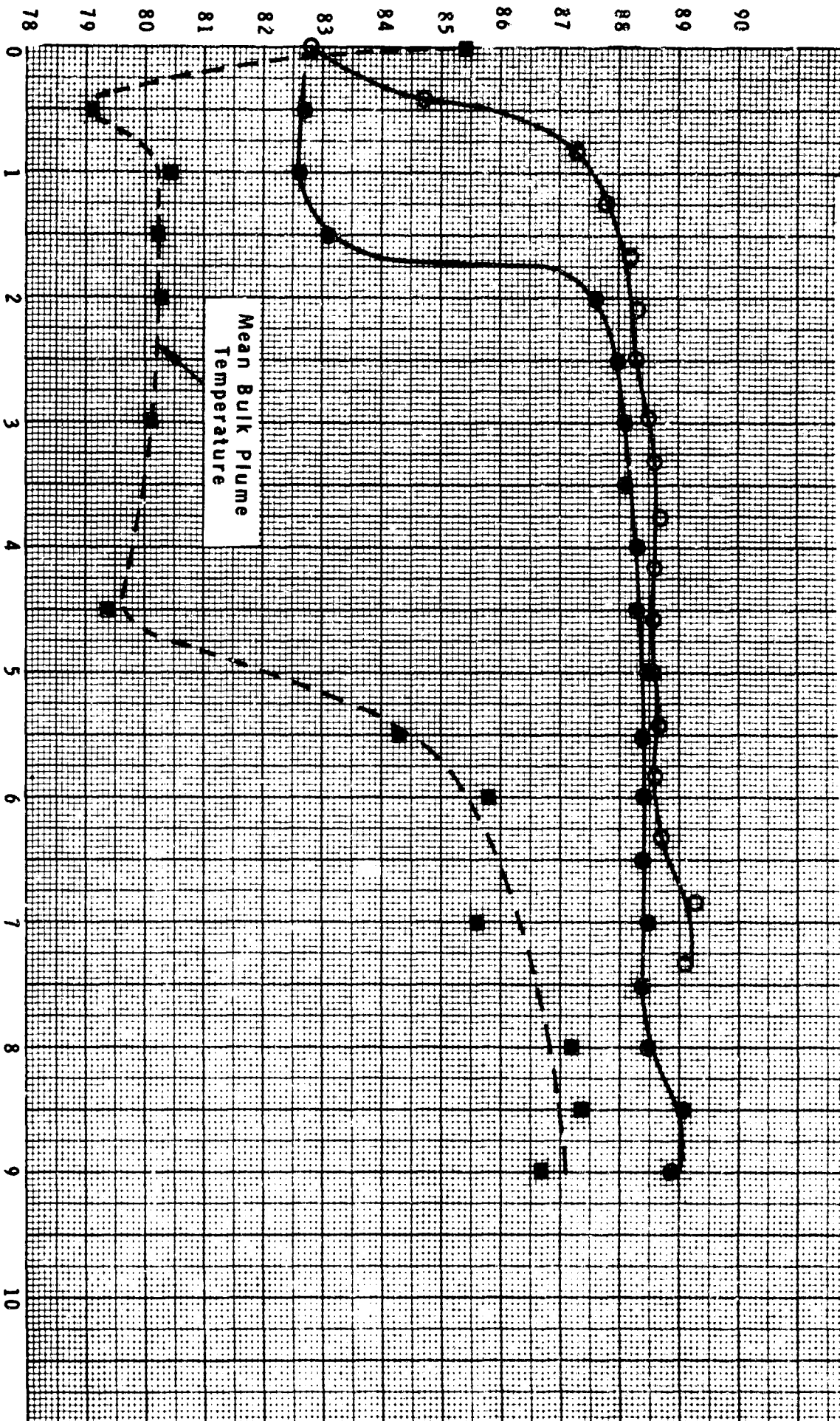
TEMPERATURE, F

CB

# SET 1 PLUME TEMPERATURE PROFILE VERTICAL FINNED FLAT PLATE IN SIMULATOR

FIGURE 73

- Q - 46.0 Btu/sec,  $t_0$  Ambient - 72.2F,  $F_1$  - 0.800,  $\sqrt{F_1}$  - 0.894
- Vertical Profile at Position X - 3/4-Inch South of True Vertical Axis
- Vertical Profile at True Vertical Axis - Center of A-B Traverse
- Mean Plume Temperature - Graphical Integration



Z, DISTANCE ABOVE HEAT SOURCE, FEET

## EXPERIMENTAL RESULTS AND DISCUSSION Continued

Figure 75 gives the predicted plume radius and flow rate in pounds per second. The experimental results of  $W$  based on the known heat flow and the mean bulk  $\Delta t$  are also shown in the figure. The flow rate  $W$  apparently does not change with penetration. This follows the earlier observation that beyond  $z = 1$  to 2 feet, there was no entrainment or propagation of the plume.

**VERTICAL FINNED CYLINDER IN SIMULATOR** Set 2 data were obtained with the cluster of seven 2-inch diameter vertical finned cylinders in the simulator. Figures 42 and 43 give details of the heat exchanger design. The temperature probe shown in Figure 45 was used to measure the simulator water temperature. The test unit was submerged 4 feet below the surface.

Plume water temperature measurements were limited to two vertical positions, at the top and 4 inches above the top of the test unit. From the previous test results with the flat-plate unit, it became apparent that propagation of the plume from the heat source tested could not be adequately studied in the simulator. The size of the test units of interest for the heat transfer studies resulted in simulator to source diameter ratios which were too small. The test data describe the variation of the plume source intensity at constant heat flux. Data were taken at center-to-center spacings of 4.38, 6, 6.5, 8.5, and 10.5 inches, and with 18-, 19.5-, and 21-inch chimney diameters at 6-inch spacing of the cylinders. Table XIII describes the range of plume source parameters covered by the data.

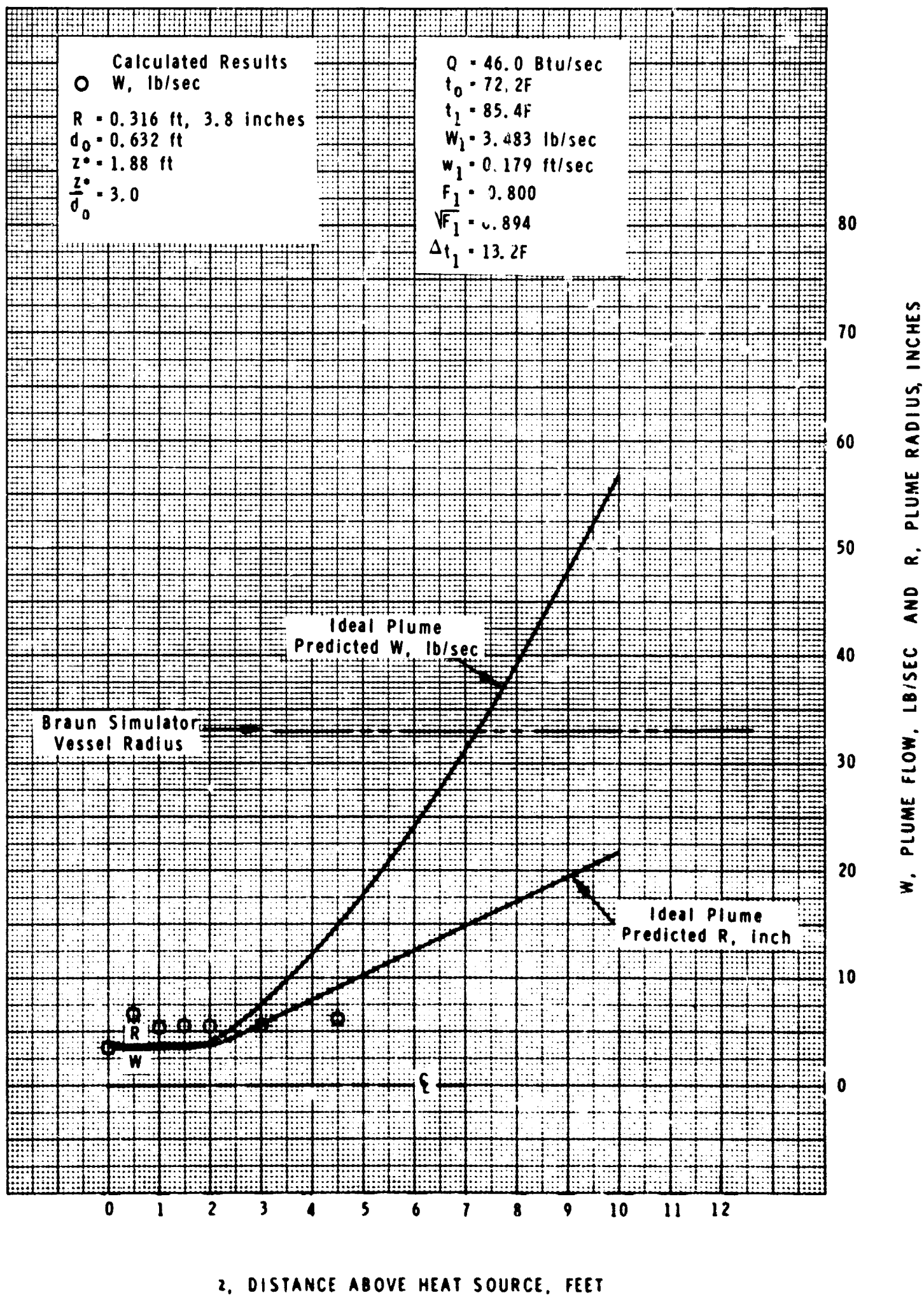
Figure 76 shows the variation of the initial mean bulk  $\Delta t$  as a function of the equivalent circular area. The most objective basis for the equivalent source radius has been assumed to be the center-to-center distance between the center cylinder and any of the outer cylinders. The trend of the curve in Figure 76 is interesting because some useful conclusions can be deduced about the intricate factors which affect the source intensity of the plume. Generally, it is difficult to assess the combined effects of spacing and open area on the entrainment rate over the height of the heat source and on the resulting intensity of the plume. Figure 76 indicates that over a threefold change of the equivalent area, from 0.8 to 2.4 square feet, the initial  $\Delta t$  is essentially constant at about 10.5 to 11.0 F. Only when the tip of the fins are virtually touching at  $A = 0.42$  square feet, a significant change in the decrease of the entrainment rate over the exchanger height results in a sharply increased  $\Delta t_1$ . Interestingly, the point representing the Set 1 data with vertical plate unit follows the trend established by the vertical cylinder data.



# SET 1 PLUME PROFILE VERTICAL FINNED FLAT PLATE IN SIMULATOR

GB

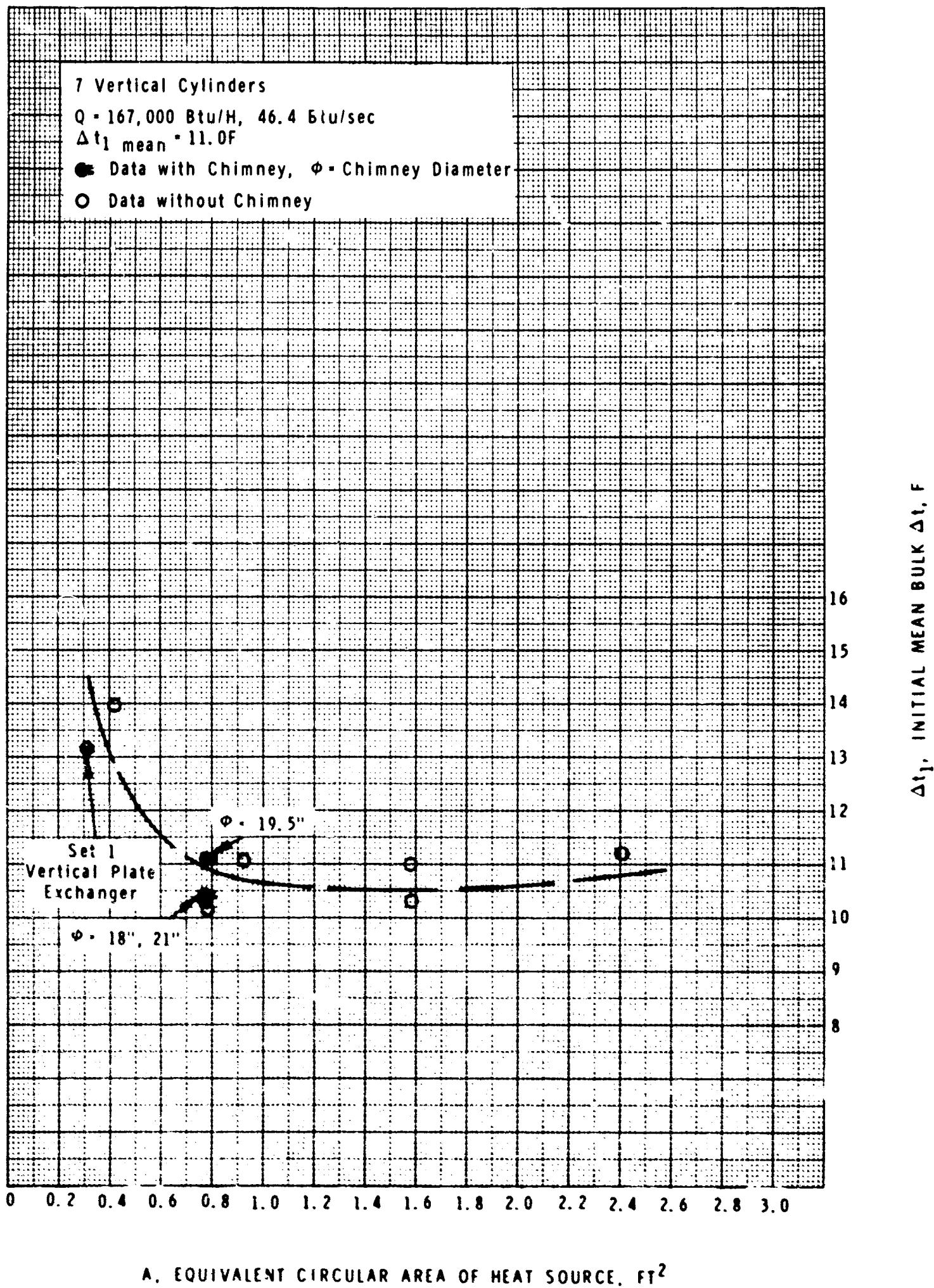
FIGURE 75



# SET 2 PLUME BUOYANCY AT SOURCE VERTICAL FINNED CYLINDERS IN SIMULATOR

GB

FIGURE 76





## EXPERIMENTAL RESULTS AND DISCUSSION Continued

The experimental data give the initial plume flow rate and velocity results plotted in Figure 77. Mass flow rate follows a trend in line with the  $\Delta t_1$  results. Velocity variation is more involved inasmuch as it depends on both the equivalent area and the mass flow rate. In Figure 77, the vertical plate results lie in the vicinity of the vertical cylinder curves.

Based on the results in Figures 76 and 77, we calculated the plume intensity parameter  $\sqrt{F_1}$  for the various geometries tested. Figure 78 shows the plume intensity as a function of source area. The results with chimneys around the heat source are also shown in Figures 76, 77, and 78. The chimney with relatively large diameter does not seem to affect appreciably the heat transfer process and the resultant plume.

We have calculated the model plume predicted for the initial conditions corresponding to the heat exchanger with 6-inch center-to-center spacing. Figure 79 gives the buoyancy decay curve and Figure 80 shows the mass flow rate and radius profiles. In Figure 79, the predicted buoyancy decay curve for the flat-plate unit is superimposed on that of the vertical cylinder. It is interesting to note that differences in the initial  $\Delta t_1$  and source diameter affect the predicted break point  $z^*$  and the resulting ratio of  $(z^*/d_o)$  in diameters. Table XIII shows that when  $\sqrt{F_1}$  increases from 0.409 to 0.894 for the two test units, the predicted value of  $(z^*/d_o)$  increases from 2.1 to 3.0 diameters.

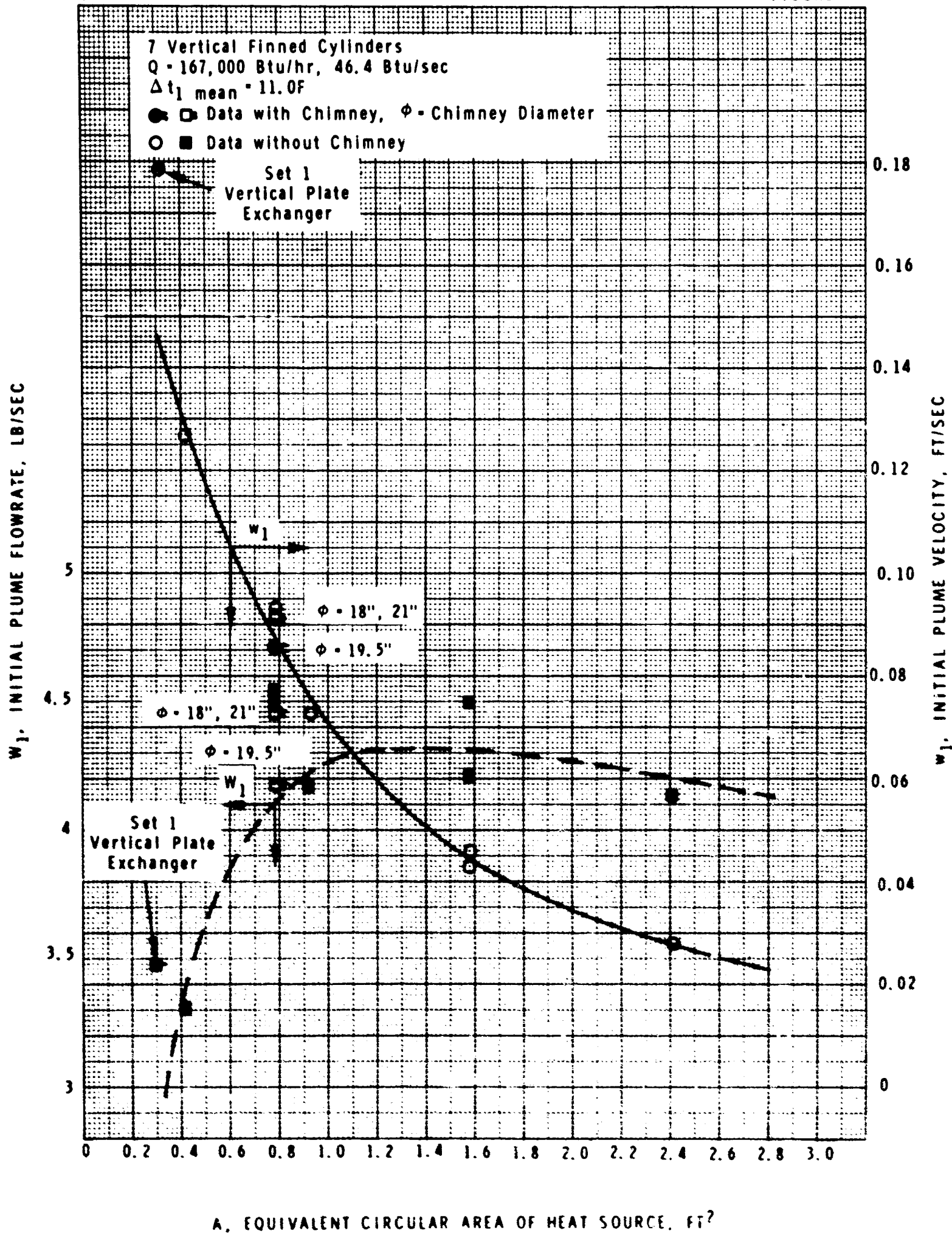
We believe the important conclusion from the Set 2 data is that over a wide range of cylinder spacings the initial mass flow rate and the  $\Delta t$  of the resultant plume are essentially constant. As the spacing increases and flow and  $\Delta t$  parameters remain unchanged, the initial intensity of the plume decreases (Figure 78).

**VERTICAL FINNED CYLINDER IN SHALLOW OCEAN** The same vertical cylinder which was used for the Set 2 experiments in the simulator was also tested in the shallow ocean. The 2-inch vertical finned cylinders were arranged with a 6-inch center-to-center spacing. Figure 63 is a photograph of the prototype natural convection heat transfer unit. Plume temperature measurements were made with the top of the heat source about 30 feet below the ocean surface. In order to investigate the effect of plume source intensity, additional data were obtained with a shroud installed at the top of the heat exchanger. The shroud had a 10-inch diameter hole at the top.

# SET 2 PLUME FLOW RATE AND VELOCITY AT SOURCE VERTICAL FINNED CYLINDERS IN SIMULATOR

GB

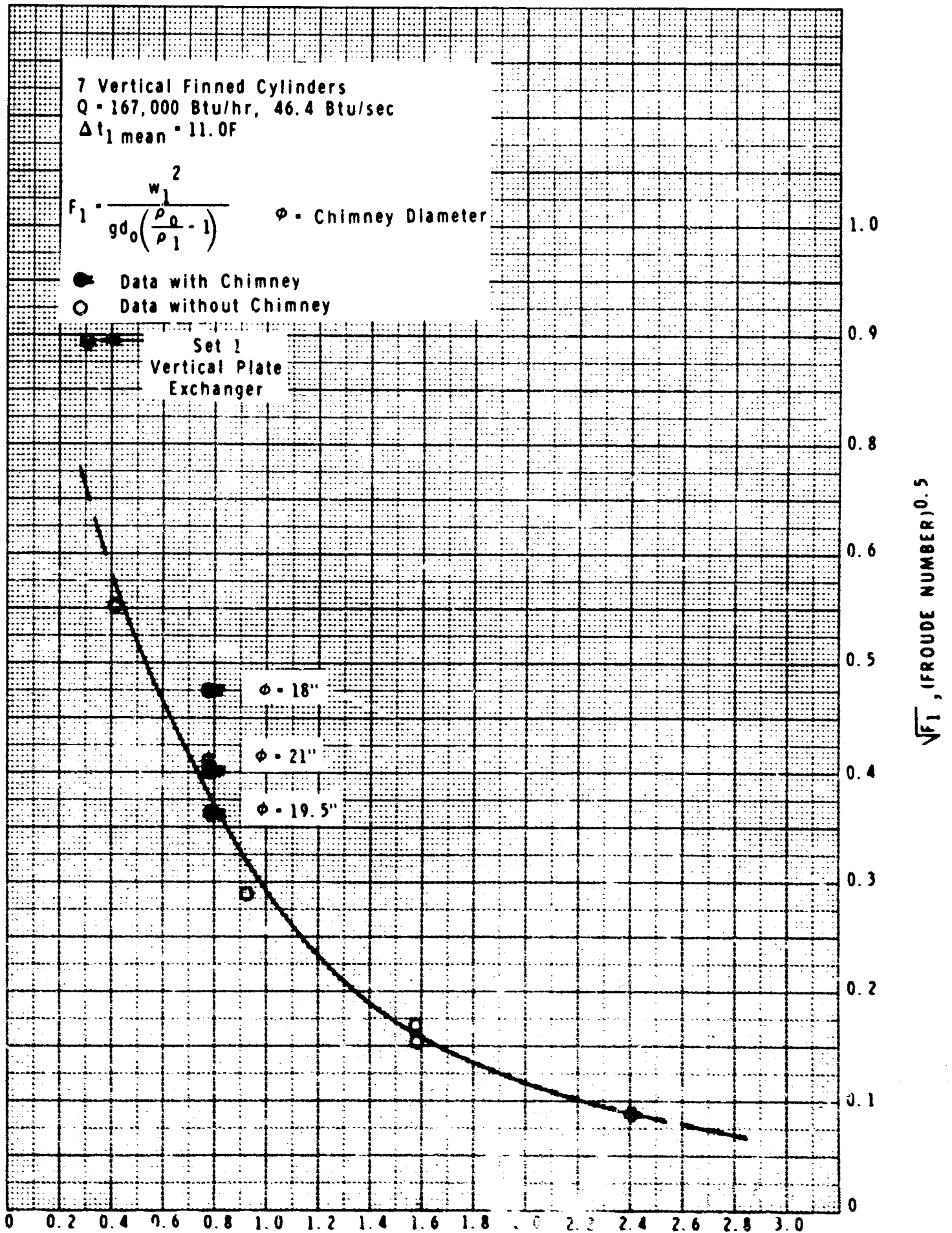
FIGURE 77



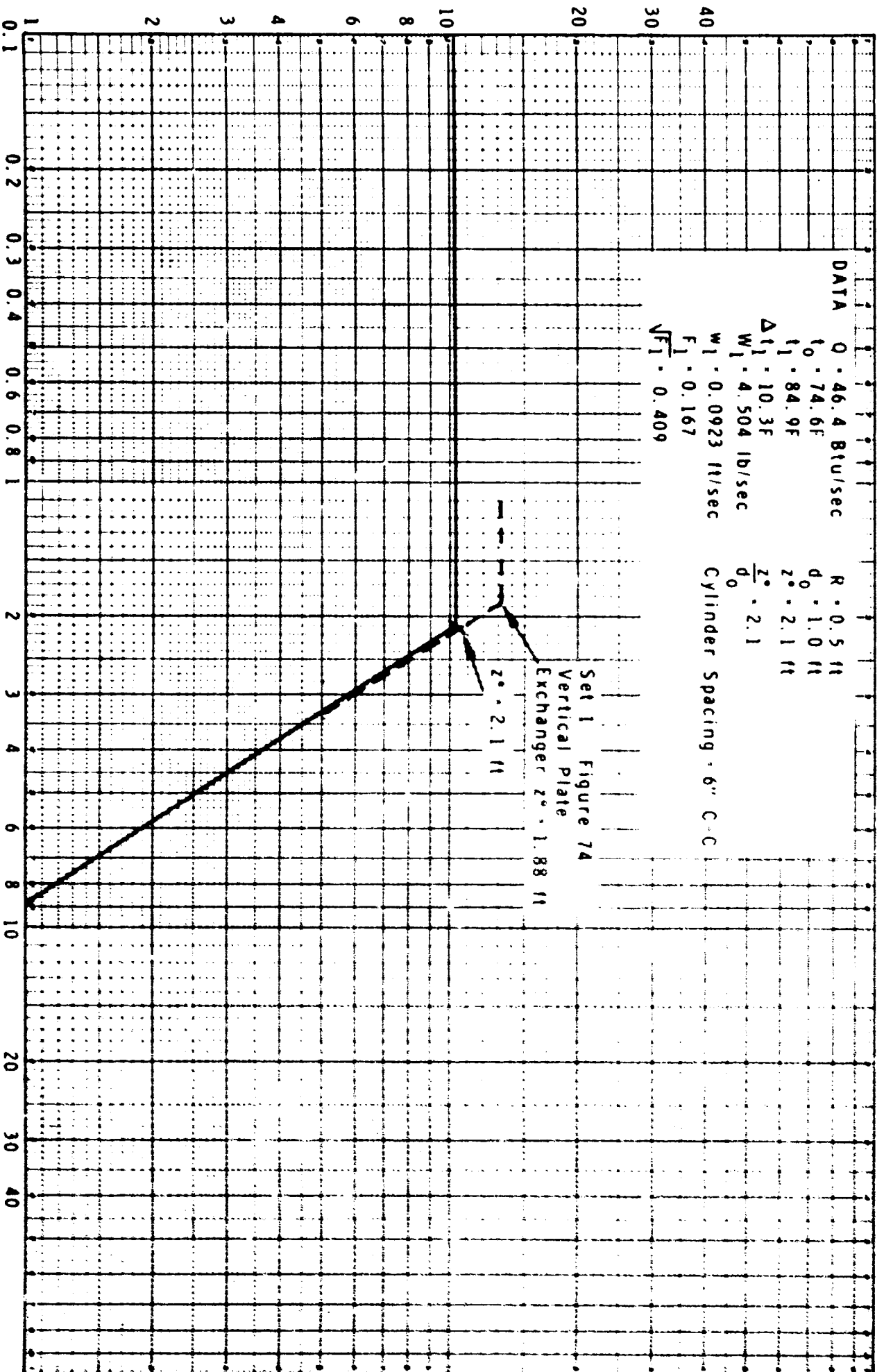
# SET 2 INTENSITY OF PLUME SOURCE VERTICAL FINNED CYLINDERS IN SIMULATOR

GB

FIGURE 78

A. EQUIVALENT CIRCULAR AREA OF HEAT SOURCE, FT<sup>2</sup>

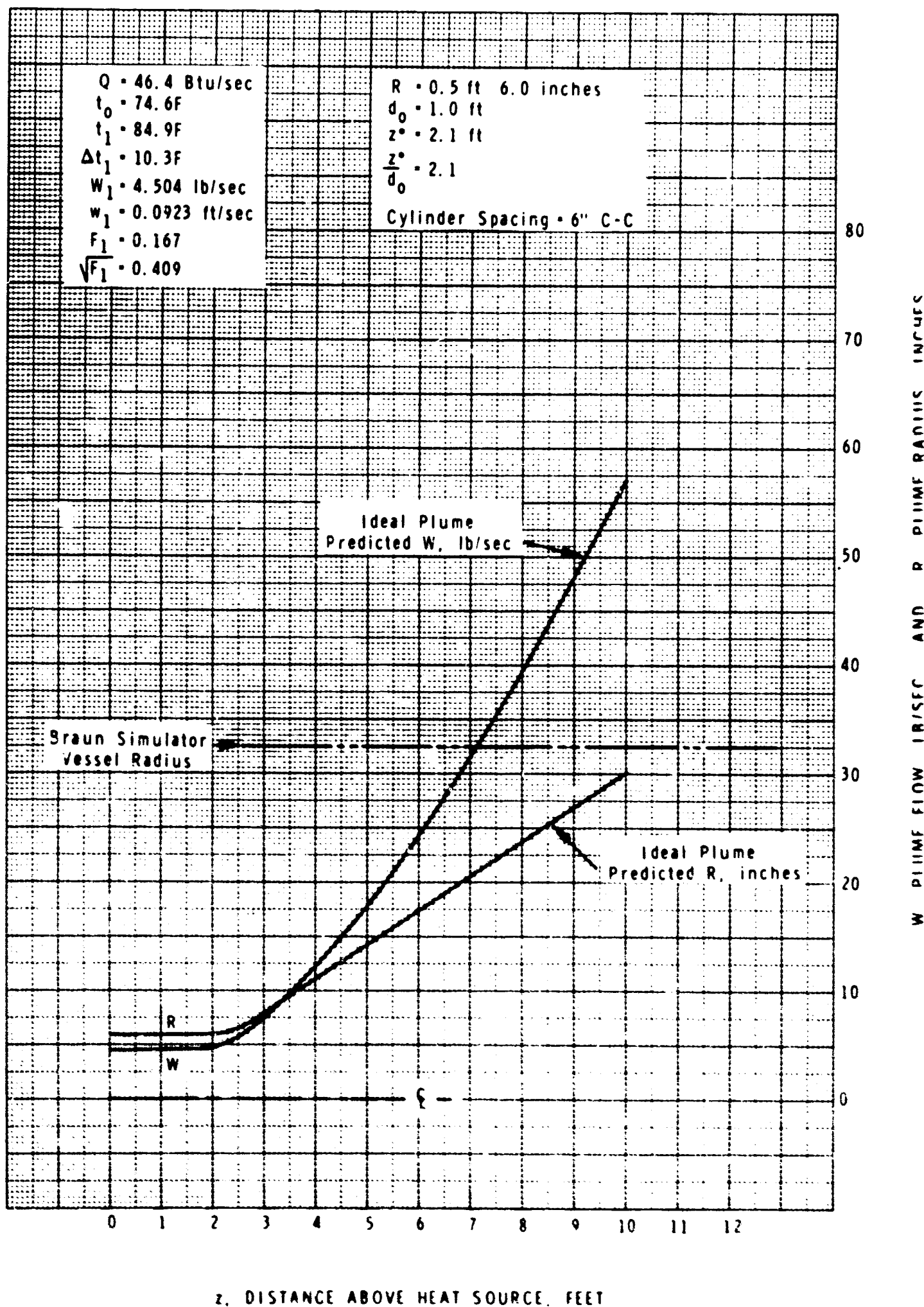
# SET 2 PLUME BUOYANCY DECAY VERTICAL FINNED CYLINDERS IN SIMULATOR



# SET 2 PLUME PROFILE VERTICAL FINNED CYLINDERS IN SIMULATOR

GB

FIGURE 80



## EXPERIMENTAL RESULTS AND DISCUSSION Continued

Figure 81 shows the shallow ocean test unit with the shroud being installed. Table XIII summarizes the plume source geometry and characteristics for Sets 3 and 4 data. The position of the test unit relative to the Port Hueneme harbor is shown in Figure 82.

A special plume temperature probe was used to measure the plume and surrounding water temperatures with relative ease and certainty as to position. Three arms of the probe were fixed 120 degrees apart and free to move vertically along guide wires. One thermocouple in the center and seven along each arm were located as tabulated in Figure 82. The supporting arms were made of 3/8-inch copper tubing. The thermocouples were made of 22-gauge copper-constantan wires. A 0.5-inch length of hot junction was bent vertically. All thermocouple wires were taped securely to the support arms and terminated at a junction box. The leads from the junction box were connected to a Leeds and Northrup potentiometer using ice for the cold junction.

Tidal data and ocean depth for the duration of the tests are plotted in Figure G-1 of Appendix G. Ambient ocean temperatures were measured at two locations identified by A1 and A2 in Figure 82. These vertical temperature profiles are given in Figures G-2 and G-3. Other ambient temperature measurements were made with the plume temperature probe. These data correspond to the readings from Thermocouples 8, 15, and 22 in Figure 82 and are plotted in Figure G-4. The uncertainty of the measured temperatures is about 0.3 F.

To compare the measured plume temperatures with those predicted from the model, the experimental data at various elevations were averaged to give the mean bulk temperature. At each elevation, the temperature difference between the plume and the ambient water was calculated from the mean bulk plume temperature and the ambient thermocouple readings. Figure 83 represents the test results for the runs made without the shroud. Figure 84 shows the test results for the experiments with the shroud.

In Figures 83 and 84, two predicted plumes are shown for each set of tests. One corresponds to the case of the uniform temperature ocean. The other represents the stratified ocean, more representative of the Port Hueneme harbor. The vertical ambient temperature used for the stratified ocean is identified by the straight line in Figure G-4. The ambient temperature gradient is equivalent to 0.16 F per foot elevation above the heat source. This gradient is representative for the curves shown in Figure G-4 and typical for shallow depths. We would not expect such vertical stratification to occur in the ocean, especially at depths from 300 to 20,000 feet. The shallow water gradients at Port Hueneme seem to be about 50 times greater than those expected in medium to deep ocean.

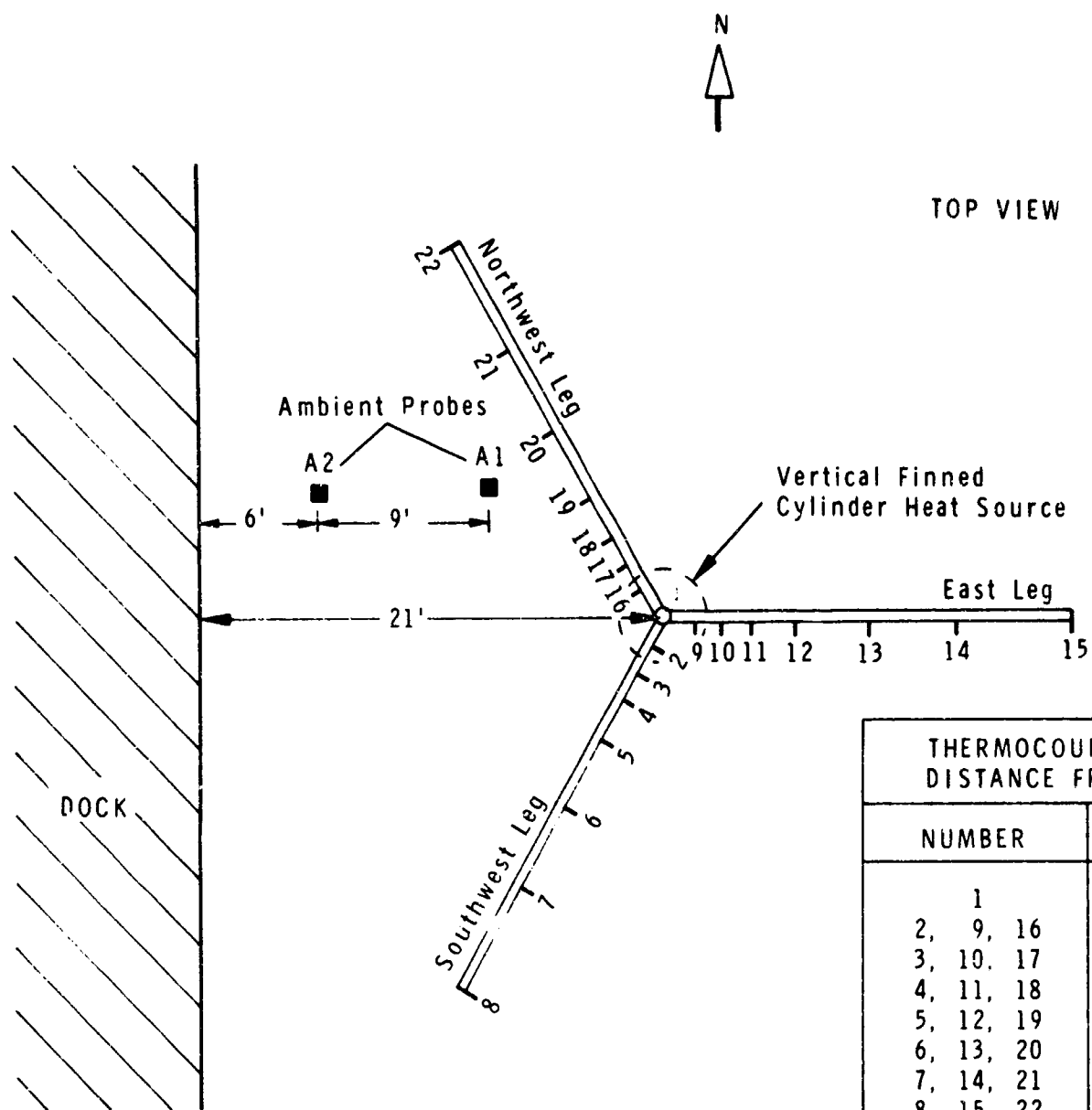
VERTICAL FINNED CYLINDER UNIT  
IN SHALLOW OCEAN

FIGURE 81



Official Photograph, U S Navy

C F BRAUN & CO  
 PLUME TEMPERATURE PROBE  
 FOR SHALLOW OCEAN TESTS

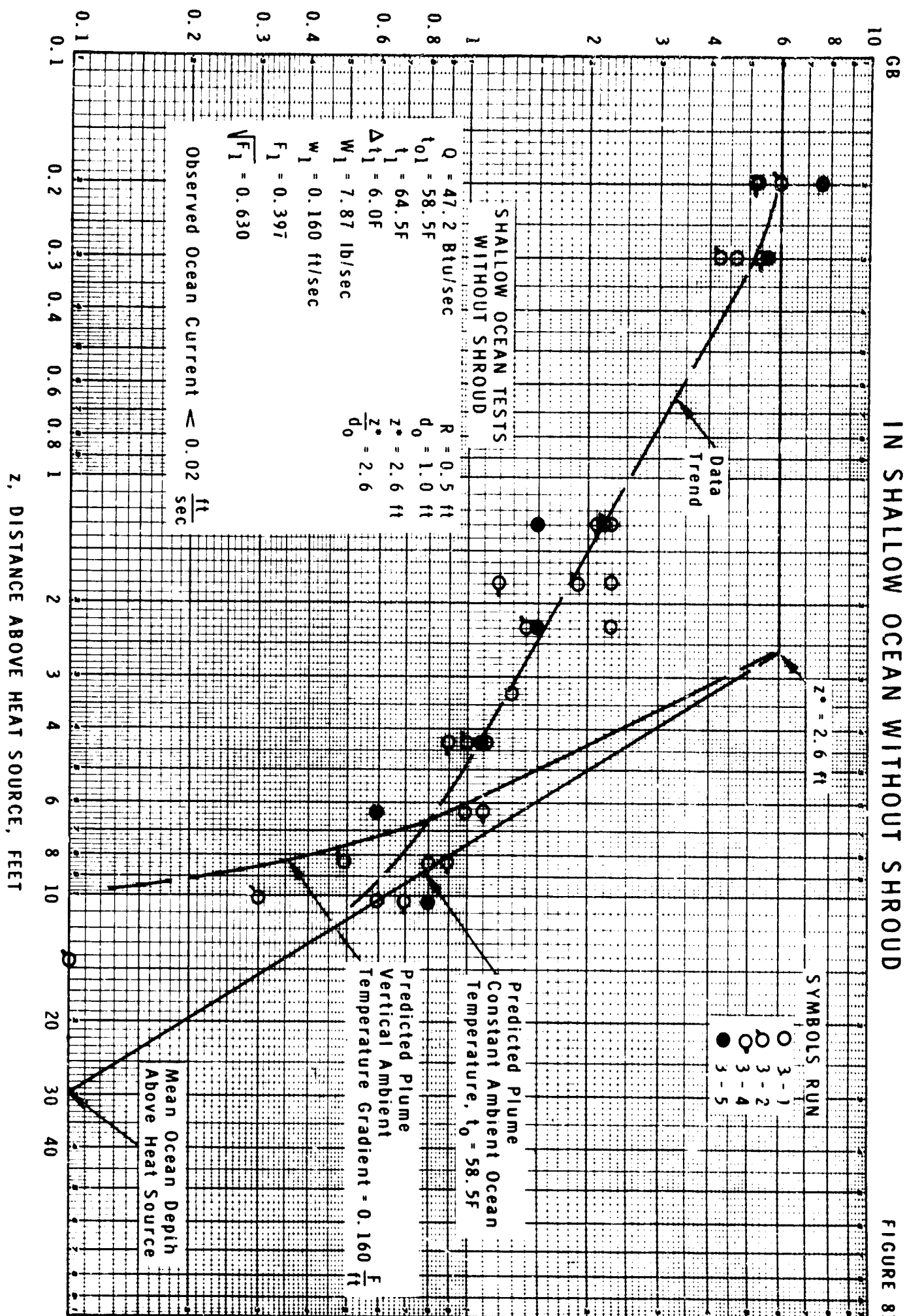


Probe Support 3/8" Tubing  
 TC 22 Gage Cu-Const  
 Bent Down 1/2 inch



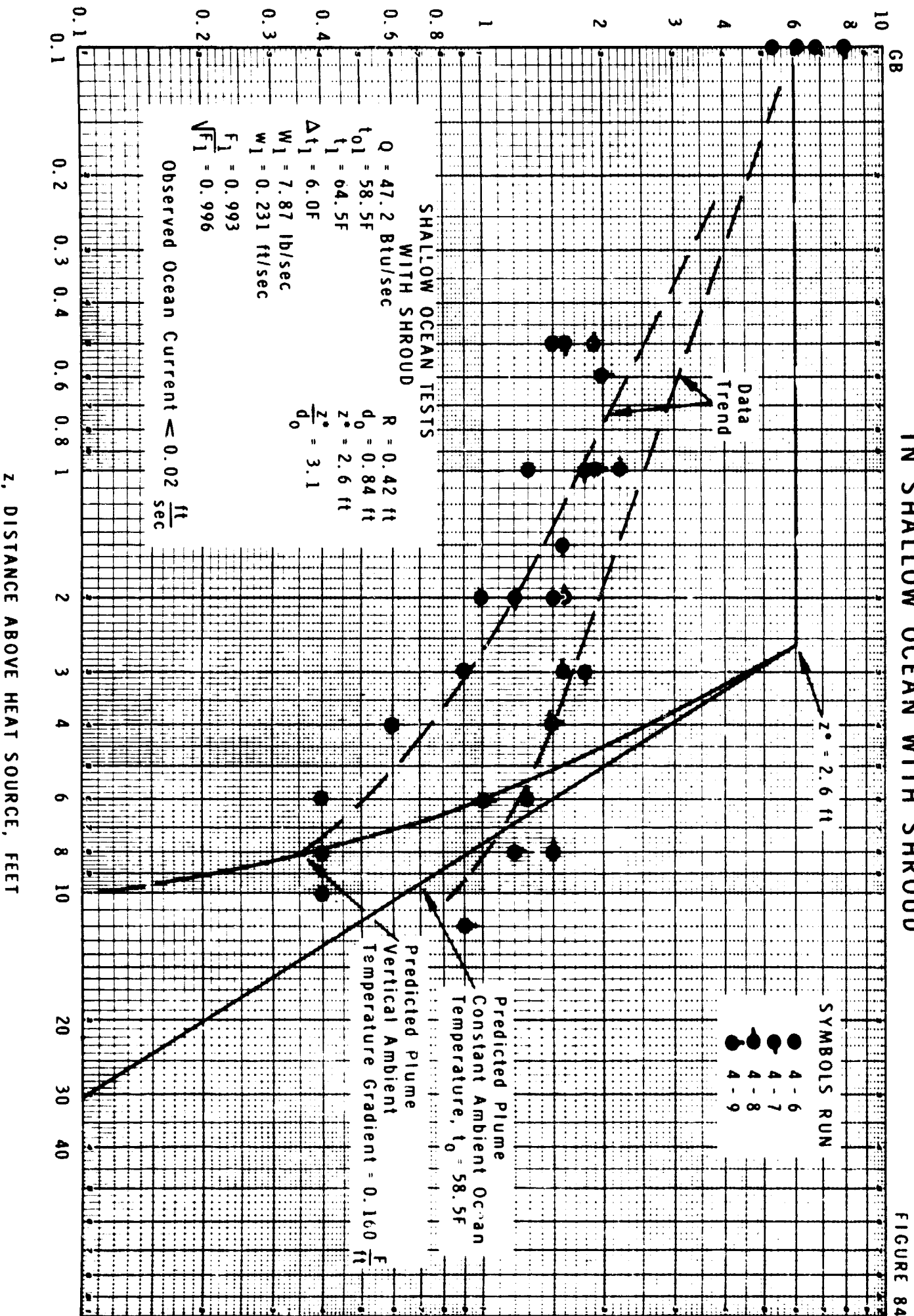
# SET 3 PLUME BUOYANCY DECAY WITHOUT SHROUD VERTICAL FINNED CYLINDER IN SHALLOW OCEAN WITHOUT SHROUD

FIGURE 83



# SET 4 PLUME BUOYANCY DECAY WITH SHROUD VERTICAL FINNED CYLINDER IN SHALLOW OCEAN WITH SHROUD

FIGURE 84



## EXPERIMENTAL RESULTS AND DISCUSSION Continued

Figures 83 and 84 indicate decay of the plume buoyancy or  $\Delta t$  starts very shortly after penetration into the ambient environment. The data with the shroud show the plume decay to be more accelerated. In spite of the scatter which is to be expected in the "real" ocean, where only natural forces are at work, a basic trend is shown by the curves. Our model indicates the stratified surrounding causes a very steep loss of buoyancy after about 3 feet or diameters of penetration. The predicted trend seems to agree with the data in the range of 6 to 10 feet.

One explanation of the accelerated deterioration of the plume could be the action of large eddies sloshing around the test region. The test unit was located about 21 feet from the dock. The measured currents were very small, less than 0.02 feet per second. The initial plume velocities were about ten times the magnitude of the measured ocean current. Therefore, the only forces which could have caused disintegration of the plume are those related to turbulence and turbulent eddies which may oscillate about a fixed point. The amplitude of oscillation can be several feet. Thus, energy of the plume could be dissipated by eddy entrainment and transport.

The predicted mass flow rate and radius profiles are shown in Figure 85. Analysis of the shallow ocean data indicates that the turbulent plume model predicts conservatively the penetration and propagation of the plume.

**NUMBER OF SOURCE DIAMETERS** The turbulent plume model involves the square root of the Froude number at the source,  $\sqrt{F_1}$ , as one of the key parameters. Froude number represents the ratio of the inertial to the gravitational force. Tables X, XI, and XII give this parameter for the three application cases. Table XIII lists  $\sqrt{F_1}$  for the four sets of data obtained. In Figures 66, 74, 79, 83, and 84, the predicted plume indicates that initially the plume travels into the surrounding liquid at constant buoyancy and momentum with zero entrainment. The break in the characteristic curve is identified by  $z^*$ , the penetration required to initiate plume propagation. As in most fluid dynamic applications,  $z^*$  would be expected to be a function of the ratio  $(z^*/d_0)$ , the number of source diameters.

In Figure 86, the results from seven different applications of the plume model are plotted to correlate the ratio  $(z^*/d_0)$  with the intensity parameter  $\sqrt{F_1}$ . The following equations represent the correlating line.

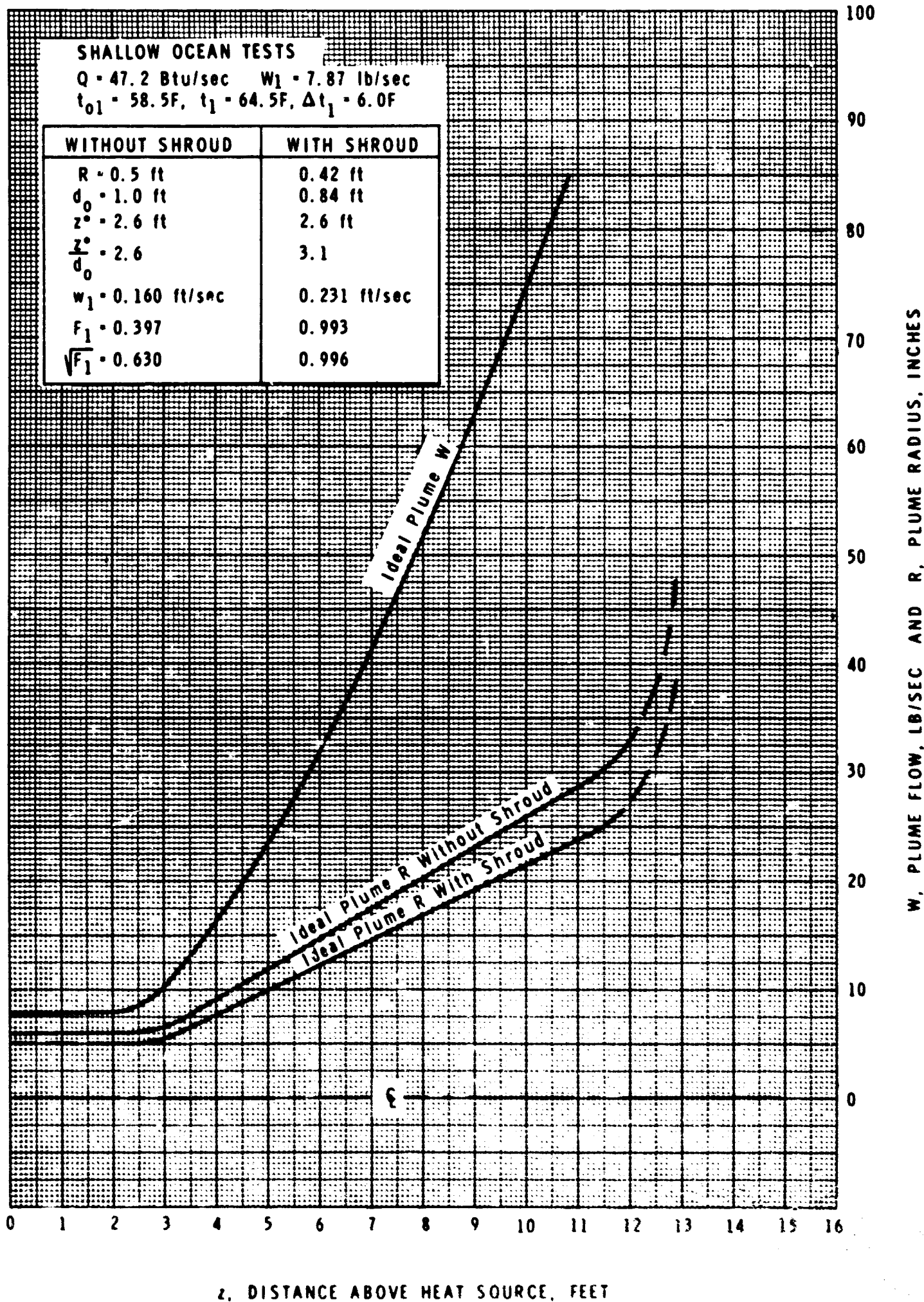
$$(z^*/d_0) = 3.1 (\sqrt{F_1})^{0.4} \quad (82)$$

$$(z^*/d_0) = 3.1 F_1^{0.2} \quad (83)$$

# SETS 3 AND 4 PLUME PROFILES VERTICAL FINNED CYLINDER IN SHALLOW OCEAN

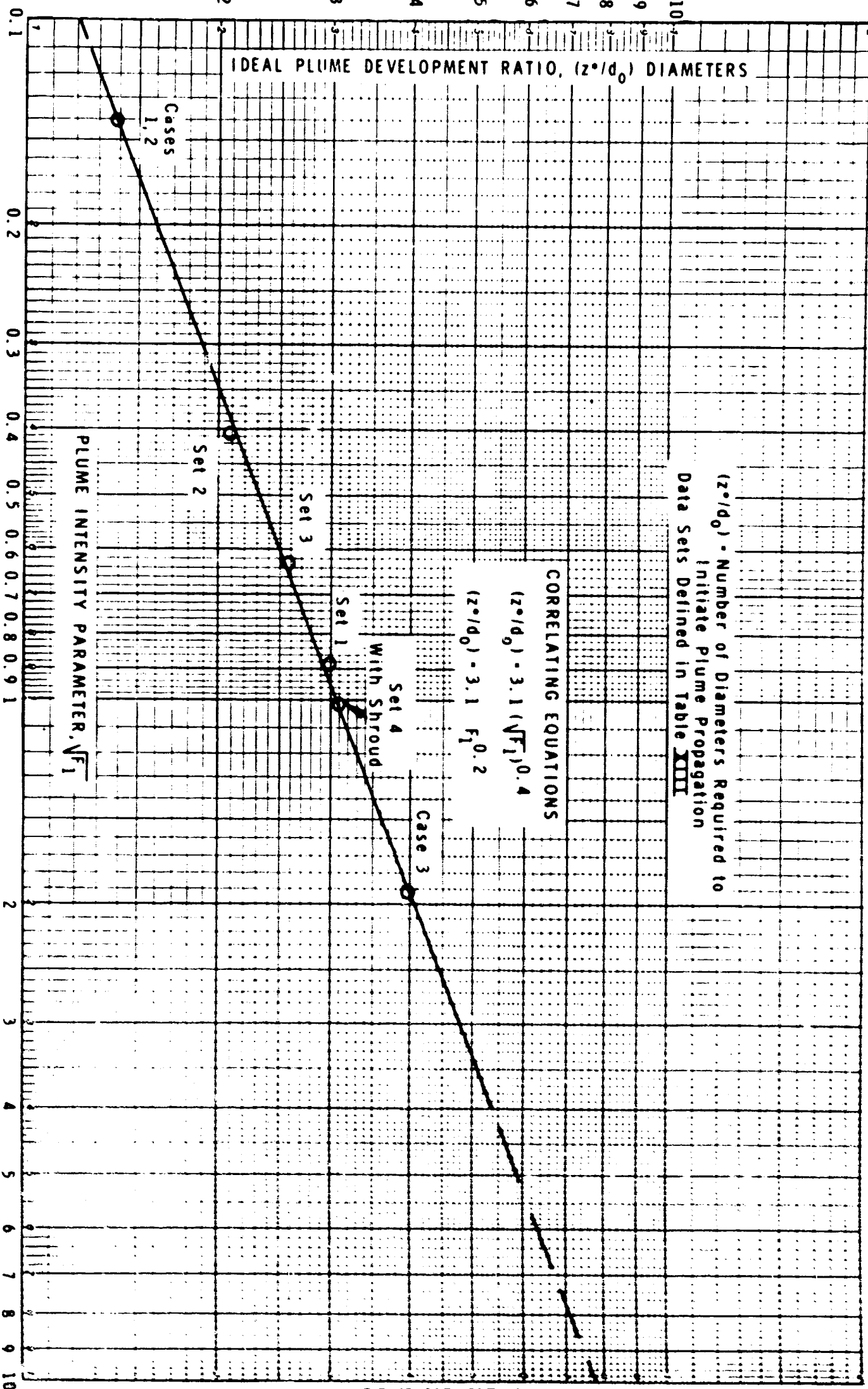
GB

FIGURE 85



# CORRELATION OF PLUME SOURCE INTENSITY WITH DEVELOPMENT DISTANCE RATIO

FIGURE 86



## EXPERIMENTAL RESULTS AND DISCUSSION Continued

Equations V-82 and V-83 follow rigorously from the turbulent plume Equations V-40 through V-44 and from the condition that the ratio  $(W/W_1) = 1$  at  $z = z^*$ . With this addition to the basic plume model, we have provided a complete set of mathematical relations which enable direct computation of the various important aspects of the ideal turbulent plume in the uniform or stratified ocean.

## CONCLUSIONS AND RECOMMENDATIONS

**CONCLUSIONS** The following conclusions are based on the study presented in this chapter.

- 1 The recommended turbulent plume model is valid for the idealized ocean with zero current. The proposed equations provide for the variation of the surrounding water temperature in a stably stratified ocean. The calculated plume gives the mass flow rate, mean bulk and maximum temperature differences, the mean velocity, and the radius of the plume as a function of penetration. The point of complete buoyancy dissipation is taken to be about 0.1 C mean bulk temperature difference. The general effect of the vertical temperature gradient in the ocean is to reduce penetration of the plume. The point of complete momentum or velocity dissipation corresponds to a distance 33 percent greater than the point for buoyancy dissipation.
- 2 The flow instability criteria indicate that for conditions which we expect, the initial velocity of the warm water is such as to provide for essentially a completely turbulent flow. The height above the heat source where laminar flow could conceivably prevail is estimated to be less than 1 foot for the several cases considered.
- 3 The effect of adiabatic cooling is to reduce the penetration of the plume. This effect is not significant.
- 4 The effect of the Coriolis force varies with the prevailing ocean currents and latitude. The buoyancy force at the heat source can be several hundredfold greater than the Coriolis force. This ratio diminishes fast as the buoyancy of the plume is dissipated. For the ideal plume with zero current, it is reasonable to neglect the effect of Coriolis on the plume. The effect of this force, if any, is reduction of the plume penetration.

## CONCLUSIONS AND RECOMMENDATIONS Continued

- 5 Ocean currents tend to greatly enhance the dissipation of the plume and can drastically reduce the penetration computed from the ideal ocean with zero current. Plume temperature data obtained in the shallow ocean generally indicate the penetration predicted by the developed model to be conservative.
- 6 For two applications at depths of 300 and 1,000 feet, the predicted penetration will not reach the ocean surface.

RECOMMENDATIONS Two aspects of the present study of the turbulent plume justify additional investigation.

- 1 Experimental data are needed on the penetration and propagation of the hot water plume. Relevant plume study should be made in a controlled environment such as the simulator column to compare actual performance with predicted results. An inexpensive study could be made with a single cartridge heating element designed for variable initial buoyancy and a very high ratio of column to source diameter. More sensitive temperature data with a relatively small temperature probe would enhance the present state of knowledge.
- 2 The portion of the present plume model for the stratified ocean provides a good approximation for the entrainment rate. But a relatively simple and rigorous correlation for the vertical velocity is lacking for the stratified case. With a modest effort, the plume model for the stratified ocean could be completed and defined by a set of consistent relationships such as those for the uniform ocean.

## TERMS AND SYMBOLS, CHAPTER V

A	Circular cross section of plume, square feet
$\bar{c}$	Velocity vector
$C_p$	Specific heat at constant pressure, Btu per (lb-F) or Cal per (g-C)
$d_0$	Diameter of circular heat source, cm or ft
e	Base of natural logarithm = 2.713
$F_1$	Froude number at source defined by Equation V-44
g	Acceleration of gravity, 980.7 cm per sec <sup>2</sup> or 32.2 ft per sec <sup>2</sup>
$g_c$	Conversion factor = 32.2 (ft-lbm) per (lb <sub>f</sub> -sec <sup>2</sup> )
H	Specific enthalpy of plume liquid, Btu per lb
J	Mechanical equivalent of heat = 778 (ft-lb <sub>f</sub> ) per Btu
L	Length of line source of heat, feet
M	Momentum flux defined by Equation V-34, (lbm-ft/sec <sup>2</sup> )
$P_1$	Absolute pressure at heat source, decibars or psia
p	Absolute pressure, (lbm-ft)/(sec <sup>2</sup> -ft <sup>2</sup> )
Q	Heat flow, Btu per hour or Btu per second
R	Radius of plume, cm or feet
$R^*$	Effective radius of plume for maximum $\Delta t$
T	Absolute temperature of plume fluid, degree R
$T_0$	Absolute temperature of surrounding fluid, degrees R
t	Temperature of plume fluid, C or F
$t_0$	Temperature of surrounding fluid, C or F
$t_1$	Temperature of plume fluid at source, C or F
$\Delta t$	Temperature of difference (t- $t_0$ ), C or F



## TERMS AND SYMBOLS, CHAPTER V Continued

u	East-west current, cm per sec
v	North-south current, cm per sec
w	Vertical velocity, cm per sec or ft per sec
$w_1$	Vertical velocity at the heat source
$w_{max}$	Maximum vertical velocity at vertical axis
W	Mass flow rate, g per sec or lb per sec
$W_1$	Mass flow rate at heat source, g per sec or lb per sec
X	Group defined by Equation V-42
x	East-west coordinate
Y	Group defined by Equation V-43
y	Radial distance from vertical axis, cm or ft or north-south coordinate
z	Vertical penetration, feet
$z^*$	Distance beyond which velocity and radius laws are valid, feet

## GREEK

$\rho$	Specific weight of plume fluid, g per cu cm, or lb per cu ft
$\rho_0$	Specific weight of fluid surrounding the plume, g per cu cm or lb per cu ft
$\rho_1$	Specific weight of plume fluid at heat source, g per cu cm or lb per cu ft
$\beta$	Coefficient of thermal expansion, $1/C$ or $1/F$
$\alpha$	Specific Volume, cu cm per g
$\mu_1$	Viscosity of the plume liquid at the heat source, lbm per (ft-sec) = cp x 0.000672
$t$	Time in seconds

## TERMS AND SYMBOLS, CHAPTER V Continued

$\Omega$  Angular velocity of rotation, radians per sec

$\bar{\tau}$  Shear stress vector, force per unit area

$\phi$  Latitude, degrees

$\nabla$  Gradient of  $\nabla p = \frac{\partial p}{\partial x} + \frac{\partial p}{\partial y} + \frac{\partial p}{\partial z}$

$\nabla^2$  Laplacian of  $\nabla^2 u = \frac{\partial^2 u}{\partial x^2} + \frac{\partial^2 u}{\partial y^2} + \frac{\partial^2 u}{\partial z^2}$

$\sigma$  Standard deviation

## SUBSCRIPTS

o Surrounding fluid at any position

o1 Surrounding fluid at heat source

o2, o3, o4...on, Surrounding fluid at positions above the heat source

1 Plume fluid at heat source

2, 3, 4...n, Plume fluid at positions above the heat source

## CHAPTER VI, DESIGNING UNDERWATER HEAT REJECTION SURFACES

## ABSTRACT

Technical aspects of designing an undersea heat rejection surface and estimation techniques for an underwater heat plume are presented in this chapter. As we point out the type of undersea power convertor influences the objectives of its heat rejection surface design. Marine fouling and corrosion affect the selection of materials and the expected operating heat transfer coefficient. Geometry of the heat transfer surface is also an important design parameter.

Results of the previous chapters are translated into a form useful for design. A step-by-step design procedure is proposed for an undersea heat rejection surface. We also include a step-by-step procedure for estimating penetration, temperature decay, and radius of an undersea heat plume.

## GENERAL CONSIDERATIONS

Designing an optimum underwater heat rejection surface for a power generator involves consideration of the entire energy conversion system and its ocean environment. As in most engineering problems, economics is the optimizing criterion. However, the necessity of high reliability and maintenance-free operation vastly changes the economics of undersea power generators from their land-based counterparts.

Currently, three types of power conversion methods are under consideration for undersea electric power generation. These are thermoelectric, fuel cell, and vapor cycle convertors. Their characteristics and sizes greatly affect heat rejection surface design.

**THERMOELECTRIC CONVERTORS** Thermoelectric generators convert heat directly to electricity with no moving parts. Since conversion efficiencies are in the order of only five to ten percent, most of the input heat is rejected to the ocean.

Usually, thermoelectric elements are contained within plate assemblies. Heat flowing across the plate is associated with a temperature difference across the element. Part of the heat is converted directly to electricity while the remainder is rejected at the cold side of the plate. Power output of a thermoelectric element is proportional to the difference between hot and cold junction temperatures square. Efficiency of a thermoelectric element also rises with increasing difference between hot and cold junction temperatures. Therefore, it is important to maximize this temperature difference.

## GENERAL CONSIDERATIONS Continued

Hot junction temperature of a thermoelectric device cannot be increased above a limit imposed by the nature of materials and working fluid thermodynamic properties. The sink temperature of an undersea thermoelectric device is fixed. Thus, a high gross heat transfer coefficient is highly desirable in order to bring the cold junction temperature as close to the sink temperature as possible. Because of the expense of adding additional thermoelectric elements, there would be an economic incentive to maximize the gross heat transfer coefficient.

**FUEL CELL CONVERTORS** A fuel cell, which also converts heat directly to electricity, can be designed to be free of moving parts. Since conversion efficiency ranges up to 75 percent, much less input heat is rejected to the ocean than with a thermoelectric convertor.

Unconverted heat in an undersea fuel cell would probably be transferred to the surrounding ocean. The actual means of effecting heat transfer would depend upon the specific design under consideration. The convertor could be built within the fuel cell or it might be external. For large devices, an external convector is likely. In this case, the electrolyte would probably be circulated by an electromagnetic pump through a heat exchanger mounted close to the cell.

With a fuel cell heat rejection exchanger, the economic incentive for optimum finning would not appear to be as great as with the thermoelectric convertor. Here, to arrive at the economic optimum exchanger, the cost of additional fins should be compared with the cost of adding additional base heat transfer surface.

**VAPOR CYCLE CONVERTOR** Vapor cycle energy convertors appeal primarily because their technology is well developed. They employ rotating machinery, which is a big disadvantage for undersea use. Efficiencies fall between those of fuel cell and thermoelectric convertors. Considerable effort has been devoted to designing surface condensers for vapor cycle convertors. It is generally recognized that vapor leaving the turbines should be at a low pressure to achieve the maximum expansion work. This means that the working fluid pressure drop in a surface condenser should be minimized. Reducing the working fluid pressure drop also lowers its heat transfer coefficient, which increases the necessary heat transfer area.

There would seem to be considerable economic incentive to increase the outside coefficient. Compactness would be advantageous in cases of high ambient pressure. Because condensing coefficients are quite large, an increase in the outer coefficient would significantly raise the heat transfer rate. Thus, a high gross heat transfer coefficient would be highly advantageous.

## MARINE FOULING, CORROSION, AND MATERIAL SELECTION

We concluded from our investigation of marine fouling on heated metal surfaces in shallow and deep ocean waters that marine growth did not occur on metal surfaces at temperatures above 100 F. However, metal and plastic structures exposed to water above ambient temperature were severely fouled in the shallow water test. On the basis of these observations, we recommend that heat rejection surfaces be designed to operate above 100 F. We also suggest that unheated structures not be exposed to warm water flowing from the rejection surfaces.

The marine fouling tests also indicated that copper, silicon bronze, aluminum bronze, naval brass, and HH brass do not allow marine growth under either ambient or heated conditions. Monel, 90-10 and 70-30 cupronickel, and titanium permitted marine growth at ambient temperature in the shallow water test. No fouling occurred on the deep ocean test unit when it was exposed five days at 300 feet and five days at 4,500 feet.

Corrosion rates for each of the ten different metals tested are given in Tables II, V, and VI. Because the two ocean tests were of short duration, the experimental corrosion rates are probably higher than would be the case for a longer test period. Shallow water test results, we believe, should be indicative of the corrosion behavior under long-term exposure.

On the basis of both the corrosion and the fouling results, we recommend 90-10 and 70-30 cupronickel, naval brass, silicon bronze, beryllium copper, HC copper, HH brass, and titanium for undersea construction materials. Because its passive film suffers a breakdown in low oxygen environments, Monel is not suggested as a deep ocean construction material. Although aluminum bronze performed satisfactorily in our experiments, there appeared to be some evidence of aluminum removal in the deep ocean tests. We recommend that aluminum bronze not be employed for deep ocean construction until this effect is further investigated.

Thermal conductivity is an important parameter in selecting materials for undersea heat rejection. To minimize the temperature drop across the base metal heat transfer surface requires the highest thermal conductivity possible. Fin material should also be of high thermal conductivity. Eckert and Drake (60) state that it is advantageous to use finned surfaces as soon as the condition

$$\frac{2k_m}{h_o a} > 5 \quad (1)$$

is fulfilled. The gross heat transfer coefficient of finned surfaces increases with fin thermal conductivity.

## MARINE FOULING, CORROSION, AND MATERIAL SELECTION Continued

Thermal conductivities of the alloys tested are listed below.

<u>ALLOY NAME</u>	<u>THERMAL CONDUCTIVITY</u> <u>BTU/HR-FT<sup>2</sup>-F/IN</u>	
	<u>TEMPERATURE RANGE 32-212 F</u>	
Monel	174	(at 212 F)
70 Cu-30 Ni	200	
90 Cu-10 Ni	310	
Al Bronze	528	(at 68 F)
Be Copper	750-900	
HH Brass	840	(at 68 F)
Naval Brass	810	
Si Bronze	225	
HC Copper	2,700	
Titanium	118	

Fouling heat transfer coefficients of 199 and 314 Btu/hr-ft<sup>2</sup>-F were calculated for the 120 F and 140 F shallow water test elements, respectively. The 100 F shallow water test element heat transfer coefficient did not appear to change with time. Heat transfer coefficients for the deep ocean elements were also nearly time invariant. The calculated fouling coefficients should represent an upper limit for deep ocean conditions.

## HEAT TRANSFER BY FREE CONVECTION

**GEOMETRY** In this investigation we considered both vertical cylindrical and vertical flat surfaces. Previous investigators (58,110) have shown that vertical surfaces have higher heat transfer coefficients than inclined ones at the same values of the other parameters. Comparing cylindrical and flat surfaces, we find that at high-heat fluxes cylindrical surfaces have higher heat transfer coefficients than flat surfaces. However, coefficients for cylinders become lower than those for flat plates as  $q/A$  is decreased. See Figure 56.

Cylinders appear more attractive than flat plates when one considers fin attachment. Fins may be spaced closer on vertical cylinders than on vertical flat plates because of geometry. Boundary layer thickness appears to be smaller on a cylindrical than on a flat surface, also for reasons of geometry. Because of this, gross heat transfer coefficients for cylinders are higher than those for flat plates, except at very low-heat fluxes.

## HEAT TRANSFER BY FREE CONVECTION Continued

Turbulent natural convection normally would prevail on an undersea heat transfer surface. In turbulent natural convection, vertical length of a flat surface does not affect the heat transfer coefficient. However, the boundary layer thickness increases as  $x^{1/2}$ . See Equation VI-3. Since fin spacing is determined by the boundary layer thickness, the higher the surface, the larger the fin spacing, and because gross heat transfer coefficient decreases with increasing fin spacing, it decreases with increasing surface height.

Our experimental results on spacing between heat transfer surfaces indicate that surfaces may be closely spaced. Spacings of 0.5 to 5.0 inches between the fin tips of two vertical finned plates had little effect upon the gross heat transfer coefficient. See Figure 51. Likewise, vertical finned cylinders could be so closely located that the fins almost touched without significantly affecting the gross heat transfer coefficient. See Figure 58.

Installing a chimney around an undersea heat rejection unit would not appear to enhance its gross heat transfer coefficient according to our experimental data. We found that locating a chimney too close to the vertical flat plate unit severely reduced the gross heat transfer coefficient. See Figure 52. Chimneys did not seem to appreciably augment heat transfer from the vertical finned 2-inch diameter cylinders. See Figure 59.

In some situations, a heat rejection unit would be placed above an underwater heat source or energy convertor. Here it is important to know how close together the two units can be spaced. Inlet clearance tests with finned flat plates and cylinders revealed that the units may be closely spaced without seriously affecting the gross heat transfer coefficient. See Figures 53 and 60. Our data indicated that at small clearances the gross heat transfer coefficient went through a maximum with respect to clearance. This was presumably due to increased side flow. The side flow contribution to both chimney and inlet clearance data must be considered when extrapolating the data to a wider unit where large side entrainment is not possible.

**EQUATIONS FOR FLAT AND CURVED SURFACES** Our vertical flat plate experimental data confirmed Saunders' correlation (97) over a Rayleigh number range of  $2.0 \times 10^9$  to  $3.62 \times 10^{12}$ . See Figure 46. We therefore recommend Saunders' expression for vertical flat-plate heat transfer coefficient prediction in turbulent natural convection heat transfer to water.

$$Nu_x = 0.17 Ra_x^{1/3} \quad (2)$$

## HEAT TRANSFER BY FREE CONVECTION Continued

We derived semiempirical expressions for the boundary layer thickness and the heat transfer coefficient which incorporated a variable Blasius law constant. From the experimental heat transfer data, we calculated a Blasius law constant which caused the predicted heat transfer coefficients to agree with the experimental trend. Using this constant, the boundary layer thickness equation is

$$\frac{\delta}{x} = 1.31 \left[ 1 + 0.978 \text{Pr}^{2/3} \right]^{1/6} \text{Pr}^{-5/18} \text{Ra}_x^{-1/6} \quad (3)$$

This equation is graphed in Figure 27, and we suggest that it be used for both flat and cylindrical vertical surfaces.

Vertical cylinder experimental data were correlated by using Equation VI-2 and a heat flux parameter. See Figure 56. This method should be valid over the experimental range of variables, which included cylinder diameters of 1.0 to 2.0 inches and  $q/A$  of 1,690 to 20,200 Btu/hr-ft<sup>2</sup> (base surface area).

We recommend the King (81) equation for prediction of laminar region heat transfer coefficients.

$$\text{Nu}_x = 0.555 \text{Ra}_x^{1/4}$$

Transition to turbulent flow usually occurs in the Rayleigh number range of  $10^9$  to  $10^{10}$ . To predict boundary layer thickness in laminar flow, we recommend the expression of Eckert and Drake (60).

$$\frac{\delta}{x} = 0.393 (0.952 + \text{Pr})^{1/4} \text{Pr}^{-1/4} \text{Ra}_x^{-1/4} \quad (5)$$

The laminar and turbulent flow heat transfer equations recommended are for a surface of constant temperature. If instead there is a constant heat flux, little error is introduced if the constant temperature expressions are employed. In laminar flow, the error is less than 7.2 percent in the Prandtl number range of one to ten. In turbulent flow, the effect on heat transfer coefficient is negligible.

**FIN OPTIMIZATION** In Chapter III, we developed a technique for fin optimization on vertical surfaces. Maximum heat dissipation rate per unit temperature difference and base surface area (gross heat transfer coefficient) was chosen as the optimizing criterion. The results of this case can be modified to obtain an economic optimum surface for a specific design.



## HEAT TRANSFER BY FREE CONVECTION Continued

Gross heat transfer coefficient, according to this technique, is a function of five variables -  $h_o$ ,  $k_m$ ,  $a$ ,  $b_c$ ,  $D$ . It increases with increasing  $h_o$ ,  $k_m$ , or  $b_c$ . A high surface coefficient,  $h_o$ , is favored by a high  $\Delta T$  and a high film temperature  $T_{avg}$ . Metal thermal conductivity has been discussed under the material selection heading. An infinite fin height will yield the highest gross coefficient. Thus, the optimum height must be determined by economics. An  $h_G$  within a few percentage points of the highest is usually reached at relatively low-fin heights.

Gross heat transfer coefficient maximizes with fin thickness,  $a$ , and fin spacing,  $D$ . The maximum  $h_G$  with respect to  $D$  occurs at such a low value of fin spacing that it is not of practical interest when dealing with water. However, the maximum  $h_G$  with respect to  $a$  is of practical importance. Figures 28 through 31 indicate the value of  $a$  which maximizes  $h_G$ . Figures 33 through 36 are design charts for determining  $h_G$  as a function of fin spacing, fin height,

$\left(\frac{2h_o}{k_m}\right)^{1/2}$ , and optimum fin thickness.

It is conceivable that optimum fin thickness from a heat transfer standpoint could, at times, not be the optimum thickness from an economic standpoint. To determine whether or not this is true, several values of  $h_G$  corresponding to selected fin thicknesses thinner than optimum should be calculated from the following equation.

$$h_G = \frac{0.924(2h_o k_m a)^{1/2} \tanh\left[\left(\frac{2h_o b_c^2}{k_m a}\right)^{1/2}\right] + h_o D}{D + a} \quad (6)$$

Then the influence of  $a$  on  $h_G$  can be subjected to economic analysis.

This fin optimization technique was based upon an idealized model of a finned heat transfer surface. The underlying assumptions are listed in Chapter III. They should be kept in mind when using the model for design.

**FIN SPACING** Fin spacing is a very important variable in optimizing a heat rejection surface. Gross heat transfer coefficient increases and optimum fin thickness decreases as fin spacing decreases. Thus, it would appear advantageous to space fins as close together as possible. There is, however, a maximum  $h_G$  with fin spacing, since  $D = 0$  and  $D = \infty$  both yield the same  $h_G$  as a vertical surface without fins. However, this maximum occurs at very small fin spacings. See Figures 33 through 36. Boundary layer interaction usually limits fin spacing before this maximum is reached.

## HEAT TRANSFER BY FREE CONVECTION Continued

To avoid boundary layer interaction altogether, one should space fins at a minimum distance of  $2\delta$ , where  $\delta$  is evaluated at the maximum length of vertical surface. When boundary layers interact, there is a short transition length, and then fully developed channel flow begins. Because fluid cannot be entrained fast enough from the open end of the channel formed by fins and base surface, bulk temperature in the channel increases. This lowers the effective temperature driving force for heat transfer, but increases the buoyancy driving force for flow. The former effect usually dominates, and the gross heat transfer coefficient diminishes.

Boundary layer prediction itself is another problem in the selection of the proper fin spacing. Experimental boundary layer temperature profile data show that over 10 percent of the total temperature driving force is present at the predicted boundary layer thickness. At twice the predicted boundary layer thickness, over five percent of the total temperature driving force remains. This indicates that the predicted boundary layer thicknesses are too low. Also, it points out that the boundary layer thickness concept itself is rather arbitrary.

Our vertical flat-plate experimental results reveal that one is safe in employing  $2\delta_{avg}$  as a fin spacing criterion. Boundary layer thickness at the maximum surface height is calculated by Equation VI-3. Then  $\delta_{avg}$  is determined by

$$\delta_{avg} = \frac{1}{x} \int_0^x \delta dx = \frac{C_\delta}{x} \int_0^x x^{0.5} dx = \frac{C_\delta}{1.5} x^{0.5} = \frac{\delta}{1.5} \quad (7)$$

The maximum deviation between predicted and experimental gross heat transfer coefficients using this approach is in the order of 20 percent. The deviation depends upon fin height. When more experimental data are obtained, it will be possible to refine the method of fin spacing prediction to include the effects of fin height.

## DESIGN METHOD

Designing an underwater heat rejection surface is complex because a large number of variables are involved. The following step-by-step procedure for turbulent flow is based upon information developed in this study. It outlines in a general fashion the steps involved. For specific designs a more detailed and streamlined approach could be developed.

## DESIGN METHOD Continued

To design an underwater heat rejection surface, one must first know the following quantities.

- Metal surface temperatures,  $T_s$
- Ambient temperature,  $T_a$
- Fin metal thermal conductivity,  $k_m$
- Heat flux,  $q/A$  (if the base surface is cylindrical)

Usually two of these quantities are known, and either metal surface temperature or heat flux is unknown. If the metal surface temperature is known, the design is straightforward. If not, a base metal surface temperature should be assumed and the design steps should be carried out. The final gross heat transfer coefficient should be employed to calculate the true design surface temperature by

$$T_s = T_a + q/Ah_{GR}$$

This temperature should be compared with the assumed surface temperature. If the two agree, the calculation is complete. Otherwise, assume a new  $T_s$  and repeat the procedure until the calculated and assumed metal surface temperatures agree.

- 1 Calculate  $\Delta T = T_s - T_a$  and  $T_{avg} = \frac{T_s + T_a}{2}$
- 2 Calculate  $h_o$  for the base surface by the equation

$$h_o = 0.17 k \left( \frac{q \beta Pr}{2} \cdot \Delta T \right)^{1/3}$$

Physical properties are evaluated at  $T_{avg}$ . Appendix B lists the properties of seawater and water. For water, the heat transfer group  $\frac{q \beta Pr}{2}$  is plotted versus temperature in Figure B-3.

- 3 If the heat transfer surface is cylindrical, correct  $h_o$  for the effect of heat flux by Figure 56. Call the corrected heat transfer coefficient  $h_{cyl}$ .

## DESIGN METHOD Continued

- 4 Assume a surface height and calculate average boundary layer thickness for the vertical surface by the equation

$$\delta_{avg} = 0.933 \times \left[ 1 + 0.978 \text{Pr}^{2/3} \right]^{1/6} \text{Pr}^{-5/18} \text{Ra}_x^{-1/6}$$

Or use Figure 27 to obtain  $\delta$  and calculate  $\delta_{avg} = \delta/1.5$ . Again, physical properties are evaluated at  $T_{avg}$ . Then fin spacing is given by  $D = 2 \delta_{avg}$ . For cylinders,  $D$  is the circumferential distance between fins. Fin spacing is proportional to the square root of surface height. Surface height should be minimized, subject to the other design constraints.

- 5 Calculate  $\left( \frac{2h_o}{k_m} \right)^{1/2}$  and select a corrected fin height  $b_c$  from the appropriate plot of  $\frac{h_G}{k_m}$  versus fin spacing, Figures 33 through 36. Infinite fin height will, of course, yield the highest  $h_G$ . However, a value of  $h_G/k_m$  within a few percentage points of the highest will be reached at relatively low heights, particularly

at large values of  $\left( \frac{2h_o}{k_m} \right)^{1/2}$ . Optimum fin height will depend upon

the economics of each specific design. To determine the effects of height upon total cost, it is probably easiest to prepare several designs using different heights, and then compare costs. This can be accomplished quickly with the graphs.

- 6 Determine optimum fin thickness,  $a$ , by Figures 28 through 31,

using previously computed values of  $\left( \frac{2h_o}{k_m} \right)^{1/2}$ ,  $b_c$ , and  $D$ .

Compute the actual fin height by  $b = b_c - \frac{a}{2}$ .

- 7 Calculate gross heat transfer coefficient,  $h_G$ , for finned vertical plates using the appropriate plot of Figures 33 through 36. For cylinders, calculate  $h_G$  by the following equation.

$$h_G = \frac{0.924 (2h_o k_m a)^{1/2} \tanh \left[ \left( \frac{2h_o b_c^2}{k_m a} \right)^{1/2} \right] + h_{cyl} D}{D + a}$$

## DESIGN METHOD Continued

- 8 Correct the gross heat transfer coefficient determined in Step 7 to conform with experimental results. Use Figure 49 to correct for fin spacing effects on the vertical finned flat plate gross heat transfer coefficient. Employ Table IX to determine the effects of fin spacing, fin height, and heat flux on  $h_G$  for vertical finned cylinders.
- 9 Assume a fouling coefficient for the surface and calculate a revised  $h_G$  by the expression

$$h_{GR} = \frac{1}{\frac{1}{h_G} + \frac{1}{h_D}}$$

- 10 Calculate the overall heat transfer coefficient  $U$ , from  $h_{GR}$  and the other heat transfer conductances involved in the specific design. Heat transfer area can be then determined from the equation

$$A = \frac{q}{U \Delta T_{\log \text{ mean}}}$$

- 11 Evaluate the design from an economic standpoint.

## PLUME PROFILE METHOD

The following procedure gives the steps involved in the computation of the plume. The method is divided into two parts. (1) Plume propagation in a uniform temperature ocean, and (2) plume propagation in a stably stratified ocean.

## Plume in uniform temperature ocean

- 1 Determine the plume source conditions. Tabulate the following variables.

$$\begin{array}{l} \text{At } z = 0 \quad R, d_0, A \\ \quad \quad \quad Q, W_1, t_0, t_1, \Delta t_1 \end{array}$$

- 2 Source intensity. At reference temperature = 32 F

Determine  $\rho_0$  at  $(32 + t_0)/2$  from Figure B-2

Determine  $\rho_1$  at  $(32 + t_1)/2$  from Figure B-2

Calculate density ratio

$$\frac{\rho_0}{\rho_1} = \frac{1 + \rho_1(t_1 - 32)}{1 + \rho_0(t_0 - 32)}$$

(V-53)

## PLUME PROFILE METHOD Continued

- 3 Calculate initial plume density from  $\alpha_{32 F}$ , Table B-1, and Equation VI-8.

$$\rho_1 = \frac{62.4}{\alpha_{32F} (1 + \beta_1 (t_1 - 32))} , \frac{\text{lb}}{\text{cu ft}} \quad (8)$$

- 4 Calculate initial velocity.

$$w_1 = \frac{W_1}{A \rho_1} \quad (9)$$

- 5 Calculate Froude parameter,  $\sqrt{F_1}$ .

$$F_1 = \frac{w_1^2}{g d_o \left( \frac{\rho_{o1}}{\rho_1} - 1 \right)} \quad (V-44)$$

- 6 Entrainment and buoyancy at any penetration. Consider Point 2 at  $z_2$ . Calculate  $X$ .

$$X_2 = \frac{z_2}{d_o} \left( \frac{\rho_o}{\rho_1} \right)^{1/2} \frac{1}{F_1^{0.5}} \quad (V-42)$$

- 7 Calculate  $W_2/W_1$ .

$$\text{For } X < 3, \frac{W_2}{W_1} = 0.32 \frac{z_2}{d_o} \left( \frac{\rho_o}{\rho_1} \right)^{0.5} \quad (V-40)$$

$$\text{For } X \geq 3, Y_2 = 0.150 X_2^{1.67} \quad (V-41)$$

$$\frac{W_2}{W_1} = Y_2 F_1^{0.5} \quad (V-43)$$

- 8 Calculate  $\Delta t_2$ .

$$\Delta t_2 = \frac{\Delta t_1}{W_2/W_1} \quad (V-46a)$$

## PLUME PROFILE METHOD Continued

- 9 Calculate
- $t_2$

$$t_2 = t_o + \Delta t_2 \quad (10)$$

- 10 Calculate
- $W_2$

$$W_2 = W_1 (W_2/W_1) \quad (11)$$

- 11 Plot buoyancy or
- $\Delta t$
- dissipation, radius, and mass flow rate results as shown in Figures 84 and 85. Buoyancy penetration extends to
- $z$
- where the mean
- $\Delta t$
- is reduced to less than 0.2 F.

- 12 Calculate
- $z^*$
- . See Figure 86

$$z^*/d_o = 3.1 (\sqrt{F_1})^{0.4} \quad (V-82)$$

$$z^*/d_o = 3.1 F_1^{0.2} \quad (V-83)$$

$$z^* = (d_o) (z^*/d_o) \quad (12)$$

Check calculated  $z^*$  with value from plot of  $\Delta t$  versus penetration.

- 13 Calculate vertical velocity

$$w_2 = w_1 (z_2 - z^*)^{-1/3} \quad (V-55)$$

Momentum penetration extends to  $z = 1.33$  times  $z$  at  $\Delta t$  less than 0.2 F.

- 14 Calculate plume radius. Calculate mean density for plume at 0.5 (
- $t_{o1} + t_1$
- ) using Equation VI-8.

$$R_2 = \sqrt{\frac{W_2}{\pi w_2 \rho_{\text{mean}}}} \quad (V-56)$$

$$R_2 = \frac{\sqrt{W_2} \sqrt[3]{z_2 - z^*}}{\pi w_1 \rho_{\text{mean}}} \quad (V-58)$$

## PLUME PROFILE METHOD Continued

15 Maximum  $\Delta t$  at vertical axis

$$\Delta t_{2\max} = 3.16 \Delta t_2 \quad (V-63)$$

If  $\Delta t_{2\max}$  from Equation V-63 is greater than  $\Delta t_1$ , then

$$\Delta t_{2\max} = \Delta t_1.$$

## Plume in stratified temperature ocean

- 1 Determine the plume source conditions. Tabulate the following variables.

At  $z = 0$   $R, d_o, A$

$Q, W_1, t_{o1}, t_1, \Delta t_1$

Equation or graph giving  $t_o$  as a function of  $z$ . Usually  $dt_o/dz = \text{constant}$ .

- 2 to 5 Source intensity - see Steps 2, 3, 4, and 5 for uniform ocean.
- 6 and 7 Entrainment and buoyancy - see Steps 6 and 7 for uniform ocean.
- 8 Calculate  $t_{n+1}$ . Consider Point 3 at  $z_3$ .

$$t_{o3} = t_{o1} + z_3 \left( \frac{\Delta t_o}{\Delta z} \right) \text{ or obtain } t_{o3} \text{ from plot.}$$

$$W_3 = W_1 (W_3/W_1) \quad (11)$$

$$9 \quad t_3 = \frac{t_2 - \frac{t_{o2} + t_{o3}}{2}}{W_3/W_2} + \frac{t_{o2} + t_{o3}}{2} \quad (V-48)$$

$$10 \quad \text{Calculate } \Delta t_3 = t_3 - t_{o3} \quad (13)$$

- 11 to 15 See Steps 11 to 15 for uniform ocean



## TERMS AND SYMBOLS, CHAPTER VI

a	Fin thickness, in
A	Area, circular cross section for plume, $\text{ft}^2$
b	Fin height, in
c	Constant
Cn	Blasius law constant
Cp	Specific heat at constant pressure, Btu/lbm-F
D	Fin spacing, in
$d_o$	Diameter of circular heat source, cm or ft
$F_1$	Froude number at source, defined by Equation V-44
g	Acceleration of gravity, $\text{ft/hr}^2$ , for plume $980.7 \text{ cm/sec}^2$ or $32.2 \text{ ft/sec}^2$
$Gr_x$	Grashof number based on x, $\frac{x^3 g \beta \Delta T}{\nu^2}$
h	Heat transfer coefficient, Btu/hr-ft <sup>2</sup> -F
k	Thermal conductivity, Btu/hr-ft-F and Btu/hr-ft <sup>2</sup> -F/in
$Nu_x$	Nusselt number based on x, $\frac{hx}{k}$
Pr	Prandtl number, $\frac{Cp \mu}{k}$
Q	Heat flow, Btu/hr or Btu/sec
q	Heat rate Btu/hr
R	Radius of plume, cm or ft
r	Radius, feet
$Ra_x$	Rayleigh number, $Gr_x Pr$
T	Temperature, F
$t_o$	Temperature of surrounding liquid, C or F

## TERMS AND SYMBOLS, CHAPTER VI Continued

$t_1$	Temperature of plume liquid at source, C or F
$\Delta t$	Temperature difference ( $t_1 - t_0$ )...etc, C or F
$U$	Overall heat transfer coefficient, Btu/hr-ft <sup>2</sup> -F
$W$	Mass flow rate, g per sec or lb per sec
$W_1$	Mass flow rate at heat source, g per sec or lb per sec
$w$	Vertical velocity, cm per sec or ft per sec
$w_1$	Vertical velocity at the heat source
$X$	Group defined by Equation V-42
$x$	Vertical coordinate, feet
$Y$	Group defined by Equation V-43
$z$	Vertical penetration, feet
$z^*$	Distance beyond which velocity and radius laws are valid, feet

## GREEK

$\alpha$	Specific volume, cu cm per g, or reciprocal specific gravity, dimensionless
$\beta$	Coefficient of thermal expansion, F <sup>-1</sup> or C <sup>-1</sup>
$\delta$	Boundary layer thickness, ft
$\Delta$	Signifies a change
$\mu$	Viscosity, lbm/ft-hr
$\nu$	Kinematic viscosity, $\mu/\rho$ , ft <sup>2</sup> /hr
$\rho$	Density, lbm/ft <sup>3</sup>
$\rho_0$	Specific weight of liquid surrounding the plume, g/cm <sup>3</sup> or lb/ft <sup>3</sup>
$\rho_1$	Specific weight of plume liquid at heat source, g/cm <sup>3</sup> or lb/ft <sup>3</sup>

## TERMS AND SYMBOLS, CHAPTER VI Continued

## SUBSCRIPTS

a	Ambient
avg	Average
cyl	Evaluated for a cylindrical surface
c	Corrected
D	Fouling
G	Gross
GR	Gross, revised
m	Evaluated for fin metal
o	Evaluated at the base surface, for plume surrounding liquid at any position
s	Surface
x	Based on length, $x$
$\delta$	Based on boundary layer thickness, $\delta$
o1	Surrounding liquid at heat source
o2, o3, o4...on	Surrounding liquid at positions above the heat source
1	Plume liquid at heat source
2, 3, 4...n	Plume liquid at positions above the heat source

## BIBLIOGRAPHY

## UNDERWATER POWER SOURCES

- 1 Beck, E J and 10 others Techniques for Underwater Power. Technical Note 545, US Naval Civil Engineering Laboratory, Port Hueneme, California, 1964
- 2 Bechtel Corporation Final Report of Research and Development Study for Deep Ocean Reactor Placement. Contract NBy-32273, San Francisco, California, 1965
- 3 Crumpler, O B et al Deep Ocean Civil Engineering. Technical Report R345, US Naval Civil Engineering Laboratory, Port Hueneme, California, 1964
- 4 Clark, R A Jr et al Feasibility Study for 3 MW (e) Nuclear Thermoelectric Power Plant. Final Report, WANL PR(A)-002, 1960
- 5 Dufrane, K A 100 kw (e) Underwater Thermoelectric Reactor Plant Conceptual Design. Martin Company Nuclear Division, 1964
- 6 Fowler, E E and Sievering, N F, Jr Nuclear Power for Ocean Applications - Its Potential and Availability. Presented at Ocean Science and Ocean Engineering Conference, Washington, D C, 1965
- 7 Luzader, J Personal Communication. Allis Chalmers Research Division, San Francisco, California, 1965

## MARINE FOULING

- 8 Caldwell, J A and Lytle, M L Bacterial Corrosion of Offshore Structures. Corrosion 9, No 4, 1953, Pages 192-196
- 9 Chadwick, W L Thermal Control of Marine Fouling at Redondo Steam Station of Southern California Edison Company. Trans ASME, February 1950, Pages 127-131
- 10 Connolly, R A Effects of Seven Year Marine Exposure on Organic Materials. Materials Research and Standards, No 4, 1963, Pages 193-201.
- 11 Davis, I E and Barham, E G Fouling on a Deep-Anchored Submarine Hull. Report 1281, US Navy Electrical Laboratory, 1965

## BIBLIOGRAPHY Continued

- 12 DePalma, John R Results of a Deep-Sea Marine Fouling and Corrosion Pretest in the Tongue of the Ocean. Inf Ocean Man, US Naval Oceanographic Office, 1962, Pages 13-62
- 13 DePalma, John R Marine Fouling and Boring Organisms in the Tongue of the Ocean, Bahamas. Inf Man Report 0-64-62, US Naval Oceanographic Office, 1962
- 14 Gray, Kenneth Properties of Materials in Deep Ocean Environment. Technical Note N-380, US Naval Civil Engineering Laboratory, 1960
- 15 Gray, Kenneth Effects of the Deep Ocean Environment on Materials. Technical Note N-446, US Naval Civil Engineering Laboratory, 1962
- 16 Hazard, P M How environment Affects Ocean Cables. Bell Lab Rec, March 1961, Page 92
- 17 Milligan, S Effect of Deep Ocean Environment. US Naval Under Ordnance Station, 1965
- 18 Moritz, C E Mine Warfare and Mine Fouling. Report 957, US Naval Ordnance Laboratory, 1944
- 19 Muraoka, James S Effects of Marine Organisms on Engineering Materials for Deep Ocean Use. Technical Report R-182, US Naval Civil Engineering Laboratory, 1962
- 20 Muraoka, James S Deep Ocean Boring Mollusc. Bio Sci 15, No 3, 1965, Page 191
- 21 Reinhart, Fred M Preliminary Examination of Materials Exposed on STU-1-3 in the Deep Ocean. Technical Note N-605, US Naval Civil Engineering Laboratory, 1964
- 22 Snoke, L R Resistance of Organic Materials and Cable Structures to Marine Biological Attack. Bell Sys Technical J 36, No 5, 1957, Pages 1,095-1,127
- 23 Steinberg, P L The Resistance of Organic Materials at Attack by Marine Bacteria at Low Temperatures. Bell Sys Technical J 40, No 5, 1961
- 24 Stewart, W C Control of Marine Fouling in Piping Systems by Treatment with Hot Water. Report 4E, No F1, 101717, US Naval Engineering Experimental Station, 1952

## BIBLIOGRAPHY Continued

- 25 Turner, Charles An Ecological Survey of the Marine Environment in the Vicinity of Canyon de las Encinas, San Diego County. Report to State Water Pollution Control Board, Resources Agency of California, 1962
- 26 Uhlig, H Corrosion Handbook. John Wiley and Sons, 1948
- 27 US Naval Civil Engineering Laboratory Structures in Deep Ocean. Engineering Manual for Underwater Construction, Technical Report 284, US Naval Civil Engineering Laboratory, 1964
- 28 Vaughan, Shiela M A Preliminary Study of Successive Animal Populations on Test Blocks on Standard-Humble Oil Tower, "Hazel", at Summerland, California. Immaculate Heart College, Los Angeles, 1964
- 29 White, H E Control of Marine Fouling in Seawater Conduits Including Exploratory Tests on Killing Shelled Mussels. Trans ASME, February 1950, Pages 117-126
- 30 Wood, E J Investigations in Underwater Fouling. Australian J Mar Fresh Res 1, No 1, 1950, Pages 85-91
- 31 Wood E J Effect of Temperature and Rate of Flow on Some Fouling Organisms. Australian J Sci 18, No 1, 1955, Pages 34-37
- 32 Woods Hole Oceanographic Institution Marine Fouling and Its Prevention. US Naval Institute, 1964
- 33 ZoBell, C E and Allen, E C The Significance of Marine Bacteria in the Fouling of Submerged Surfaces. J Bact 29, No 3, 1935, Pages 239-251
- 34 ZoBell, C E The Sequence of Events in the Fouling of Submerged Surfaces. Scripps Inst Ocean, No 35, 1938, Page 18

## DEEP OCEAN CORROSION

- 35 Brouillette, C V Corrosion Rates in Port Hueneme Harbor. Corrosion, Vol 1, August 1958
- 36 Gray, K O Materials Testing in the Deep Ocean. Materials Protection, July 1964

## BIBLIOGRAPHY Continued

- 37 Muraoka, James S The Effects of Marine Organisms on Engineering Materials for Deep Ocean Use. Technical Report R-182, US Naval Civil Engineering Laboratory, March 1962
- 38 Woods Hole Oceanographic Institution Marine Fouling and Its Prevention. Chapter 21, US Naval Int, 1952

## DEEP OCEAN MOORING

- 39 Bascom, Willard Ocean Waves. Scientific American, August 1959
- 40 Cawley, John H and Little, A D, Inc Navigational Requirements for Oceanography vs Precision Available, Cambridge, Massachusetts
- 41 Frautschy, J D Notes on Wire Rope and Equipment Handling. Scripps Institute of Oceanography, LaJolla, California
- 42 Isaacs, Faughn, Schick, and Sargent Deep Sea Moorings. Scripps Institute of Oceanography, LaJolla, California, 1963
- 43 Milligan, S Effect of Deep Ocean Environment on Underwater Installations. US Naval Underwater Ordnance Station, Newport, Rhode Island
- 44 Schneider, Mahan, and Burton Tow Cable Snaploads. Underwater Technology Division, ASME, December 1964
- 45 Thompson and Logan Cable Testing for Oceanographic Applications. US Navy Electronics Laboratory, San Diego, California
- 46 US Naval Civil Engineering Laboratory Structures in Deep Ocean. Engineering Manual for Underwater Construction, Chapter 3, Reconnaissance and Positioning, Port Hueneme, California, March 15, 1964

## NATURAL CONVECTION HEAT TRANSFER

- 47 Appl, F C and Hung, H M Finned Surfaces with Optimum Fins of Restricted Length. Symposium on Air-Cooled Heat Exchangers, ASME, presented at Seventh National Heat Transfer Conference, Cleveland, Ohio, August 10, 1964
- 48 Baron, J R and Finston, M Free Convection Past a Vertical Flat Plate. Some Numerical Results, Naval Supersonic Laboratory MIT, AD - 227 554, March 1959

## BIBLIOGRAPHY Continued

- 49 Bayley, F J An Analysis of Turbulent Free Convection Heat Transfer. Proceedings of the Institution of Mechanical Engineers, Vol 169, 1955, Pages 361-358
- 50 Braun, W H and Heighway, J E An Integral Method for Natural Convection Flows at High and Low Prandtl Numbers, NASA Report, AD - 238 898, June 1960
- 51 Bartolsky, S L Free Convection Heat Transfer on a Vertical Plate Under Conditions of Nonuniform Surface Temperature. Institute of Technology USAF, W-PAF3 MS Thesis, 1958
- 52 Bodoia, J R and Osterle, J F The Development of Free Convection Between Heated Vertical Plates. Journal of Heat Transfer, Vol 84 C, 1962, Pages 40-44
- 53 Carne, J B Heat Loss by Natural Convection From Vertical Cylinders. Philosophical Mag and Journal of Science, London, Edinberg, Dublin, Vol 24, Series 7, 1937, Pages 634-653
- 54 Chapman, A J Heat Transfer. Macmillan, London, 1960
- 55 Clark, R A, Jr et al Feasibility Study for 3 MW (e) Nuclear Thermoelectric Power Plant. Final Report WANL-FR (A) 002, Westinghouse Electric Corp, Astronuclear Laboratory, Pittsburgh, Pennsylvania, December 31, 1960
- 56 Colburn, A P and Hougen, O A Bulletin of University of Wisconsin, Engineering Experiment Station, Series No 70, 1930, Page 44
- 57 Cumo, M, Lopez, S, and Pinchera, G C Numerical Calculation of Extended Surface Efficiency. Presented at Seventh National Heat Transfer Conference, Cleveland, Ohio, August 10, 1964
- 58 Dropkin, D and Somerscales, E Heat Transfer by Natural Convection in Liquids Confined by Two Parallel Plates Which Are Inclined at Various Angles With Respect to the Horizontal. ASME Paper 64-HT-22
- 59 Duffin, R J A Variational Problem Related to Cooling Fins. J Mathematics and Mechanics, Vol 8, No 1, 1959, Pages 47-56
- 60 Eckert, E R G and Drake, R M Heat and Mass Transfer. New York, McGraw-Hill, 1959, Pages 312-322



## BIBLIOGRAPHY Continued

- 61 Eckert, E R G and Jackson, T W Analysis of Turbulent Free Convection Boundary Layer on a Flat Plate. NACA Report 1015, 1951
- 62 Eckert, E R G and Soehngen, E Interferometric Studies on The Stability and Transition to Turbulence of a Free Convection Boundary Layer, Proceedings of the General Discussion on Heat Transfer. Institution of Mechanical Engineers - ASME, London, 1951, Pages 321-323
- 63 Elenbaas, W The Heat Dissipation of Parallel Plates by Free Convection. Physica, Vol 9, No 1, 1942, Pages 1-28, Ibid 9, No 8, 1942, Pages 865-874
- 64 Fairbanks, D R and Marks, M An Optimization Procedure for Finning in Free Convection. ASME Paper 65-HT-12, presented at the ASME-AIChE Heat Transfer Conference, Los Angeles, California, August 8-11, 1965
- 65 Fritsch, C A and Grosh, R J Free Convective Heat Transfer to Supercritical Water Experimental Measurements. Journal of Heat Transfer, Vol 85C, No 4, 1963, Page 289
- 66 Fujii, T Experimental Studies of Free Convection Heat Transfer. Bull Japan Soc Mech Engrs, Vol 2, No 8, 1959, Page 559
- 67 Gardner, K A Efficiency of Extended Surface. Trans ASME Vol 67, 1945, Pages 621-631
- 68 Gebhart, B Transient Natural Convection From Vertical Elements. Journal of Heat Transfer, Vol 85C, 1961, Page 61
- 69 Ibid Transient Natural Convection from Vertical Elements - Appreciable Thermal Capacity. Journal of Heat Transfer, Vol 85C, 1963, Page 10
- 70 Gebhart, B and Adams, D E Measurement of Transient Natural Convection on Flat Vertical Surfaces. Journal of Heat Transfer, Vol 85C, 1963, Page 25
- 71 Goldstein, R J and Eckert, E R G The Steady and Transient Free Convection Boundary Layer on a Uniformly Heated Vertical Plate. International J of Heat and Mass Transfer, Vol 1, 1960, Page 208
- 72 Griffith, E and Davis, A H The Transmission of Heat by Radiation and Convection. Great Britain Department of Scientific and Industrial Research, Special Report 9, 1922

## BIBLIOGRAPHY Continued

- 73 Harper, D R and Brown, P W Mathematical Equations for Heat Conduction in the Fins of Air-Cooled Engines. NACA Technical Report 158, 1922
- 74 Hellums, J D and Churchill, S W Dimensional Analysis and Natural Circulation. CEP Symposium Series, Vol 57, No 32, 1961, Page 75
- 75 Hill, R C An Experimental Investigation of Free Convection Heat Transfer From a Nonisothermal Vertical Flat Plate. M S Thesis, University of California, Berkeley, 1961
- 76 Hsu, S T, Hsieh, C, and Vatsaraj, B C An Extended Surface with Finned Pins Under Free Convection Cooling. ASME Paper 65-HT-55, presented at ASME-AICHE Heat Transfer Conference, Los Angeles, California, August 8-11, 1965
- 77 Jakob, M Heat Transfer. John Wiley and Sons, New York, 1949
- 78 Jakob, M and Dow, W M Heat Transfer from a Cylindrical Surface to Air in Parallel Flow With and Without Unheated Starting Sections. Trans ASME, Vol 68, 1946, Pages 123-134
- 79 Kern, D Q Process Heat Transfer. McGraw-Hill Book Company, New York, 1950
- 80 King, W J Heat Transfer from Vertical Parallel Plates. Refrig Eng, Vol 19, 1930, Page 163
- 81 Ibid Basic Laws and Data of Heat Transmission, III Free Convection. Mechanical Engineering, Vol 54, 1932, Page 347
- 82 Koh, J C Y and Price, J F Laminar Free Convection from a Nonisothermal Cylinder. ASME Paper 64-HT-5
- 83 Kraus, A D Extended Surfaces for Heat Transfer. Electro Technology, February 1961, Page 73
- 84 Larson, J R and Schoenhals, R J Turbulent Free Convection in Near Critical Water. US Atomic Eng Comm Report COO-1177-16, August 1964
- 85 Libby, B C Transient Heat Transfer and Velocity Profile by Free Convection from a Heated Vertical Cylinder to a Hydrocarbon Polymer of High Viscosity. AD - 140 629, 1957
- 86 Lorenz, E Ann Phys Lpz, Vol 13, 1881, Page 582

## BIBLIOGRAPHY Continued

- 87 Ibid Die Wärmeübertragung an Einer Ebener Senkrechten Platte an Obie Natürlichen Konvektion. Z Technical Phys, Vol 15, 1934, Page 362
- 88 Mabuchi, I Laminar Free Convection From a Vertical Cylinder With Uniform Surface Heat Flux. Trans Japan Soc Mech Engrs, Vol 27, No 180, 1961, Page 1,306
- 89 McAdams, W H Heat Transmission. Third Edition, New York, McGraw-Hill, 1954
- 90 Ostrach, S Laminar Free Convection on a Vertical Plate. NACA Technical Note 2635, 1952
- 91 Ibid An Analysis of Laminar Free Convection Flow and Heat Transfer About a Plate Parallel to the Direction of the Generating Body Force. NACA Technical Report 1111, 1953
- 92 Pohlhausen, E Technical Mech Thermodynam. Berlin, Vol 1, 1930, Page 391
- 93 Regnier, G M and Kaplan, C Visualization of Natural Convection on a Plane Wall and in a Vertical Gap by Differential Interferometry, Transitional and Turbulent Regimes. Proc of 1963 Heat Transfer and Fluid Mechanics Institute, 1963, Page 95
- 94 Robin, M and Schwab, B Convection Naturelle Entre Plaques Paralleles Verticales. CEA-650, 1957
- 95 Rutkowski, J Free Convection from Heated Surfaces, Laminar Boundary Layers. AD - 76 228, 1955
- 96 Ibid Natural Convection Heat Transfer. Two and Three Dimensional Effects from Flat Plates. AD - 61 705, 1955
- 97 Saunders, O A Natural Convection in Liquids. Proc Royal Society, London, Series A, Vol 172, 1939, Pages 55-71
- 98 Scherberg, M G Natural Convection Near and Above Thermal Leading Edges on Vertical Walls. International J of Heat and Mass Transfer, Vol 5, 1962, Pages 1,001-1,010
- 99 Ibid Natural Convection from Wall Sections at Arbitrary Temperature Distribution by an Integral Method. International J of Heat and Mass Transfer, Vol 7, 1964, Pages 501-506
- 100 Schlichting, H Boundary Layer Theory. New York, McGraw-Hill, 1960

## BIBLIOGRAPHY Continued

- 101 Schmidt, E Zeit fur die Gesamte Kalte. Industrie, Vol 35, 1928, Page 213
- 102 Schmidt, E On the Application of the Calculus of Finite Differences to Technical Heating and Cooling Problems (title translated). Festschrift zum siebzigsten Geburtstag August Foepppls, Julius Springer, Berlin, 1924, Page 179
- 103 Schmidt, E and Beckman, M Tech Mech Thermodynam. Berlin, Vol 1, 1930, Page 341
- 104 Schuh, H Einige Probleme bei Freier Stromung Zuher Flussigkeiten (unpublished). See Gottingen Monographien, Vol B Grenzschichten, 1946
- 105 Siegel, R and Norris, R H Tests of Free Convection in a Partially Enclosed Space Between Two Heated Vertical Plates. Trans ASME, Vol 79, 1957, Pages 663-672
- 106 Sparrow, E M Laminar Free Convection on a Vertical Plate with Prescribed Nonuniform Wall Heat Flux or Prescribed Nonuniform Wall Temperature. NACA Technical Note 3508, 1955
- 107 Sparrow, E M and Gregg, J E Laminar Free Convection from a Vertical Plate with Uniform Surface Heat Flux. Trans ASME, Vol 78, 1956, Pages 435-440
- 108 Ibid Similar Solutions for Free Convection from a Nonisothermal Vertical Plate. Trans ASME, Vol 80, 1958, Page 379
- 109 Ibid Nearly Quasi-steady Free Convection Heat Transfer in Gases. Journal of Heat Transfer, Vol 82, 1960, Pages 258-260
- 110 Starner, K E and McManus, H N An Experimental Investigation of Free Convection Heat Transfer from Rectangular Fin Arrays. Journal of Heat Transfer. Vol 85C, 1963, Page 273
- 111 Sverdrup, H U, Johnson, M W, and Fleming, R H The Oceans, Their Physics, Chemistry, and General Biology. New York, Prentice-Hall, 1942
- 112 Touloukian, Y S, Hawkins, G A, and Jakob, M Heat Transfer by Free Convection from Heated Vertical Surfaces. Trans ASME, Vol 70, 1948, Page 13
- 113 Tuan, Y Heat Transfer in Natural Convection Flow of Water. MS Thesis, University of Washington, Seattle, 1959

## BIBLIOGRAPHY Continued

- 114 Van Dyke, M S Boundary Layer Temperature in Natural Convection Flow of Water. MS Thesis, University of Washington, Seattle, 1960
- 115 Waibler, P J Natural Convection Heat Transfer with Water at High Grashof Numbers. PhD Thesis, University of Illinois, 1958
- 116 Walker, R C Interferometer Study of The Effect of Reduced Pressure on Free Convection from a Vertical Plate. AD - 292 178, 1962
- 117 Welling, J R and Wooldridge, E B Free Convection Heat Transfer Coefficients from Rectangular Vertical Fins. ASME Paper 64-WA/HT-33, 1964
- 118 Wordsworth, D V Laminar Free Convection Between Heat Producing Vertical Plates in a Liquid. AERE-E/R-1270, 1953

## TURBULENT PLUME AND JET FLOW

- 119 A Meteorological Survey of the Oak Ridge Area, 1948-1952. US Atomic Energy Commission, Weather Bureau, Oak Ridge, Tenn, Report ORO-99
- 120 Albertson, M L, Dai, Y B, Jensen, R A, and Rouse, H Diffusion of Submerged Jets. Trans ASCE, Vol 115, 1950, Pages 639-679
- 121 Alexander, L G, Baron, T, and Comings, E W Transport of Momentum, Mass, and Heat in Turbulent Jets. University of Illinois Eng Expt Station, Bulletin Series No 413, Vol 50, No 66, May 1953
- 122 Batchelor, G K Heat Convection and Buoyancy Effects in Fluids. Quarterly J of the Royal Meteorological Society, Vol 80, 1954, Pages 339-358
- 123 Broido, A and McMasters, A W The Influence of a Fire Induced Convection Column on Radiological Fallout. Div of Forest Fire Research, California Forest and Range Expt Station, Forest Service, US Dept of Agriculture, Technical Paper 32, March 1959 - AD 254071
- 124 Bryant, L W and Cowdrey, C F Effects of Velocity and Temperature of Discharge on the Shape of Smoke Plumes from a Funnel - Experiments in a Wind Tunnel. Proc Inst Mech Engrs, Vol 169, 1955, Pages 371-399

## BIBLIOGRAPHY Continued

- 125 Clark, R A, Jr et al Feasibility Study for 3 MW (e) Nuclear Thermoelectric Power Plant. Final Report WANL-PR (A) 002, Westinghouse Electric Corp, Astronuclear Laboratory, Pittsburgh, Pa, December 31, 1960
- 126 Cleeves, V and Boelter, L M K Isothermal and Nonisothermal Air-Jet Investigations. Chemical Engineering Progress, Vol 43, No 3, 1947, Pages 123-134
- 127 Cooper, L H N Vertical and Horizontal Movements in the Ocean. American Association for the Advancement of Science, Publication No 67, Oceanography, Edited by Mary Sears, 1962, Pages 599-621
- 128 Corrsin, S and Uberoi, M S Further Experiments on Flow and Heat Transfer in a Heated Turbulent Air Jet. NACA Technical Note 1865, 1959
- 129 DeWitt, K J and Thodos, G Coefficient of Thermal Expansion - Reduced State Correlation for Water in the Gaseous and Liquid States. Can J of Chem Eng, December 1963, Pages 258-259
- 130 Fofonoff, N P Conference on Physical and Chemical Properties of Seawater, 1958. Office of Naval Research and the Committee on Oceanography, Publication No 600, NAS-NRC, 1959
- 131 Forstall, W and Gaylord, E W Momentum and Mass Transfer in a Submerged Water Jet. Trans ASME, J Appl Mech, Vol 22, 1955, Pages 161-164
- 132 Förthmann, E Turbulent Jet Expansion. NACA Technical Memo 789, 1934
- 133 Fultz, D Experiments Combining Convection and Rotation and Some of their Possible Implications. Proc First Midwestern Conference on Fluid Dynamics, 1950 - Ann Arbor, J W Edwards, 1951, Pages 297-304
- 134 Fye, P M Modern Measurements of Ocean Currents. Woods Hole Oceanographic Institution paper presented at ASME Meeting, 1961, Page 6
- 135 Geary, J E The Effect of Wind upon the Mixed-Layer Depth. Master's Thesis, Naval Postgraduate School, Monterey, California, 1961 - AD 262322

## BIBLIOGRAPHY Continued

- 136 Ginevsky, A S Approximate Motion Equation in Problems of the Turbulent Jet Theory. Izv Akad Nauk SSSR Mekhan Mashinostroenie, No 5, 1963, Page 134
- 137 Haltiner, G J On the Theory of Convective Currents. Tellus, Vol 11, No 1, 1959, Pages 4-15
- 138 Idelchik, I E Calculation Method of Transient Heat and Mass Transfer in a Free Jet. Khimich Promst, No 4, 1963, Page 57
- 139 Izyumov, M A, Khzmalyan, D M, and Yakovlevsky, O V Propagation of Plane Jet System. Inzh-Fiz Zh, Vol 2, vyp 4, 1962, Page 269
- 140 Koczy, F F Vertical Eddy Diffusion in Deep Water. Nature, Vol 178, September 15, 1956, Pages 585-586
- 141 Kristmanson, D and Danckwerts, P V Studies in Turbulent Mixing - I Dilution of a Jet. Chemical Engineering Science, Vol 16, 1961, Pages 267-277
- 142 LaFond, E C Processing Oceanographic Data. US Navy Hydrographic Office, Washington, D C, H O Publication No 614, 1951
- 143 Lilly, D K On Numerical Simulation of Buoyant Convection. Tellus, Vol 14, No 2, 1962, Pages 148-172
- 144 Meade, P J Convection from a Small, Continuous Source of Heat in a Calm, Neutral Atmosphere. Air Ministry, Meteorological Research Committee, 1955, MRP 952, AD Number 117799
- 145 Morton, B R, Taylor, G I, and Turner, J S Turbulent Gravitational Convection from Maintained and Instantaneous Sources. Proc Roy Soc, Vol A234, 1956, Pages 1-23
- 146 Naylor, P P and Bisshopp, F E On the Influence of Coriolis Forces on Onset of Thermal Convection. Technical Report 54, May 1964 - AD 600590
- 147 Oceanic Observations of the Pacific, 1949 University of California Press, 1957
- 148 Pai, S I Fluid Dynamics of Jets. New York, Van Nostrand, 1954
- 149 Ibid On Turbulent Jet Mixing of Two Gases at Constant Temperature. Technical Note BN-33, University of Maryland, College Park, Maryland, June 1954, - AD 36967

## BIBLIOGRAPHY Continued

- 150 Phillips, O M The Upper Ocean Layers. Hydronautics, Inc  
Technical Report 2311, May 1963 - AD 416746
- 151 Priestley, C H B and Ball, F K Continuous Convection from an  
Isolated Source of Heat. Quarterly J of the Royal  
Meteorological Society, Vol 81, 1955, Pages 144-157
- 152 Proudman, J Dynamical Oceanography. New York, John Wiley  
and Sons, 1953
- 153 Ricou, F P and Spalding, D B Measurements of Entrainment by  
Axisymmetrical Turbulent Jets. J Fluid Mechanics, Vol 11, 1961,  
Pages 21-32
- 154 Robinson, A and Stommel, H The Oceanic Thermocline and the  
Associated Thermohaline Circulation. Tellus, Vol 11, 1959,  
Pages 295-308
- 155 Rouse, H, Yih, C S, and Humphreys, H W Gravitational  
Convection from a Boundary Source. Tellus, Vol 4, 1952,  
Pages 201-210
- 156 Saunders, P M Penetrative Convection in Stably Stratified  
Fluids. Tellus, Vol 14, 1962, Pages 177-194
- 157 Schlichting, H Boundary Layer Theory. New York, McGraw-Hill  
Book Co, 1962
- 158 Schmidt, W Turbulente Ausbreitung eines Stromes Erhitzter  
Luft. Zeitschrift fur angewandte Mathematik und Mechanik,  
Vol 21, 1941, Pages 265-278 and 351-363
- 159 Scorer, R S Experiments on Convection of Isolated Masses of  
Buoyant Fluid. J Fluid Mech, Vol 2, 1957, Pages 583-594
- 160 Steiger, M H, Hinz, W, Sforza, P M, and Trentacoste, N Studies  
in Three-Dimensional Viscous Free-Mixing. I - Finite  
Difference Solutions. II - Experimental Results. American  
Institute of Aeronautics and Astronautics, Second Aerospace  
Sciences Meeting, New York, Paper 65-49, January 1965
- 161 Stommel, H Lateral Eddy Viscosity in the Gulf Stream System.  
Deep Sea Research, Vol 3, 1955, Pages 88-90
- 162 Sverdrup, H U Oceanic Circulation. Proc Fifth Int Cong for  
Applied Mechanics, Cambridge, Mass, 1938, Pages 279-293 -  
New York, John Wiley and Sons, 1939



## BIBLIOGRAPHY Continued

- 163 Sverdrup, H U, Johnson, M W, and Fleming, R H The Oceans, Their Physics, Chemistry, and General Biology. New York, Prentice-Hall, 1942
- 164 Swallow, M Deep Currents in the Ocean. Oceans, Vol 8, No 3, March 1961, Page 7
- 165 Szablewski, W Asymptotic Laws of Turbulent Expansion of a Vertical Gas Jet in a Uniform Medium Taking into Account Archimedes' Buoyancy Principle. Zeitschrift für angewandte Mathematik und Mechanik, Vol 44, December 1964, Pages 595-603
- 166 Taylor, G I Flow Induced by Jets. J of Aerospace Sciences, Vol 25, 1958, Pages 464-465
- 167 Taylor, G I Experiments with Rotating Fluids. Proc Roy Soc, Vol A100, 1921, Pages 114-121 + Plate 2
- 168 Taylor, G I Experiments with Rotating Fluids. Proc First International Congress for Applied Mechanics, Delft, 1924, Pages 89-96 + Plates VII to X
- 169 Taylor, G I Dynamics of a Mass of Hot Gas Rising in Air. US Atomic Energy Commission MDDC 919, LADC 276, 1945
- 170 Taylor, G I Fire Under Influence of Natural Convection. Int Symp on the Use of Models in Fire Research, NAS-NRC Publication 786, 1961, Pages 10-31
- 171 Timma, E Turbulent Round and Plane Jets Developing in a Counterflow. Izv Akad Nauk Estonsk SSR, Vol 11, Ser Fiz Mat Tekhn Nauk No 4, 1962, Page 253
- 172 Tollmien, W Calculation of Turbulent Expansion Processes. Zeitschrift für angewandte Mathematik und Mechanik, Vol 6, 1926, Pages 1-12, - NACA Technical Memo 1085, 1945
- 173 Turner, K S Model Experiments Relating to Thermal with Increasing Buoyancy. Quarterly J Roy Met Soc, Vol 89, No 379, 1963, Pages 62-74
- 174 Viilu, A An Experimental Determination of the Minimum Reynolds Number for Instability in a Free Jet. J Appl Mech, Trans ASME, Series E, Vol 84, 1962, Pages 506-508

## BIBLIOGRAPHY Continued

- 175 Von Arx, W S An Introduction to Physical Oceanography.  
Reading, Mass - Addison-Wesley Publishing Co, 1962
- 176 Wilson, R A M and Danckwerts, P V Studies in Turbulent  
Mixing - II A Hot Air Jet. Chem Eng Sci, Vol 19, November 1964,  
Pages 885-895
- 177 Yih, C S Free Convection Due to a Point Source of Heat. Proc  
First US National Congress of Applied Mechanics, 1951  
Pages 941-947

## APPENDIX A

## ENGINEERING AGREEMENT - AUGUST 21 1964

Braun and NCEL engineers have agreed that the steps, tests, and procedures outlined and defined below are at this time considered adequate to accomplish the current objectives of the study program.

## PHASE I, LITERATURE SURVEY AND CONSTRUCTION OF MATHEMATICAL MODELS

- 1 Survey current literature for information related to natural convection heat transfer and heat plume configuration in a deep ocean environment.
- 2 Develop a mathematical model for the natural convection heat transfer coefficient and induced flow from a submerged heat source with vertical finned plates or vertical finned cylindrical heat rejection surfaces.
- 3 Develop and construct a mathematical model to predict the configuration of the heat plume from a heat rejection surface in ocean environment.

## PHASE II, FOULING AND CORROSION TESTS ON HEATED SURFACES IN OCEAN ENVIRONMENT (MODIFIED BY CHANGE "B", MAY 24, 1965)

- 1 Survey the literature for information useful in prediction of fouling and corrosion of different materials in deep ocean environment at metal surface temperatures ranging from 100 F to 140 F.
- 2 Design and perform field observation tests to provide data on fouling and corrosion rates of three different materials at temperatures ranging from 100 F to 140 F in an ocean environment at depths from 15 feet to 6,000 feet. The following tests will be performed.

## ENGINEERING AGREEMENT - AUGUST 21, 1964 Continued

- a SHALLOW WATER TEST Prepare four test specimens for tests of fouling and corrosion of three different materials at ambient, 100 F, 120 F, and 140 F. Perform these tests at depths of 15 to 20 feet, adjacent to a pier in San Diego harbor for a period of 120 days. Gather and correlate the following data from these tests. (1) Photographs of test specimens before and after the test period. (2) Rate of power consumption for each heated specimen. (3) Metal surface temperature for each test specimen. (4) Ambient water temperature. (5) Current velocity. (6) Dissolved oxygen content. (7) Salinity. And (8) record observations relative to fouling and corrosion immediately on removing specimens from the ocean and return specimens to laboratory for further study.

Readings on Items 2, 3, 4, and 5 will be taken weekly during the test period. Data on Item 6 will be collected every two weeks. Measurements of Item 7 will be at the beginning and end of the test period.

- b 300-FOOT DEPTH TESTS Prepare four test specimens for tests of fouling and corrosion of three different materials at ambient, 100 F, 120 F, and 140 F. Perform these tests at a depth of approximately 300 feet in Southern California coastal waters for an uninterrupted period of five days. Gather and correlate the following data from these tests.

(1) Photographs of test specimens before and after the test period. (2) Rate of power consumption of the heated specimens. (3) Metal surface temperature of test specimens. (4) Ambient water temperature. (5) Current velocity. (6) Dissolved oxygen content. (7) Salinity. And (8) record observations relative to fouling and corrosion immediately on removing specimens from the ocean and return specimens to laboratory for further study.

Readings on Items 2 and 3 will be taken at 4-hour intervals, and for Items 4 and 5, twice daily. Data will be collected on Items 6 and 7 at the beginning and at the end of the test period.

- c 4,500-FOOT TEST Same as b, 300-Foot Tests, except that the tests will be performed at a depth of approximately 4,500 feet and readings on Items 4 and 5 will be taken at 24-hour intervals instead of 12-hour intervals.

## ENGINEERING AGREEMENT - AUGUST 21, 1964 Continued

- 3 Evaluate, analyze, and correlate collected data for application to the overall program objectives and to establish tentative fouling factors for calculation of heat transfer coefficients.
- 4 Prepare an interim report covering this phase of the work.

## PHASE III, LABORATORY HEAT TRANSFER TESTS (MODIFIED BY CHANGE "A", DECEMBER 9, 1964)

- 1 Establish a definitive test program for laboratory experiments on heat transfer from heated cylindrical and flat-finned sections to both still and laterally moving fresh water at ambient temperature.
- 2 Fabricate three test units and one clearance-plate assembly. The test units shall be fabricated of carbon steel with copper heat-transfer surfaces. The clearance-plate assembly shall be capable of attachment to either of the two cylindrical test units and shall incorporate an adjustable baffle to vary the inlet clearance. The test units shall be comprised of the following sections.
  - a Seven 1-inch diameter cylinders
  - b Seven 2-inch diameter cylinders
  - c Two finned flat plates
- 3 Conduct an experimental test program to develop reproducible, steady state heat transfer coefficient data for the test units. The following data will be collected from each test.
  - a Power input to each test module
  - b Metal surface temperature
  - c Ambient water temperature

Temperature data will be gathered in the plume when the power input is sufficient to generate a measurable temperature rise above ambient.

## ENGINEERING AGREEMENT - AUGUST 21, 1964 Continued

- 4 Conduct heat transfer tests on two cylindrical test sections and one flat-plate test unit before fins are installed. Each of the two cylindrical units shall be tested at four different power levels. The flat-plate unit shall be tested at twelve different power levels. These tests should establish the relationship between the actual heat transfer coefficients for the test sections and published data. Testing of the two cylindrical units is to give data for correlation of performance using different cylindrical surfaces. All test sections may be modified if necessary to collect meaningful data from the finned test units.
- 5 Perform tests using three different fin spacings and three different heights to check the validity of the mathematical prediction of optimum fin spacing height combinations for individual finned plates and the 2-inch diameter finned cylinders.
- 6 Perform experiments with the test units using five different flat-plate spacings and five different arrangements of the 2-inch diameter cylinders to evaluate the interactions between adjacent heat-transfer surfaces. Spacing between surfaces shall be varied in these tests with fins at their optimum spacing.
- 7 Evaluate the effect of three different types of chimneys on the flat-plate test unit and on the 2-inch diameter cylindrical test unit.
- 7A Determine the effect of inlet flow area on natural convection heat flow by testing the flat-plate unit and the 2-inch cylindrical unit with the clearance-plate assembly attached. Each of the two units shall be tested with four different inlet clearances for a minimum of eight tests.
- 8 Perform about twenty-four tests to evaluate the effect of four different current magnitudes and directions on the heat transfer characteristics of the units and measure the effect of superimposed currents on the upwelling from the heat source.
- 9 Correlate the data and results of these tests for application to the heat transfer and plume mathematical models and for use in the design of a prototype heat rejection unit for ocean testing.
- 10 Prepare an interim report covering this phase of work.

## ENGINEERING AGREEMENT - AUGUST 21, 1964 Continued

## PHASE IV, CONCEPTUAL DESIGN STUDY AND OCEAN TESTING OF A HEAT REJECTION UNIT PROTOTYPE

- 1 Conduct a conceptual design study of a heat rejection unit for use in deep ocean to reject waste heat from a 500 kw (e) fuel cell.
- 2 Perform detailed design and fabricate a prototype heat rejection unit for test purposes. The prototype unit will be designed to represent a minimum section of a full-scale convector necessary to provide meaningful test data applicable to the design concept. It will employ a heat source of 250 kw or less. The heat rejection unit will be mounted on a base to simulate operating conditions of a power unit installed on the ocean bottom. Power will be provided from an external source for test purposes.
- 3 Run tests with the prototype unit for uninterrupted period of 48 hours to gather data on heat transfer performance and heat plume configuration. The tests will be conducted in ocean water at a location where currents of 0.1 to 1.0 knots are expected. Sufficient depth is required to allow room above the prototype for development of the heat plume. Present calculations indicate that a water depth of 30 to 35 feet will be adequate. The test unit should probably be located about this same distance from the pier or other obstruction in order to ensure free circulation and normal plume development.

Vary the power input in order to obtain heat transfer data at different metal surface temperatures and collect the following data. (1) Photographs of the prototype unit before and after the test period. (2) Rate of power consumption at 4-hour intervals. (3) Temperature of the heat rejection surface at 24 points at 4-hour intervals. (4) Ambient water temperature in the test area at 4-hour intervals. (5) Current magnitude and direction at 4-hour intervals. (6) Thermistor measurements of the temperature field of the plume at 4-hour intervals. (7) Dissolved oxygen concentration at beginning and end of tests. (8) Salinity at beginning and end of tests. And (9) record observations relative to fouling and corrosion at end of test.

- 4 Analyze, evaluate, and correlate collected data for applicability to the overall program objectives.

## ENGINEERING AGREEMENT - AUGUST 21, 1964 Continued

- 5 Check the heat transfer mathematical model and make necessary corrections.
- 6 Check the mathematical model for plume characteristics and make necessary corrections.
- 7 Prepare a final report on the results of the overall program.



## APPENDIX B

## PHYSICAL PROPERTIES OF SEAWATER AND WATER

TABLE B-1

SPECIFIC VOLUME OF SEAWATER - FROM SVERDRUP (111)  
(35 ‰ SALINITY, 0 DEGREES C)

<u>PRESSURE</u> <u>DECIBARS</u>	$\alpha_{35,0,P}$ <u>cm<sup>3</sup>/gm</u>
0	0.97264
500	0.97040
1,000	0.96819
1,500	0.96602
2,000	0.96388
2,500	0.96177
3,000	0.95970
3,500	0.95766
4,000	0.95566
4,500	0.95368
5,000	0.95173
5,500	0.94981
6,000	0.94791
6,500	0.94605
7,000	0.94421
7,500	0.94239
8,000	0.94060
8,500	0.93883
9,000	0.93709
9,500	0.93537

TABLE B-2

COEFFICIENT OF THERMAL EXPANSION OF  
SEAWATER, 35 ‰ SALINITY - FROM SVERDRUP (111)  
VALUES OF ( $\beta \times 10^6$ ) IN 1/C

<u>PRESSURE</u> <u>DECIBARS</u>	<u>TEMPERATURE, C</u>							
	<u>-2</u>	<u>0</u>	<u>5</u>	<u>10</u>	<u>15</u>	<u>20</u>	<u>25</u>	<u>30</u>
0	23	51	114	167	214	257	297	334
2,000	80	105	157	202	241	278	-	-
4,000	132	152	196	233	266	-	-	-
6,000	177	194	230	-	-	-	-	-
8,000	-	231	246	-	-	-	-	-
10,000	-	276	287	-	-	-	-	-

TABLE B-3

VISCOSITY OF SEAWATER - FROM SVERDRUP (111)  
35 ‰ SALINITY

<u>TEMPERATURE</u> <u>DEGREES C</u>	<u>VISCOSITY</u> <u>CENTIPOISE</u>
0	1.89
5	1.61
10	1.39
15	1.22
20	1.09
25	0.96
30	0.87

TABLE B-4

SPECIFIC HEAT OF SEAWATER - FROM SVERDRUP (111)  
35 ‰ SALINITY

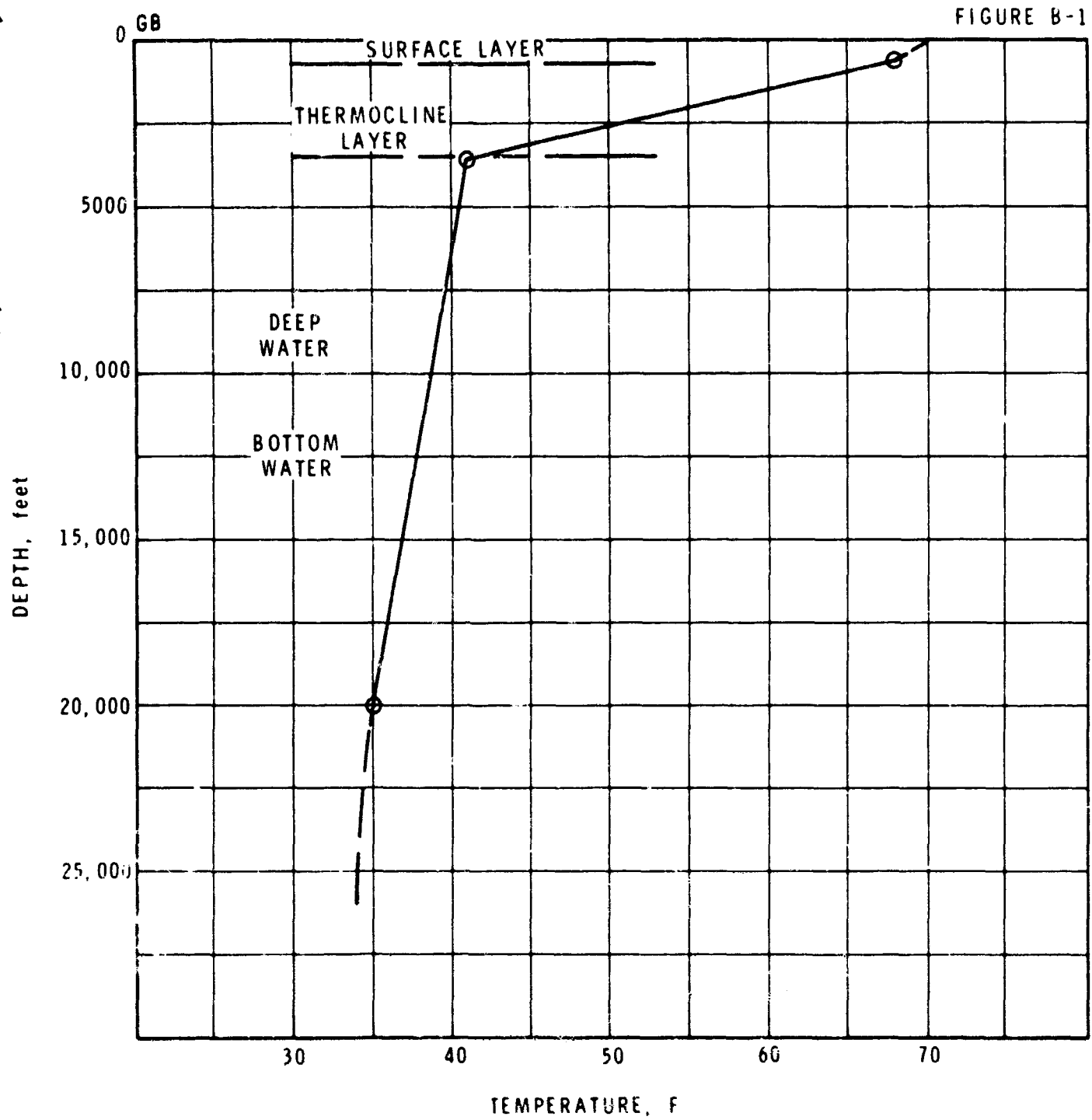
SPECIFIC HEAT AT ONE ATMOSPHERE PRESSURE

<u>TEMPERATURE</u> <u>DEGREES C</u>	<u>C<sub>p</sub> 1ATM</u> <u>CAL/GM-C</u>
--	--

-2	0.942
0	0.941
5	0.938
10	0.935
15	0.933
20	0.932

PRESSURE CORRECTION TO C<sub>p</sub> 1ATM - FROM SVERDRUP (111)  
VALUES OF (C<sub>p</sub> 1ATM-C<sub>p</sub>) CAL/GM-C

<u>PRESSURE</u> <u>DECIBARS</u>	<u>-2</u>	<u>0</u>	<u>5</u>	<u>10</u>	<u>15</u>	<u>20</u>
2,000	0.0171	0.0159	0.0136	0.0120	0.0110	0.0105
4,000	0.0315	0.0291	0.0248	0.0220	0.0203	-
6,000	0.0435	0.0401	0.0340	-	-	-
8,000	-	0.0492	0.0416	-	-	-
10,000	-	0.0566	0.0479	-	-	-

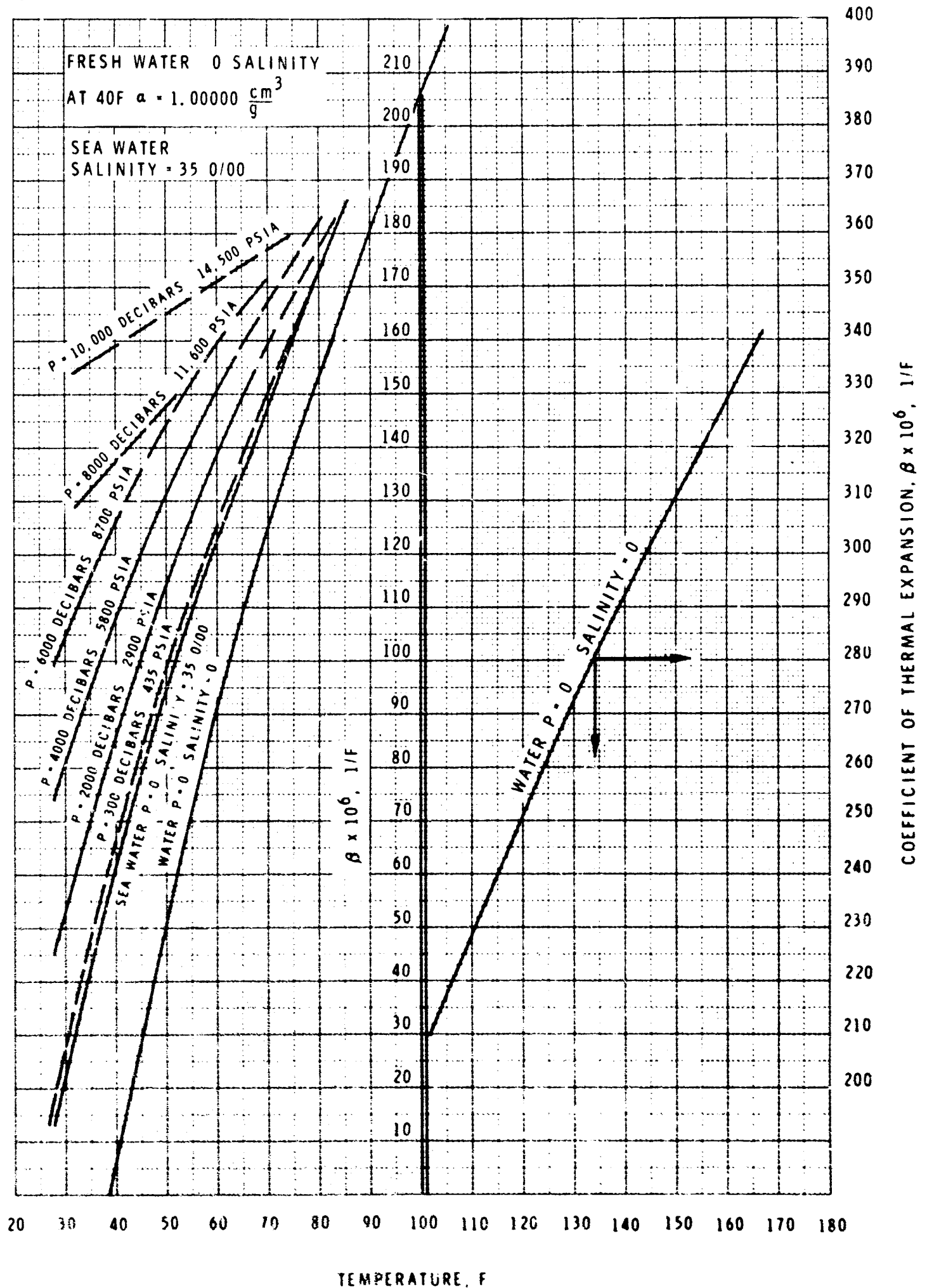
VERTICAL TEMPERATURE GRADIENT  
FOR MODEL OCEAN

C F BRAUN &amp; CO

# THERMAL EXPANSION OF WATER PER DEGREE F

GB

FIGURE B-2

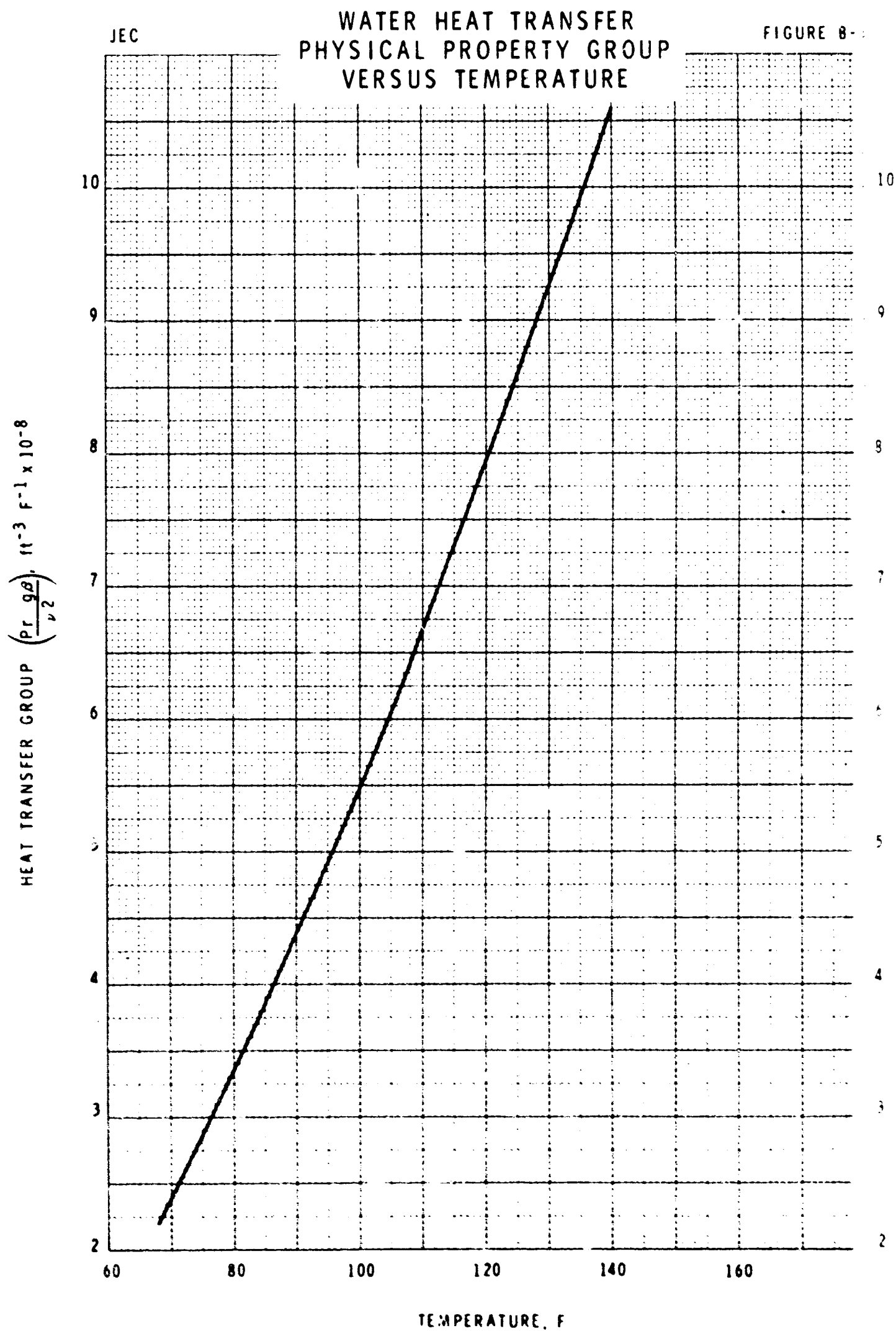


Water physical property data were obtained from the following sources.

Density	International Critical Tables, Volume III, Page 25
Viscosity	Langes' Handbook, Page 1,708
Specific Heat	Langes' Handbook, Page 1,579
Thermal Conductivity	McAdams, Heat Transmission, McGraw-Hill, Page 456

Thermal expansion coefficients of water were calculated from density data. Figures B-3 and B-4 plot the important heat transfer physical property groups,  $\frac{Pr}{\sqrt{2}}$  and  $Pr$  versus temperature.

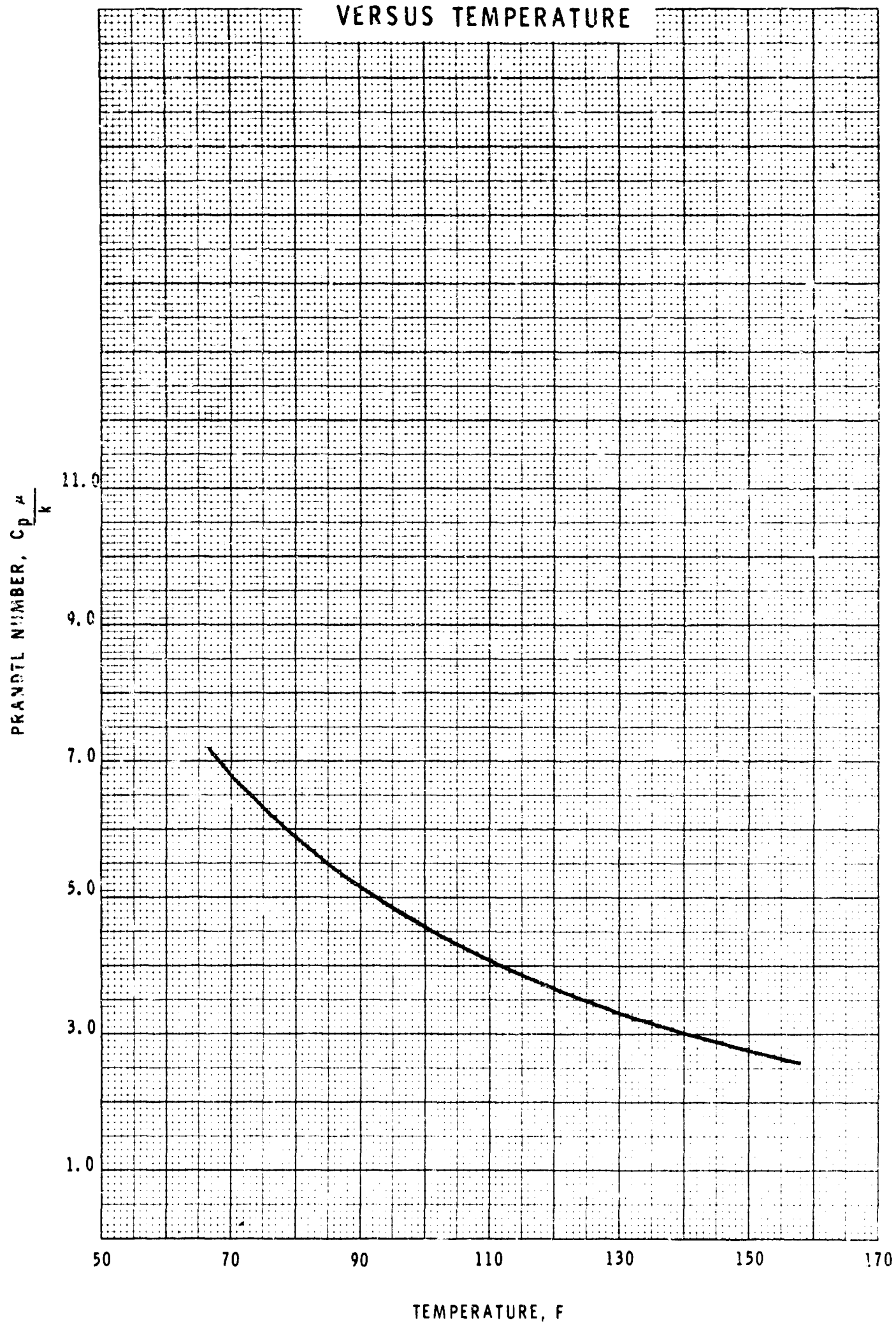
$\sqrt{2}$



JEC

WATER PRANDTL NUMBER  
VERSUS TEMPERATURE

FIGURE B-4





## APPENDIX C

## A DEEP OCEAN MOORING SYSTEM

## DESIGN

The following criteria were established for the mooring system to both support the experiment and moor the attending vessel.

- 1 The anchor weight was to be maintained at a minimum to facilitate handling from a small vessel.
- 2 The test unit was to be supported 50 to 100 feet above the bottom with provision for adjustment to suit bottom conditions.
- 3 The buoys, cables, and fittings specified were to be available as standard purchased items without having to be specially manufactured for this application.

A taut line mooring system is ideally suited to meet these criteria. It supports the experiment off the bottom at a relatively constant distance and minimizes the dynamic force imparted to the system by surface wave action or disturbance. The design basis for such a system is given in Deep Sea Moorings by Isaacs, Faughn, Schick and Sargent of Scripps Institute.

This type of mooring is relatively simple. The mooring cable is weighted by a clump anchor at the bottom and is held taut by a buoy positioned near the surface. The buoy applies a vertical upward force which is compensated for by the weight of the cable and the clump anchor. The only horizontal forces are caused by subsurface currents on the buoy and cable, and by wind and current forces on the vessel and other surface elements. The anchor can be prevented from dragging by use of sufficient weight in the clump anchor or by attachment of a separate fluted anchor. See Figure 20.

The first step in designing the mooring is to establish estimated wind and water drag forces. In the spring and summer months, weather records applicable to the test area show that the surface current ranges from 0.5 knots to 1.5 knots with winds averaging 5 knots in the morning hours and about 20 knots in the afternoon. Winds in excess of 25 knots are very seldom experienced except under storm conditions which are infrequent. Data taken on previous test operations indicated that the maximum subsurface currents to be expected were in the order of 0.5 knots at 100 to 300-foot depths and 0.2 knots near the bottom at 5,000 to 6,000-foot depth. This information and the assumption of linear rate of change between these points were used to establish the expected current profile for design purposes.

## DESIGN Continued

Preliminary calculations indicated that the size of cable and buoys, and the weight of the clump anchor required for maximum conditions, would exceed the capacity of the available vessel. For that reason, the design conditions were cut back to a maximum of 1 knot surface current and 25 knot winds. In order to justify this decision, it was necessary to provide positive indication of the actual drag on the line and to make provision for reducing the load if necessary. With these factors in mind, the system was designed so that the first surface buoy would submerge when the load and dip calculated for a 15 knot wind was experienced and the second surface buoy would submerge at conditions equal to the design for a 25 knot wind. With this indication the vessel could maneuver to prevent overloading of the system in case of short time adverse weather conditions. The mooring configuration for these different operating conditions is shown in Figure 21.

With the design basis for drag forces established, it is then possible to proceed with preliminary and final calculations to establish the characteristics of the system and the requirements of the components. The next steps in sequence are (1) calculate the total surface drag under the assumed design conditions, (2) calculate the weight and horizontal drag of the submerged elements of the system, (3) estimate the angles of the wire at the submerged buoy and at the anchor, (4) estimate the dip and excursion of the submerged buoy, (5) repeat the above calculations until satisfactory values of buoyancy, anchor weight, and line size are established, (6) calculate and establish pennant lengths to connect the submerged buoy to the surface buoys and the vessel, (7) select the system components that as nearly as possible meet the design requirements, and (8) recalculate and adjust the system design to accommodate available equipment as necessary.

Calculations including dip and excursion and vector force diagrams for a system for use at 5,000-foot depth are given later. A ballasting table was prepared to provide for on-site adjustment of buoyancy to suit actual depth at the test site.

The selection or design of system components is an integral part of the system design. Some of the factors involved in this phase of design are outlined below.

## DESIGN Continued

**DANFORTH TYPE ANCHOR** The horizontal component of force on the anchor for this system design ranged from a minimum of say 100 pounds for slack conditions to nearly 900 pounds for the maximum design conditions. Since the effective weight of the clump anchor on the bottom is decreased as the surface drag is increased, its horizontal holding power is least effective when most needed. A spade or Danforth type anchor, on the other hand, maintains maximum holding power so long as the shaft is kept essentially parallel to the bottom. The holding power of this type anchor ranges from 10 to 50 times the weight of the anchor depending on bottom conditions and method of attachment. For these reasons, a 60-pound Danforth anchor was selected for attachment to the clump anchor by a 100-foot length of weighted chain. Actually a 70-pound Danforth was used because it was available. A 50-pound weight was attached to the shaft of the anchor to ensure that it would remain horizontal. A chain 200 feet long was used so that maximum holding power would still be in effect during the period when the clump was lifted 50 to 75 feet off the bottom for attachment of the submerged buoy.

**CLUMP ANCHOR** The clump anchor was sized to offset the total system buoyancy. A cylindrical weight of uniform cross section was built up in order to minimize the tendency to rotate during lowering. Fins were attached to help damp out any rotation that might be initiated by external forces.

**CONNECTION BETWEEN ANCHOR AND TEST UNIT** Even with careful winch operation, the connection between the anchor and the test unit will become slack momentarily when the clump anchor first touches bottom. Under this condition, most wire rope has a tendency to kink. For that reason, chain was used for this section of the system in order to reduce the possibility of damage or failure.

## DESIGN Continued

**WEAK LINK** There is always a possibility that an anchor may hang up in a crevice or obstruction on the bottom. As it was essential to recover the test unit in this case, it was necessary to provide for recovery even if the anchor did hang up. At the same time, some protection against premature failure of the link under dynamic loading during lowering is desirable. One organization has reported that they have experienced either premature failure or failure to function on the average of one time out of seven when weak links were used. After consideration of several different types of weak link installations, the one shown in Figure 22 was designed for this operation. Two links are hooked up in tandem to decrease the risk of premature loss. The links were made of material with well defined strength characteristics and they were precision machined to calculated areas within close tolerance. Duplicate sections were broken to further confirm the accuracy of the calculations and machining. The links were restrained so that no rotational effect could be transmitted to them. The link used was designed to fail at a pull of 13,000 pounds. At the conclusion of the deep ocean test, the links were broken to again check the accuracy of the design. One failed at 12,800 pounds, the other at 12,400 pounds.

**WIRE ROPE SELECTION** Accurate information on the characteristics of the wire rope selected for the load line is necessary for the design of a system such as this. Dependable data on breaking strength, stretch, rotation, torque to restrain rotation, and handling characteristics was not available. The data and information that were available were incomplete and in some cases misleading. A preliminary selection was made based on available information, but then extensive tests were run to establish the exact data for system design.

The 3/8-inch 1 x 19 wire rope selected had a formula breaking strength of 17,300 pounds. Actual breaking strength of the run used was 19,500 pounds. A section of the cable incrementally loaded up to 6,000 pounds unwound the equivalent of eight turns per 100 feet and elongated a total of 6 inches per 100 feet. When a loaded cable is run over a sheave and subjected to dynamic loading, the elongation is normally two to three times the straight load elongation. This testing indicated that total stretch would not exceed 1 1/2 percent. In actual operation, the total elongation approached 10 percent. This factor is often overlooked in establishing the basis for wire rope selection for ocean use. The torque required to prevent rotation and unwinding was checked for different load conditions and ranged from 3.0 foot pounds at 3,000-pound loading to 7.8 foot pounds at 6,000-pound loading.

## DESIGN Continued

Tests were also run to establish the approximate number of turns required in a slack line to cause kinking and the effect of reloading the line once it was kinked. These tests indicated that approximately 25 turns per 100 feet were required to kink a slack line of this type and size. Reloading resulted in tightening of the kink and line damage.

Other types of line are available with better twist, elongation, and kinking characteristics as well as higher strength to weight ratios, but the cost of such line may run to several dollars per foot compared to several cents per foot for the line selected. This factor is quite important when several thousand feet of line are required.

**WIRE ROPE CONNECTORS** As a result of the wire rope tests, valuable information was gained on the effectiveness and efficiency of different types of wire rope fittings and connectors. For example, the swaged-on eyes on test sections of the cable failed at 75 to 80 percent of the formula breaking strength of the line. Connections made with cable clamps failed at 50 to 70 percent of the formula breaking strength of the line. As a result of this experience, a preformed cable grip was tested and found to be effective at loadings in excess of the formula breaking strength of the line. As these grips were less expensive, easier to install, and more reliable, they were used for all wire rope connections in the system.

**BUOYS** Surplus buoys were located that could be used to meet the requirements of the system design. A single buoy was not available of the size and weight required for the submerged buoy. Two standard Navy net buoys approximately 4 feet 9 inches in diameter were used for this service. This required ballasting of one to reduce the buoyancy to the design figure, but it also provided flexibility in that only adjustment of ballast was required to adjust the system for use at different depths within the range of the design. The surface buoys used were also slightly oversized and were ballasted as required. All buoys were pressure-tested before use and pressured with nitrogen gas after ballasting.

## DESIGN Continued

LINE LOAD INDICATOR AND METER WHEEL Some method of measuring the load on the line and the footage of line out is essential in placement and retrieval of a mooring or test installation. Standard equipment is available to perform these functions but since the design is specialized, it is usually expensive and only available on long-term delivery. For these reasons, a simplified unit was designed and used for the test series. A weighted sheave was used on the line between the winch drum and the lowering sheave. The line sheave was sized so that an attached mechanical counter read directly in feet. The displacement of the weight on the sheave is proportional to the tension of the line. The weight guide was calibrated to show the approximate line load. The accuracy of this device was well within the limits of our requirements. Only a few days were required to design, fabricate, and install it, and the total cost was 3 to 4 percent of the cost of a manufactured device with a six-week delivery.

ATTACHMENT OF ELECTRICAL LINES TO LOAD LINE The power and instrument cables used were capable of supporting 500 to 1,000 feet of their own weight. In order to provide for dynamic loadings and factor of safety, these cables were attached to the load line at 200 foot intervals. Standard Kellums grips were placed on the electrical cables and looped through the eye of preformed grips attached to the load line. Allowance was made between each point of connection for stretch of the load line without pull on the electrical lines. This method of attachment was suitable for short time test operation. An alternative method of attachment that provided for rotation of the load line without twisting of the electrical cables and for the wear to be expected on long-time operation was developed but was not required for this particular test series.

## CONCLUSIONS

The taut line mooring concept is well suited to test operations of this nature. The design, materials, and equipment selected proved satisfactory in actual operation. During the 4,500-foot test period, surface winds ranged from 5 to 22 knots. The buoy system worked as expected and the anchorage held without slippage for the full test period.

Provision for ballasting buoys to adjust for actual depth at the test site is important. If excess buoyancy is used, the system may be damaged by surface wave action during placement. If buoyancy is insufficient, excess dip may cause failure and implosion of the submerged buoys.

CONCLUSIONS Continued

The system proved to be an effective and economical means of supporting a test unit a fixed distance off bottom and carrying power and instrument cables between the surface and the test unit. If, however, the operation is to be continued for any extended period of time or designed for periodic reuse, an improved method of attaching the power lines to the load line should be used. The method used resulted in some twisting of the electrical lines about the load line that was difficult to unwind. Although no failures were experienced during these test periods due to wear at the attachment points, provision should be made to reduce this risk if the system is used for longer periods of time. It is desirable to conduct such tests at a site that can be definitely located relative to a fixed point. If the test site is not within radar range of land, a firmly anchored marker buoy is required.

The data generally available on wire rope characteristics are not adequate for detailed design of a deep ocean system. Tests should be performed on sections of the actual cable run to be used in order to establish the critical data needed for final design. Additional allowance must be made for stretch in deep ocean operations.

The components of a deep ocean test system cannot be observed after they are lowered into position. There is no way to make repairs or replace failures after placement without retrieving the entire system. These factors make design checking, thorough component inspection, and check-out operations critical to the success of any deep ocean operation.

## COMPUTATIONS

The following computations were developed for the 4,500-foot test. An initial depth of 5,000 feet was assumed to permit variations in exact test depth.

## ASSUMPTIONS

Mooring as shown in Figure 20, depth 5,000 feet

<u>WIND VELOCITY</u>	<u>CURRENT VELOCITY</u>
15 knots to submerge B2	1.0 knot at surface
25 knots to submerge B3	0.5 knot at 300 foot depth
	0.2 knot at 5,000 foot depth
	Linear change in velocity between currents at depths noted

<u>VESSEL CHARACTERISTICS</u>	<u>BUOY CHARACTERISTICS</u>
170 square feet project wind area	B1 - 57-inch diameter
1,500 square feet wetted surface	B2 - 36-inch diameter
	B3 - 36-inch diameter

## ROUGH CALCULATIONS

Drag on Vessel

$$\text{Wind Force } F = KAV^2 \quad (1)$$

$$\text{Current Drag } R_s = f_s AV_k^{1.83} \quad (2)$$

$$25 \text{ knot wind } F = 350 \text{ pounds}$$

$$15 \text{ knot wind } F = 127 \text{ pounds}$$

$$1.0 \text{ knot current } R_s = 15 \text{ pounds}$$

Drag on Buoys

B3 on surface, Equation (1) applies

$$15 \text{ knot wind } F = 5 \text{ pounds}$$

$$1.0 \text{ knot current } R_s = \text{negligible}$$

Submerged Buoys

$$R = C_d A V_f^2 \quad (3)$$

$$B1 \text{ in } 1.0 \text{ knot current } R = 56 \text{ pounds}$$

$$B2 \text{ or } B3 \text{ in } 1.0 \text{ knot current } R = 22 \text{ pounds}$$



## COMPUTATIONS Continued

## Drag on Cables

Projected area for 5/8-inch plus 7/8 electrical and  
3/8 load cable

$$A = .156 \text{ ft}^2/\text{ft}$$

Drag, Equation (3) applies

$$R = .172 V_f^2 \text{ lbs/ft}$$

Weights corrected for salt water density

5/8-inch electrical cable	.111 lb/ft
7/8-inch electrical cable	.185
3/8-inch 1 x 19 load cable, .90 (.247)	<u>.223</u>

Total	.519 lb/ft
-------	------------

90 percent of support cable weight is used because of a  
10 percent stretch found in situ.

Experiment Package	50 pounds
--------------------	-----------

## Summary

<u>COMPONENT</u>	<u>WEIGHT POUNDS</u>	<u>DRAG (POUNDS)</u>	
		<u>15 KNOT WIND</u>	<u>25 KNOT WIND</u>
Vessel		142	365
B3		5	22
B2		22	22
B1		56	56
Pennants B1-B2, B2-B3		Say 60	Say 80
Cable B1-300 ft ) -4,900 ft	2,540	44	44
Cable 300-5,000 ft)		283	283
Experiment	50		
Chain	80		
Total Drag at Anchor, $F_{h1}$		612	872
Total Drag at B1, $F_{h2}$		285	545
Total Drag at B2, $F_{h3}$			409
Total Weight, W	2.670		

## COMPUTATIONS Continued

## Dip Computations for B1

$$\text{Total B} = 2,670 \text{ lb} + 2,400 \text{ lb anchor} = 5,070$$

Assume following weight distribution

$$\begin{aligned} B1 &= 4,000 \\ B2 &= 700 \\ B3 &= 300 \end{aligned} \quad \text{Total B} = 5,000$$

25 knot case, all buoys submerged

$$\alpha_1 = \tan^{-1} \frac{F_{h1}}{B} = 6^\circ 13' \quad (4)$$

$$\alpha_2 = \tan^{-1} \frac{F_{h2}}{B-W} = 20^\circ 30' \quad (5)$$

$$D = L - \frac{360L}{2\pi(\alpha_2 - \alpha_1)} (\sin \alpha_2 - \sin \alpha_1) = 145' \quad (6)$$

Similarly for the 15 knot case, B1 and B2 submerged

$$\alpha_1 = 3^\circ 28'$$

$$\alpha_2 = 16^\circ 48'$$

$$D = 87'$$

## Length of Pennants

The length of pennants are found by constructing vector diagrams for drag and buoyant forces on the Buoys B1 and B2 as shown in Figure C-1. The vector force on B1 in the 15 knot wind case is  $F_{h1}$  - the drag on B1 or 229 pounds. The other forces are found similarly.

Length of B1-B2 is first determined for the 15 knot wind case to be 144 feet. Then the length of B2-B3 is determined to be 99 feet. These pennant lengths are rounded to 150 feet and 100 feet.

## COMPUTATIONS Continued

DETAIL COMPUTATIONS In the detail computations, drag forces are found for smaller increments of cable length and a vector diagram is plotted as shown in Figure C-2 to determine the shape of the cable. The lengths and approximate depths of elements determined in the rough computations are used to get more precise drag forces. These drags are summarized as follows.

<u>ITEM</u>	<u>AVERAGE DEPTH</u>	<u>WEIGHT</u>	<u>DRAG (15 KNOTS)</u>	<u>DRAG (25 KNOTS)</u>
Vessel	0	-	142	365
Pennant B3 Vessel	-	-	-	-
B3	0	-300	5	22
Pennant B2-B3 (100')	0/0-25'	52	0	23
B2	0/50'	-700	22	22
Pennant B1-B3 (150')	50/100'	78	40	34
B1	100'/150'	-4,000	39	31
Cable B1-300' (250')	240'/300'	130	44	29
Cable 300'-1,000'	700'	363	79	79
Cable 1,000'-2,000'	1,500'	519	91	91
Cable 2,000'-3,000'	2,500'	519	63	63
Cable 3,000'-4,000'	3,500'	519	44	44
Cable 4,000'-4,950'	4,475'	493	25	25
Chain 50'	4,975'	80	1	1
Test Rig	4,950'	50	Say 5	Say 5
Total Buoyancy		-5,000	600	534
Total Weight		+2,803		

The drag and buoyant force on each element are determined from the table and a vector diagram is accurately laid out. Figure C-2 shows that a 15 knot wind will not quite submerge B2. The 25 knot wind will just submerge B3. This verifies the selection of buoyancy and pennant lengths assumed in the rough calculations.

## TERMS AND SYMBOLS, APPENDIX C

A	Projected area, $\text{ft}^2$
B	Buoyancy, lbs
$C_d$	Current drag coefficient on submerged element, assumed 1.1
D	Dip, ft
F	Wind force, lbs
$F_{h1}$	Total drag above anchor, lbs
$F_{h2}$	Total drag above Buoy B1, lbs
$F_{h3}$	Total drag above Buoy B2, lbs
$f_s$	Current drag coefficient on surface element, assumed 0.01
K	Wind drag coefficient, assumed 0.0025
L	Length of mooring cable between B1 and anchor, ft
R	Current drag on submerged element, lbs
$R_s$	Current drag on submerged element, lbs
V	Wind velocity, miles per hour
$V_f$	Current velocity, ft per second
$V_k$	Current velocity, knots
W	Total weight of mooring cable and test unit, lbs
$\alpha_1$	Angle of cable at Buoy B1
$\alpha_2$	Angle of cable at Buoy B2

## APPENDIX D

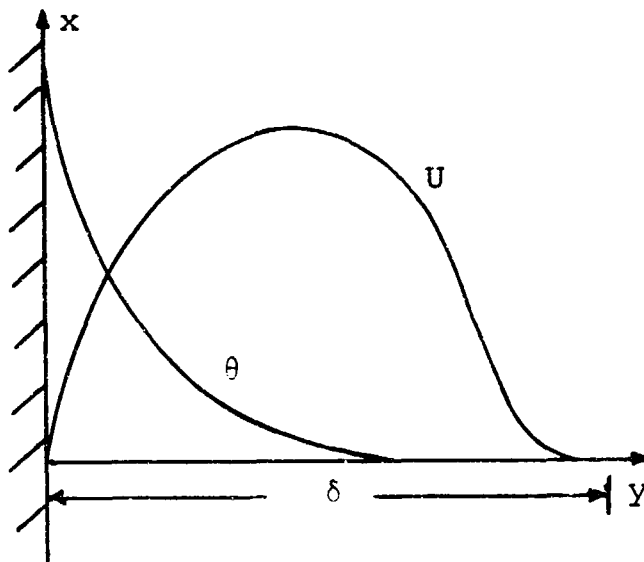
## LAMINAR AND TURBULENT NATURAL CONVECTION BOUNDARY LAYER EQUATIONS

## LAMINAR BOUNDARY LAYER - ECKERT AND DRAKE (60) APPROACH

To solve the boundary equations express the temperature and velocity fields with the following equations.

$$\theta = \theta_w \left(1 - \frac{y}{\delta}\right)^2 \quad (1)$$

$$U = U_1 \frac{y}{\delta} \left(1 - \frac{y}{\delta}\right)^2 \quad (2)$$



These fulfill the boundary conditions

$$y = 0 \quad \theta = \theta_w, U = 0$$

$$y = \delta \quad \theta = 0, U = 0$$

The maximum velocity occurs at a distance  $y = \delta/3$  from the wall according to Equation D-2. Its value is

$$U_{\max} = \frac{4}{27} U_1 \quad (3)$$

## LAMINARY BOUNDARY LAYER Continued

The boundary layers for temperature and velocity are assumed equal, even though for water the thermal boundary layer is smaller than the velocity boundary layer. Sparrow and Gregg (108) performed an analysis in which different thicknesses were assumed. The results differed only slightly from this more simplified analysis.

The x-direction momentum equation equates the time rate of momentum change in the x direction with the acting forces. The only forces of any significance are the buoyancy force and the friction force. Assuming the pressure constant and the velocity outside the boundary layer to be zero, the momentum equation becomes

$$\frac{d}{dx} \int_0^l U^2 dy = g\beta \int_0^l \theta dy - \nu \left( \frac{dU}{dy} \right)_w \quad (4)$$

Assuming that heat is transported in the x-direction only and that viscous dissipation is negligible, the boundary layer energy equation becomes

$$\frac{d}{dx} \int_0^l U \theta dy = - \alpha \left( \frac{d\theta}{dy} \right)_w \quad (5)$$

The integrals in D-4 and D-5 can be solved by introducing temperature and velocity profiles D-1 and D-2

$$\int_0^l U^2 dy = \frac{U_1^2 \delta}{105}, \quad \int_0^l \theta dy = \frac{\theta_w \delta}{3}$$

$$\int_0^l \theta U dy = \frac{1}{30} U_1 \theta_w \delta$$

## LAMINAR BOUNDARY LAYER Continued

Now the boundary layer equations take the form

$$\frac{1}{105} \frac{d}{dx} (U_1^2 \delta) = \frac{1}{3} g \beta \theta_w - \nu \frac{U_1}{\delta} \quad (6)$$

$$\frac{1}{30} \theta_w \frac{d}{dx} (U_1 \delta) = 2\alpha \frac{\theta_w}{\delta} \quad (7)$$

To solve the equations, try  $U_1$  and  $\delta$  as exponential functions of  $x$

$$U_1 = C_1 x^m, \quad \delta = C_2 x^n$$

Introducing these expressions, and equating the exponents for a given summand gives

$$C_1 = 5.17 \nu \left( \frac{20}{21} + \frac{\nu}{\alpha} \right)^{-1/2} \left( \frac{g \beta \theta_w}{\nu^2} \right)^{1/2} \quad (8)$$

$$C_2 = 3.93 \left( \frac{20}{21} + \frac{\nu}{\alpha} \right)^{1/4} \left( \frac{g \beta \theta_w}{\nu} \right)^{1/4} \left( \frac{\nu}{\alpha} \right)^{-1/2} \quad (9)$$

Now the maximum velocity within the boundary layer becomes

$$U_{\max} = \frac{4}{27} U_1 = 0.766 \frac{\nu}{x} (0.952 + \text{Pr})^{-1/2} G_{rx}^{1/2} \quad (10)$$

The boundary layer thickness is

$$\delta/x = 3.93 \text{Pr}^{-1/2} (0.952 + \text{Pr})^{1/4} G_{rx}^{-1/4} \quad (11)$$

$$\text{Heat flux at the wall is given by } q/A = -K \left( \frac{d\theta}{dy} \right)_w = h \theta_w \quad (12)$$

Since  $\left( \frac{d\theta}{dy} \right)_w = - \frac{2\theta_w}{\delta}$  by Equation D-1

$$h = \frac{2K}{\delta} \quad (13)$$

and the Nusselt number is

$$\frac{hx}{K} = \text{Nu}_x = \frac{2x}{\delta}$$





## TURBULENT BOUNDARY LAYER Continued

The momentum equation equates time rate of change of momentum with the algebraic sum of the buoyant and shear forces.

$$\frac{d}{dx} \left( \delta \int_0^1 U d\eta \right) = g\beta \int_0^1 \theta d\eta = g \frac{\tau_w}{\rho} \quad (18)$$

The energy equation equates heat transferred through the wall with the heat gain in the boundary layer.

$$\left( \frac{q}{A} \right)_w = \rho C_p \frac{d}{dx} \left( \delta \int_0^1 U \theta d\eta \right) \quad (19)$$

Shear stress on a flat surface is given by Schlichting (100) as

$$\tau_w = C_n^{-3/2} \frac{U_1^2 \rho}{g} \left( \frac{\nu}{U_1 y} \right)^{1/2} \quad (20)$$

The Reynolds analogy relates wall heat flux and shear stress, and is valid when  $Pr = 1$

$$\left( \frac{q}{A} \right)_w = g \frac{\tau_w C_p \theta_w}{U_1} \quad (21)$$

Jakob (77) shows that the above relation holds for fluids of Prandtl numbers ranging from 5 to 50 if multiplied by  $Pr^{-2/3}$ . Then Equation D-21 becomes

$$\left( \frac{q}{A} \right)_w = g \frac{\tau_w C_p \theta_w}{U_1} Pr^{-2/3} \quad (22)$$

Employing velocity and temperature profiles given in Equations D-16 and D-17 along with Equations D-20 and D-22, Equations D-18 and D-19 are evaluated as

$$0.054 \frac{d}{dx} \left( \delta U_1^2 \right) = \frac{0.25 g \beta \left( \frac{q}{A} \right)_w C_n^{3/2} Pr^{2/3}}{U_1^{1/2} \nu^{1/2} C_p} - \frac{U_1^{3/2} \nu^{1/2}}{\delta^{1/2} C_n^{3/2}} \quad (23)$$

## TURBULENT BOUNDARY LAYER Continued

$$12.62 \nu^{1/2} C_n^{-3/2} Pr^{-2/3} = \frac{d}{dx} \left( \delta^{3/2} U_1^{1/2} \right) \quad (24)$$

Equations D-23 and D-24 are solved by introducing

$$U_1 = C_1 x^m \quad (25)$$

$$\delta = C_2 x^n \quad (26)$$

After substituting these expressions back into Equations D-23 and D-24 and equating coefficients, we find that

$$m = n = 1/2$$

and

$$C_1 = \left( \frac{12.62 \nu^{1/2}}{C_n^{3/2} Pr^{2/3}} \right)^2 C_2^{-3} \quad (27)$$

$$C_2 = \left\{ 8090 C_n^3 \left[ 1 + \frac{1}{0.978 Pr^{2/3}} \right] Pr^{-2} \frac{x^3}{Gr_x} \right\}^{1/6} \quad (28)$$

The reference velocity  $U_1$ , given by Equation D-25 becomes

$$U_1 = 1.76 \frac{\nu}{x} Gr_x^{1/2} \left[ 1 + 0.978 Pr^{2/3} \right]^{-1/2} \quad (29)$$

Reynolds number based on the maximum boundary layer velocity is given by

$$Re_{max} = \frac{U_{max} x}{\nu} = \frac{0.676 Ra_x^{1/2}}{Pr^{1/2} \left[ 1 + 0.978 Pr^{2/3} \right]^{1/2}} \quad (30)$$

## TURBULENT BOUNDARY LAYER Continued

Heat transfer coefficient expressed as the Nusselt modulus is

$$Nu_x = 0.624 Cn^{-1} Pr^{5/18} \left[ \frac{Ra_x}{1 + 0.978 Pr^{2/3}} \right]^{1/3} \quad (31)$$

Boundary layer thickness, given by Equation D-26, becomes

$$\delta/x = 4.5 Cn^{-1} \left[ 1 + 0.978 Pr^{2/3} \right]^{1/6} Pr^{-5/18} Ra_x^{-1/6} \quad (32)$$

## APPENDIX E

## CONCEPTUAL DESIGN OF AN UNDERSEA HEAT REJECTION SURFACE

The heat rejection surface conceptual design is based on the assumed operating parameters of a 500 kw (e) fuel cell. One of the more promising fuel cell concepts for undersea use employs hydrazine and hydrogen peroxide as fuel and oxidizer and a KOH solution as an electrolyte. Figure E-1 shows a typical schematic of a  $N_2H_4 - H_2O_2$  fuel cell for undersea application (7). In this design, the KOH solution is circulated by an electromagnetic pump through the cell, the liquid-vapor separator, and the heat exchanger. Heat produced by irreversibility in the fuel cell operation is rejected to the surrounding ocean by the heat exchanger. Pressure balancing between the system and ambient ocean is employed to minimize weight and cost of the power plant.

In this conceptual design study, we are only interested in the heat rejection surfaces of the exchanger. However, to design a heat rejection surface requires knowledge of the operating parameters of the cell. A fuel cell, such as Figure E-1 describes, has not been operated under water, and as far as we know a 500 kw (e)  $N_2H_4 - H_2O_2$  fuel cell has not been designed. For this reason, the necessary fuel cell operating parameters are assumed and the heat rejection surface design is based thereon.

It is assumed that fuel cell design and site location have specified the following parameters.

Fuel cell thermal efficiency - 45 percent  
Heat liberated by fuel cell - 610 kw  
Heat rejected to ocean by the heat exchanger  
(80 percent of liberated heat) -  $1.67 \times 10^6$  Btu/hr  
KOH solution concentration - 30 percent

Inlet KOH solution temperature - 170 F  
Outlet KOH solution temperature - 130 F  
Ambient temperature of ocean - 50 F  
Cylindrical tube exchanger with tube dimensions - 2-inch OD by 0.134-inch wall  
Tube material - duplex construction, nickel inside, 90 - 10 cupronickel outside

KOH solution flow rate -  $1.11 \times 10^5$  lbs/hr  
Allowable KOH solution intube friction pressure drop - 0.2 psi  
KOH solution intube heat transfer coefficient referred to the outside diameter -  $h = 0.018 G^{0.8}$   
Ocean water salinity - 35 o/oo  
Depth - 1,670 ft  
Pressure - 500 decibars (725 psi)

## CONCEPTUAL DESIGN OF AN UNDERSEA HEAT REJECTION SURFACE Continued

We assume that it is economically advantageous to minimize the base surface heat transfer area, subject to the design constraints. Thus, the overall heat transfer coefficient,  $U$ , must be as high as possible. For some design cases, minimum base surface area may not yield minimum cost. For instance, extra fin metal placed on a tube may sometimes cost more than the base surface plus the fins it eliminates. A detailed design should include an analysis of the effect of fin weight upon total cost.

Vertical orientation of the exchanger promotes a high gross heat transfer coefficient. Even though the log mean temperature driving force is unaffected, the effective temperature driving force is greater if the KOH solution enters the top of the exchanger and flows downward. This is because channel temperatures between the fins are likely to be lower, especially near the upper end of the exchanger. A low-tube height and a high-fin metal conductivity also promote high gross heat transfer coefficients.

The following quantities have been calculated from the assumptions and other information in this report.

Log mean temperature difference - 99 F

Seawater physical properties at 90 F (used throughout the calculations)

$$\beta = 2.15 \times 10^{-4} \text{ F}^{-1}$$

$$C_p = 0.93 \text{ Btu/lbm-F}$$

$$k = 0.35 \text{ Btu/hr-ft-F}$$

$$\nu = 0.0263 \text{ ft}^2/\text{hr}$$

$$\mu = 1.69 \text{ lbm/ft-hr}$$

Fin metal - HC copper ( $k_m = 2,640 \text{ Btu/hr-ft}^2\text{-F/in}$ )

Fouling coefficient,  $h_D = 500 \text{ Btu/hr-ft}^2\text{-F}$

Metal heat transfer resistance,  $\frac{t}{k_m} = 4.35 \times 10^{-4} \frac{\text{hr-ft}^2\text{-F}}{\text{Btu}}$

Design computations for the fuel cell heat rejection exchanger basically follow the step-by-step procedure presented in Chapter VI. Additional steps are included for calculation of the inside heat transfer coefficient, tubeside pressure drop and velocity, and number of tubes. The revised procedure is outlined below.

- 1 Assume the number of vertical tubes,  $n$ , and calculate the tubeside mass flow rate.

$$G = \frac{W}{n A_{\text{tube}}}$$

## CONCEPTUAL DESIGN OF AN UNDERSEA HEAT REJECTION SURFACE Continued

2 Calculate  $h_{io} = \frac{1}{\frac{1}{h} + \frac{t}{k_m}}$

Where  $h = 0.018 G^{0.8}$

- 3 Determine tubeside pressure drop per unit length by the Fanning Equation (89), which is valid for turbulent flow.
- 4 Assume a tube length and calculate base surface area, base surface heat flux, and tubeside pressure drop. Compare the calculated tubeside pressure drop with the allowable value.
- 5 Compute base metal surface temperature with the expression

$$T_s = T_B - \frac{q}{A h_{io}}$$

- 6 Determine  $h_{GR}$  using the step-by-step procedure of Chapter VI.
- 7 Calculate the overall heat transfer coefficient,  $U$ , by the following equation:

$$U = \frac{1}{\frac{1}{h_{GR}} + \frac{1}{h_{io}}}$$

Compute the base surface heat transfer area with the expression

$$A = \frac{q}{U \Delta T_{\log \text{ mean}}}$$

- 8 Compare the calculated and assumed base surface areas. If they agree, the design is complete for the assumed number of tubes. If the calculated and assumed base surface areas do not agree, assume a new tube length and repeat Steps 4 through 7.
- 9 Repeat the design for several numbers of vertical tubes and determine the number of tubes which yields the minimum base surface heat transfer area.

The following calculation is performed for the case -  $n = 7$ .

- 1 Tubeside mass flow rate

$$G = \frac{W}{n A_{\text{tube}}} = \frac{1.11 \times 10^5}{7(0.0164)} = 9.59 \times 10^5 \text{ lbm/ft-hr}$$

## CONCEPTUAL DESIGN OF AN UNDERSEA HEAT REJECTION SURFACE Continu.

- 2 Inside coefficient referred to outside tube diameter

$$h = 0.018 G^{0.8} = 0.018 (9.59 \times 10^5)^{0.8}$$

$$= 1.10 \times 10^3 \text{ Btu/hr-ft}^2\text{-F}$$

$$h_{io} = \frac{1}{\frac{1}{h} + \frac{t}{k_m}} = \frac{1}{9.09 \times 10^{-4} + 4.34 \times 10^{-4}}$$

$$= 744 \text{ Btu/hr-ft}^2\text{-F}$$

- 3 Tubeside pressure drop per unit length

$$\frac{\Delta P}{\Delta X} = \frac{f G^2}{g_c d} = \frac{(0.004) (9.59 \times 10^5)^2}{(4.18 \times 10^{-9}) (84) (0.0167) (144)}$$

$$= 4.35 \times 10^{-3} \text{ psi/ft}$$

The friction factor  $f$  was determined from Reference 85 Page 156.

- 4 Assume a tube length of 23.5 feet

$$A = n x S = (7) (23.5) (0.523) = 86 \text{ ft}^2$$

$$q/A = \frac{1.67 \times 10^6}{86} = 1.94 \times 10^4 \text{ Btu/hr-ft}^2$$

$$\Delta P = x \frac{\Delta P}{\Delta X} = (23.5) (4.34 \times 10^{-3}) = 1.02 \times 10^{-1} \text{ psi}$$

- 5 Base metal surface temperature

$$T_S = T_B - \frac{q}{A h_{io}} = 150 - \frac{1.94 \times 10^4}{744}$$

$$= 124 \text{ F}$$

- 6 Determination of  $h_{GR}$  by Chapter VI method

$$(a) \quad h_o = 0.17 k \left[ \frac{g_p Pr \Delta T}{v^2} \right]^{1/3}$$

$$= (0.17) (0.35) \left[ \frac{(4.18 \times 10^9) (2.15 \times 10^{-4}) (4.50) (74)}{(0.0263)^2} \right]^{1/3}$$

$$= 209 \text{ Btu/hr-ft}^2\text{-F}$$

## CONCEPTUAL DESIGN OF AN UNDERSEA HEAT REJECTION SURFACE Continued

$$(b) \quad h_{cyl} = 1.52 h_o = 318 \text{ Btu/hr-ft}^2\text{-F} \quad (\text{Figure 56})$$

$$(c) \quad D = \frac{1.87 \left[ 1 + 0.978 \text{Pr}^{2/3} \right]^{1/6} x^{1/2}}{\text{Pr}^{5/18} \left( \frac{\text{Ra}_x}{x^3} \right)^{1/6}}$$

$$= \frac{1.87 \left[ 1 + 0.978 (4.5)^{2/3} \right]^{1/6} (23.5)^{1/2}}{(4.5)^{5/18} (4.33 \times 10^{10})^{1/6}}$$

$$= 0.125 \text{ ft or } 1.50 \text{ in}$$

$$(d) \quad \left( \frac{2h_o}{k_m} \right)^{1/2} = \left[ \frac{2(209)}{2,640} \right]^{1/2} = 0.40 \text{ in}^{-1/2}$$

$$b_c = 4.0 \text{ in, (Figures 33 and 34)}$$

$$(e) \quad a = 0.64 \text{ in, (Figures 28 and 29)}$$

$$b = b_c - \frac{a}{2} = 3.68 \text{ in}$$

$$(f) \quad h_G = \frac{0.924 (2h_o k_m a)^{1/2} \tanh \left[ \left( \frac{2h_o b_c^2}{k_m a} \right)^{1/2} \right] + h_{cyl} D}{D + a}$$

$$= \frac{0.924 \left[ 2(209)(2,640)(0.64) \right]^{1/2} \tanh \left\{ \left[ \frac{2(209)(16)}{(2,640)(0.64)} \right]^{1/2} \right\}}{1.50 + 0.64}$$

$$+ \frac{(318)(1.5)}{1.50 + 0.64} = 574 \text{ Btu/hr-ft}^2\text{-F}$$

(g) No experimental correction is applied to this case.

$$(h) \quad h_{GR} = \frac{1}{\frac{1}{h_G} + \frac{1}{h_D}} = \frac{1}{1.74 \times 10^{-3} + 2.00 \times 10^{-3}}$$

$$= 268 \text{ Btu/hr-ft}^2\text{-F}$$



## CONCEPTUAL DESIGN OF AN UNDERSEA HEAT REJECTION SURFACE Continued

## 7 Overall heat transfer coefficient and base surface area

$$U = \frac{1}{\frac{1}{h_{GR}} + \frac{1}{h_{io}}} = \frac{1}{3.74 \times 10^{-3} + 1.34 \times 10^{-3}}$$
$$= 197 \text{ Btu/hr-ft}^2\text{-F}$$

$$A = \frac{Q}{U \Delta T_{\log \text{ mean}}} = \frac{1.67 \times 10^6}{(197)(99)} = 86 \text{ ft}^2$$

This area agrees with the assumed area, so the calculations for this case are complete.

The following table summarizes calculated heat rejection surface designs for four different numbers of tubes.

## CONCEPTUAL DESIGN OF AN UNDERSEA HEAT REJECTION SURFACE Continued

TABLE E-1

## HEAT REJECTION SURFACE DESIGN COMPUTATIONS

	NUMBER OF TUBES			
	<u>7</u>	<u>10</u>	<u>20</u>	<u>100</u>
1 G (lbm/hr-ft <sup>2</sup> )	9.69x10 <sup>5</sup>	6.78x10 <sup>5</sup>	3.39x10 <sup>5</sup>	6.78x10 <sup>4</sup>
2 h <sub>io</sub> (Btu/hr-ft <sup>2</sup> -F)	749	612	396	125
3 Tubeside pressure drop (psi)	1.05x10 <sup>-1</sup>	4.18x10 <sup>-2</sup>	7.12x10 <sup>-3</sup>	1.54x10 <sup>-4</sup>
4 Tube length (ft)	23.5	17.2	10.0	3.75
Base surface heat flux (Btu/hr-ft <sup>2</sup> )	1.94x10 <sup>4</sup>	1.85x10 <sup>4</sup>	1.59x10 <sup>4</sup>	8.49x10 <sup>3</sup>
5 Surface temperature T <sub>s</sub> (F)	124	120	110	82
6 h <sub>o</sub> (Btu/hr-ft <sup>2</sup> -F)	209	206	195	154
h <sub>cyl</sub> (Btu/hr-ft <sup>2</sup> -F)	318	303	275	151
Fin spacing, D, (in)	1.50	1.32	1.01	0.69
Fin height, b, (in)	3.68	3.70	3.75	3.80
Fin thickness, a, (in)	0.64	0.60	0.50	0.40
h <sub>G</sub> (Btu/hr-ft <sup>2</sup> -F)	574	584	589	592
h <sub>GR</sub> (Btu/hr-ft <sup>2</sup> -F)	268	270	271	271
7 U (Btu/hr-ft <sup>2</sup> -F)	197	188	161	85.5
8 Base surface area (ft <sup>2</sup> )	86	90	105	197

## CONCEPTUAL DESIGN OF AN UNDERSEA HEAT REJECTION SURFACE Continued

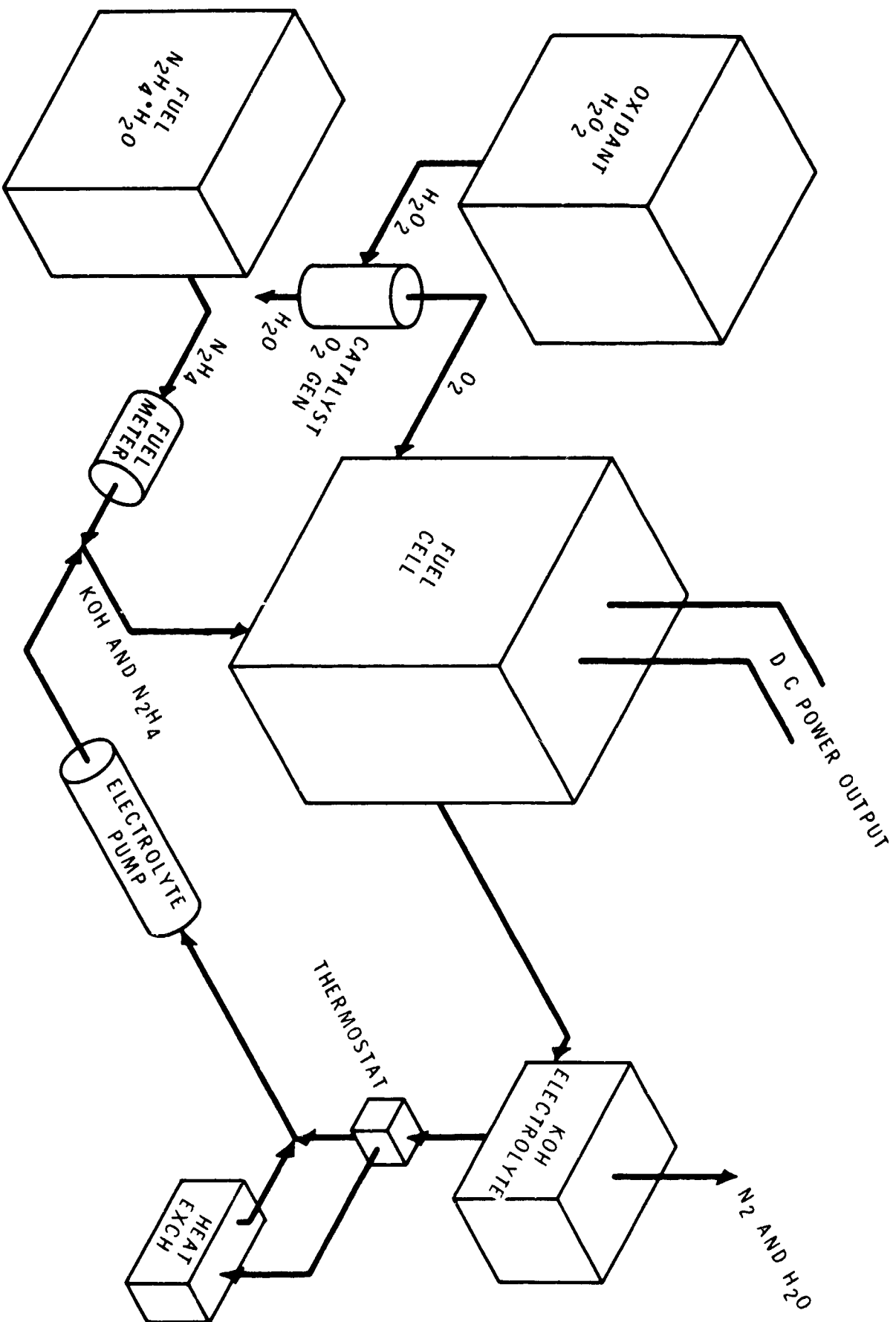
The computed designs show that base surface heat transfer area decreases with number of tubes over the range considered. Seven tubes yielded the smallest base surface heat transfer area. Because of the extreme length, it would be advisable to construct a multipass exchanger. If a four-pass (each six feet long) exchanger were used, 180-degree return bends would increase the total tubeside pressure drop to 0.2 psi - the allowable value. Therefore, this arrangement is recommended for design.

A detailed design of this exchanger should include an investigation of different fin height-spacing-thickness combinations on each pass. Also, it should include an investigation of the economics of extra fin weight versus base surface plus fins eliminated.

If the allowable pressure drop had been great enough, base surface heat transfer area would have minimized with number of tubes. The minimum is caused by two opposing effects. Inside heat transfer coefficient increases as the number of tubes decreases because of reduced flow area. On the other hand, gross heat transfer coefficient decreases with a reduction in number of tubes. This causes the overall heat transfer coefficient to maximize and the base surface heat transfer area to minimize.

# $\text{N}_2\text{H}_4 - \text{H}_2\text{O}_2$ FUEL CELL SIMPLIFIED SCHEMATIC

FIGURE E-1



## TERMS AND SYMBOLS, APPENDIX E

a	Fin thickness, in
A	Base surface heat transfer area, $\text{ft}^2$
$A_{\text{tube}}$	Inside cross sectional area of a tube, $\text{ft}^2$
b	Fin height, in
$C_p$	Specific heat at constant pressure, $\text{Btu/lbm-F}$
d	Inside tube diameter, ft
D	Fin spacing, in
g	Acceleration of gravity - $\text{ft/sec}^2$
$g_c$	Conversion constant = $4.18 \times 10^9 \frac{\text{lbm}}{\text{lbf}} \times \frac{\text{ft}}{\text{hr}^2}$
G	Mass flow rate, $\text{lbm/hr-ft}^2$
h	Heat transfer coefficient, $\text{Btu/hr-ft}^2\text{-F}$
k	Thermal conductivity, $\text{Btu/hr-ft}^2\text{-F/in}$ or $\text{Btu/hr-ft-F}$
n	number of tubes
P	Pressure, psia
Pr	Prandtl number, $C_p \mu / k$
q	Heat flow rate, $\text{Btu/hr}$
S	Base surface area per unit tube length, $\text{ft}^2/\text{ft}$
t	Tube metal thickness, in
T	Temperature, F
U	Overall heat transfer coefficient, $\text{Btu/hr-ft}^2\text{-F}$
x	Vertical coordinate dimension, ft
w	Mass rate, $\text{lbm/hr}$

## TERMS AND SYMBOLS, APPENDIX E Continued

## GREEK

$\beta$	Coefficient of thermal expansion, $F^{-1}$
$\Delta$	Signifies a change
$\mu$	Viscosity, $\text{lbm/ft-hr}$
$\rho$	Density $\text{lbm/ft}^3$
$\nu$	Kinematic viscosity, $\text{ft}^2/\text{hr}$

## SUBSCRIPTS

a	Ambient
avg	Average
B	Bulk
c	Corrected
cyl	Cylinder
D	Fouling
G	Gross
GR	Gross revised
io	Inside, but referred to base surface
m	Evaluated for fin metal
o	Evaluated at base surface
S	Surface

## APPENDIX F

## CASE 3 - PLUME CALCULATIONS

The following calculations illustrate application of the plume model to the problem defined for Case 3. The problem and results are given in Table XII and Figures 66, 69, and 70. Symbols are defined at the end of Chapters V and VI.

## PROBLEM

Exchanger depth = 25 feet

Constant surrounding temperature,  $t_o = 15.556$  C (60 F)

Warm water leaving exchanger,  $t_1 = 21.111$  C (70 F)

Vertical velocity leaving exchanger,  $w_1 = 15.240$  cm/sec or 0.5 ft/sec

Diameter of exchanger,  $d_o = 1.5$  feet

## POINT 1

$z = 0$  feet

$d_o = 1.5$  feet or 45.72 cm

Cross sectional flow area,  $\text{cm}^2 = 729.66 d_o^2$  where  $d_o$  is in feet

Flow area =  $(729.66)(1.5)^2 = 1,642 \text{ cm}^2$

From Equation V-51b, approximate  $P_1 = 10 + \frac{25}{3.3} = 17.6$  decibars

## Mass Flow Rate

At the mean plume temperature,  $t_{ave} = \frac{60 + 70}{2} = 65$  F or 18.333 C

From Table B-1 in Appendix B

$$\alpha_{35,0,P} = 0.97256 \text{ cm}^3/\text{g}$$

From Figure B-2 in the appendix at  $t/2 = \frac{18.333}{2} = 9.2$  C, or 48.6 F

$$\beta = 88.0 \times 10^{-6} \text{ 1/F or } 158.5 \times 10^{-6} \text{ 1/C}$$

From Equation V-52

$$\begin{aligned} \alpha_{35,18.333,P} &= 0.97256 (1 + 158.5 \times 10^{-6} \times 18.333) \\ &= 0.97539 \text{ cm}^3/\text{g} \end{aligned}$$

$$\text{Mass flow rate, } w_1 = \frac{(15.240)(1,642)}{(0.97539)} = 25,655 \text{ g/sec}$$

$$\text{Mass flow ratio} = \frac{w_1}{w_1} = 1.000$$

## POINT 1 Continued

Froude number, using appropriate temperature units

$$\text{At } t_o/2 = \frac{15.556}{2} = 7.8 \text{ C} \quad \beta_o = 144 \times 10^{-6} \text{ 1/C (Figure B-2)}$$

$$\text{At } t_1/2 = \frac{21.111}{2} = 10.6 \text{ C} \quad \beta_1 = 172 \times 10^{-6} \text{ 1/C (Figure B-2)}$$

From Equation V-53,

$$\frac{\rho_o}{\rho_1} = \frac{1 + \beta_1 t_1}{1 + \beta_o t_o} = \frac{1 + 172 \times 10^{-6} \times 21.111}{1 + 144 \times 10^{-6} \times 15.556}$$

$$\frac{\rho_o}{\rho_1} = \frac{1.003631}{1.002240} = 1.001387$$

From Equation V-44,

$$F_1 = \frac{(15.240)^2}{(980.7)(45.72)(1.001387-1)} = 3.735$$

$$\sqrt{F_1} = 3.735 = 1.933$$

Mean bulk temperature difference

$$\Delta t_1 = t_1 - t_o = 21.111 - 15.556 = 5.555 \text{ C}$$

## Summary

$$z = 0 \text{ feet} \quad d_o = 1.5 \text{ feet (45.72 cm)} \quad w_1 = 15.240 \text{ cm/sec}$$

$$W_1 = 25,655 \text{ g/sec} \quad \rho_o/\rho_1 = 1.001387$$

$$F_1 = 3.735 \quad \sqrt{F_1} = 1.933$$

$$t_o = 60 \text{ F} = 15.556 \text{ C} \quad t_1 = 70 \text{ F} = 21.111 \text{ C}$$

$$\Delta t_1 = 5.555 \text{ C}$$



## POINT 2

$$z_2 = 5 \text{ feet}$$

Mass flow ratio,  $w_2/w_1$

From Equation V-42, assuming  $(\rho_0/\rho_1)^{1/2} = 1$

$$X = \frac{5}{(1.5)(1.933)} = 1.724$$

For  $X < 3$  from Equation V-40

$$\frac{w_2}{w_1} = \frac{(0.32)(5)}{(1.5)} = 1.067$$

$$w_2 = (1.067)(25,655) = 27,374 \text{ g/sec}$$

From Equation V-46b

$$\Delta t_2 = \frac{5.555}{1.067} = 5.206 \text{ C}$$

$$t_2 = 5.206 + 15.556 = 20.762 \text{ C}$$

## POINT 3

$$z_3 = 10 \text{ feet}$$

From Equation V-42

$$X = \frac{(10)}{(1.5)(1.933)} = 3.448$$

For  $X > 3$  from Equation V-41

$$Y = (0.150)(3.448)^{1.67} = 1.184$$

From Equation V-43

$$w_3/w_1 = (1.184)(1.933) = 2.289$$

$$w_3 = (2.289)(25,655) = 58,724 \text{ g/sec}$$

## POINT 3 Continued

From Equation V-46b

$$\Delta t_3 = \frac{5.555}{2.289} = 2.427 \text{ C}$$

$$t_3 = 2.427 + 15.556 = 17.983 \text{ C}$$

Points 4, 5, and 6 are similarly calculated. As the penetration,  $z$ , increases, the parameter  $X$  and  $W/W_1$  increase.

## MEAN VELOCITY

The calculated results are used to check the fictitious penetration,  $z^*$ , beyond which the buoyancy or mean bulk  $\Delta t$  decay follows the  $z^{-5/3}$  relation. From Figure 66, the extrapolation of the straight-line portion of the temperature decay curve gives  $z^* = 6$  feet, and the ratio  $(z^*/d_0) = 4$  diameters. From Equation V-83, the predicted

$$(z^*/d_0) = (3.1)(3.735)^{0.2} = 4.0 \text{ diameters}$$

Equation V-55 is used to calculate the mean velocity  $w$  at the various penetration points, using  $w_1 = 15.240$  cm per second.

At Point 2,  $z = 5$  feet

$$w_2 = (15.240)(5-6)^{-1/3}$$

Since  $(z-z^*)$  is negative, expansion of the plume has not begun and

$$w_2 = w_1 = 15.240 \text{ cm per sec}$$

At Point 3,  $z = 10$  feet

$$w_3 = (15.240)(10-6)^{-1/3} = 9.585 \text{ cm per sec}$$

Table XII gives the mean velocities at the six values of  $z$  under consideration.

## PLUME RADIUS

The plume radius at various distances from the heat source is calculated from Equation V-57.  $W$  and  $w$  are already available. To simplify the computation without sacrificing any accuracy,  $\rho$  in Equation V-57 can be assumed constant at all distances and equal to the value at  $t_{ave} = 65$  F. The previously calculated value is

$$\rho_{ave} = \frac{1}{\alpha_{35,18.333,p}} = \frac{1}{0.97539} = 1.025230 \text{ g/sec}$$

The justification for carrying the value of  $\rho$  to six decimal places is to maintain accuracy in case density differences or ratios are required during the solution. Substituting the constant value of  $\rho$  into Equation V-57, the equation for the plume radius is the following.

$$R, \text{ feet} = \frac{1}{54.6} \sqrt{\frac{W}{w}}$$

Using the values of  $W$  and  $w$  from Table XII

$$\text{At Point 2, } z = 5 \text{ feet} \quad R \cong R_1 = 0.75 \text{ feet}$$

$$\text{At Point 3, } z = 10 \text{ feet}$$

$$R = \frac{1}{54.6} \sqrt{\frac{58,724}{9.585}} = 1.436 \text{ feet}$$

MAXIMUM  $\Delta t$ 

The maximum temperature difference at the axis of the plume is calculated as 3.16 times the mean bulk  $\Delta t$ . The distance from the heat source where max  $\Delta t$  is equal to the initial  $\Delta t_1$  is determined as follows.

- 1 Divide the initial  $\Delta t_1$  by 3.16

$$\text{For Case 3, } \frac{\Delta t_1}{3.16} = \frac{5.555}{3.16} = 1.758 \text{ C}$$

- 2 After plotting the mean bulk  $\Delta t$  profile in Figure 69, the point at which the mean bulk  $\Delta t = 1.758$  C corresponds to  $z = 12$  feet. This determines the vertical portion of the max  $\Delta t$  profile.

## APPENDIX G

## PORT HUENEME HARBOR TEST DATA

TABLE G-1

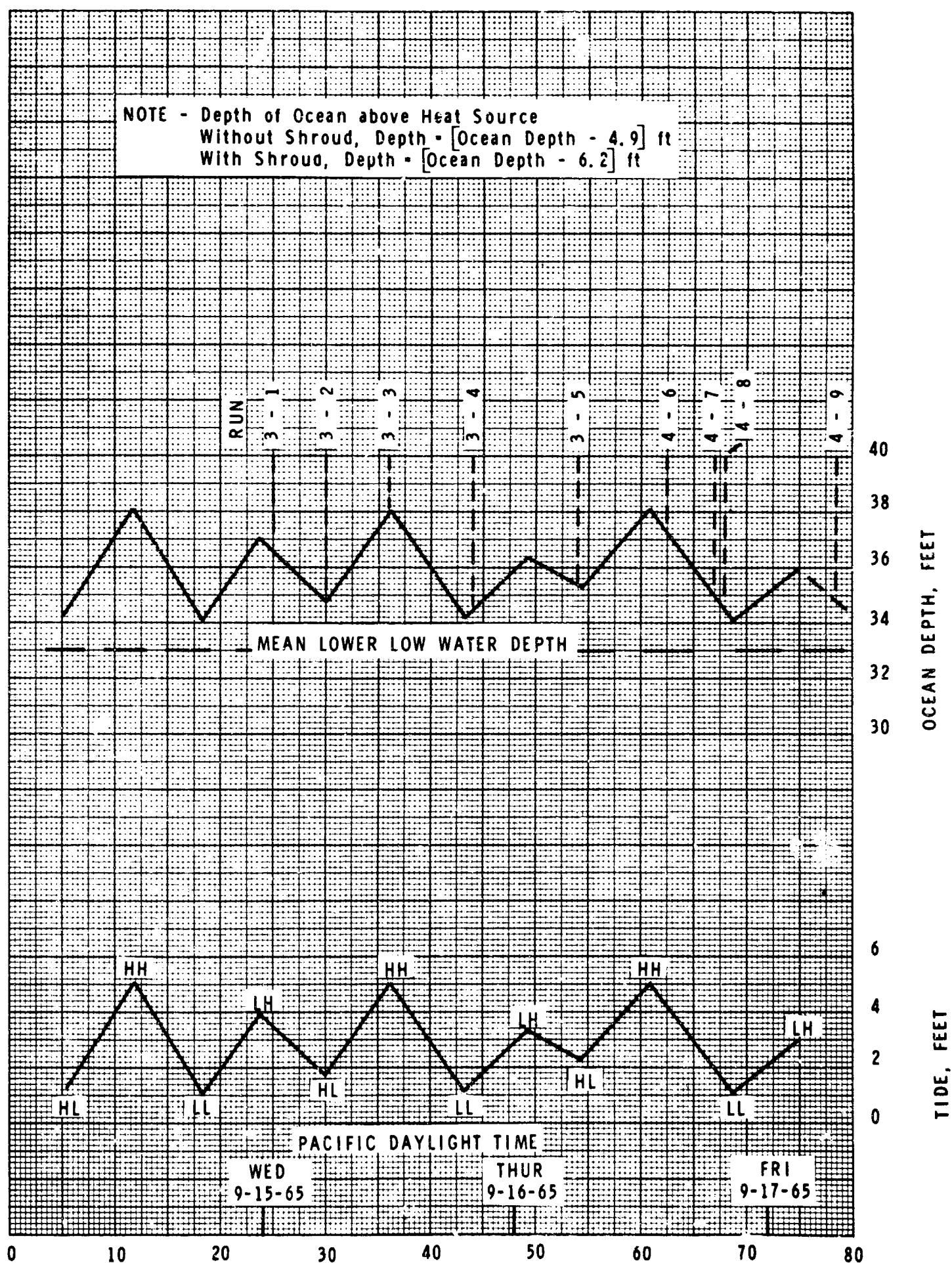
## GROSS HEAT TRANSFER COEFFICIENT DATA

<u>DATE</u>	<u>TIME (HRS)</u>	<u>HEAT FLUX (BTU/HR-FT<sup>2</sup>) x10<sup>-4</sup></u>	<u>AVERAGE TEMPERATURE T<sub>avg</sub> (F)</u>	<u>TEMPERATURE DIFFERENCE T<sub>S</sub> - T<sub>a</sub> (F)</u>	<u>GROSS HEAT TRANSFER COEFFICIENT (BTU/HR-FT<sup>2</sup>-F)</u>
9-15-65	0035	1.16	70.2	27.4	423
	0210	1.16	70.3	28.6	405
	0600	1.13	71.7	28.6	396
	0615	1.15	72.0	29.6	387
	0635	1.17	72.4	30.1	389
	0715	1.15	72.8	30.5	377
	0725	1.17	72.9	30.7	381
	1200	1.18	74.0	32.2	369
	1300	1.17	74.5	33.1	354
	1920	1.16	72.4	28.0	415
	2000	1.19	73.8	28.4	418
9-16-65	0620	1.15	72.2	30.0	383
	0700	1.16	71.8	29.2	397
	1410	1.18	74.6	28.9	407
	1510	1.18	73.8	29.7	396
	1850	1.17	72.3	29.7	394
	1910	1.17	71.5	28.1	416
	1925	1.18	72.2	29.5	400
	2000	1.19	72.0	29.1	407
	2025	1.19	72.0	29.2	406
	2045	1.19	71.4	27.9	424
9-17-65	0610	1.15	73.9	30.4	378
	0650	1.16	73.7	29.9	386
	0710	1.16	74.4	31.3	371

GB

## OCEAN TIDE AND DEPTH

FIGURE G-1

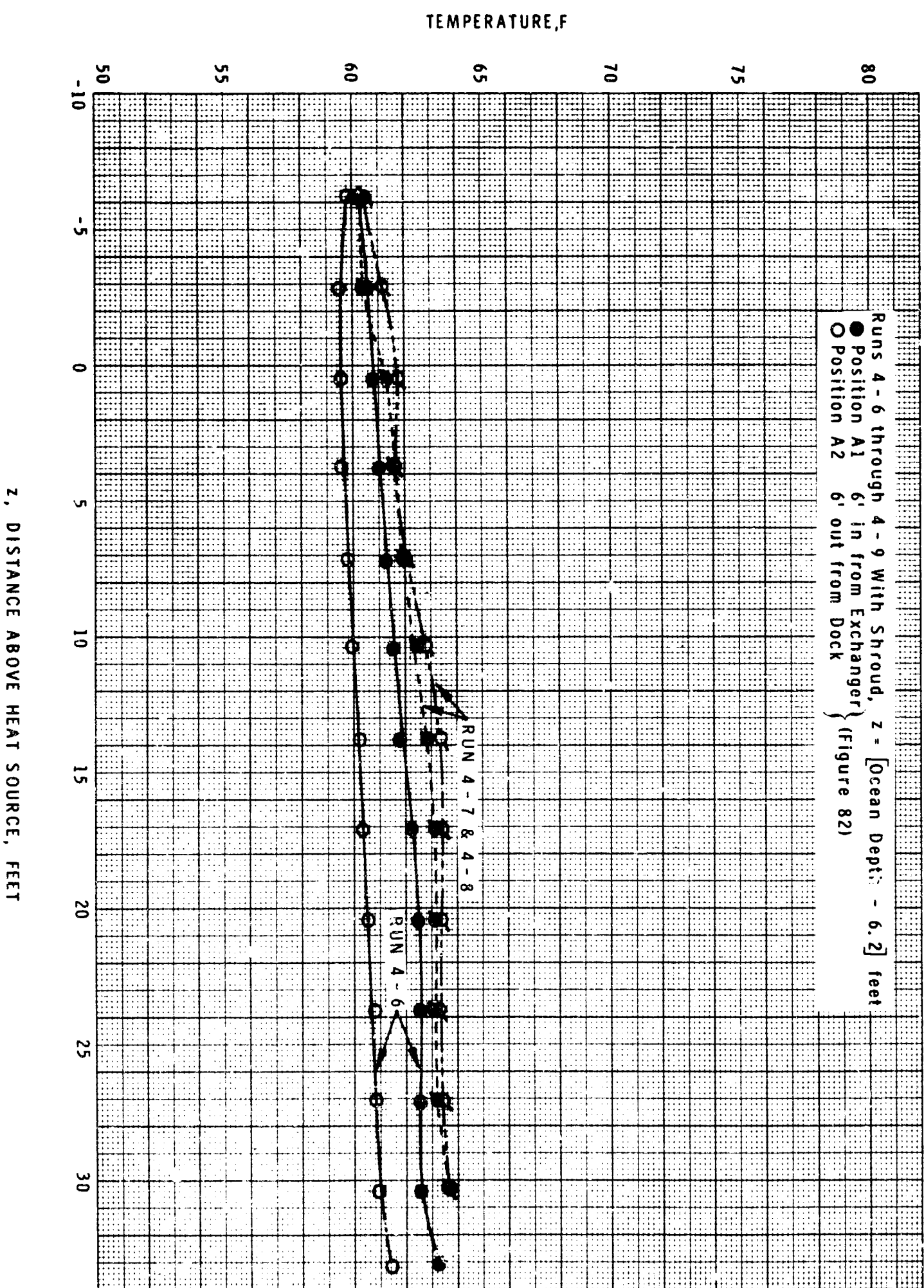


TIME FROM 0000 TUESDAY, SEPT 14, 1965, HOURS

CB

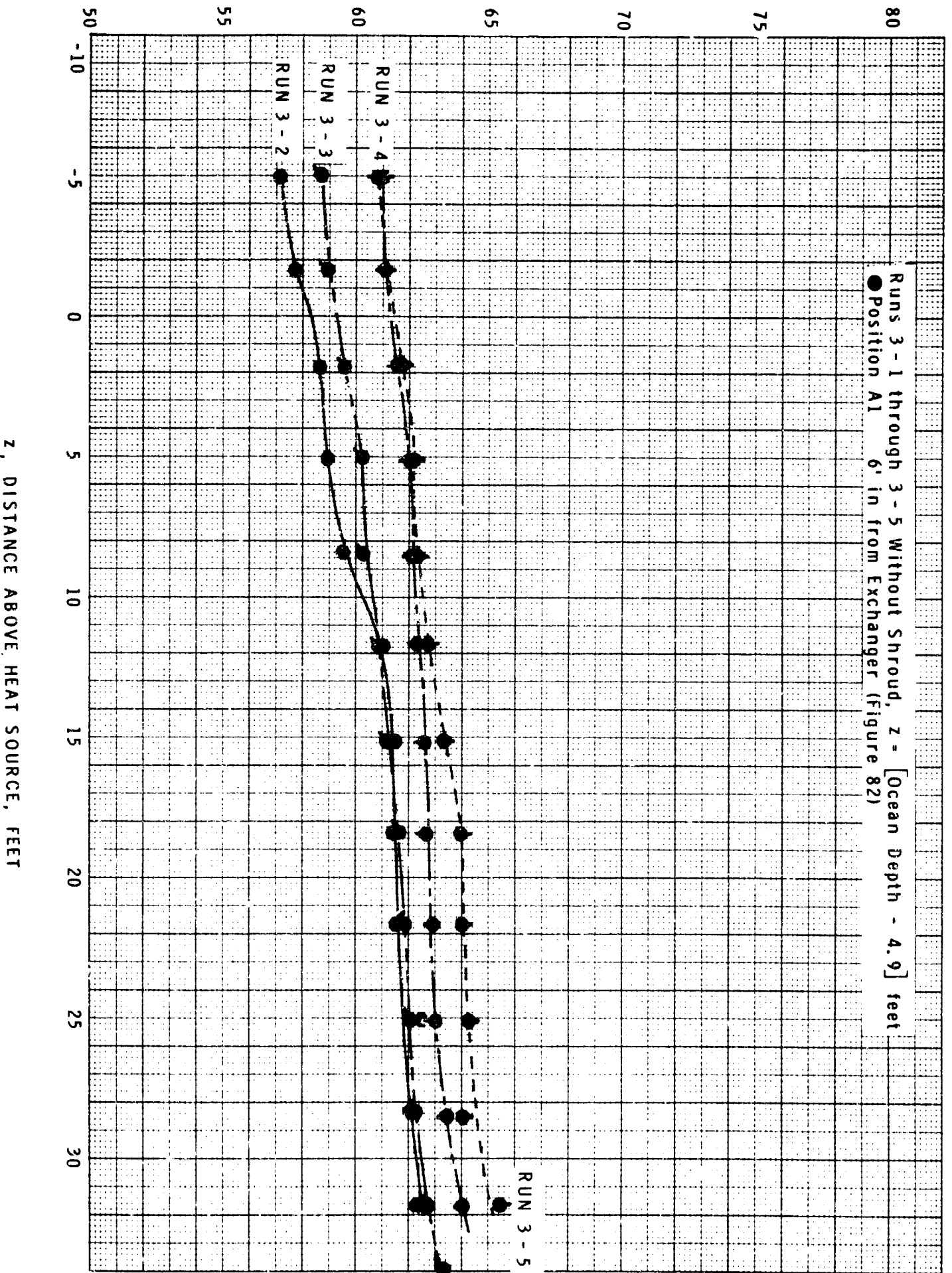
# OCEAN TEMPERATURE PROFILE

FIGURE G-3



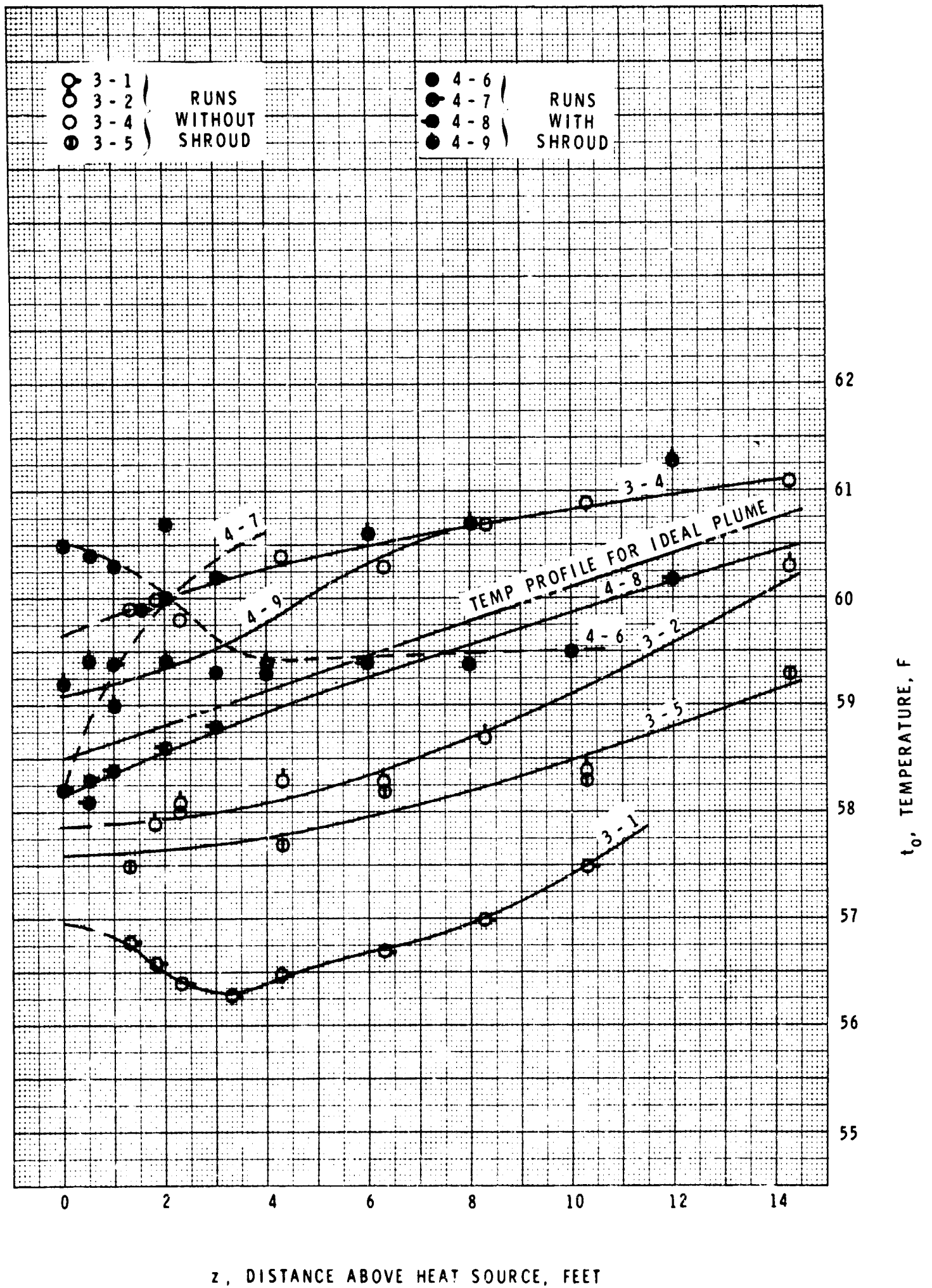
# OCEAN TEMPERATURE PROFILE

FIGURE G-2



# OCEAN AMBIENT TEMPERATURE PLUME TEMPERATURE PROBE DATA

FIGURE G-4





UNCLASSIFIED

Security Classification

## DOCUMENT CONTROL DATA - R&amp;D

(Security classification of title, body of abstract and indexing annotation must be entered when the overall report is classified)

1. ORIGINATING ACTIVITY (Corporate author) C F BRAUN & CO Alhambra, California		2a. REPORT SECURITY CLASSIFICATION Unclassified	
		2b. GROUP	
3. REPORT TITLE  STUDY OF HEAT TRANSFER AND FOULING OF HEAT TRANSFER SURFACES IN THE DEEP OCEAN			
4. DESCRIPTIVE NOTES (Type of report and inclusive dates) Final - July 1964 to 26 November 1965			
5. AUTHOR(S) (Last name, first name, initial)			
6. REPORT DATE 26 November 1965		7a. TOTAL NO. OF PAGES 252	7b. NO. OF REFS 177
8a. CONTRACT OR GRANT NO. NBy-32274		9a. ORIGINATOR'S REPORT NUMBER(S)  Project No. 2650-P	
b. PROJECT NO.		9b. OTHER REPORT NO(S) (Any other numbers that may be assigned this report)	
c.			
d.			
10. AVAILABILITY/LIMITATION NOTICES  Distribution of this document is unlimited			
11. SUPPLEMENTARY NOTES		12. SPONSORING MILITARY ACTIVITY  U. S. Naval Civil Engineering Laboratory Port Hueneme, California 93041	
13. ABSTRACT  Covered both theoretically and by extensive correlated tests are free convection at Rayleigh Numbers above $10^{10}$ , with varying geometries and radii of curvature of heat rejection surfaces. A design method is developed, with examples of its use for design of rejection devices for power development in sea water. A prototype was built and tested in Port Hueneme Harbor.  The extent of and dissipation of a plume of heated water over the convector are predicted theoretically and correlated with laboratory tests and the harbor tests.  Selected materials were exposed for corrosion and marine fouling at shallow water, 300 feet and 4,500 feet deep in the open ocean; heat transfer results were correlated with those predicted theoretically and determined in full scale laboratory experiments. No fouling was observed on heated surfaces at 100, 120 and 140 degrees F, but fouling appeared to be accelerated on non-heated parts of the test apparatus exposed to the warmed water.			

DD FORM 1473  
1 JAN 64

UNCLASSIFIED

Security Classification

14. KEY WORDS	LINK A		LINK B		LINK C	
	ROLE	WT	ROLE	WT	ROLE	WT
Heat transfer Heat distributing units Fouling Corrosion Surfaces Convection						

## INSTRUCTIONS

1. **ORIGINATING ACTIVITY:** Enter the name and address of the contractor, subcontractor, grantee, Department of Defense activity or other organization (*corporate author*) issuing the report.

2a. **REPORT SECURITY CLASSIFICATION:** Enter the overall security classification of the report. Indicate whether "Restricted Data" is included. Marking is to be in accordance with appropriate security regulations.

2b. **GROUP:** Automatic downgrading is specified in DoD Directive 5200.10 and Armed Forces Industrial Manual. Enter the group number. Also, when applicable, show that optional markings have been used for Group 3 and Group 4 as authorized.

3. **REPORT TITLE:** Enter the complete report title in all capital letters. Titles in all cases should be unclassified. If a meaningful title cannot be selected without classification, show title classification in all capitals in parenthesis immediately following the title.

4. **DESCRIPTIVE NOTES:** If appropriate, enter the type of report, e.g., interim, progress, summary, annual, or final. Give the inclusive dates when a specific reporting period is covered.

5. **AUTHOR(S):** Enter the name(s) of author(s) as shown on or in the report. Enter last name, first name, middle initial. If military, show rank and branch of service. The name of the principal author is an absolute minimum requirement.

6. **REPORT DATE:** Enter the date of the report as day, month, year, or month, year. If more than one date appears on the report, use date of publication.

7a. **TOTAL NUMBER OF PAGES:** The total page count should follow normal pagination procedures, i.e., enter the number of pages containing information.

7b. **NUMBER OF REFERENCES:** Enter the total number of references cited in the report.

8a. **CONTRACT OR GRANT NUMBER:** If appropriate, enter the applicable number of the contract or grant under which the report was written.

8b, 8c, & 8d. **PROJECT NUMBER:** Enter the appropriate military department identification, such as project number, subproject number, system numbers, task number, etc.

9a. **ORIGINATOR'S REPORT NUMBER(S):** Enter the official report number by which the document will be identified and controlled by the originating activity. This number must be unique to this report.

9b. **OTHER REPORT NUMBER(S):** If the report has been assigned any other report numbers (*either by the originator or by the sponsor*), also enter this number(s).

10. **AVAILABILITY/LIMITATION NOTICES:** Enter any limitations on further dissemination of the report, other than those

imposed by security classification, using standard statements such as:

- (1) "Qualified requesters may obtain copies of this report from DDC."
- (2) "Foreign announcement and dissemination of this report by DDC is not authorized."
- (3) "U. S. Government agencies may obtain copies of this report directly from DDC. Other qualified DDC users shall request through \_\_\_\_\_."
- (4) "U. S. military agencies may obtain copies of this report directly from DDC. Other qualified users shall request through \_\_\_\_\_."
- (5) "All distribution of this report is controlled. Qualified DDC users shall request through \_\_\_\_\_."

If the report has been furnished to the Office of Technical Services, Department of Commerce, for sale to the public, indicate this fact and enter the price, if known.

11. **SUPPLEMENTARY NOTES:** Use for additional explanatory notes.

12. **SPONSORING MILITARY ACTIVITY:** Enter the name of the departmental project office or laboratory sponsoring (*paying for*) the research and development. Include address.

13. **ABSTRACT:** Enter an abstract giving a brief and factual summary of the document indicative of the report, even though it may also appear elsewhere in the body of the technical report. If additional space is required, a continuation sheet shall be attached.

It is highly desirable that the abstract of classified reports be unclassified. Each paragraph of the abstract shall end with an indication of the military security classification of the information in the paragraph, represented as (TS), (S), (C), or (U).

There is no limitation on the length of the abstract. However, the suggested length is from 150 to 225 words.

14. **KEY WORDS:** Key words are technically meaningful terms or short phrases that characterize a report and may be used as index entries for cataloging the report. Key words must be selected so that no security classification is required. Identifiers, such as equipment model designation, trade name, military project code name, geographic location, may be used as key words but will be followed by an indication of technical context. The assignment of links, roles, and weights is optional.